UNIVERSITY OF OXFORD

DEPARTMENT OF ENGINEERING SCIENCE

THERMO-MECHANICAL PERFORMANCE AND NOVEL APPLICATIONS OF NANOCOMPOSITES INCORPORATING METAL-ORGANIC FRAMEWORKS

MAHDI EZWAN MAHMOUD
BALLIOL COLLEGE

AUGUST 2017

A dissertation submitted for the degree of Doctor of Philosophy

PREFACE

This dissertation is submitted for the degree of Doctor of Philosophy in the University of Oxford, United Kingdom. The research work described throughout this dissertation was carried out by the author in the period between October 2013 to December 2016, under the supervision of Professor J.C. Tan in the Department of Engineering Science at the University of Oxford.

To the best of my knowledge, the work described in this dissertation is original, except where due reference has been made of the work(s) of others, and nothing has been included that is the outcome of work done in collaboration of others, except where specifically noted. No part of this dissertation, or any similar to it, has been, or is currently being submitted for any degree at this or any other university. This dissertation is less than 60,000 words in length.

Mahdi E. M.
Oxford
August 2017

ABSTRACT

This work investigated the thermo-mechanical responses of two classes of prototypical polymer/Metal-Organic Framework (MOF) composites: Matrimid/Zeolitic Imidazolate Framework (ZIF)-8 and Polyurethane (PU)/ZIF-8, and explored their potential application in the uptake/retention of iodine and the reversible uptake of ethylene. The aim is to develop a structure-property relationship and elucidate the influence of ZIF-8 nanoparticles on the performance of the nanocomposite, while establishing a contrast between glassy (Matrimid) and rubbery (PU) matrices *vis-à-vis* its interactions with ZIF-8 nanoparticles (MOF fillers).

Experimental techniques such as dynamic mechanical analysis, uniaxial tensile tests, and nanoindentation were employed to study the variation to thermo-mechanical properties as a function of the concentration(s) of MOF nanoparticles. With 30 wt.% ZIF-8 content, it was demonstrated that the addition of filler nanoparticles decreased the quasi-static mechanical properties of the Matrimid/ZIF-8 nanocomposite (17.5% decrease in the Young's modulus and ~90% drop in ductility), but benefit the PU/ZIF-8 nanocomposite (~700% increase in the Young's modulus while retaining ~70% ductility of the neat PU matrix). The dynamic mechanical response of Matrimid/ZIF-8 nanocomposite remained almost comparable with its matrix, but PU/ZIF-8 nanocomposite exhibited tunability in its dynamic response. Higher concentrations of ZIF-8 nanoparticles resulted in a significant rise in storage moduli and decrease in loss moduli.

The PU/ZIF-8 (30 wt.% of ZIF-8) nanocomposite exhibited significant uptake/retention of iodine (~32 wt.%) and reversible uptake of ethylene (~0.6 mmol g^{-1} at 5 °C). This is attributed to the molecular accessibility afforded by the PU matrix in conjunction with the porosity and chemical affinity of the 2-methylimidazolate ligands with iodine and ethylene guest species. In contrast, the glassy Matrimid matrix demonstrated poorer uptake performance due to its limited accessibility and robust microstructural features, which greatly limited the interactions between the ZIF-8 nanoparticles with iodine and ethylene. It was also confirmed that the response of the matrix dictates the overall performance of the nanocomposites because they constitute the structural majority of the composite system, and determine crucial factors such as accessibility to the functional MOF nanoparticles incorporated within.

ACKNOWLEDGEMENTS

Verba Volant, Scripta Manent

I would like to extend my utmost gratitude to Yayasan Khazanah (YK) for comprehensively funding my studies in the University of Oxford. This also extends to Balliol College and the Department of Engineering Science (Oxford) for granting me provisional funding(s) to attend academic conferences throughout my studentship.

I would like to warmly thank my academic supervisor, Prof. J.C. Tan, who has been instrumental in guiding me throughout my studies and refining my approaches towards my work, culminating in this thesis, a book chapter, and a few publications.

A special thanks goes out to the Research Complex at Harwell (RCaH) and LIMA for granting access to equipment (Dr G. Stenning, Dr M. Jura, Dr J. Taylor, and Dr K. Dragnevski) and providing expert consultations. I would also like to acknowledge Dr J. Silvestre at the University of Alicante for our collaborative effort and testing our samples at his laboratory.

An (special) honourable mention goes out to my college mates (Hadrien M. and Nikola G.) for keeping my sanity in check throughout my studies and for the occasional shenanigans in Oxford, Amsterdam, Roses, and Morocco.

I would also like to thank my immediate colleagues from the MMC Lab (Matthew, Abhijeet, Jason, and Kirill) for their continuous help, advice, fun times, and occasional light banter, which kept things less than mundane and monotonic. This extends to the people in ETB 40.35 (Rango & Rodolfo, etc) as well.

This thesis is dedicated to my *khânevâde*, and those who have been supportive of my endeavours in the course of my graduate studies.

TABLE OF CONTENTS

NOMENCLATURE

Acronyms	Full term
2-D	Two-Dimensional
3-D	Three-Dimensional
6FDA-DAM	2,2-bis(3,4-carboxyphenyl) hexafluoropropanedianhydride diaminomesitylene
A_c	Contact area established under the indenter tip
AFM	Atomic Force Microscopy
Au	Gold
BDC	Benzene-1,4-dicarboxylic acid
bmim	1-Butyl-3-Methylimidazolium
BTC	Benzene-1,3,5-tricarboxylic acid
C_2H_4	Ethylene
C_2H_6	Ethane
$CHCl_3$	Chloroform
C_p	Heat capacity
CNT	Carbon Nanotube
CP	Coordination Polymer
CPO	Metal Organic Framework-74
CuTPA	Copper Terephthalate
DMA	Dynamic Mechanical Analysis
dobdc	2,5-dioxido-1,4-benzenedicarboxylate
dox	Doxorubicin
E	Young's modulus
E'	Storage modulus

E”	Loss modulus
E*	Dynamic modulus
E_i	Young’s modulus (Indenter tip)
EM	Electron Microscopy
E_r	Reduced modulus
FEG-SEM	Field Emission Gun-Scanning Electron Microscope
Fe_3O_4	Magnetite; Iron (II,III) Oxide
GO	Graphene Oxide
GC	Graphitised Carbon
G_f	Fracture energy
H	Nanohardness
H-bonds	Hydrogen Bonding
HKUST-1	Hong Kong University of Science and Technology-1
I_2	Iodine
IL	Ionic Liquid
IRMOF	Isoreticular Metal-Organic Framework
IUPAC	International Union of Pure and Applied Chemistry
LiTFSI	Bis(trifluoromethane)sulfonimide lithium salt
MIL	Materials Institute Lavoisier
mIm	2-methylimidazolate
MMMs	Mixed-Matrix Membranes
MOF	Metal-Organic Framework
P84	Polyimide P84® (Evonik Fibres GmbH)
P	Normal Indentation Load

PAN	Polyacrylonitrile
PCM	Phase-Changing Materials
PEBAX	Polyether-Block-Amides (Arkema)
PEK-c	Cardo polyetherketone
PEEK	Polyether ether ketone
PEO	Polyethylene Oxide
PIM	Polymer of Intrinsic Microporosity
PMMA	Poly (methyl metacrylate)
Pt	Platinum
PTMSP	Poly-1-trimethylsilyl-1-propyne
PU	Polyurethane
PP	Pennisetum Purpuruem
PVA	Poly (vinyl alcohol)
PVDF	Polyvinylidene difluoride
rGO	Reduced Graphene Oxide
SA	Stearic Acid
SAV	Solvent Accessible Volume
S_{BET}	Brunauer-Emmett-Teller (BET) surface area
SBU	Secondary Building Unit
SEM	Scanning Electron Microscope
tan δ	Loss tangent (Dissipation factor)
TEM	Transmission Electron Microscope
Tf_2N	(Trifluoromethylsulfonyl)imide
TGA	Thermogravimetric analysis

T_g	Glass transition temperature
T_β	Secondary (β) relaxation temperature
T_m	Melting temperature
THF	Tetrahydrofuran
UV	Ultraviolet
vdW	van der Waals
ν_i	Poisson's ratio (Indenter tip)
XRD	X-Ray diffraction
ZIF	Zeolitic Imidazolate Framework
ZnQ	Zinc-(bis-8-hydroxyquinoline)
ZJU	Zhejiang University
ZrO	Zirconium Oxide
ε^*	Dynamic strain
σ^*	Dynamic stress
σ_t	Tensile strength
σ_y	Yield strength

PUBLICATIONS

Articles published as a result of the works described in this thesis are listed below:

- E.M. Mahdi and J.C. Tan, 'Comprehensive composite materials II, Elsevier Publishing, *Vol. III Metal-Matrix Composites, Chapter 25*: "Metal-Organic Framework (MOF) Based Composites", In Press (2017).

- E. M. Mahdi and J.C. Tan, 'Dynamic molecular interactions between polyurethane and ZIF-8 in a polymer-MOF nanocomposite: Microstructural, thermo-mechanical, and viscoelastic effects', *Polymer*, 97, pp. 31-43 (2016).

- E. M. Mahdi, A.K. Chaudhari and J.C. Tan, 'Capture and immobilisation of iodine (I_2) utilising polymer-based ZIF-8 nanocomposite membranes', *Molecular Systems Design & Engineering*, 1, pp. 122-131 (2016).

- E. M. Mahdi and J.C. Tan, 'Mixed-matrix membranes of zeolitic imidazolate framework (ZIF-8)/Matrimid nanocomposite: Thermo-mechanical stability and viscoelasticity underpinning membrane separation performance', *Journal of Membrane Science*, 498, pp. 276–290 (2016).

- N. W. Khun, E. M. Mahdi, S. Ying, T. Sui, A.M. Korsunsky, J. C. Tan, 'Fine-scale tribological performance of zeolitic imidazolate framework (ZIF-8) based polymer nanocomposite membranes', *APL Materials*, 2, 124101 (2014).

CHAPTER ONE

Introduction

The recent attraction of employing polymeric membranes to afford wide ranging energy-and environmental-oriented applications has reached a new zenith [1-3]. The cost competitiveness underpinning emergent membrane technology [4], combined with the ease of processability and stability of organic polymers makes it a strong contender for many important industrial applications, namely selective gas separations [5, 6], pervaporation [7], desalination, and water purification [8, 9]. In fact, the study of its practical applicability will go a long way into propelling membrane technology to the forefront of commercial applications, owing largely to its promising intrinsic material functions, inert characteristics, and lower overall energy requirements [1, 2, 4]. However, current implementations of neat polymeric membranes for high-throughput processes suffer from several major drawbacks; for instance, reduced materials performance associated with membrane degradation [10-12], which necessitates its constant replacement or additional structural reinforcement(s).

There is a rapidly growing body of works demonstrating the huge potential of enhancement in the functional properties of neat polymeric membranes and composite systems, which have been highlighted by several excellent review articles [1, 2, 4, 5]. There are various proposals being made to address the inadequacy of neat polymeric membranes, particularly with regards to improvement in processing techniques [13, 14], and through the incorporation of filler phases that could alter the physico-chemical characteristics of polymeric mixtures. Processing methods, such as plasma techniques and surface modifications have been demonstrated to be effective in producing durable membranes that are potentially viable for high-end applications, *e.g.* polymer electrolyte membranes [15].

These methods produced improved gas separation performance [16], sensory abilities [17], together with reports of the scope to tailor the mechanical properties of novel composite membranes, including the Young's modulus [18, 19], tensile strength [20], and toughness [21].

Although some of the strategies outlined above were successful in enhancing the functional performance of polymeric membranes, other attempts were not, which goes to show that such improvements were not universally achievable. It might instead be dependent upon specific combinations of polymer matrix, filler inclusion, or processing techniques [22, 23]. Notwithstanding the above, subsequent developments witnessed in emerging fields such as hybrid nanomaterials and fine-scale characterisation techniques promise to address certain core challenges linked to these issues, where the inclusion of nano-sized fillers with improved dispersion may generate a good combination of mechanical [24] and functional performance [25]. Indeed, this is the rationale behind the concept of *nanocomposites* [23], for which the integration of a relatively small quantity of nanofillers into a polymer matrix will result in a marked improvement to the physico-chemical properties of novel polymer-based composites.

Notably, the last decade has witnessed the advent of a revolutionary new class of porous hybrid materials, termed Metal-Organic Frameworks (MOFs) [26, 27]. MOFs are constructed through the self-assembly of metal ions/-oxo clusters coordinated by versatile organic linkers, yielding numerous 2-D [28] and 3-D nanoporous compounds, the latter typically exhibiting exceptionally high surface area (1000-10,000 m^2 g^{-1}) [29]. Of the numerous materials discovered to date [30], Zeolitic Imidazolate Frameworks (ZIFs) [31, 32] represent a topical sub-family of MOFs, whose framework structures closely mimic the diverse topology of inorganic zeolites. While the chemical stability of ZIFs reflects those of zeolites [31], their thermo-mechanical properties [33, 34] and structural stability [35, 36]

are relatively weaker compared to their inorganic counterparts. Nevertheless, given their highly tuneable physico-chemical properties [35], ZIF-and MOF-based nanocomposites [37, 38] are at the forefront of novel nanocomposite research, targeting gas separation and purification processes [39, 40], pervaporation [41], and electrochemical energy conversion and storage systems [42]. Particularly, the prevalence of organic ligands intrinsic to the framework of ZIFs and MOFs may open up the possibility of bonding with organic sub-groups abundant in macromolecular polymers, yielding a good combination of malleability, durability, and material stability [43, 44]. These advantages work towards making MOFs applicable, both in physically and chemically demanding environments, further expanding its possible applications.

A large proportion of studies reported on polymer/MOF nanocomposites are concerned with the functional performance alone, focussing predominantly on selective adsorption and diffusion properties that govern the permselectivity of MOF-composites [6, 39, 45]. In contrast, corresponding studies pertaining to either the mechanical properties or the thermo-mechanical stability of MOF-composites, hitherto, remain remarkably scarce [37]. It is imperative that the mechanical, thermal, and (time-dependent) viscoelastic properties of MOF-based nanocomposites be studied in greater detail, because a comprehensive understanding of these physical properties will enable the prediction, rational design, and engineering of bespoke materials for practical applications.

1.1 Motivations and research questions

The recent proliferation of MOFs in a multitude of aforementioned applications is indicative of its vast potential for near future upscaling and subsequent widespread commercialisation.

Its potential for mass-scale industrial production and applicability in industrial settings is currently being vigorously explored by many researchers and organisations (such as MOF Technologies) across the world. It should also be pointed out that the rapid development of MOFs takes place in tandem with the development of other MOF-based materials, such as MOF-based composites. However, it is quite well known that the works involving MOF-based composites are tightly focussed on performance enhancement due to the synergistic effect between the MOFs and the selected matrix in the composite system, as pointed out in the previous section. As a result of this, there is a distinct but noticeable knowledge gap between the synthesis/formation of MOF-based composites and its subsequent functional performance in terms of materials' characteristics.

In order to move beyond the laboratory in the realm of MOF-based composites, it is imperative that this aforementioned gap be closed/eliminated. Elucidating the physico-chemical characteristics of MOF-based composites and its corresponding structure-property relationship represents the first shift towards industrial applications and upscaling the production of MOF-based composites. It is reasoned that the data that needs to be collected for this purpose can be realised using established techniques such as the dynamic mechanical analyses (DMA), uniaxial tensile test, nanoindentation, and various other characterisation and imaging methods (XRD, AFM, and SEM, amongst others). The determination of the physico-chemical characteristics and the structure-property relationship of the MOF-based composites can then be used to rationalise the performance data reported in published works, which represents the impetus of linking materials' characteristics and its performance. Importantly, this work intends to answer the following research questions:

- What are the advantages of forming a ZIF-8 (prototypical MOF in this work) – based composite system?

- What are the effects of the introduction of ZIF-8 nanoparticles (crystalline fillers) into a polymer matrix (polymers in this work, glassy: Matrimid, rubbery: PU) in the context of quasi-static, thermo-mechanical, and viscoelastic properties of the subsequently formed composites?
- What are the effects (if any) of the polymer matrix upon the subsequent polymer/ZIF-8 nanocomposites in the context of the aforementioned properties?
- Are the polymer/ZIF-8 nanocomposites viable for applications that are viable for ZIF-8 nanoparticles (such as gas sorption/separation of C_2H_4 and liquid adsorption of I_2), and how well does it compare performance-wise?

1.2 Research objectives

The objectives of this research are:

- To synthesise two distinct classes of polymer/MOF nanocomposite, with ZIF-8 as the prototypical MOF (crystalline fillers) and Matrimid (glassy) and polyurethane (rubbery) as the representative matrices.
- To determine the quasi-static, thermo-mechanical, and viscoelastic responses of the two classes of prototypical polymer/Metal-Organic Framework (MOF) composites: Matrimid/ZIF-8 and PU/ZIF-8.
- To develop a structure-property relationship and elucidate the influence of ZIF-8 nanoparticles (and the matrices) on the performance of the nanocomposite using previously published data, while establishing a contrast between glassy (Matrimid) and rubbery (PU) matrices *vis-à-vis* its interactions with ZIF-8 nanoparticles.

- To explore the viability of both classes of nanocomposites for the uptake/retention of I_2 (liquid adsorption) and the reversible uptake of C_2H_4 (gas adsorption).

1.3 Thesis organisation

This thesis will begin with a quick literature review for state-of-the-art polymer/MOF nanocomposites and its reported applications (Chapter 2), followed by detailing the techniques and methods that were used to fabricate and determine (Chapter 3) the thermo-mechanical, viscoelastic, and quasi-static properties of the glassy Matrimid®/ZIF-8 nanocomposites (Chapter 4) and rubbery PU/ZIF-8 nanocomposites (Chapter 5), and finally the application of the prototypical polymer/MOF nanocomposites for the adsorption and retention of I_2 (Chapter 6) and reversible uptake of C_2H_4 (Chapter 7). The structure-property relationship between the nanoscale (crystalline) MOF fillers and the (glassy and rubbery) polymer matrices and their respective influences on the nanocomposites will be detailed in Chapters 4-5, while its viability (and performance) for the aforementioned applications will be elucidated in Chapters 6-7. The work will be concluded in Chapter 8, which will also include potential future pursuits.

CHAPTER TWO

Literature Review (State-of-the-Art)

This chapter will primarily focus on the definition of MOFs and its corresponding (nano)composites, the fabrication routes, the viscoelastic, thermo-mechanical, and macro-mechanical characterisation, and reported applications of MOF-(nano)composites in literature. The author intends to critically review the current state-of-the-art *vis-à-vis* MOF-(nano)composites in the context of the aforementioned criteria. This chapter will also serve as a guideline and explain the theoretical aspects that will be used to explain the analyses and results that will be detailed in subsequent chapters of this thesis.

2.1 Introduction

Hybridising materials at the molecular level has altered the playing field, so to speak, *vis-à-vis* composites. The formation of "traditional" macroscale composite systems [46] is a well-established endeavour amongst the materials science and engineering community. Recent advances in nanomaterials synthesis and processing technology has progressed to the point where it is possible to form bespoke composites at the nano/molecular level, resulting in remarkable physico-chemical properties that were absent in its respective constituent materials.

Metal-Organic Frameworks (MOFs) [27] is a subclass of hybrid (inorganic-organic) materials that has witnessed very intense developments in the last decade [47]. Periodic metallic cores (or metal secondary building units, SBUs [48]) coordinated by

multifunctional organic linkages (ligands) to form 3-D frameworks, MOFs have vast potential to be utilised for gas storage, sorption and separation, energy conversion, catalysis, optoelectronics, and sensing applications [49, 50]. MOFs are also renowned for its astounding physico-chemical properties, such as its large surface area exceeding 1000 m^2 g^{-1} and chemical tunability [29], alongside its unprecedented framework flexibility [51] and lattice dynamics [50, 52]. However, its porous architecture comprising of organic building blocks renders MOFs susceptible to degradation from increased temperatures [34] and humidity [53], and when subject to mechanical stresses/strains prevalent in real-world applications [13]. The formation of MOF-derived composites or MOF-composite systems, in part, are to mitigate these undesirable effects, making MOFs tenable beyond its usual remit of mild temperatures and low pressure applications.

The underpinning concept of MOF-composites, ranging from state-of-the-art synthesis methods to create these composite systems, to characterisation techniques that can be utilised to unravel their structure-property relationships, will be presented. We shall also discuss recent exemplars pertaining to emergent technologies employing MOF-composite materials.

2.1.1 What are metal-organic frameworks (MOFs)?

The very term Metal-Organic Framework (MOF) is self-descriptive; MOFs are constructed from periodic metallic centres (or SBUs [48]) coordinated by organic linkages, forming a 3-D framework architecture. MOFs are porous crystalline materials featuring diverse structural and chemical variabilities. This combination results in a few unique attributes, such as:

i) Despite the presence of metals, because of (highly directional) coordination bonding of the organic ligands around a metallic core, MOFs lack the malleability associated with metallic bonds while possessing the flexibility of its organic ligands [51], thus giving 3-D structural compliance at molecular length scales [50, 52].

ii) Nanoscale porosity and long-range ordered framework dramatically increase the accessible surface area of MOFs, with surface areas reported to be 1,000 - 10,000 $m^2 g^{-1}$ [54], differing on net topology and connectivity [55].

iii) Integration of both metallic (inorganic) and organic constituents within the extended framework opens up numerous possibilities for tuning a broad range of physical properties [49] and chemical affinity [56, 57], which are absent in purely inorganic or organic materials alone.

Due to the lack of a formal naming convention for MOFs, neither from the IUPAC [58] nor researchers working in the field, most structures are named after the institution or groups that first reported them, or by adopting designations of analogous inorganic structures that they resemble. A few topical examples are illustrated below:

i) Zeolitic Imidazolate Framework (ZIFs), named as such due to its framework net topologies mimicking those of inorganic zeolites (Si−O−Si aluminosilicates) [59].

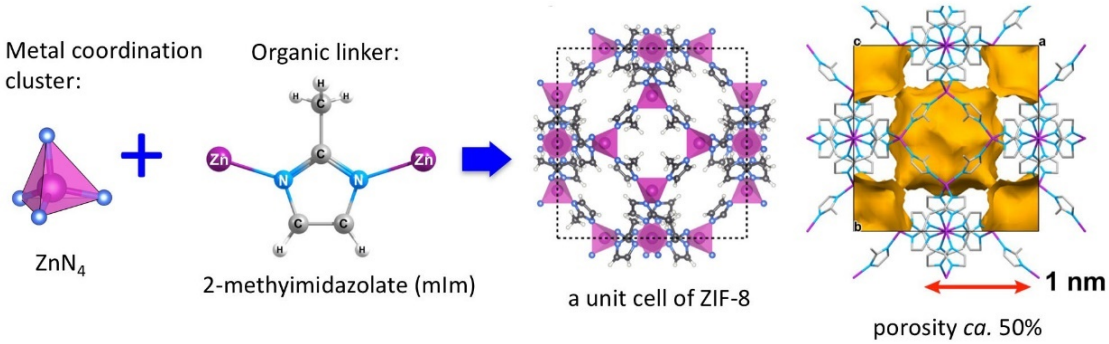

Fig. 2.1 Molecular building blocks of a topical ZIF structure termed ZIF-8, whose chemical formula is $Zn(mIm)_2$, where mIm = 2-methylimidazolate. It is built from tetrahedrally coordinated ZnN_4 clusters linked by mIm organic ligands to form a sodalite cage. The Zn−mIm−Zn bridging linkages in ZIF-8 subtend an angle of 145° at the mIm ring centre, analogous to the Si−O−Al angle in conventional aluminosilicate zeolites. Yellow surfaces correspond to the solvent accessible volume (SAV) at ~50%; note the narrow aperture (window opening) entering the larger internal pore whose size is ~1 nm. Colour code: zinc, purple; carbon, grey; nitrogen, blue; hydrogen, white [33].

ii) HKUST-1 (Hong Kong University of Science and Technology), named as such due to the University being the first to report this copper paddle-wheel MOF [60].

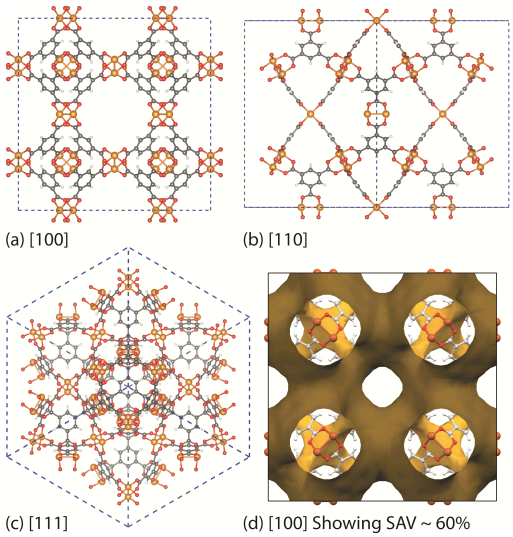

Fig. 2.2 The molecular structure of HKUST-1, whose chemical formula is $Cu_3(BTC)_2$ where BTC = benzene-1,3,5-tricarboxylic acid. Crystallographic views down the (a) [100], (b) [110], (c) [111], and (d) [100] directions displaying its solvent accessible volume (SAV) of ~60%. Colour code: copper, orange; carbon, grey; oxygen, red; hydrogen, white [52].

iii) UiO (University of Oslo), named as such due to the research group from the University first reporting this zirconium(Zr)-based MOF [61].

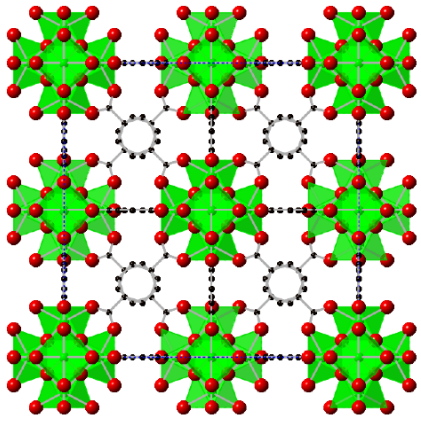

Fig. 2.3 Framework structure of UiO-66, whose chemical formula is $Zr_6O_4(OH)_4(CO_2)_{12}$. The inorganic building block is 12-coordinated ZrO clusters. Colour code: zirconia, green; carbon, dark grey; oxygen, red. Hydrogen on the organic linkers are omitted for clarity.

Given the varied chemical and structural nature(s) of MOFs, the permutation of possible MOFs is virtually limitless. Whilst thousands of MOF structures have been discovered to date, only a small subset of these structures have been identified as potentially useful and hence under detailed investigations. These include MOF families depicted in Figs. 2.1-2.3, and other popular examples reported in literature such as MILs (Materials Institute Lavoisier), IRMOFs (isoreticular metal-organic frameworks) [62], and CPO-27-M (M = Mg, Mn, Co, Ni, and Zn) [63].

Familiarity with the fundamentals of MOFs is needed to truly appreciate its functionality and applicability in a multitude of settings. The next sub-section will discuss the many viable routes of synthesising MOF-composites, which is a subclass of hybrid materials that are fast gaining traction in the vibrant field of MOF materials.

2.2 MOF synthesis and fabrication routes to yield MOF-composites

The aforementioned advantages of MOFs and its applicability in a myriad of scientific/engineering applications also mean that it is not without its shortcomings. Certain MOF materials are especially susceptible to high temperatures [64], less-than-inert chemical environment [65], and moisture/humidity [66]. The short-term/extended exposure of MOFs to these factors would inevitably result in material degradation, amorphisation and loss of porosity, and ultimately, structural decomposition. Despite the enormous potential applicability of MOFs, its actual applications may be limited to a select few, due to the aforementioned susceptibilities.

The formation of MOF-composites is partly to address foregoing practical challenges. MOF acting as (secondary) filler phases masks its vulnerabilities while remaining accessible, which amplifies its applicability. Examples of polymer/MOF composites in literature are ubiquitous, such as HKUST-1/PMMA [33] and CuTPA/PVA [67] systems, the former using a polymer matrix to form free standing HKUST-1 MOF composites bearing features that are similar to the spin-coated PMMA membranes (Fig. 2.4), while the latter was developed to improve the gas transport properties of pure PVA membranes *via* the introduction of porous CuTPA MOF fillers.

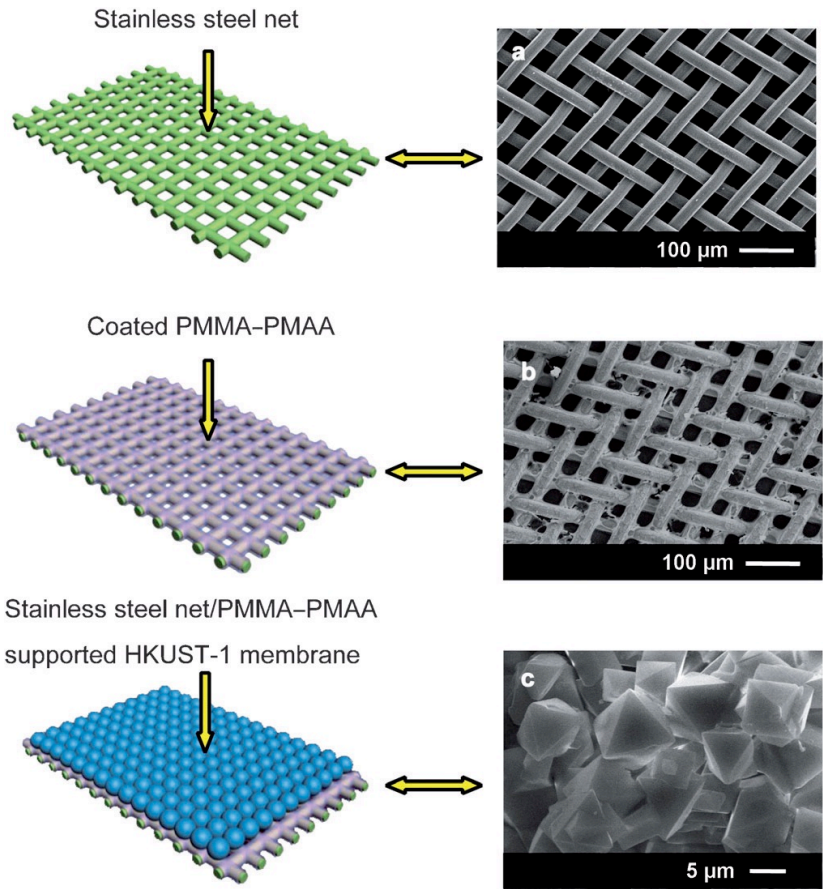

Fig. 2.4 The HKUST-1/PMMA composite, made up of layers of mesh stainless steel and polymer (PMMA) support, followed by an overgrown functional layer comprising polycrystals of HKUST-1 [33].

The formation of MOF-composites is divided into two possible approaches depicted in Fig. 2.5; MOFs as matrices, and MOFs as additives/fillers. These approaches can be further divided into subclasses of MOFs, based on their respective methods of synthesis [68].

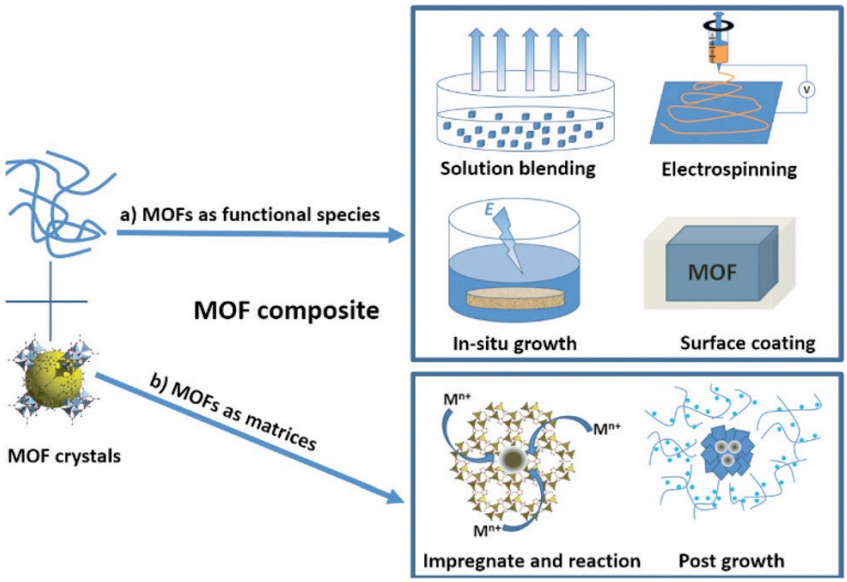

Fig. 2.5 The subclasses of MOF-composites, where (a) MOFs are fillers, and (b) MOFs as matrices [68]

The utilisation of MOFs as matrices is in a class of its own, due to the fact that the functional species in the composite is encapsulated within the nanosized cavity/cages or framework of the MOFs. Therefore, *in situ* or bottom-up synthesis seems to dominate processes intending to utilise MOFs as matrices. The customisability of MOF *vis-à-vis* its metallic core and organic ligands will allow for bespoke matrices, which is especially useful for specific applications such as miniature sensing or opto-electronic devices. Reported examples include [69] (Fig. 2.6), [70], and [71]; the reader may also consult recent reviews (e.g. [68, 72, 73]) for further details. However, for focus and brevity, the discussion of the rest of the chapter will be on composites in which MOFs act as fillers.

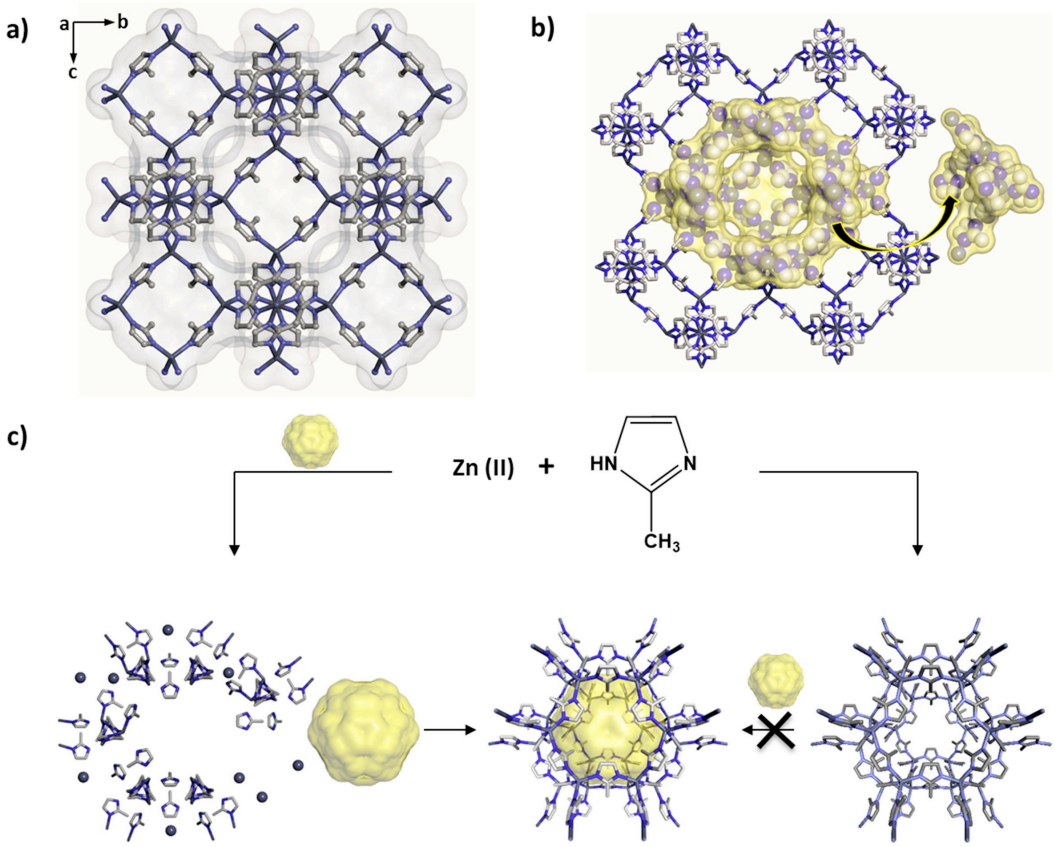

Fig. 2.6 The formation of MOF-composites containing an encapsulated guest species, where the MOF serves as a matrix. Molecular self-assembly process was employed to bestow luminescent properties to the optically inactive ZIF-8 host framework [69].

By far the most common approach of MOF-composites involves the introduction of MOFs as fillers/secondary phases. The presence of MOFs within the composites introduces secondary microstructures, which were previously unavailable in the (neat) matrices themselves. This can also be looked upon as introducing a platform where the MOFs can realise its full potential without being aggravated by factors such as extended temperatures or pressures, which is a real concern for MOFs due to its weaker coordination bond strengths. Some of the more commonly reported matrices featuring MOFs as fillers

encompass: graphene oxide (GO) [74], Matrimid [75], PVDF [76], and macroporous oxide bonded Silicon Carbide (ob-SiC) and Aluminium Oxide [77]. The synthesis route of MOF-composites involves a few commonly known methods, such as [68]:

i) Solution blending

ii) Electrospinning

iii) *In situ* growth

2.2.1 Solution blending

By far the most common route of MOF-composite synthesis, solution blending involves the dispersion of MOFs (as-synthesised micro/nanoparticles) in solvents (e.g. THF, $CHCl_3$, Acetone) and mixing with blended solvents containing the intended matrix, usually (glassy or rubbery) polymers or oxides. The solubility of polymers in organic solvents greatly simplifies the processing of MOF-composites, as the matrix (polymers or oxides) can be dispersed in miscible solvents *via* heating, rigorous stirring, or sonication. A similar process is also applicable for fine-scale MOF particles, where it can be dispersed in selected organic solvents. If both dispersed solvents are miscible, the formation of MOF composites involve the simple mixing of both suspensions to form a homogenous MOF-composite solution. The addition of a binder or an alkalising agent into the mixture would facilitate the formation of the composite and the interactions between the MOFs and matrices [78], however, in most cases (depending on the matrix), simple mechanical mixing-and-stirring over a set period of time is adequate [79]. Song *et al*. [80] demonstrated that it is important to retain the pre-fabricated MOF nanoparticles as a colloidal suspension (i.e. avoid drying and

re-dispersion that cause aggregation) in order to achieve the optimal level of mixing and dispersion in a polymer matrix.

Once a homogenous solution is obtained, it can be moulded or formed into thin membranes *via* a range of established techniques, such as doctor-blade casting [43, 81, 82], dip coating [83], and spin coating [72]. Reported works on MOF-composite utilise these approaches due to their simplicity and easily controllable processing parameters. However, problems associated with solution blending include the difficulty in minimising aggregation of MOF particles within the matrix and the poor interfacial adhesion between certain MOF particles and the matrix phase, resulting in the formation of defects (e.g. voids and pin holes) and free volumes, which might weaken structural stability and affect subsequent material performance [84].

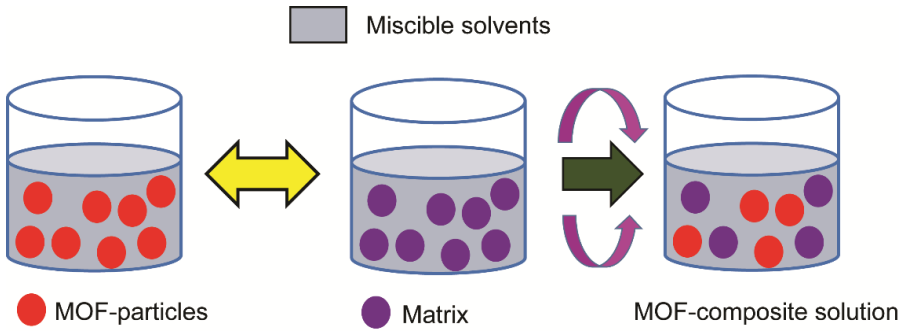

Fig. 2.7 Solution blending approach to produce polymer (matrix)/MOF (filler) solutions, which can then be used to produce MOF-composites *via* techniques such as spin/dip coating, electrospinning, and doctor blade casting techniques popular in modern polymer processing.

2.2.2 Electrospinning

This method propels the MOF-composite solution droplets across a strong electric field generated through very high voltages (~10s kV) to draw out fine, continuous fibres with

diameters ranging from several µm down to 100s of nm [85]. While this is a facile method for generating MOF-composite fibres, the processing parameters could be highly sample dependent, encompassing applied voltage, solvent type, solution viscosity, and droplet discharge rate. A schematic depicting this approach is shown in Fig. 2.8 [86].

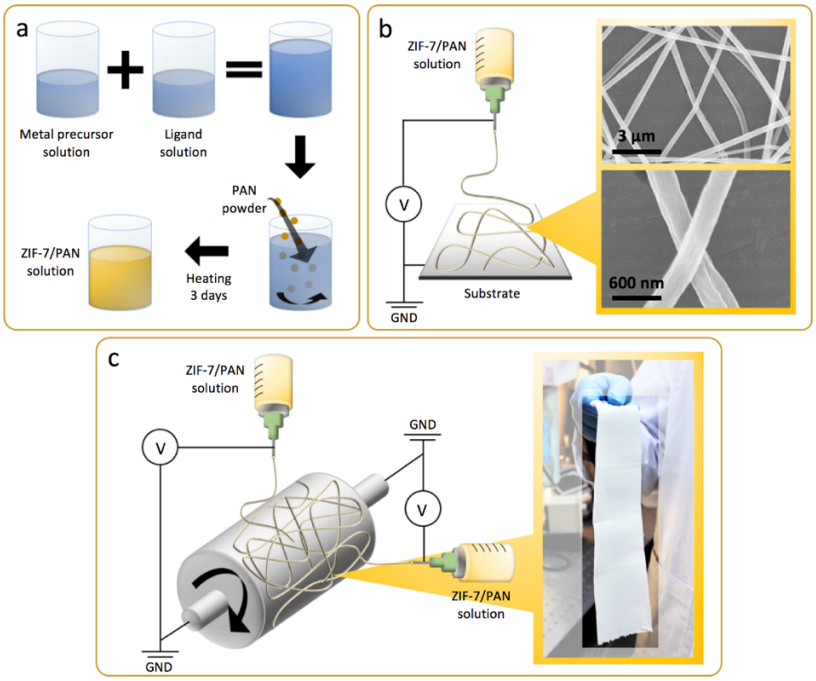

Fig. 2.8 Schematics and images of the MOF-composite electrospun fibres, with (a) PAN/ZIF-7 solution prepared *via* the solution blending method, (b) A single nozzle electrospinning setup, and an SEM image of the resulting PAN/ZIF-7 fibres, (c) Free-standing MOF-composite textile produced with a mutinozzle electrospinning setup equipped with a drum collector [86].

The formation of MOF-composite fibres greatly expands its realm of potential applications, due to the fact that these fibres can be compiled to form nonwoven mats [87] and large-area porous membranes [88], which are appealing for gas and liquid separations [89, 90]. The electrospinning technique is also amenable to automation and scaling up for manufacturing continuous free-standing textiles (Fig. 2.8(c)) [86]. Fig. 2.9 shows scanning electron

microscopy (SEM) images of MOF-composites produced by overgrowing MOF crystals onto an electrospun PAN fibre mat. It can be seen that the MOF nanoparticles have coated the fibres, where in Fig. 2.9(a), the S_{BET} of the electrospun fibres (PAN/ZnO/ZIF-8) were reported to be 1760 ± 260 m^2 g^{-1} against the S_{BET} of ZnO, which was reported to be ~10 m^2 g^{-1}, while in Fig. 2.9 (b), the S_{BET} of the PAN/Al_2O_3/MIL-53-NH_2 electrospun fibres was reported to be 700 ± 100 m^2 g^{-1}. This marks a significant increase in the accessible surface area of the MOF-composite due to its comprehensive distribution across the fibres; this microstructure offers ready interaction with its surroundings while being robustly supported by the underlying electrospun scaffolding.

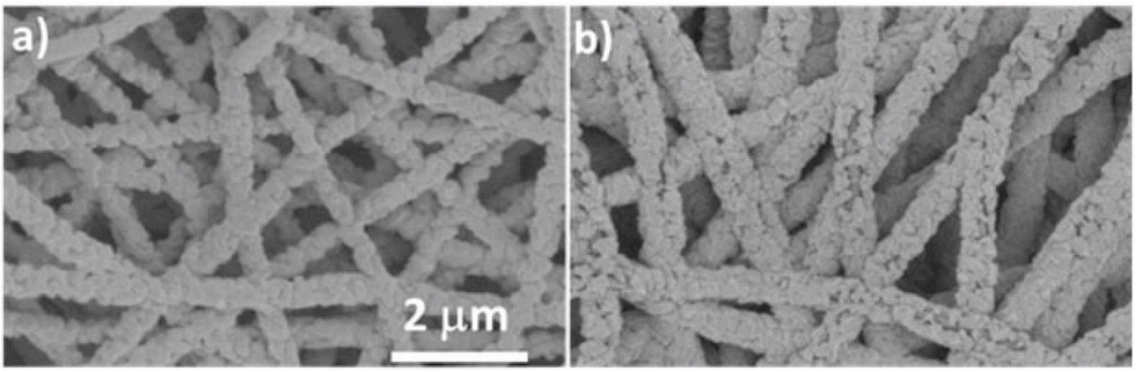

Fig. 2.9 SEM images of (a) PAN/ZnO/ZIF-8, and (b) PAN/Al_2O_3/MIL53-NH_2 electrospun fibre mats with an overgrown layer of functional MOF crystals [88].

2.2.3 *In situ* growth of MOF-composites

The production of MOF-composites *via in situ* growth involves placing the matrices and seed MOF solutions into a common controlled environment; a common approach involves immersing the intended matrices (solid substrates) into the MOF starting solutions (reactants), thereby precipitating *in situ* growth of MOF nanoparticles/thin films/nanosheets onto the matrix, culminating in the formation of MOF-composites.

The adhesion and distribution of MOFs upon the matrix is reliant upon the type of matrices (whether metal, polymers, or oxides) and types of MOF (depending on the organic ligands), however, the majority of reported works seem to suggest that weak interactions are dominant. The adhesion and interactions between the MOFs and its matrices can be enhanced *via* heating or sonication [83, 91]. A schematic of this approach is detailed in Fig. 2.10. The simple concept behind this approach, where only close contact between MOF solutions and its matrix is required, makes for a very versatile technique of producing MOF-composites, where it can be adapted into well-established methods, such as hydrothermal and solvothermal methods [92, 93], dip coating [94], and electrochemistry, amongst others.

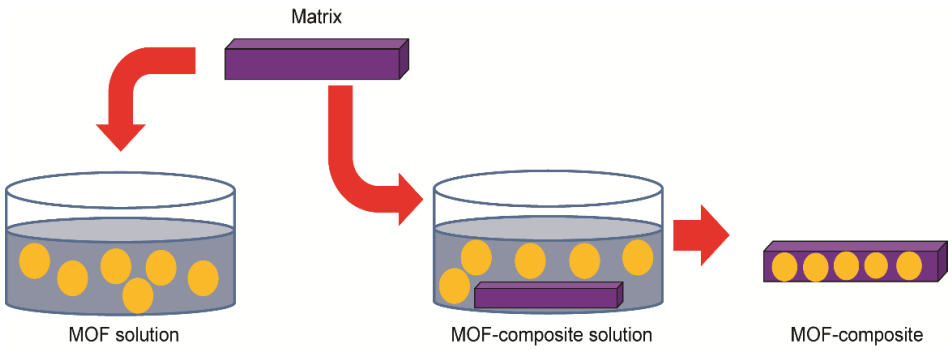

Fig. 2.10 A schematic illustrating the *in situ* growth of MOF-composites onto a chosen supporting substrate, such as metal, polymers, or oxides acting as the matrix material.

2.2.4 Benefits against conventional nanocomposite systems

Conventional nanocomposite systems are made up of a matrix and a filler; the fillers are (usually) mechanically robust and introduced into the composite as a stabilisation and strengthening agent. Their presence, although at small concentrations (typically under 5 wt.%), are reported to result in tremendous improvements towards the stability and

mechanical response of the resulting composites [95, 96]. Example of common fillers in nanocomposites include silica [97], alumina [98], and carbon nanotubes [99], and more recently, GO [100].

Similar to conventional fillers, the utilisation of MOFs as fillers may also result in some degree of structural stabilisation and modification of the mechanical properties of the neat polymer matrix [78]. However, the difference between conventional fillers and MOFs is that MOFs are bestowed with unique attributes, such as accessible porosity with specific chemical affinity, high surface areas, and high selectivity *vis-à-vis* certain gas/liquid species. Therefore, the presence of MOFs serves a dual purpose; they may mechanically enhance the composites (depending on combination of matrix type and filler loading wt.%) while also introducing previously unavailable functionalities into the resulting composites.

It was reported that pure gas permeabilities (e.g. H_2, CO_2, O_2, N_2, and CH_4) were significantly enhanced without sacrificing selectivity, simply by raising the concentration of MOF nanoparticles in Matrimid/ZIF-8 nanocomposites (compared with neat Matrimid (polymer matrix) with poor permeability) [80]. Another example concerns a PVDF/UiO-66 membrane, which has been shown to be capable of selective dye separation in a liquid solution, which is unattainable by the neat PVDF (matrix) itself [78]. Another interesting example involves tuning the frictional coefficient of neat Matrimid polymer by incorporating ZIF-8 nanoparticles (up to 30 wt.%) [101] to modify the tribological performance of Matrimid/ZIF-8 nanocomposites.

2.3 Physical properties characterisation and structure-property relationships of MOF-composites

The previous sections present the basics towards understanding MOF-composites; the overall scenario encompassing MOFs, its corresponding composites, possible synthesis routes, and benefits against conventional composites materials have been briefly discussed. An aspect that was touched upon but not elaborated up till this point is the applicability of MOF-composites. For it to be applicable, it needs to be mechanically robust and possess the coveted characteristics by said applications. It is therefore imperative that its physical properties be precisely determined and controlled prior to envisioning design for an application; this will ensure that the composite will be up to the rigours of the task.

By and large, the determination of the physical properties of MOF-composites are a consequence of many reported application works; they form an integral part of the work, but are rarely the main focus of the study. Nevertheless, there are a number of reported works that focussed specifically on the physical properties of MOF-composites. An aspect that is often overlooked is the fact that the physical properties of the MOF-composites (in the context of its mechanical, thermal, optical, magnetic, and electrical properties) will dictate the eventual performance of the MOF-composite systems. The author intends to pioneer a more systematic study and detailed investigation of MOF-composite systems in this important direction.

The microstructural and physical correlations of MOF-composites can be determined using a variety of established techniques, such as electron microscopy (EM), uniaxial tensile testing, nanoindentation, and thermogravimetric analyses (TGA), among others. This section will detail the methods that have been used to characterise the physical properties of MOF-composites based on recent results reported in literature, and discuss the ramifications of these methods *vis-à-vis* the analyses of physical properties and the establishment of structure-property relationship of representative MOF-composite systems.

2.3.1 Imaging of microstructures, phases, and interfaces

2.3.1.1 Electron microscopy (EM)

Electron microscopy (EM) is a powerful imaging tool to visualise the intricate microstructural features associated with MOF-composites. EM is effective in resolving the fine-scale morphologies of MOF particles and its surrounding matrix, enabling a better understanding of the microstructural integrity of the MOFs, matrices, and corresponding MOF-matrix interfaces. EM techniques can also be used to study how the composite microstructure evolves upon external stimulation and mechanical loading [102].

There are numerous examples available in literature where EM have been used to image the top surface and cross-sectional morphology of MOF-composites [80]. The most common form of EM being used is the scanning electron microscope (SEM) (Fig. 2.11), due to its simplicity in sample preparation and excellent images obtainable at high magnifications (30,000-50,000×). Given that majority of MOF-composite samples are non-conductive, they need to be sputter coated with a thin layer of Au/Pt prior to SEM imaging. Imaging is done in high vacuum (~10^{-4} Pa) and at 5-30 keV, which leaves matrices such as polymers vulnerable to electron damage if left uncoated.

While the transmission electron microscope (TEM) [103] can also be used for imaging polymer/MOF composites, relatively fewer examples exist due to its more involved sample preparation requirements. However, TEM offers significantly higher magnification capabilities (reaching ~1,000,000× or greater), and the capacity to individually image MOF nanoparticles embedded inside the composites, as shown in Fig. 2.12.

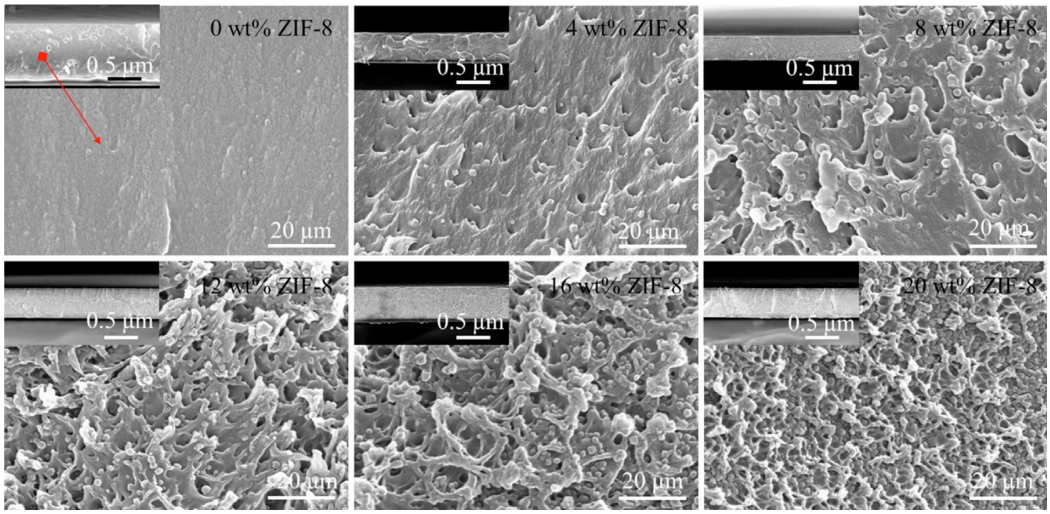

Fig. 2.11 SEM micrographs showing the cross sections of PEK-c/ZIF-8 nanocomposites at multiple wt.% loading of ZIF-8 [104].

SEM images shown in Fig. 2.11 can be used to identify whether the MOF nanoparticles (ZIF-8) and matrix are blended or remain as distinct separate phases, the distribution of MOF particles throughout the matrix, and the preservation of the morphological features of the MOF particles post-blending with the matrix. These factors are directly correlated to the performance of these composites, as discussed in Shahid *et al.* [84], where it was mentioned that the agglomeration and uneven distribution of MOF particles within the matrix may result in decreased gas separation performance, and Ordoñez *et al.* [105], where separate phases of MOF particles and matrices within a composite resulted in changes to the macro-mechanical properties of the nanocomposites, such as the decrease of ductility and the increase of yield strength.

Understanding the nature of the interaction between MOF particles and its matrix will help determine whether or not it is viable for its intended applications. An example that could be used to illustrate this point is gas separation performance; the accessibility of MOF particles and its distribution dictates if gases will be able to come into contact with the MOF particles,

which practically guarantees the selectivity of the composite. In the event that access to the MOF particles within the composite is restricted, its gas separation performance will be adversely affected. TEM characterisation provides a complementary picture pertaining to the distribution of MOFs underneath the sample surface, examples are depicted in Figs. 2.12-2.13, which can be used to detect the presence of any internal defects such as cracks or pin holes [103], or indeed to ascertain the development of nanosized phases in an individual strand of electrospun MOF-composite fibre [86].

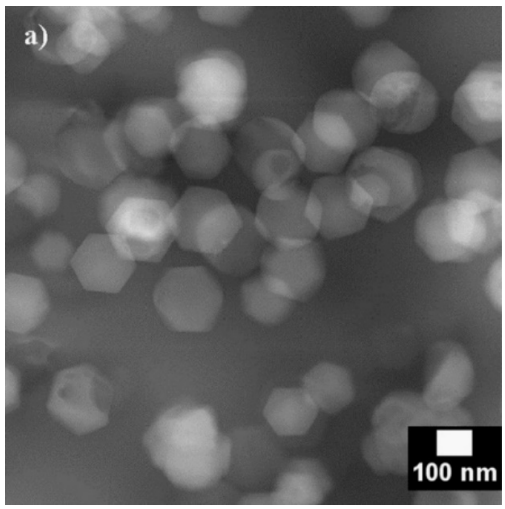

Fig. 2.12 TEM micrograph of a 20 vol.% ZIF-8 nanoparticles integrated in a Matrimid matrix [103].

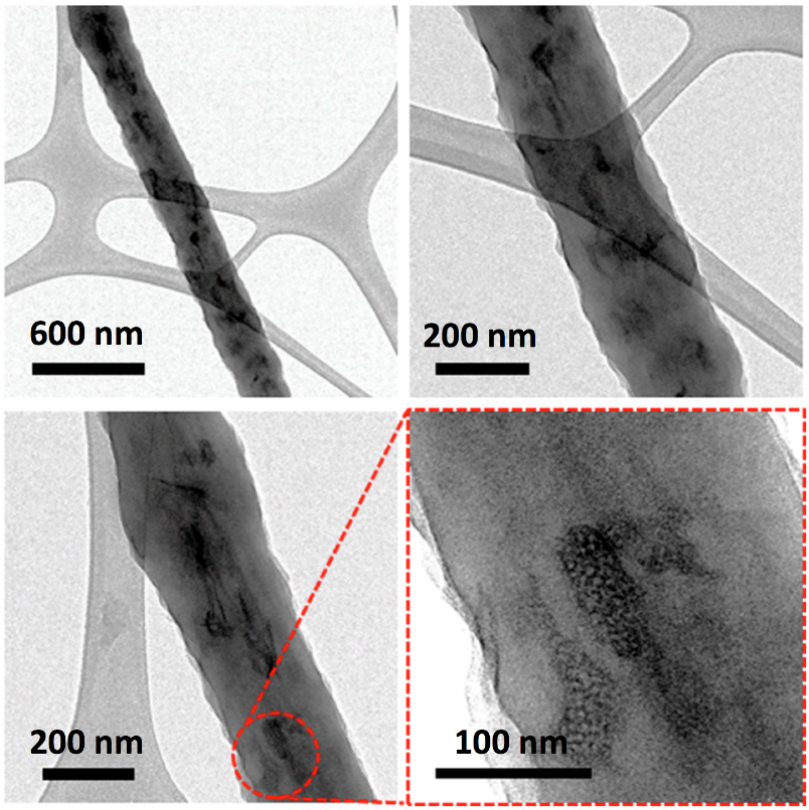

Fig. 2.13 TEM micrographs of PAN/ZIF-7 nanocomposite fibre made by electrospinning method, showing ~100 nm crystals of MOF embedded in an individual fibre [86].

2.3.2 Mechanical properties and structural resilience

Information about the mechanical properties and the physical durability of MOF-composites is imperative to afford practical applications. Mechanical behaviour under small and large strain deformations need to be quantified as a means of simulating real world loading conditions, where MOF-composites will be subjected to a combination of external forces and/or cyclic thermo-mechanical loading. Many techniques are available for mechanical characterisation at different length scales, and this section will explore these methods and its correlation in the context of structure-property relationship and the subsequent applications of MOF-composites.

2.3.2.1 Uniaxial stress-strain response

The uniaxial tensile test is a well-established engineering method in determining a variety of mechanical properties, such as yield (σ_y) and ultimate tensile strength (σ_t), elastic moduli (E), and fracture energy (G_f).

Tests are usually conducted using a universal testing machine (UTM), which is made up of two crossheads; one to drive the load as per the settings on the sample, the other to record the changes in length of the specimens. A highly customisable machine, its gauge length, load cells, and grips can be exchanged as per the needs of the experiment. These variables are sample-dependent, and imperative towards the determination of the quasi-static mechanical properties of small composite specimens (~mm to cm). The samples used for the tests are usually rectangular in shape, with the dogbone configuration being a popular choice. Uniaxial tensile tests are destructive; the samples will be loaded up till the point of failure, upon which the test terminates. This is done in order to obtain the full range of mechanical response of the sample and to discern points at which it plastically deforms, its maximum strength, and its elongation-at-failure (ductility), all of which are important parameters in engineering product design. The simplicity associated with sample preparation, repeatability, and straightforward data analysis render the large-strain uniaxial tensile test the first choice for the determination of the macro-mechanical properties of MOF-composites and electrospun fibres.

Smith *et al.* [106] reported that physical aging of the glassy polymer matrices (Matrimid, PIM-1, PTMSP) within a MOF-composite membrane could also substantially deteriorate its ductility, plausible mechanisms of which are depicted in Fig. 2.14. The large-strain mechanical response of MOF-composites was discussed in Denny *et al.* [78] in the context

of dye separation/filtration, where a collection of MOF-composites (UiO-66, MIL-101, MIL-53, and ZIF-8 in PVDF matrix) were synthesised, and one such composite system was utilised for dye separation applications. Results from the uniaxial tensile test suggested that these composites are adequately robust against mechanical stress and the rigours of filtration under concentrated pressure. Another study reported by Li *et al.* [53] proved to be interesting in the context of mechanical properties; they immobilised room temperature ionic liquid (IL = [bmim][Tf_2N]) into the cages of ZIF-8 and incorporated these IL@ZIF-8 into PEBAX for CO_2 separation applications. They reported enhanced ultimate tensile strength and ductility for the samples alongside improved CO_2 separation properties, as detailed in Fig. 2.15.

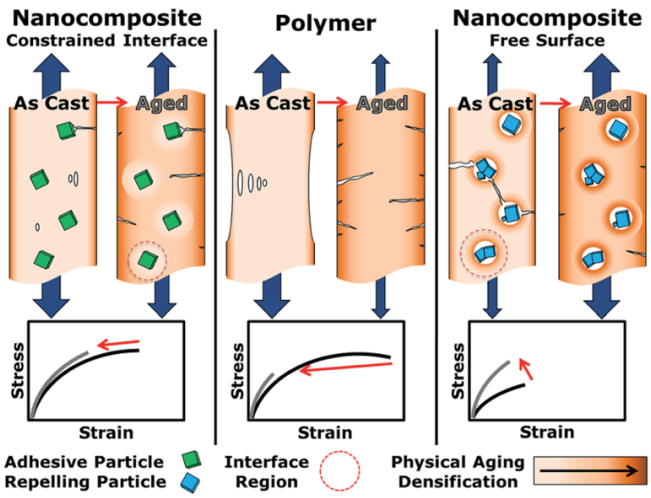

Fig. 2.14 Possible uniaxial deformation mechanisms controlled by interactions between the MOF filler phase and the surrounding matrix phase, taking into consideration potential effects of physical aging [106].

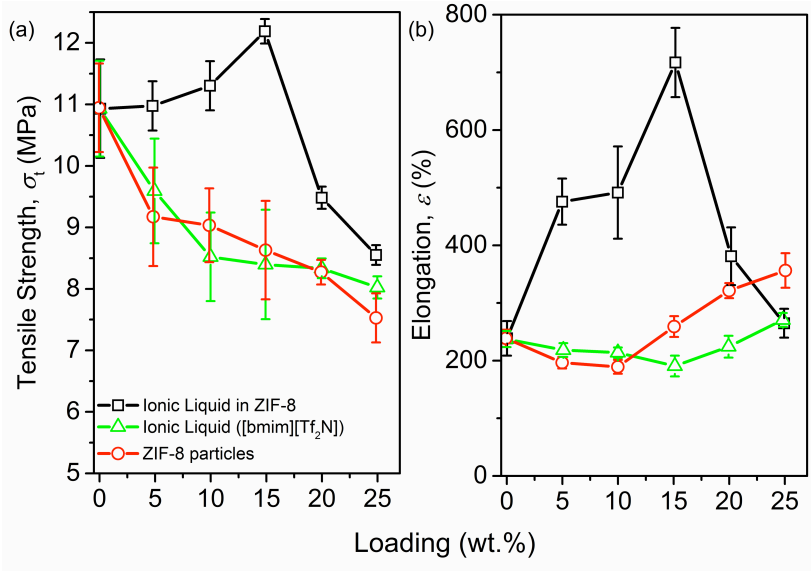

Fig. 2.15 (a) Tensile Strength, σ_t, and (b) elongation-at-break for IL, IL@ZIF-8, and ZIF-8 particles encased in PEBAX forming the composites, adapted from [53]. The introduction of the IL into ZIF-8 resulted in improved performance for CO_2 separation abilities and increased the tensile strength and elongation of the membrane.

2.3.2.2 Nanomechanical response from nanoindentation

The instrumented nanoindentation method makes measured indents using a calibrated diamond tip onto the surface of a sample, and determine its local mechanical response (penetration depths 100s nm to several μm), encompassing Young's moduli (E) and nanohardness (H) [107]. Assuming an isotropic response of the samples, then as per the Oliver & Pharr method [108]:

$$\frac{1}{E_r} = \frac{1-\nu^2}{E} + \frac{1-\nu_i^2}{E_i} \tag{2.1}$$

where E_r is the reduced modulus (derived from contact stiffness recorded by indenter), and E_i and ν_i are Young's modulus and Poisson's ratio of the indenter tip, respectively. In the

case of heterogeneous materials, the magnitude of E derived from Eqn. (2.1) is indicative of the *stiffness* of samples under (fully reversible) elastic deformation [109]. On the other hand, the nanohardness (H) provides a measure of the structural resistance of the sample against any (irreversible) plastic deformation, which is defined by:

$$H = \frac{P}{A_c} \tag{2.2}$$

where P is the normal indentation load and A_c is the contact area established by the indenter tip under that applied load.

The nanoindentation method is a convenient approach in determining the E and H of MOF-composites. It is complementary to the uniaxial stress-strain tests which require much larger sample sizes. The minute nature of the test will also allow for the probing of specific areas to determine interactions between MOFs and its matrix, such as the interface(s) between the constituents, or MOF-rich and matrix-only areas, enabling us to discern the respective similarities or differences between these respective areas at the micrometre length scale.

The body of work in literature involving the utilisation of the nanoindentation method to determine the nanomechanical properties of a range nanocomposites is growing [110], but remains scarce for MOF-based composites. However, the applicability of the nanoindentation method to probe the nanomechanical properties of other similar and analogous composites are widely reported in literature. Zhu *et al.* [92] reported the use of the nanoindentation method to probe the nanomechanical and nanotribological performance of a PVA/GO composite, and the method was proven to be sensitive enough to be able to discern the improvement in the elastic moduli and hardness changes to the films as a result of the introduction of 0.5 wt.% of GO (see Fig. 2.16). Similarly, Lee *et al.* [111] reported

probing the nanomechanical properties of a Nafion/sulfonated GO (N/sG) using the nanoindentation method, where the Young's moduli and nanohardness of the polymer composite improved upon being annealed (see Fig. 2.17). Both works reported the use of GO (inorganic) filler, which can be assumed to be an analogue of MOFs in this case, as MOFs may also act as a (relatively against the matrix) hard filler in polymer/MOF (nano)composites, allowing us to assume that a technique that can be used to probe the aforementioned polymer composites should also be viable for probing the nanomechanical response of the polymer/MOF nanocomposites.

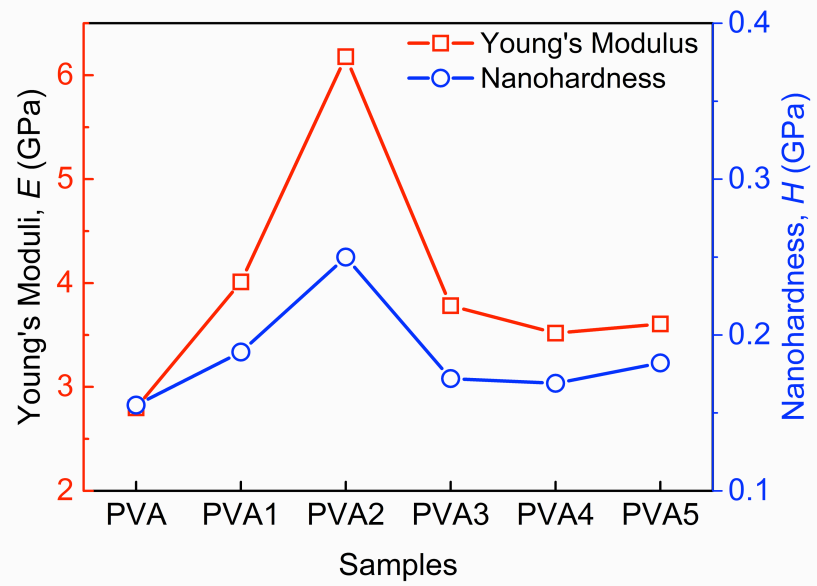

Fig. 2.16 Young's modulus and nanohardness of PVA and PVA/GO (0.5 wt.%) films collected using the nanoindentation method, adapted from [92].

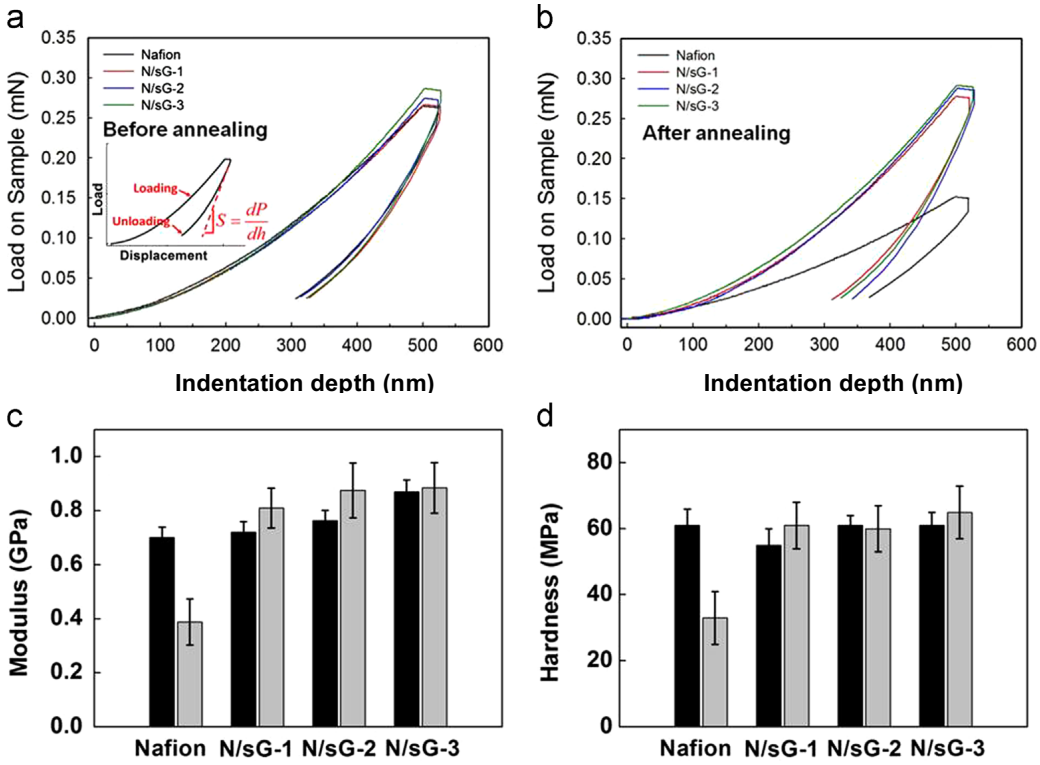

Fig. 2.17 Plots of displacement *vs*. load of Nafion (N) and N/sG-1, N/sG-2, and N/sG-3 (a) before, and (b) after annealing, which are used to derive the (c) Young's moduli, and (d) nanohardness of the polymer composite [111].

2.3.2.3 Dynamic Mechanical Analysis (DMA)

Viscoelastic properties [112] represent the core mechanical characterisation of polymeric materials and soft matter, the majority of whose deformation are time-temperature dependent due to its inherent viscous behaviour. The incorporation of MOFs into polymeric/soft matrices have been shown to affect the linear viscoelastic response of the composite at small strains (<0.5%). These changes can be quantified by the determination of the viscoelastic responses of the composite *via* its storage (E') and loss (E'') moduli, dissipation factor ($\tan \delta = E''/E'$), and the accompanying relaxation temperatures (T_α, T_β,

T_γ). These viscoelastic responses are representative of what is called the *dynamic modulus* (E^*), as detailed by Eqn. (2.3):

$$E^* = \frac{\sigma^*}{\varepsilon^*} = E' + iE'' \tag{2.3}$$

where σ^* and ε^* are the time-varying oscillatory stress and strain, respectively, while $i = \sqrt{-1}$ is designated as the imaginary loss modulus term *E*". The major difference between the Young's modulus (*E*) and dynamic modulus (E^*) is that, the latter captures the ratio of *dynamic* stress (σ^*) with respect to an oscillatory strain (ε^* adopting a sinusoidal waveform), as opposed to a steadily increasing deformation imposed in nanoindentation measurements (see §2.3.2.2).

In the context of MOF-composites, *E*' is representative of the amount of (recoverable) elastic strain energy stored within samples during oscillatory deformation of polymeric chains, while the *E*" corresponds to the amount of energy dissipated through inelastic processes due to entropic motions or rotations of polymeric chains. The determination of the real and imaginary parts of the dynamic modulus [Eqn. (2.3)] by means of Dynamic Mechanical Analysis (DMA) experiments provide us insights into the molecular behaviour of the MOF-composites as a function of frequency and temperature.

The amount of reported work in literature pertaining to the viscoelastic response of MOF-composites is scarce, with only a few reported examples. However, similar to §2.3.2.2, it is assumed that the hybrid nature of MOFs (inorganic and organic) will allow us to use inorganic and organic filler representations to determine the viability of the DMA technique in analysing polymer/MOF nanocomposites [113]. Inorganic fillers are especially favoured, where Gardea *et al.* [114] used the DMA technique to determine the applicability of a PEEK/CNT composite as an energy dampener. They reported that the introduction of

the CNT into the PEEK matrix resulted in a significant decrease in the storage modulus (*E*') of the composite (40%), confirming its viability as an energy dampener. The *E*' and tan δ plots reported in their work is shown in Fig. 2.18. Ridzuan *et al.* [115] investigated the thermo-mechanical response of a *Pennisetum purpuruem* (PP)/glass-reinforced epoxy hybrid composite (grass fibre filler), where the DMA technique was used to determine the T_g of the composite. The introduction of the PP grass fibres increased the *E*' of the composite, which is further increased at a 5% alkali treatment of the composite, attributed to increased stiffness and improved interfacial interactions between the constituents of the composite. Concurrently, the loss modulus (*E*") was lowest for the neat epoxy, while it is highest for the alkali-treated composite (see Fig. 2.19).

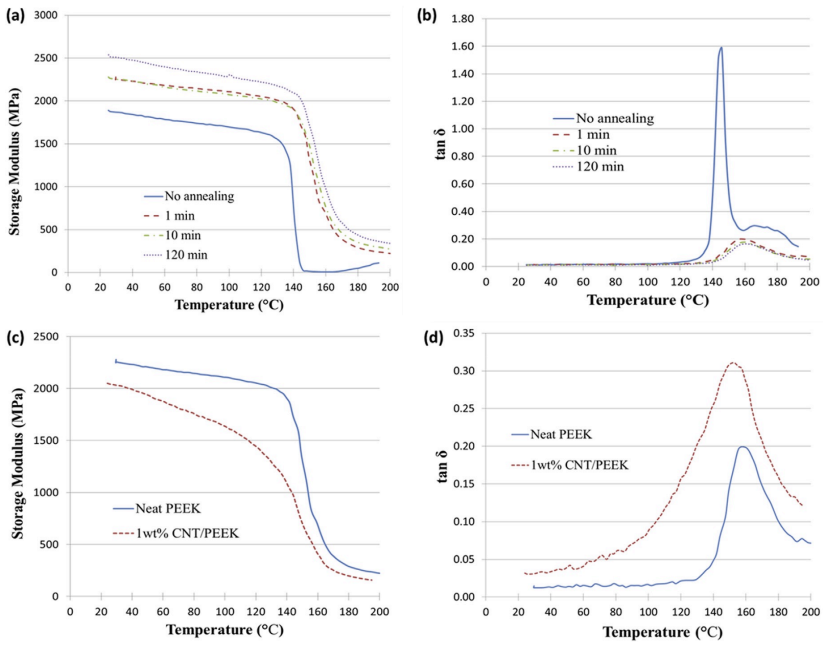

Fig. 2.18 (a) Storage Modulus (*E*'), and (b) tan δ for the neat PEEK samples annealed at 240 °C at 1, 10, and 120 mins, while (c) comparison of *E*' of the neat PEEK and 1 wt.% CNT/PEEK, and (d) comparison of tan δ of the neat PEEK and 1 wt.% CNT/PEEK [114].

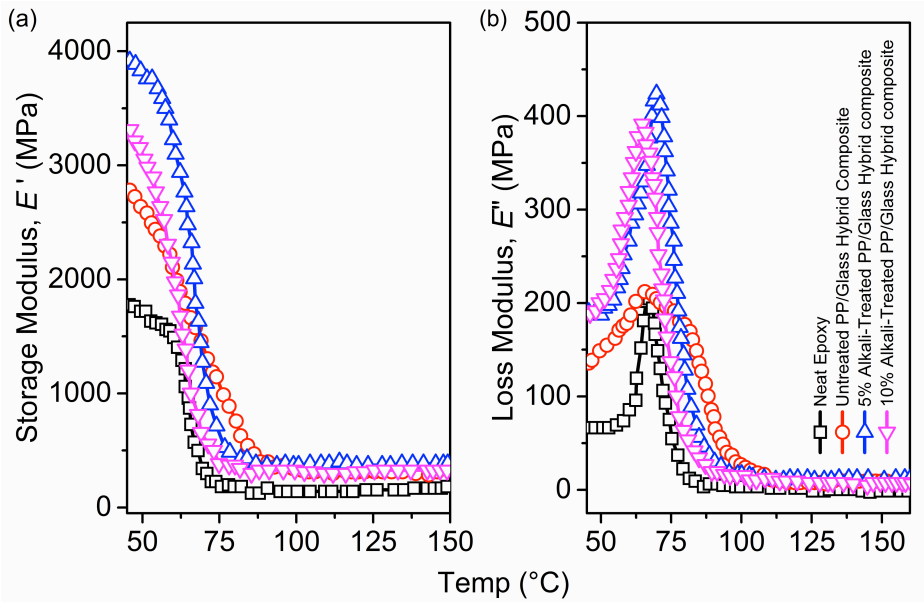

Fig. 2.19 The *E*' and *E*" of the neat epoxy, untreated PP/glass-reinforced epoxy hybrid composite, and 5 and 10% treated PP/glass-reinforced epoxy hybrid composite, adapted from [115].

As reported by these aforementioned works, the DMA technique allow us to probe the molecular interaction and response of the composites as a function of frequency and temperature. The hybrid nature of MOFs and the intricate and interwoven interactions between the MOFs and its matrices will result in a dynamic response of the composite towards external stimuli, and it is assumed, based on these reports, that the DMA technique is indeed viable for probing and determining the thermo-mechanical response of polymer/MOF nanocomposites.

2.3.3 Thermal stability

The physical properties of MOF-composites, detailed in the previous sections, are highly

reliant upon its response to temperature fluctuations. In effect, both fillers and potential matrices (metals, polymers, and oxides) are susceptible to temperature fluctuations, especially MOFs, where the organic ligands will decompose at high temperatures (typically beyond ~200-300°C). Polymers also exhibit phase changes at increased temperatures. The thermal profile of MOF-composites will provide a unique insight into whether decomposition occurs simultaneously between the MOFs and matrices, or whether the MOFs and matrices act as separate entities within one bulk structure. Determining the nature of the response of MOF-composites towards temperature effects will elucidate the strength of the molecular interactions between its constituent materials, which will be immensely helpful in materials design in the context of its application.

2.3.3.1 Thermogravimetric Analysis (TGA)

Thermogravimetric analysis (TGA) is a method that quantifies the physical (and chemical) changes of samples as a function of temperature. Typically, it involves subjecting a sample to a set temperature range and recording changes to its weight relative to the temperature increase (or decrease). This method is commonly used to acquire a thermal decomposition profile of a sample and to determine the temperatures at which a certain constituent of the samples decomposes. It is an established and common method that is frequently used to determine the thermal decomposition temperature of various MOFs, such as ZIF-8 [116], HKUST-1, and MILs [117]. In the case of MOFs, it is also useful to establish the temperature at which entrapped solvents or specific guest molecules in MOF could be removed from the pores by means of heating, but without collapsing the MOF (host) framework.

Within this context, the TGA method could also be utilised to determine the thermal decomposition profile of MOF-composites, with examples being the work of Feijani *et al.* [118], who reported the thermal decomposition profile of PVDF/MIL-53(NH_2-MIL-53) nanocomposites, and Zhang *et al.* [119], who reported the thermal decomposition profile of ZIF-8/6FDA-DAM. The thermal decomposition profile of both composites showed that the presence of MOF particles somewhat altered the thermal decomposition profile *vis-à-vis* the matrices, where the onset of decomposition varies based on the concentration of MOF particles in the composite. This could be attributed to the 'pinning' or 'displacement' effect of the MOF particles upon the matrix; combined weak interactions between the MOF particles and the matrix will either prevent it from degrading, thus extending its thermal decomposition profile, or quicken its decomposition, thus shortening its thermal decomposition profile. Whether the thermal decomposition profile is extended or shortened is dependent upon the nature of the matrix and the combined interactions between the MOF fillers and the matrix. Example thermal decomposition profiles depicting both cases are shown in Fig. 2.20.

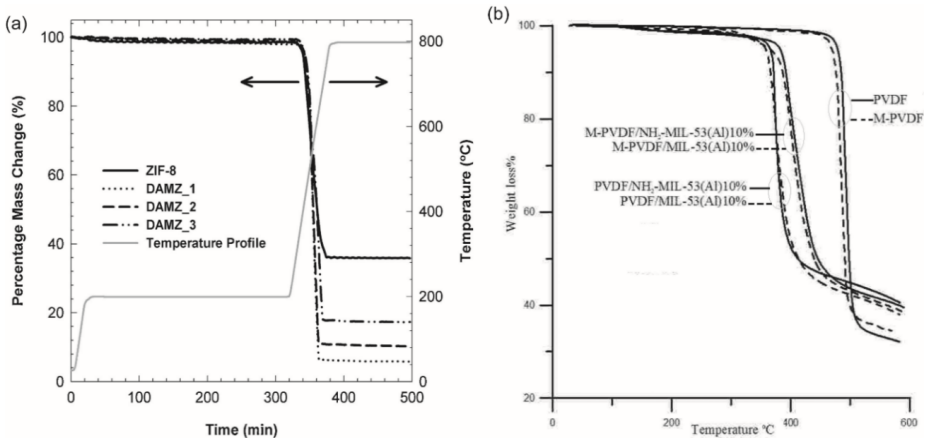

Fig. 2.20 TGA plots of MOF-composites, with (a) ZIF-8/6FDA-DAM composites, and (b) M-PVDF/NH_2-MIL-53 (Al) [118, 119].

2.4 Potential technological applications of MOF-composites

MOFs are potentially useful for applications such as gas storage and separations [120], sensors [121], semiconductors [122], biomedicine [123], and catalysis [124]. However, real world applications of MOFs beyond the laboratory may result in its degradation and subsequent decomposition, especially at high temperatures, mechanical stresses, and humidity. The applicability of MOFs is then incumbent upon the ability of the matrix to shield them from direct exposure to the environment while simultaneously making them accessible to a select few species. Robust MOF-composites remains the best choice, and the prospective benefits of encasing MOFs in other matrices (especially polymers and oxides) or by encapsulating another functional guest molecule into MOF pores have been elucidated in this chapter.

This section will discuss reported works on the applicability of MOFs for gas separations, sensors, and biological applications. It should also be pointed out that the potential applications of MOF-composites are not only limited to these applications, however for the sake of context and brevity, only the aforementioned applications will be focussed upon. The structure-property relationship and its subsequent effect on the applicability of MOF-composites will also be touched upon in this section.

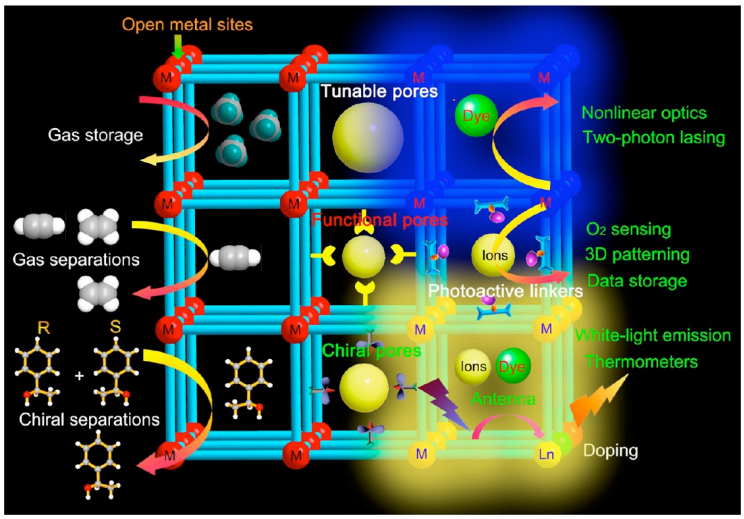

Fig. 2.21 A graphical summary of the diverse potential utilisation of multifunctional MOF materials, including MOF-composites [125].

2.4.1 Gas capture and separation using polymer/MOF composites

MOF is synonymous with gas separation, with a variety of reported works pertaining to separation of combined CO_2/CH_4, amongst others [126]. Song *et al.* [80] discussed the use of Matrimid/ZIF-8 nanocomposites for this very purpose, due to the affinity of both Matrimid and ZIF-8 towards CO_2, while Dong *et al.* [127] reported the usage of a MIL-68(Al)/Matrimid nanocomposites for combined CO_2/CH_4 separation as well. The properties governing the separation properties of MOF-composites seems to be the accessibility of the MOF particles within the matrices, and the pore size/aperture of the MOFs itself, where the size of the gas molecules needs to be relatively smaller than the accessible pores in the matrix and the pores within MOFs. However, by virtue of its framework flexibility the collective vibrational dynamics in MOFs (e.g. gate-opening mode in ZIF-8 and breathing mode in ZIF-7 [50]), it could allow passage of molecules whose size is slightly bigger than that of its pore aperture. Gas permeability and selectivity can be

modified and enhanced by incorporating MOF nanoparticles into neat polymer matrices [128, 129].

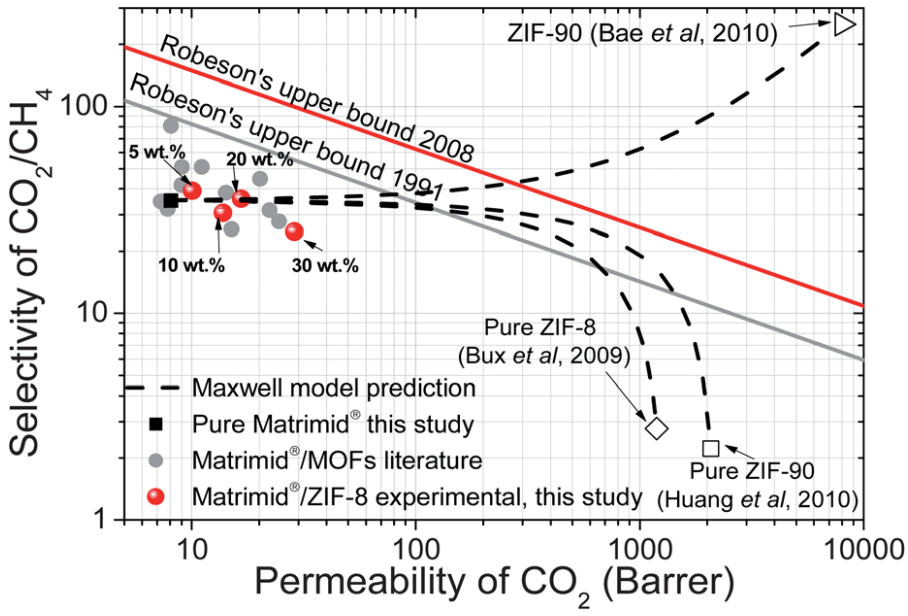

Fig. 2.22 CO_2/CH_4 selectivity *vs*. the permeability of CO_2 of Matrimid/ZIF-8 nanocomposites in terms of the weight fraction of ZIF-8. The upper bound trade-off lines refer to Robeson's upper bound summarised in 1991, and updated in 2008 [80].

Works on gas separation using MOF-composites are ubiquitous in literature [130-132], and a common theme across these works is the fact that the gases that are to be separated needs to share a certain level of chemical affinity with the MOF particles. The selectivity of gases pertaining to MOF particles are by and large governed by pore sizes, geometry, and functional group interactions and polarisation between the gases and the MOFs (since certain gases might prefer certain chemical groups such as the methyl group of ZIF's organic linkers). Since the permutation of possible MOFs is, in theory, essentially limitless, it is conceivable that the design of MOFs [133] and its corresponding matrix can be optimised for a bespoke composite that target specific gas species (CO_2, H_2, CH_4, and N_2).

Bachman *et al.* [134] discussed the utilisation of a M_2(dobdc)/6FDA-DAM nanocomposites for the selective uptake of ethylene (C_2H_4). They posited that the presence of the M_2(dobdc) (M = Mg, Mn, Fe, Co, Ni, and Zn) fillers resulted in a few added advantages over a neat 6FDA-DAM: decreased plasticisation of the polymer matrix (*via* framework-matrix interactions reducing the polymer chain mobility), increased selectivity of C_2H_4 over ethane (C_2H_6), and increased permeability (for C_2H_4) and nanocomposite stability against added pressure and increased temperature. It was also established that the uptake of C_2H_4 scales with the amount of M_2(dobdc) in the composite membrane, where the 25 wt.% Ni_2(dobdc) and 33 wt.% Co_2(dobdc) corresponded to increased selectivities of C_2H_4 of 2.7 (6FDA-DAM) to 4.6 for the former, and 2.7 (6FDA-DAM) to 5.0 for the latter. This is not surprising, as there are reports in literature pertaining to the use of MOF for the separation of acetylene from ethylene/acetylene mixtures [135], and it is assumed that MOFs are capable of capturing/separating other hydrocarbon mixtures as well. It was concluded that this significant increase in the uptake of C_2H_4 is due to the excellent synergy between the polymer matrix (6FDA-DAM) and the MOF fillers (M_2(dobdc)), which allows for the C_2H_4 gas molecules to diffuse interchangeably between the polymer chain molecules and the MOF fillers, increasing the limit of gas molecules that can be retained within the nanocomposites (see Fig. 2.23).

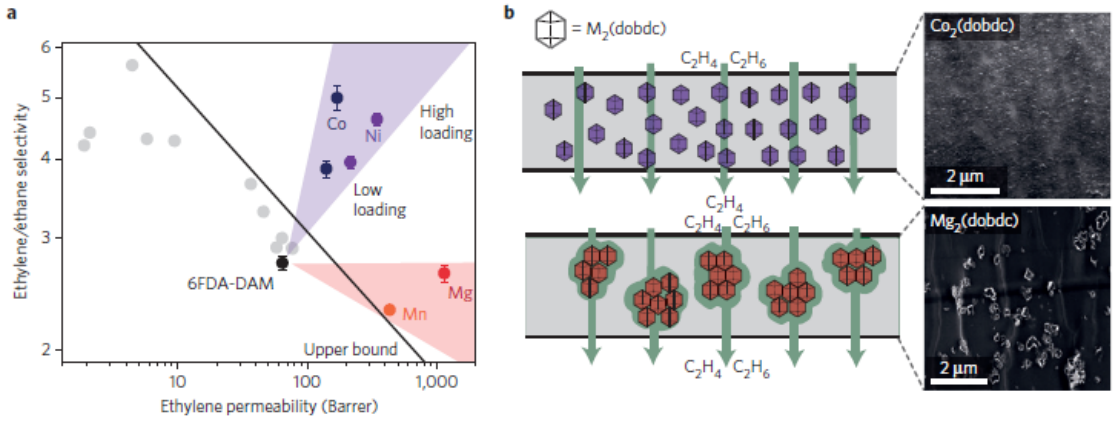

Fig. 2.23 (a) Membrane performance at 2 bar feed pressure and 35 °C relative to the upper bound for polymers. Membrane loadings by weight are 10 % and 33 % for Co_2(dobdc), 6% and 25% for Ni_2(dobdc), and 13% for Mn_2(dobdc). Uncertainty in selectivity represents propagation of uncertainty in permeability based on two independent membrane samples, and each sample was measured twice to ensure that no plasticisation or conditioning effects. Grey circles represent neat polymers from the literature, (b) TEM images of 33 % Co_2(dobdc) and 23 % Mg_2(dobdc) membrane cross-sections and corresponding illustrations of the proposed transport mechanisms, where purple hexagons represent Co_2(dobdc) or Ni_2(dobdc) nanocrystals and red hexagons represent Mg_2(dobdc) or Mn_2(dobdc) nanocrystals [134].

Ploegmakers *et al.* [136] studied a collection of polymer/MOF composites for ethylene/ethane (C_2H_4/C_2H_6) separation. The polymer matrix in this case was P84, while the MOF fillers include Cu_3BTC_2, FeBTC, and MIL-53 (Al). The loadings of the composites were 20 wt.% MOF fillers against 80 wt.% of the polymer matrix. It was established in their work that the sorption capabilities (*vis-à-vis* C_2H_4) of the Cu_3BTC_2 was significantly higher (390 cm^3 (STP) cm^{-3} at 11 bar) than that of FeBTC (170 cm^3 (STP) cm^{-3} at 11 bar) and MIL-53 (Al) (150 cm^3 (STP) cm^{-3} at 11 bar). They attributed this significant difference to

the large surface area of Cu_3BTC_2 and the affinity between copper ions and the C_2H_4 gas molecules. The addition of these MOF fillers to form P84/M (M = Cu_3BTC_2, FeBTC, and MIL-53 (Al)) composites resulted in a few marked difference in terms of sorption capability of the resulting membranes: permeability fluctuated (non-significant increase/decrease) in relation to C_2H_4/C_2H_6, although it did not differ much from that reported by P84, proving the presence of non-selective voids in the composite due to the introduction of MOF fillers. However, C_2H_4/C_2H_6 selectivity almost doubled for the P84/ Cu_3BTC_2 composites (from 4.1 to 7.1, see Fig. 2.24).

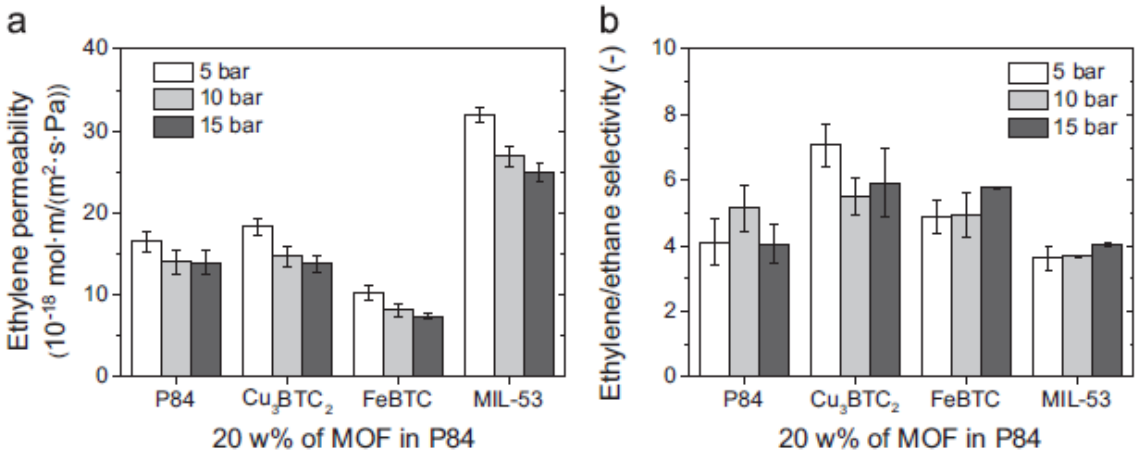

Fig. 2.24 (a) average C_2H_4 permeability, and (b) C_2H_4/C_2H_6 selectivity of native P84 and 20 wt.% Cu_3BTC_2, FeBTC, and MIL-53 (Al) MMMs at 5, 10, and 15 bar mixed gas feed pressure [136].

2.4.2 Opto-electronics, sensors, and host-guest interactions

Reported works on MOFs as sensors and opto-electronic devices are currently growing [137]. Many reported encapsulating guest molecules within the MOFs itself; in effect, the MOFs will act as matrices instead of fillers. The interactions between the encapsulated guest molecules and the metal core or organic ligands in the presence of a stimulant (gases, electrons, and heat, for example) and the internal interactions between the metal cores and organic ligands of the MOFs with the encapsulated guest molecules induce physical responses that can be interpreted as a reaction to external stimuli (e.g. photonic excitation, thermal load, mechanical strain, and chemical uptake).

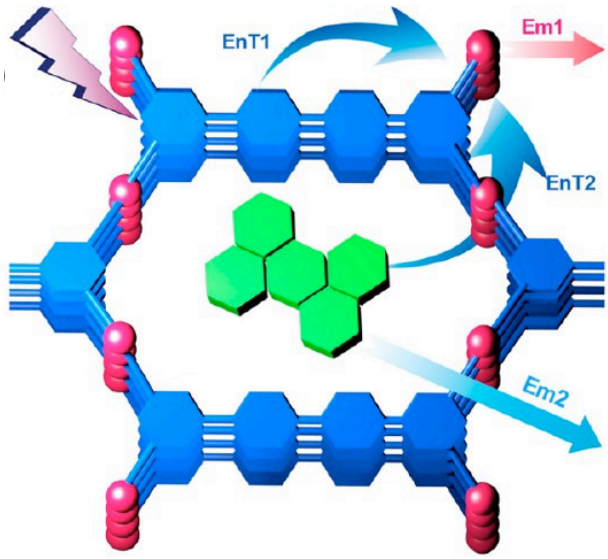

Fig. 2.25 A representation of a light emitting device fabrication involving MOFs, in this case, ZJU-88⊃Perylene (20-80 °C), with EnT: Energy Transfer; and Em: Emission; blue: ZJU-88 and green: perylene [125].

The porosity and accessible active sites (metallic core and organic linkers) of MOFs make it suitable for entrapment/encapsulation of guest molecules. Unique host-guest interactions within nanoscale pore confinement have been demonstrated using novel MOF-composites. This gives way to devices such as microelectronics, lighting, and sensors. Previous approaches on encapsulating guest molecules such as the *ex situ* approach (e.g. post-synthetic infiltration of functional guests) is limited by extended processing times and size dependent encapsulation, where only molecules that are significantly smaller than the pore openings will have a chance of infiltrating the MOF's cages. Instead, the bottom-up approach, or *in situ* self-assembly approach, seems to circumvent these limitations, where the MOFs forms around the guest molecules.

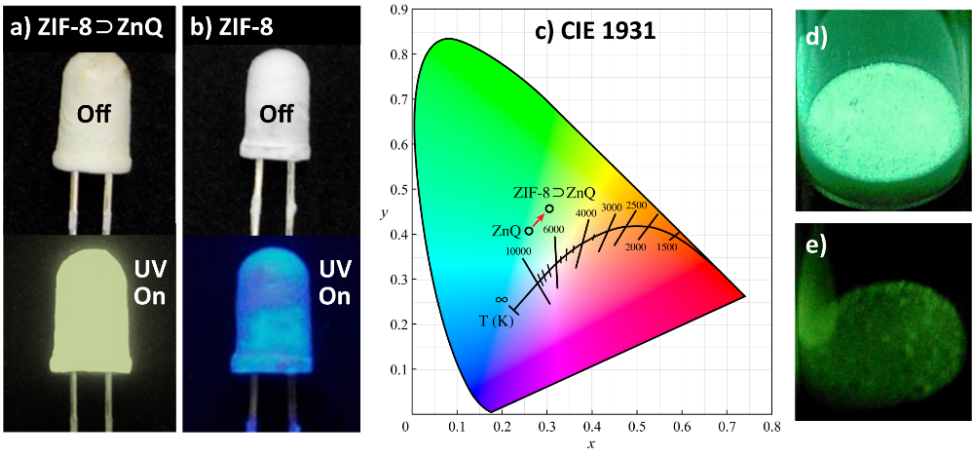

Fig. 2.26 *In situ* encapsulation of an electroluminescent guest molecule (ZnQ) in ZIF-8, resulting in formation of ZnQ@ZIF-8 composite. (a-c) Exposing the MOF-composite to UV irradiation results in the emission of yellow light (visible) due to the π-π interactions between ZnQ and ZIF-8. (d-e) Encapsulated guest also show enhanced photostability when shielded within the MOF pores [69].

Host-guest interaction(s) is representative of a case when the MOFs act as matrices instead of fillers. The close proximity and electronic interactions between the MOFs and the guest molecules facilitate energy transfer between the porous host and the functional guest species. This may occur in the presence of external stimuli such as under the irradiation of UV-light, or when subject to pressure or an electrical potential. Fig. 2.26 shows an example of this phenomenon; electroluminescent ZnQ complex (Zn-(bis-8-hydroxyquinoline)) is encapsulated into ZIF-8, forming ZnQ@ZIF-8 composite. Upon exposure to UV-light, the composite emits visible yellow colour, rendering it suitable for photonic applications.

2.4.3 Biomedical and biological applications

Given the numerous chemical and structural variability of MOFs, it is possible to synthesise bio-compatible MOFs, aptly called bio-MOFs. Bio-MOFs are especially useful in the context of drug delivery and medical diagnosis, due to their aforementioned bio-compatibility, high surface area, and accessible porosity to transport and deliver small drug molecules. The flexible nature of the pores of MOFs allow for the design of bio-MOFs to house a very specific drug; this encapsulated drug will then be transported to the target area, and the drug will be released *via* a trigger mechanism, such as ultrasound or pH, which acts to dissociate the organic linkers making up the MOFs, thus releasing the encapsulated drug (cargo) [138]. This process is summarised in Fig. 2.27.

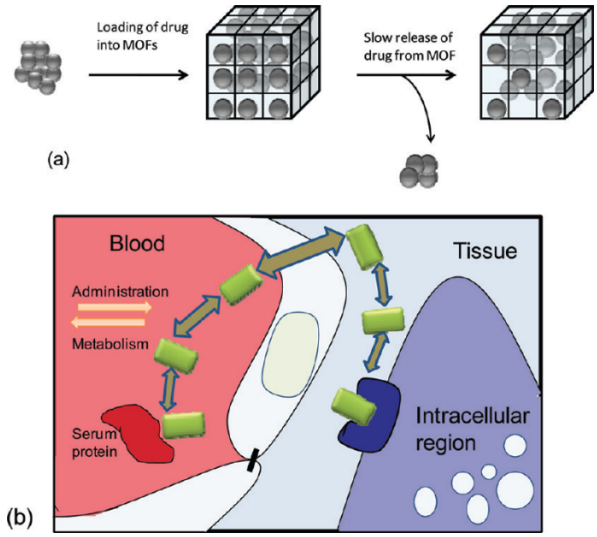

Fig. 2.27 The mechanism pertaining to the drug delivery of MOFs, with (a) loading of drugs into the MOFs, and (b) the release of the drugs at designated sites [139].

There are limited reports in literature pertaining to bio-MOFs or bio-compatible MOFs. Adhikari *et al.* [140] utilised Zn-BTC and Fe-BTC (both bio-compatible MOFs) as a loading vehicle for doxorubicin (dox), which is an anti-cancer drug. Loading dox into Zn/Fe-BTC was done *in situ* to form a MOF-drug composite, and the release of dox was achieved *via* reduced pH (acidic), which decomposes the organic ligand of the MOFs. Zhao *et al.* [141] took a dual approach *vis-à-vis* MOF-composites; they fabricated a Fe_3O_4/UiO-66 core-shell composite, where UiO-66 was loaded with dox, while Fe_3O_4 acts as a contrasting agent for magnetic resonance imaging (MRI). The core-shell composite demonstrated excellent drug loading capabilities and sustained drug release rates, and produces outstanding MRI images.

Despite the aforementioned examples and others, Li *et al.* [68] pointed out that study on MOF-composites, as opposed to MOFs, for biomedical applications, are limited to MOFs acting as a matrix. However, if our assumptions are based on the previously mentioned works on bio-MOFs, it can be assumed that the reverse would also hold true; compatible

MOFs, loaded with drugs, can be used as fillers and incorporated into matrices to form MOF (drug-loaded)-composites. These composites would be extremely useful for external applications; as similar trigger mechanisms can be used to trigger the release of the drug from the MOFs. The robustness of the matrix would also serve to allow transport and widespread distribution of these simple and effective MOF-composites.

2.5 Chapter summary

This chapter discussed the advent of metal-organic framework (MOF) materials, focussing on its corresponding composites (with MOFs as fillers), physico-chemical characterisations, and viable applications. Advances made in the field of MOF-composites are well reported in recent literature, and the fast paced nature of MOFs and the ongoing development of MOF-composites makes it an exciting and worthwhile endeavour. The next chapter will detail the fabrication of the polymer/MOF nanocomposites, its physico-chemical characterisation using the methods and techniques detailed in this chapter, and the experimental setup for using these polymer/MOF nanocomposites for adsorption applications.

CHAPTER THREE

Materials & Methods

This chapter will detail the experimental procedures employed throughout this work. The experimental work is divided into four distinct stages; the synthesis of ZIF-8 nanoparticles and the fabrication of the polymer/ZIF-8 nanocomposites, the thermo-mechanical, viscoelastic, and macro-mechanical characterisation of these nanocomposites, its utilisation for I_2 adsorption and reversible uptake of C_2H_4 gas molecules. The details pertaining to each method will be elucidated throughout this chapter in the following subsections.

3.1 Synthesis of Metal-Organic Framework (MOF) nanoparticles: Zeolitic Imidazolate Framework (ZIF)-8

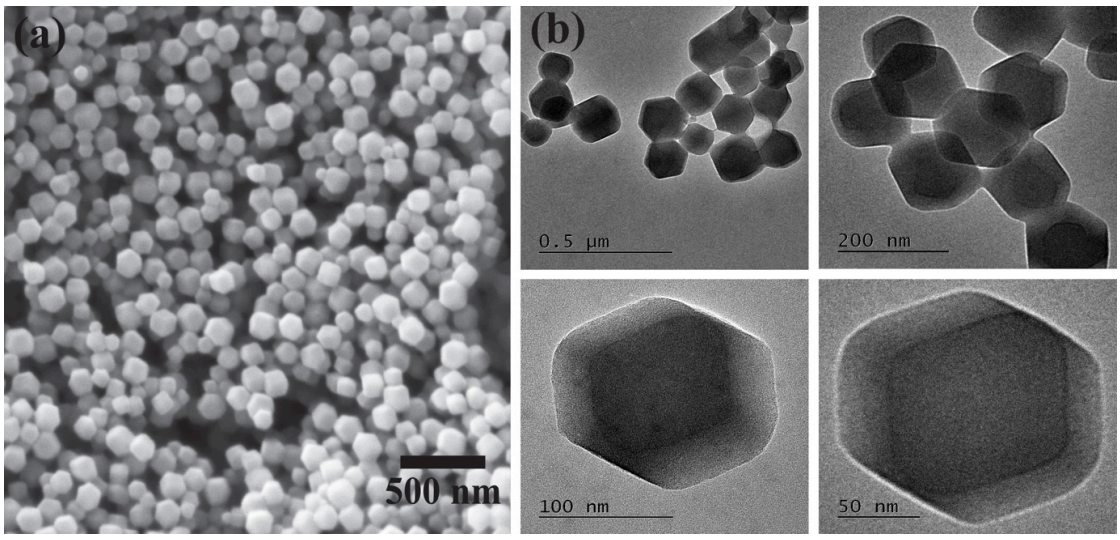

Fig. 3.1 The synthesised ZIF-8 nanoparticles, with (a) FEG-SEM images taken at ~30,000× magnification, and (b) TEM images taken at ~80,000-120,000× magnification. The particle size was determined to be 147.26 ± 7.05 nm (see Appendix A.1)

ZIF-8 nanoparticles shown in Fig. 3.1 were prepared in accordance to a previously reported rapid room-temperature synthesis approach [142]. 2.61 g of $Zn(NO_3)_2 \cdot 6H_2O$ and 5.74 g of 2-methylimidazole (purchased from Fisher Scientific and used as is without any further purification) were dissolved in 87 ml of methanol (CH_3OH), respectively. The resulting solutions were mixed and vigorously stirred for an hour, forming a milky white solution after a few minutes. The resulting ZIF-8 nanoparticles were then separated from the solution *via* centrifugation at 8,000 rpm for 10 minutes, and then (without drying) re-dispersed as a colloidal suspension in chloroform ($CHCl_3$). Another set of ZIF-8 nanoparticles was also prepared, but dispersed in tetrahydrofuran (THF) instead of $CHCl_3$, which is then stored for future use. A sample of these nanoparticles were imaged with FEG-SEM and TEM, and the images are shown in Fig. 3.1, exhibiting multi-faceted crystal structures, speculated to be rhombic dodecahedron [143].

3.2 Fabrication of polymer/MOF nanocomposites

This section and its subsequent subsections will detail the fabrication of two classes of polymer/MOF composites: Matrimid/ZIF-8 (glassy polymer matrix) and PU/ZIF-8 (rubbery polymer matrix). Although the methods of fabricating both nanocomposites share distinct similarities, differences are also apparent, especially in the types of solvents used and the vacuum curing temperature, which is reliant on the nature of the matrix.

3.2.1 Fabrication of Matrimid/ZIF-8 nanocomposites

The Matrimid polymer solution was prepared by dissolving Matrimid® 5218 flakes (a fully imidized thermoplastic polyimide supplied by Huntsman Corp.) in $CHCl_3$ for a total of 24-48 hours, until the flakes were visually determined to have completely dissolved in the $CHCl_3$-laden solution. Subsequently, the previously synthesised ZIF-8 nanoparticles dispersed as colloids were added in stages to the Matrimid solution, corresponding to Eqn. 3.1:

$$\text{ZIF-8 } wt.\% = \left(\frac{m_{\text{ZIF-8}}}{m_{\text{ZIF-8}} + m_{\text{Matrimid}}} \right) \times 100\% \tag{3.1}$$

where $m_{\text{ZIF-8}}$ is the weight of the ZIF-8 nanoparticles dispersed in $CHCl_3$ and m_{Matrimid} is the weight of the Matrimid flakes dissolved in $CHCl_3$. This results in the production of three distinct samples of nanocomposites, featuring varied ZIF-8 loadings (see Fig. 3.2) of 10, 20, and 30 wt.%. These distinct nanoparticle loadings for the nanocomposites were selected to coincide with the works reported by Song *et al*. [80] and Ordonez *et al.* [105]. The performance data reported by Song *et al.* (capture and separation of CO_2, CH_4, H_2, and N_2) will also be used as a comparison with the structure-property data collected from this work, therefore, it is prudent that the nanoparticle loadings and synthesis conditions closely match those reported in that work to ensure a proper and accurate comparison between both sets of data. The volume fraction data corresponding to these weight percent loadings are shown in Fig. 4.8. Also, it is important to point out that the application of the *colloidal solution mixing* approach may significantly reduce the possibility of nanoparticle agglomeration, otherwise witnessed in nanocomposites produced by re-dispersion of dried ZIF-8 nanoparticles [105].

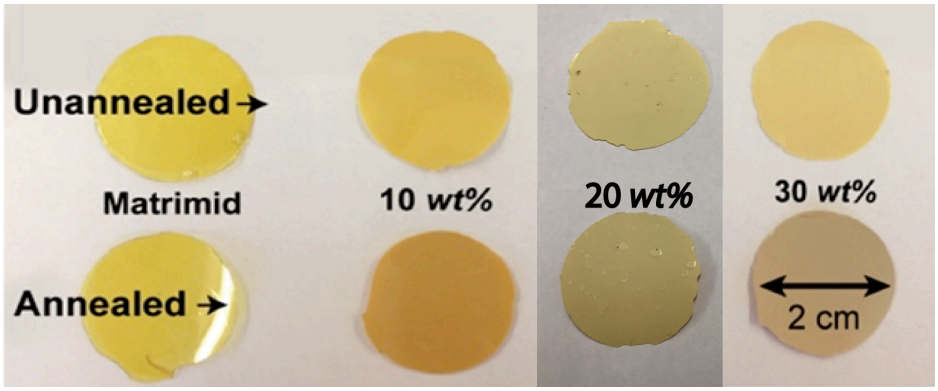

Fig. 3.2 Matrimid/ZIF-8 nanocomposites prepared by colloidal-based solution mixing approach [80], followed by casting *via* the doctor-blade technique, and annealing at 180 ºC for ~24 hours in vacuum.

To fabricate the nanocomposites depicted in Fig. 3.2, the resulting Matrimid/ZIF-8 solutions were cast using the doctor-blade method at a speed of 10 mm s^{-1} onto a cleaned (acetone) glass substrate, resulting in an average thickness of ~135 µm for the nanocomposites. The resultant nanocomposites were then transferred to a glove bag saturated with $CHCl_3$ vapour, and left to slow-cure for 24 hours, after which they were removed from the glove bag and placed in a vacuum oven, and cured for an additional 24 hours at 60 ºC (one batch) and 180 ºC (one batch). After 24 hours, the nanocomposites were removed from the glass substrate (*via* submersion in water), had its thickness measured (see Fig. 3.3), and stored for subsequent studies.

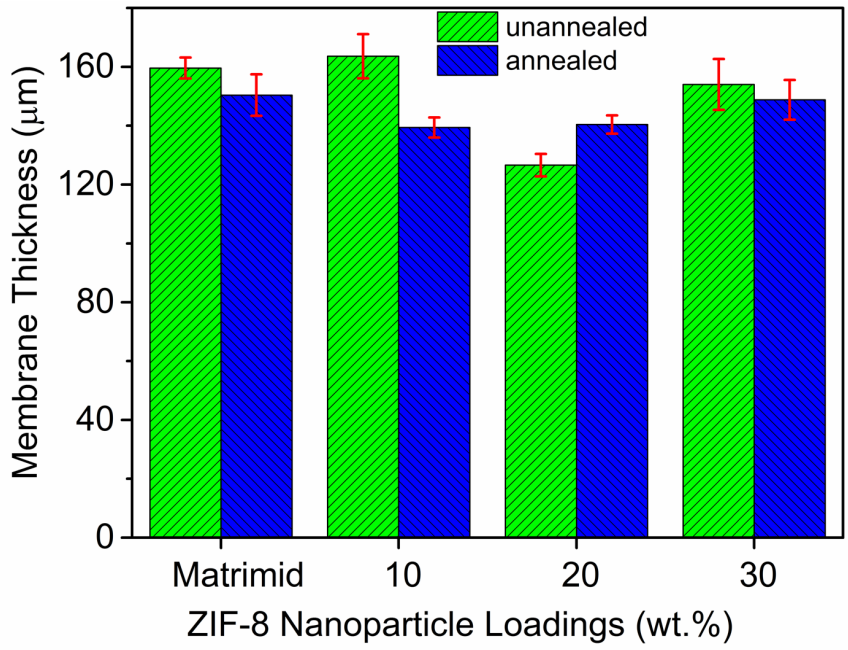

Fig. 3.3 The average thickness of taken from 5 strip samples of the Matrimid/ZIF-8 nanocomposites (5 mm × 60 mm).

3.2.2 Fabrication of Polyurethane (PU)/ZIF-8 nanocomposites

The polyurethane (PU) polymer solution was prepared by dissolving Poly [4,4'-methylenebis(phenyl isocyanate)-*alt*-1,4-butanediol/di(propylene glycol)/polycaprol actone] beads (purchased from Sigma Aldrich and used as is without further alterations) in THF for a total of 24-48 hours, until the pellets were visually determined to have completely dissolved in the THF-laden solution. Fig. 3.4 details the chemical structure(s) of the PU molecular building blocks.

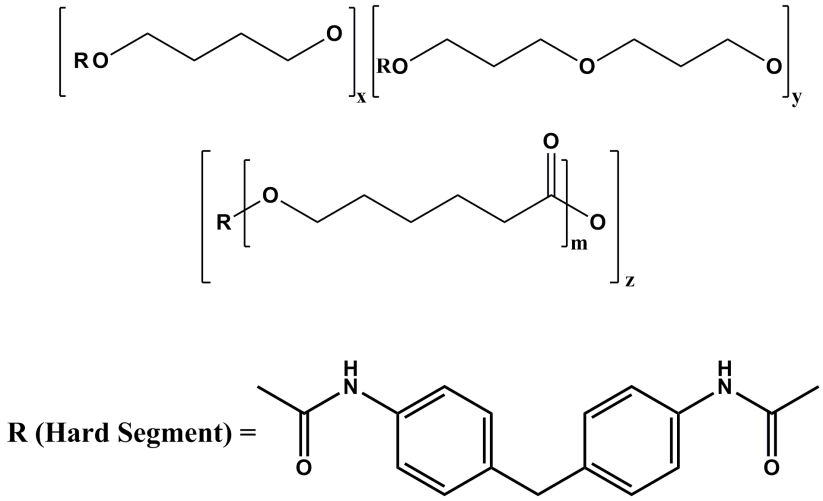

Fig. 3.4 The chemical structure of the PU used in this work. The hard segment (marked R in the main structure) could form secondary (weak) chemical bonds with the ZIF-8 nanoparticles via its carbonyl and amine groups.

The previously synthesised and dispersed colloidal ZIF-8 nanoparticles (THF) were added in stages to the PU solution, corresponding to Eqn. 3.2:

$$\text{ZIF-8 } wt.\% = \left(\frac{m_{\text{ZIF-8}}}{m_{\text{ZIF-8}} + m_{\text{PU}}} \right) \times 100\% \tag{3.2}$$

where $m_{\text{ZIF-8}}$ is the weight of the ZIF-8 nanoparticles dispersed in THF, and m_{PU} is the weight of the PU beads dissolved in THF. This results in the production of four distinct nanocomposites, featuring varied ZIF-8 loadings (Fig. 3.5): 10, 20, 30, and 40 wt.%. As per §2.3.1, the nanoparticle loadings were selected to match those of the Matrimid/ZIF-8 nanocomposites (up to 30 wt.%) to simplify the subsequent comparisons between both classes of nanocomposites. The 40 wt.% sample was synthesised due to the absence of the risk of sample failure, hence allowing the study of highly loaded (ZIF-8) samples, and also

due to the supposition of Song *et al.* [80] that higher loadings of ZIF-8 nanoparticles results in significantly improved (gas separation) performance. The corresponding volume fraction of the nanocomposites are shown in Fig. 5.4.

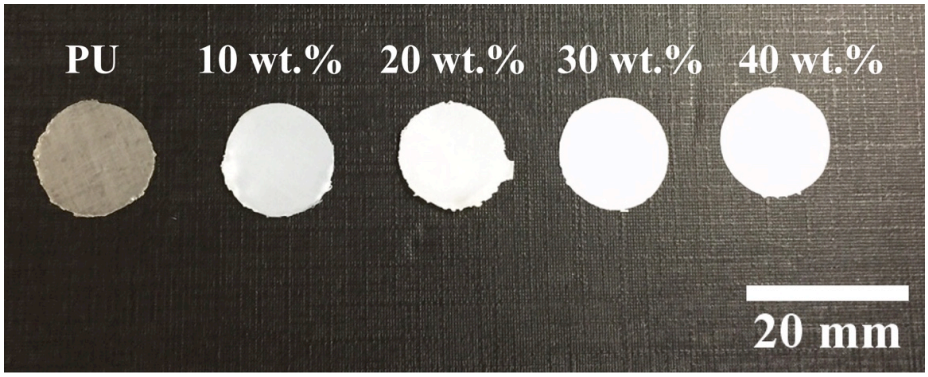

Fig. 3.5 The PU/ZIF-8 nanocomposites. Notice the increased opacity of the nanocomposites with increased ZIF-8 nanoparticle wt.% loading.

The PU/ZIF-8 nanocomposite solutions were cast using the doctor-blade method at a speed of 15 mm s^{-1} onto a PTFE substrate, resulting in an average thickness of ~100 μm (see Fig. 3.6). The (greater) variability of the thicknesses seen in Fig. 3.6 is the result of the casting and drying process: the nanocomposite solution was casted onto a PTFE substrate instead of glass substrate as it was more difficult to remove the dried nanocomposite from the latter (due to the favourable surface interactions between the dried PU and PU nanocomposite and the glass substrate). The PU and PU nanocomposites remained stubbornly stuck to the glass substrate, and significant and careful effort is needed to remove the nanocomposite to avoid the creation of micro-damages in the nanocomposite that could serve as stress risers. PTFE, on the other hand, is an ideal choice as a substrate due to its poor and almost non-existent interactions with the surface of PU. PU and its nanocomposites detached themselves upon drying from the PTFE substrate with minimal (almost no) effort. However, the poor surface

interactions also resulted in the greater variance of the thickness of the nanocomposites: when drying, the nanocomposite will shrink as it has no 'anchor' (ie. surface interactions) to hold it in place in its original casted shape, size, and thickness, and this shrinkage resulted in a relatively smaller (size-wise) nanocomposite, as the bulk of the casted solution will gravitate towards the centre of the nanocomposite, which creates a thickness gradient across the samples. Also, relatively greater amounts of THF was used to disperse the nanoparticles and PU beads (compared to the Matrimid solutions), especially for the PU nanocomposites, therefore, despite casting almost similar amounts of PU nanocomposite solution (~20-40 ml), the rate of evaporation of the solvents vary from sample to sample. The more viscous solutions resulted in thicker (0, 30, and 40 wt.%) nanocomposites, as the small amount of THF will quickly evaporate, culminating in the shrinkage of the samples as it did not have the time to settle into a fix shape and configuration prior to the THF being removed. This results in a thicker sample overall. Less viscous solution means that it contains more THF, which will take a relatively longer time to evaporate compared to its more viscous counterpart. This slower evaporation of THF allows for the nanocomposite solution to settle into a fixed shape and configuration *before* the complete evaporation of THF, and once it evaporates, the chances of this semi-dry solution to shrink is a lot less compared to its more viscous counterpart. This subsequently results in a thinner and larger sample (10-20 wt.%). The resultant nanocomposites were then transferred to a glove bag saturated with THF vapour, and left to slow-cure for 24 hours, after which they were removed from the glove bag and placed in a vacuum oven, and dried for an additional 24 hours at 85 ºC to remove any remaining occluded THF solvents. After 24 hours, the nanocomposites were detached from the PTFE substrate *via* submersion in water, and stored for subsequent studies.

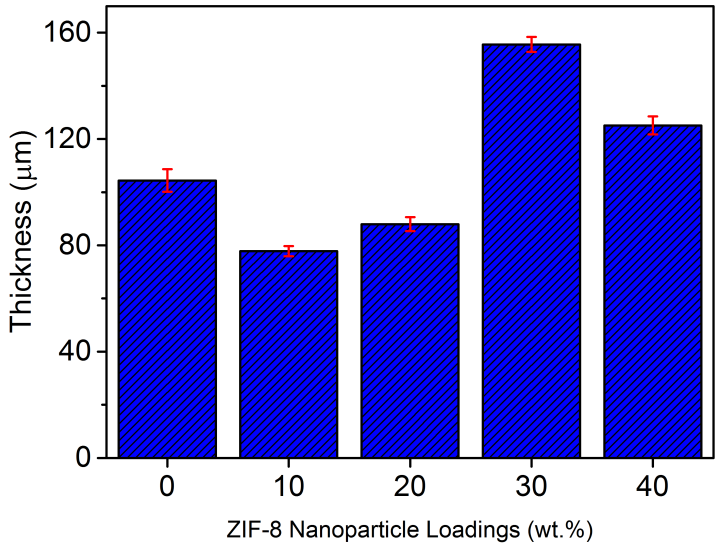

Fig. 3.6 The average thickness of taken from 5 strip samples of the PU/ZIF-8 nanocomposites (5 mm × 60 mm).

3.3 Materials characterisation

The characterisation methods in this work were selected for their respective capabilities to determine the morphological, mechanical, thermal, and viscoelastic properties of the polymer/ZIF-8 nanocomposites. The settings pertaining to these methods will be detailed in the following subsections.

3.3.1 The determination of the morphological features and chemical characteristics of the polymer/MOF nanocomposites

The first step in characterising the polymer/MOF nanocomposites is to determine its morphological, physical, and chemical characteristics. Methods that can be used to realise this include electron and probe microscopy and X-ray methods. The results reported by

these methods can be used to establish a common feature related to the polymer/MOF nanocomposites, and allow us to carefully study its microstructural makeup.

3.3.1.1 Scanning Electron Microscope (SEM)

The cross-sectional morphology of the nanocomposites was examined using a Field Emission Gun Scanning Electron Microscope (TESCAN LYRA3 FEG-SEM/FIB apparatus). The nanocomposite samples (Matrimid and all the PU samples) were immersed and fractured in a bath of liquid nitrogen (LN_2 at 77 K) and mounted at a 90º angle on a stub using adhesives, exposing the through-thickness surface. Each sample was coated with gold (Au) using a sputter coater for a period of 30 seconds, prior to imaging at 5-15 kV under high vacuum.

3.3.1.2 Transmission Electron Microscope (TEM)

TEM was used to image the ZIF-8 nanoparticles reported in §3.1. A small sample of the ZIF-8 nanoparticles was taken from the dispersion (< 1 ml) and re-dispersed and sonicated in CH_3OH (~10 ml). A drop of this sonicated solution was placed onto a copper specimen support grid. This droplet was allowed to dry prior to being imaged in the TEM (JEOL USA JEM-2100Plus). The sample was then imaged at ~200,000-500,000× at high vacuum.

3.3.1.3 Atomic Force Microscopy (AFM)

Atomic force microscopy (AFM) surface characterisation was conducted using the MFP-3D AFM (Asylum Research, Oxford Instruments) in tapping mode and AC-air topography settings. The samples, each measuring 5×10 mm^2, were mounted on stainless steel coupons (using carbon tapes and adhesives) to reveal the top surface of nanocomposite for imaging. Two samples were prepared for each class of nanocomposite, and imaging was conducted from 20 μm × 20 μm to 1 μm × 1 μm for an all-encompassing surface topography of the samples.

3.3.1.4 X-Ray Diffraction (XRD)

X-ray diffraction (XRD) was conducted using the Rigaku-2250 setup, operating at 45 kV and a tube current of 200 mA using the CuK_α source (1.5418 Å). The scanning rate was set to 0.5º min^{-1} with a continuous scanning range of 2θ = 5-30º (where all the major peaks for MOFs are expected to be present).

3.3.2 Thermo-mechanical properties characterisation

The determination of the thermo-mechanical and viscoelastic properties of the polymer/MOF nanocomposites is crucial in establishing its response to multiple external stimuli, in effect giving us a glimpse into its applicability to real world settings as detailed in §2.3.2.3 and §2.3.3.1. This sub-section will describe the methods used to characterise and analyse the samples prepared for this work.

3.3.2.1 Thermogravimetric Analyses (TGA)

The thermal stability and decomposition of the nanocomposites was investigated using the TGA-Q50 (TA Instruments), equipped with an induction heater (maximum temperature of 1000 ºC) and a platinum (Pt) sample holder. Samples weighing an average of ~4 mg were loaded onto the sample holder and heated from 50-1000 ºC at a rate of 10 ºC min^{-1}, to the point of complete decomposition. The raw data was collected and plotted using TA Analyser, which is TA Instrument's propriety software.

3.3.2.2 Dynamic Mechanical Analyses (DMA)

Temperature-dependent viscoelastic measurements were performed using the TA Instruments Q800 Dynamic Mechanical Analyser (DMA) equipped with an LN_2 dewar attachment. The experiments were performed at a heating rate of 3 ºC min^{-1} from -100 to 400 ºC (for Matrimid and Matrimid-based nanocomposites), and -80 to 120 ºC (for PU and PU-based nanocomposites). The DMA was calibrated to a pair of tension film clamps and fixed to a gauge length of 12.5 mm, with all samples tested under multi-frequency strain uniaxial tensile mode. The static force was set to 0.1 N, and the force track was set to 125% at an oscillatory strain of 0.1 %. The oscillating frequency was cyclically alternated between 5, 10, 15, 20, and 25 Hz (Matrimid-based nanocomposites) and 2, 5, 10, 15, 20, 25, 30, 35, 40 Hz (PU-based nanocomposites) as the temperature was steadily increased throughout the experiments.

3.3.2.4 Differential Calorimetric Scanning (DSC)

The melt behaviour of the nanocomposites was analysed using a DSC (Q2000, TA instruments) instrument. Hermetically-sealed Al pans were used to house the samples, set to ~2.5 mg per sample for the Matrimid-based composites, and ~1.5 mg for the PU-based composites (the difference in weight is due to the much lower density of the polymers and the fixed dimensions of the Al pan). The weights of the samples and the pans were recorded, and the DSC was calibrated to an empty hermetically-sealed Al pan prior to the experiments. The Matrimid-based nanocomposites were heated from 0 - 400 ºC at a rate of 10 ºC min^{-1}, while the PU-based nanocomposites were heated from -70 – 350 ºC at a rate of 10 ºC min^{-1}. The samples were held at their starting temperatures (0 ºC for Matrimid-based composites and -70 ºC for PU-based composites) for 5 minutes prior to the start of the experiments (all conducted under nitrogen flow) to stabilise the temperature gradient between the samples and the Al pans. The raw data was collected from the machine and subsequently plotted to study the melt behaviour, phase changes, and interactions between the ZIF-8 nanoparticles and its polymer matrices.

3.3.3 Quasi-static mechanical response

The quasi-static mechanical response is important in this work to establish the intrinsic bulk mechanical properties of the polymer/MOF nanocomposites, such as the elastic moduli, hardness, toughness, and ductility. Details pertaining to these experiments are explained below.

3.3.3.1 Nanoindentation

Quasi-static nanomechanical properties, particularly the Young's modulus (*E*) and indentation hardness (*H*) were determined *via* nanoindentation experiments using the MTS NanoIndenter XP (Agilent Technologies, USA), equipped with a Berkovich three-sided pyramid diamond tip. We made a series of 15-20 indentations in a rectangular grid (50 × 30 μm) for each sample being probed (three samples tested per wt.%). The Poisson's ratio in this study is assumed to be ~0.2 (Matrimid-based nanocomposites at compression strain of less than ~5%) and ~0.5 (PU-based nanocomposites at compression strain of less than ~5%, assuming incompressibility typical of a rubbery polymer material) [144]. The load-displacement plots generated for each indentation was used to derived the *E* and *H* values (see §2.3.2.2) for the samples, and the reported values are the average of 45-60 indents.

3.3.3.2 Large-strain uniaxial tensile test

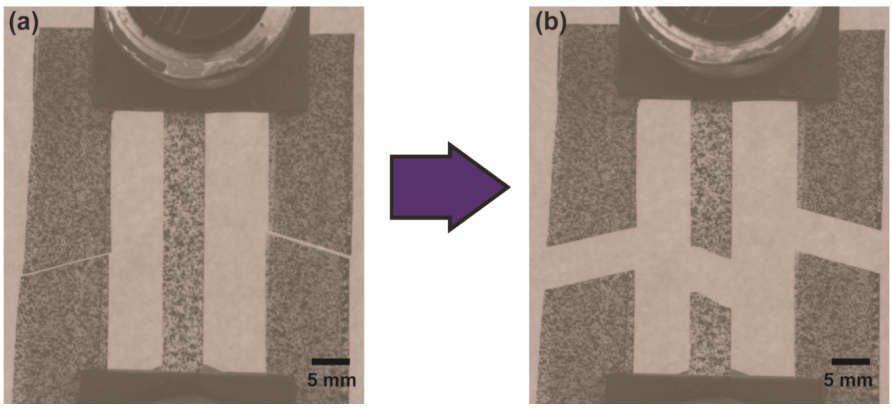

Fig. 3.7 The experimental setup for the uniaxial tensile test employing the universal testing machine (Instron Model 5582) with a PU/ZIF-8 nanocomposite (40 wt.%) nanocomposite sample (centre strip), where (a) initial loading of the sample, and (b) the sample at failure. The test was conducted at an elongation rate of 10 mm min^{-1} using a 100-N load cell. The samples are speckled with fine black paint for Digital Image Correlation (DIC) analysis, while the left and right strip is a paper frame that was glued onto the sample to prevent the sample from slipping during loadings while also serving as a dimensional guidance (gauge length of 30 mm).

The stress-strain plots were determined using the Instron universal testing machine (Model 5582), equipped with a 100-N load cell. The width and gauge length of the test coupons were 5 mm and 30 mm, respectively. The samples were securely clamped to the rigs, and were subjected to a tensile load applied at 0.5 mm min^{-1} (Matrimid-based nanocomposites) and 10 mm min^{-1} (PU-based nanocomposites) until fracture/failure. The load-displacement plots were converted to nominal stress-strain plots using Digital Image Correlation (DIC), where images of speckled test coupons undergoing tensile deformation were taken at 5 fps (Fig. 3.7), and these images were later processed using DaVis® software to calculate the

uniaxial strain profile of the test coupons from the previously captured images. These strain profiles were then matched to the stress values calculated from the gauge length and cross sectional area using MATLAB® to produce a nominal stress-strain plot for the polymer/ZIF-8 nanocomposites (see Appendix A.2). In the case of the PU/ZIF-8 nanocomposites, the generated stress-strain profile were also fitted using the Ogden model [145] *via* Abaqus®, employing its built-in hyperelastic function fitting module.

3.4 Iodine (I_2) capture

A solution of 10 mM of I_2 was prepared with cyclohexane (C_6H_{12}) as its base; both were purchased from Sigma Aldrich and used as is without further modifications or purification. The previously synthesised PU/ZIF-8 (30 wt.%) and Matrimid/ZIF-8 (30 wt.%) nanocomposites were dried in a vacuum oven for 24 hours at 85 °C prior to the I_2 uptake experiments to remove any moisture or solvents remaining on the surface of or within the nanocomposites. These nanocomposites were then carefully weighed, and the weight was recorded for each sample. The nanocomposites were then placed in a 5 mL glass vial, and 1 mL of the aforementioned I_2 solution were pipetted into the vials and hermetically sealed using an airtight cap. The vials were kept away from direct exposure to sunlight in order to prevent UV degradation from influencing I_2 uptake. Photos of the vials were taken at designated intervals of 0, 1, 2, 4, 6, 24, 48, 72, and 96 hours. At the end of the uptake experiments, the nanocomposites were removed from the solution, washed, and subsequently weighed. A control experiment was designed using the polymers and its corresponding nanocomposites submerged in C_6H_{12} for 96 hours, and subsequently weighed afterwards to compare the weight of the samples before and after (96h) submersion. This

control experiment was carried out to ensure that the uptake demonstrated by the samples was not influenced by the uptake of C_6H_{12}.

The samples exhibiting the highest level of capture and retention of I_2 was used for desorption experiments, where the sample was submerged in ethanol and allowed to desorb for a set amount of time (~ 4h). Photos were taken of the desorption experiments to visually monitor the level of I_2 released from the samples. The I_2-adsorbing nanocomposite were subjected to multiple characterisation techniques to confirm its uptake and retention capabilities.

3.4.1 Thermogravimetric Analysis (TGA) for Iodine (I_2) capture study

The influence of I_2 uptake towards the thermal and structural modifications of the pristine nanocomposites was determined using the TGA technique. The device used in this work is the TGA-Q50 (TA instruments), which comes with its own induction-heating chamber and Pt sample holder. A portion of the nanocomposites were carefully sectioned from the main sample (~1.5 mg), and placed onto the platinum (Pt) sample holder. Prior to the experiments, the sample holder was calibrated to zero weight in order to prevent any foreign particles or objects from influencing the readings. The samples were then subjected to the heat treatment outlined and programmed into the software: heating rate of 10 °C min^{-1}, initial temperature of 50 °C and final temperature of 800 °C. These parameters and temperatures were selected in order to guarantee that the samples (which includes Matrimid, PU, and ZIF-8) undergo the total range of thermal phase change and decomposition. The weight percent (wt.%) variation of the samples were recorded at every temperature interval, and these data were then used to construct thermal decomposition plots of the polymer matrices and their corresponding nanocomposites, with and without I_2 guest molecules.

3.4.2 Nanoindentation (I_2 capture study)

The settings and experimental setup described in §3.3.3.1 were also used for this experiment, the only difference being that the samples were indented as quickly as possible after being removed from the I_2 (C_6H_{12}) solution to avoid evaporation or interaction with its surroundings from influencing the quasi-static nano-mechanical properties of the polymers and polymer/MOF nanocomposites.

3.5 Reversible uptake of ethylene (C_2H_4) with the polymer/MOF nanocomposites

This part of the work was carried out as a collaboration with the Department of Inorganic Chemistry of the University of Alicante, Spain, where the samples prepared in this work was sent to confirm its viability for the reversible uptake of C_2H_4 gas molecules.

A total of four samples were selected for the reversible uptake C_2H_4 experiment due to time and equipment access limitations. The selected samples were Matrimid, PU, and their corresponding 30 wt.% nanocomposites (Matrimid/ZIF-8 30 wt.% and PU/ZIF-8 30 wt.%). The samples were cut into small rectangular pieces (1 mm × 3 mm) up to a total of ~200 mg of samples. The samples were then outgassed at ultra-high vacuum conditions at 358 K (85 °C) for 24 h prior to the experiments in a 9 mm sample bulb. A custom-built manometric equipment was used to measure the adsorption/desorption isotherms of C_2H_4 vapour at 278 K (5 °C) and 308 K (35 °C).

3.6 Chapter summary

This chapter detailed the synthesis, fabrication, characterisation, and application of the polymer (glassy or rubbery)/MOF nanocomposites. The methods were carefully selected to elucidate material properties such as the morphology, thermo-mechanical, and quasi-static mechanical response of the nanocomposites to external stimuli such as quasi-static and dynamic loads and a wide range of temperatures. Its viability *vis-à-vis* its physical and chemical characteristics was also tested by having the nanocomposites used for I_2 adsorption reversible uptake of C_2H_4. The next chapter will detail the collected and analysed results pertaining to Matrimid/ZIF-8 nanocomposites.

CHAPTER FOUR

Matrimid®/ZIF-8 nanocomposites: The influence of thermo-mechanical stability and viscoelasticity upon separation performance

This chapter will predominantly focus on one class of polymer/MOF nanocomposite; the Matrimid/ZIF-8. This class of polymer/MOF nanocomposite represents the glassy polymer/MOF combination, which comes with its own unique set of features and challenges due to the nature of glassy polymers and its interactions with the organic features of ZIF-8 (in this case, deprotonated 2-methylimidazole (mIm)). The pristine Matrimid and its corresponding ZIF-8 nanocomposites (10 wt.%, 20 wt.%, and 30 wt.%) were prepared in accordance to the methods and techniques described in the previous chapter (§3.2.1), and were characterised using the techniques detailed in §3.3. The following subsections will describe the results reported by these tests, and the implications on its usage in applications such as gas capture and separations reported in literature. The works and results discussed in this chapter has been published in Mahdi *et al.* [146].

4.1 Rationale

The applicability of MOFs for gas capture and separation is well documented in literature [147-149]. Examples of MOFs reported in literature for gas capture and separation applications include ZIF-8 [150] and HKUST-1 [148] corresponding to CO_2/CH_4 capture and separation and Xenon (Xe)/Krypton (Kr) separation, respectively. The large reactive surface area and the intrinsic porosity of MOFs render selective gas capture and separation possible [29].

ZIF-8, in particular, is especially favoured for CO_2 capture and separation applications. The high surface area of ZIF-8 (1650 m^2 g^{-1}), its large pore size (5.6 Å *vs.* the molecule size of CO_2 of 2.3 Å) and solvent accessible volume (SAV~0.5), and its chemical affinity with CO_2 (via its mIm ligands) render ZIF-8 particularly suitable for CO_2 capture and separation [59].

Despite successful lab-scale experimentation *vis-à-vis* gas capture and separation of CO_2 using ZIF-8 (nano)particles, the fact remains that the previously reported works utilised ZIF-8 in *powder* form, which might not translate well into real world applications due to deliverability issues, where dispersing and retaining powders for gas capture and separation applications might require a more elaborate setup (such as a mould to hold the powders in place) to contain the powders while being used for gas capture and separation. There are also a few problems associated with loose powders of ZIF-8 nanoparticles; they tend to agglomerate when dried, susceptible to high temperature, and are also quite reactive towards moisture in the air (H_2O adsorption), all of which negatively affect its subsequent performance [151].

The benefits of forming MOF-nanocomposites, as per the problems mentioned above, have been detailed in §2.2.4. Basically, the introduction of MOFs into a viable, accessible, and robust matrix will protect the MOF (nano)particles from its surroundings while allowing for its full functionality without compromising its structural integrity. The works of Song *et al.* [80] and Ordonez *et al.* [105] are testaments to this approach, where ZIF-8 nanoparticles were introduced into a Matrimid (glassy) matrix, which is a robust and durable glassy polymer used for aerospace applications. The nanocomposites in their works are used for CO_2/CH_4 gas separation applications, with positive results reported by both authors in terms of permselectivity of the nanocomposites for CO_2, which both attributed to the presence of ZIF-8 nanoparticles in the nanocomposite and its intrinsic affinity for CO_2 gas molecules.

The approach of forming polymer/MOF (nano)composite to enhance the gas capture and separation of CO_2 is not limited to the aforementioned authors, in fact, it has been explored rigorously by other authors using other polymer/MOF combination for the capture and separation of CO_2 from CO_2/CH_4 gas mixture. Smith *et al*. [152] reported the Ti-UiO-66/PIM-1 composite for the separation of CO_2 from flue gases (combined hydrocarbons), while Rodenas *et al*. [153] combined CuBDC nanosheets and polyimide to form CuBDC/PI composite for CO_2/CH_4 separation. All of these works have something in common: they posited that the formation of nanocomposites *via* the addition of nano-sized MOFs into polymers produced promising improvements; for instance, an ~150% increase in permeability for Ti-UiO-66/PIM-1 composites (5 wt.% loading) was reported as opposed to its neat PIM-1 matrix, accompanied by an increased in separation selectivity of 30-80% *vis-à-vis* CO_2/CH_4.

The polymer/MOF combination approach, besides improving the gas capture and separation performance of the resulting nanocomposite, also has the added advantage of improving the deliverability of the MOFs. The MOFs are now encased within a durable, robust, and accessible polymer matrix that allows it to capture and separate CO_2 while remaining unperturbed by the presence of moisture and high temperatures in its surroundings, elements that might result in damaged MOFs.

However, it should be pointed out that there is a crucial gap in the aforementioned works, and in fact, in literature pertaining to polymer/MOF (nano)composites: they lack a detailed study on the physico-chemical characteristics of the formed nanocomposites. The aforementioned studies focussed on the improved performance and deliverability of the polymer/MOF composites while neglecting to characterise its subsequent mechanical

performance such as its (tensile and yield) strength or thermal behaviours. In the context of real-world applications, it is imperative that the thermal and mechanical characteristics be detailed and quantified, as it plays a major role in subsequent materials' design. Elucidating these characteristics will also help determine the viability of polymer/MOF combination towards CO_2 (and any other gases) gas capture and separation, especially in the context of materials durability against factors such as temperature and continuous vibrations. It will also be useful when intending to upscale the production of the nanocomposites.

This chapter is predicated on closing the knowledge gap between the nanocomposites' performance and its physico-chemical properties. For this purpose, the Matrimid/ZIF-8 nanocomposite combination was selected. This particular system was selected as it has been reported twice in literature for the same application (capture and separation of CO_2/CH_4) by different authors [80, 105], thus establishing its distinct viability for the capture and separation of CO_2/CH_4. Both authors also agree that the introduction of ZIF-8 into Matrimid resulted in enhanced gas capture and separation performance, due to Matrimid's intrinsic affinity for CO_2 itself being amplified by the presence of ZIF-8. Importantly also, Matrimid is a glassy polymer (T_g >300 C) at room temperature, and it was selected to form a contrast to works of polymer/MOFs involving rubbery polymer as its matrix (see Chapter 5). Its performance data is readily available in published form, which will be used in this chapter to establish a correlation between the structure-property characteristics developed in this chapter and the reported gas capture and separation performance (CO_2, H_2, CH_4, and N_2) of the nanocomposites.

This chapter will discuss the systematic thermo-mechanical and viscoelastic characterisation of a prototypical ZIF-8 glassy polymer nanocomposite, in this case represented by Matrimid/ZIF-8 nanocomposite system. It is expected that the methodologies developed herein can be adopted to characterise a broad range of existing

and upcoming MOF-based nanocomposite systems, regardless of the nature of the MOFs or matrices [45].

4.2 Microstructural features of Matrimid/ZIF-8 nanocomposites

Figs. 4.1 and 4.3 present SEM images revealing the representative microstructures observed at the cross section of the Matrimid and its corresponding nanocomposites (unannealed and annealed). It can be seen that there is excellent dispersion and homogeneity of ZIF-8 nanoparticles embedded within the Matrimid matrix (further confirmed by XRD analyses, see Fig. 4.5). However, the lower loadings of ZIF-8 nanoparticles (~10 wt.%) appear to produce a better overall dispersion and blending of ZIF-8, as opposed to those incorporating higher loadings. Despite the visual observation, it should be pointed out that there are 'empty' regions within the nanocomposites, which are regions that lack the presence of ZIF-8 nanoparticles. This is evident in Fig. 4.2 (a-c), where there are grid numbers (defined as the 1 μm^2 of an equally divided grid in a FEG-SEM image of the nanocomposite) that shows 0 frequency of ZIF-8 nanoparticles. These concentrations of ZIF-8 nanoparticles within certain regions could be construed as the occurrence of (slight) aggregation and agglomeration, although visual observation discounted this for the 10 wt.% sample due to its lack of clumps of ZIF-8 nanoparticles in the images. The usage of the solution mixing approach [80] did not preclude the prevalence of agglomeration and aggregation in the higher loaded samples, however, as the 20 wt.% and 30 wt.% samples (Fig. 4.1 (c)-(d)) show regions with concentrated clumps of ZIF-8 nanoparticles. This is further evident in the particle distribution analyses of the 30 wt.% sample shown in Fig. 4.2 (b)-(c), where there are quite a few regions that show increased concentrations of ZIF-8 nanoparticles beyond the average ZIF-8 nanoparticles per grid stipulated in the distribution analyses.

This observation indicates that there is an optimal wt. % loading for the blending of Matrimid and ZIF-8 nanoparticles, where both phases could be seamlessly integrated. In fact, the rhombic dodecahedron crystallographic habit [143] characteristic of ZIF-8 is indistinguishable from the micrographs (see Fig. 4.1), confirming that the nanoparticles are indeed very well encapsulated (by a thin layer of Matrimid) and assumed an approximately spherical shape, which is energetically more favourable [154].

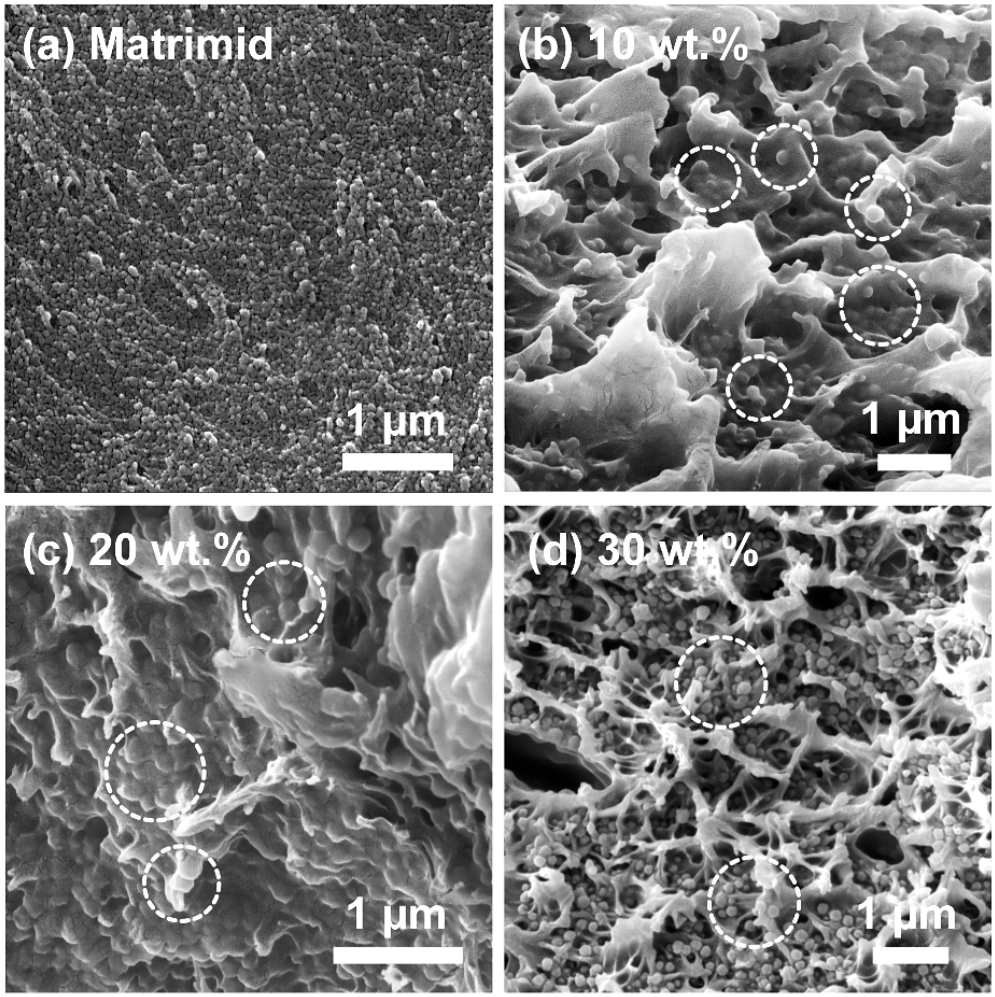

Fig. 4.1 SEM cross-sectional microstructures of Matrimid/ZIF-8 nanocomposites unannealed samples (cured at 60 °C in vacuum), showing (a) Matrimid, (b) 10 wt.%, (c) 20 wt.%, and (d) 30 wt.% of ZIF-8 nanoparticles. White dashed markers indicate representative areas where the polymer-encapsulated ZIF-8 nanoparticles are visible.

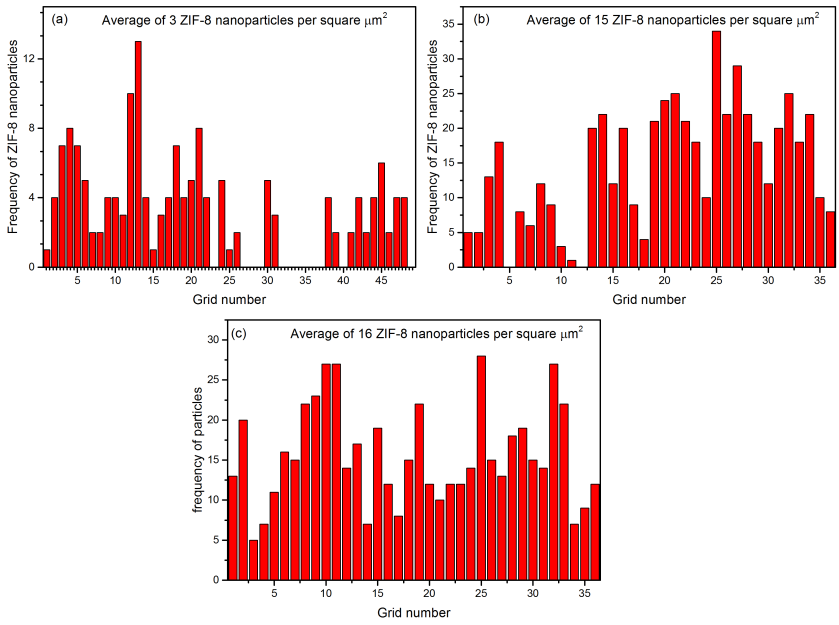

Fig. 4.2 The quantitative distribution of the ZIF-8 nanoparticles throughout the nanocomposite, where (a) Matrimid/ZIF-8 10 wt.%, (b) Matrimid/ZIF-8 20 wt.%, and (c) Matrimid/ZIF-8 30 wt.%. Each grid number represents an area of 1 μm^2, sectioned equally from the SEM images of the samples (see Appendix B.1) [155].

It should be emphasised that the micron-sized cavities and pores visible in the SEM images (Fig. 4.1(b)) are reminiscent of the classic 'cup-and-cone' ductile fracture mode, as the cross-sectional samples were prepared by the freeze-and-fracture technique in an LN_2 medium. Interestingly, the SEM micrographs reveal that the nanocomposites actually experienced a reasonable degree of ductile failure at the microscopic length scale under 77 K. In light of this, we may infer that ZIF-8 nanoparticles embedded in Matrimid disrupt the molecular packing of the polymeric chains; while this effect improves the overall gas permeability [80], it also gives rise to microscopic defects acting as *stress risers* [43] that are susceptible to localised deformation under load (see Appendix B.2).

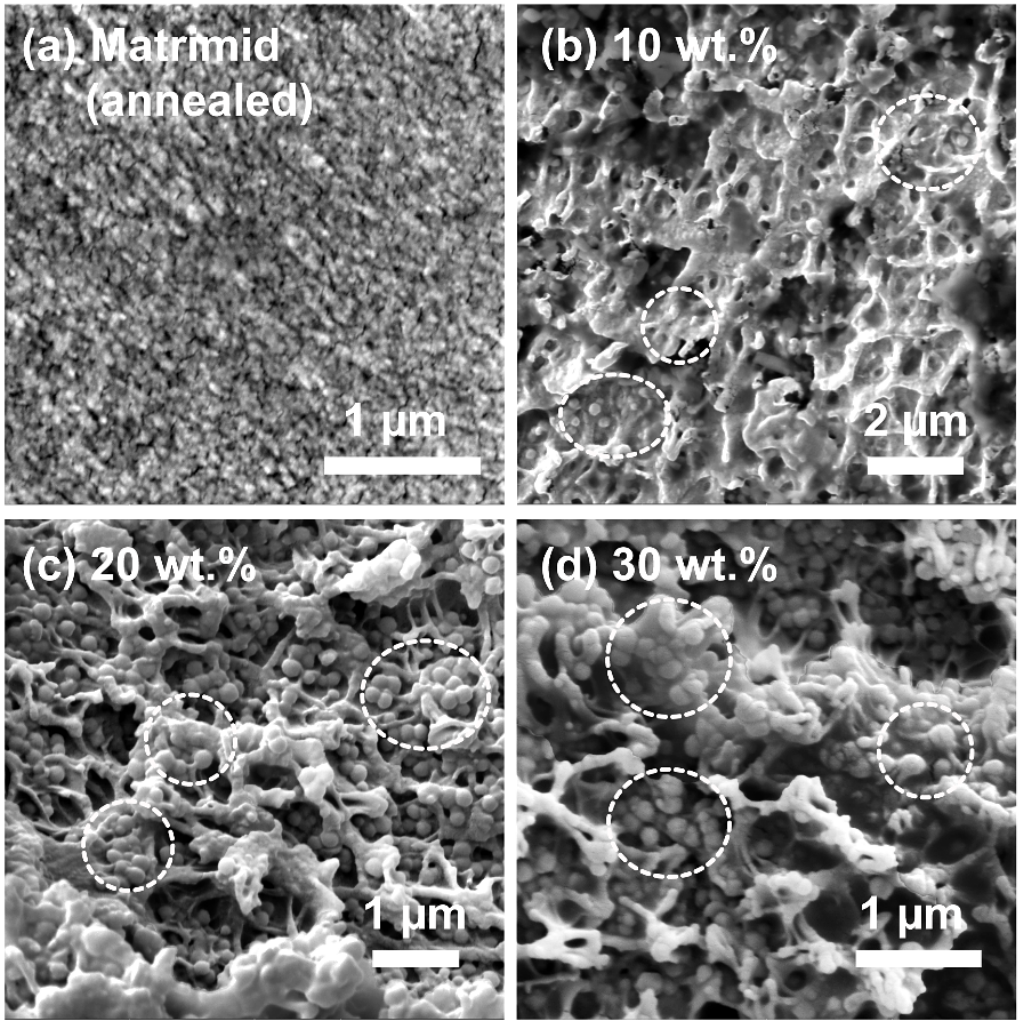

Fig. 4.3 SEM cross-sectional morphology of Matrimid/ZIF-8 nanocomposites subjected to an annealing heat treatment at 180 °C in vacuum. (a) Matrimid, (b) 10 wt.%, (c) 20 wt.%, and (d) 30 wt.% ZIF-8 nanoparticles. White-dashed markers highlight the presence of the polymer-encapsulated ZIF-8 nanoparticles.

The microstructures of the corresponding annealed Matrimid and its nanocomposites are shown in Fig. 4.3. Similar to the unannealed nanocomposites, higher loadings demonstrate increasing agglomeration and aggregation, as evidenced by the close packing and prominence of ZIF-8 nanoparticles within the nanocomposites, reminiscent of the microstructures found in the unannealed nanocomposites (Fig. 4.1). The primary difference

between the unannealed and annealed nanocomposites is that the trapped solvents within ZIF-8 and Matrimid have been completely evacuated, as the annealing temperature of 180 ºC is substantially higher than the boiling point of $CHCl_3$ (~60 °C), which is the solvent used for materials processing. Moreover, Matrimid undergoes secondary relaxation (β) at 80-90 ºC [156], leading to the molecular stretching of the polymer bonds accompanied by rotations of the side groups, both of which help in accelerating the removal of $CHCl_3$. As a consequence of annealing, the fracture surfaces in Fig. 4.3 suggest that a predominantly brittle failure mechanism is at play, where relatively fewer ductile deformation events can be identified, particularly at higher wt.% loadings. The quantitative evaluation of the distribution of ZIF-8 nanoparticles within the annealed nanocomposite in Fig. 4.4 demonstrated similar feature as the ones shown by Fig. 4.2, where ZIF-8 nanoparticles distribution throughout the nanocomposite improved with increased loading (from an average of 4 ZIF-8 nanoparticles per μm^2 for the 10 wt.% sample, to 17 ZIF-8 nanoparticles per μm^2 for the 30 wt.%). In the annealed samples, the regions with high concentration of ZIF-8 nanoparticles are more evident, as seen in Fig. 4.4 (a), where there are many regions that lack ZIF-8 nanoparticles, while in Fig. 4.4 (c), there are regions that have significantly lower number of ZIF-8 nanoparticles.

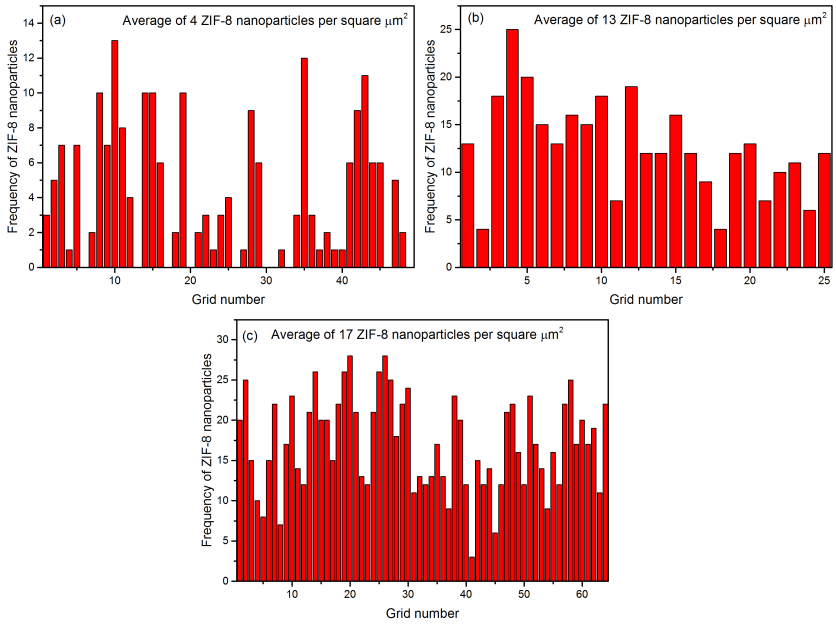

Fig. 4.4 The quantitative evaluation of the distribution of ZIF-8 nanoparticles within the annealed nanocomposites, where (a) Matrimid/ZIF-8 10 wt. %, (b) Matrimid/ZIF-8 20 wt.%, and (c) Matrimid/ZIF-8 30 wt.%. The grid number represents marked area that measures 1 μm^2 each. For the images used to derive these numbers, see Appendix B.1 [155].

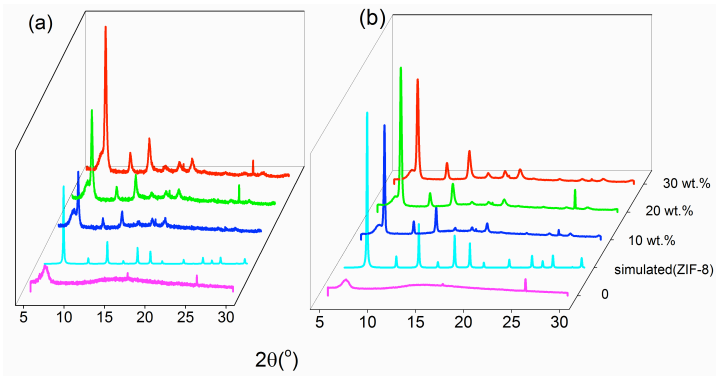

Fig. 4.5 The X-Ray Diffraction (XRD) diffractograms of the a) unannealed and b) annealed Matrimid, Matrimid/ZIF-8 nanocomposites, and simulated ZIF-8 XRD patterns, from which it was determined that crystallinity is directly proportional to both ZIF-8 nanoparticle loadings and annealing conditions (see Appendix B.3).

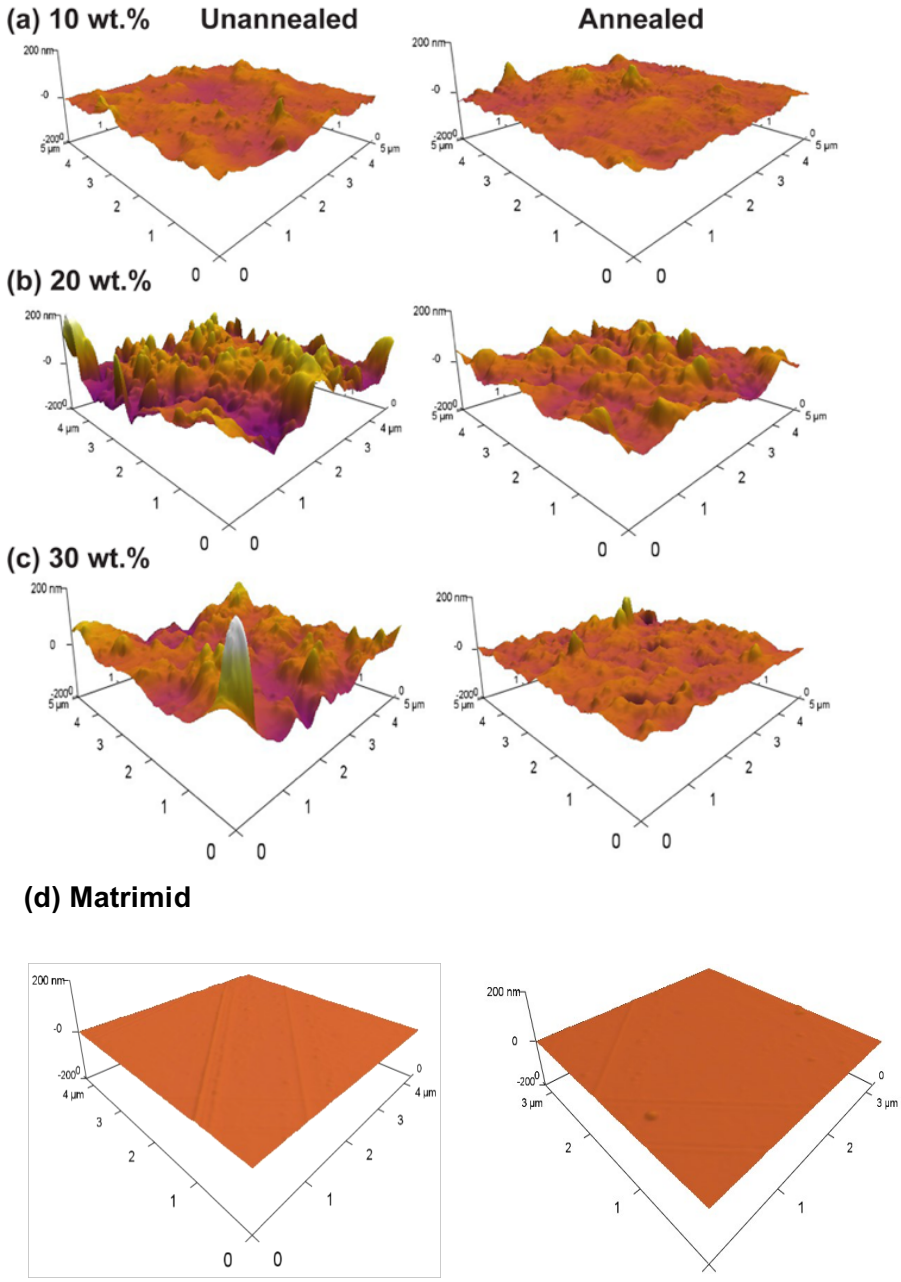

Fig. 4.6 AFM 3-D scans showing top surface topography of the unannealed (left panel) and the annealed (right panel) Matrimid/ZIF-8 nanocomposites, incorporating (a) 10 wt.%, (b) 20 wt.%, and (c) 30 wt.% of ZIF-8 nanoparticles. The (d) Matrimid surface topography serves as a baseline to the changes caused by the presence of the ZIF-8 nanoparticles. All images show the same height topography scale (±200 μm).

Fig. 4.6 shows the AFM images acquired from the vicinity of the top surface of the unannealed and annealed nanocomposites, respectively. Both sets exhibit distinctive height topography, which can be linked to the embedded nanoparticles and the corresponding wt.%. Nominally, the size of the protruding topographic features lies in the range of 150-200 nm across, thereby consistent with Matrimid-coated ZIF-8 nanoparticles, for which the size of the as-synthesised nanoparticles is relatively smaller, see Fig. 3.1(a). Therefore, it is clear that ZIF-8 is not only embedded inside the nanocomposites (as revealed by SEM cross sections, Figs. 4.1 & 4.3, and XRD in Fig. 4.5), but also present near the top subsurface layers, suggesting that a homogeneous dispersion of ZIF-8 nanoparticles was achieved throughout the matrix. The presence of the ZIF-8 nanoparticles and annealing of the nanocomposites also resulted in the altered surface roughness of the samples, as seen in Fig. 4.7. The surface roughness of the nanocomposites increases when the ZIF-8 nanoparticles loading increases, while annealing seems to decrease the overall roughness of the nanocomposites.

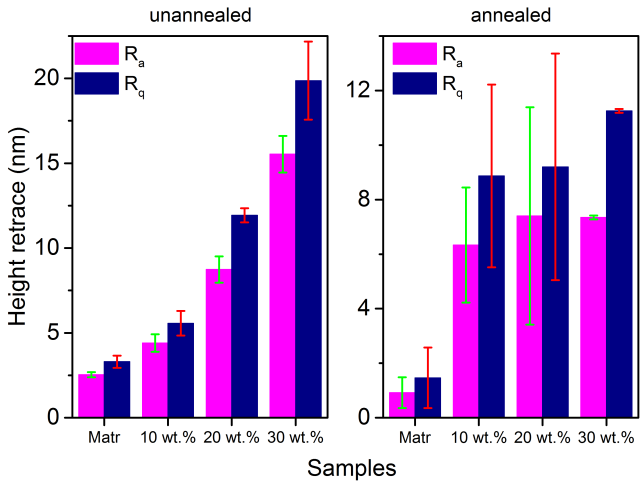

Fig. 4.7 The R_a (roughness average) and R_q (root mean square roughness) plots of the unannealed and annealed Matrimid/ZIF-8 nanocomposites derived from the AFM scans (3 sets of scans were used for average values). The roughness plots these values were derived from can be found in Appendix B.4.

Our SEM and AFM studies highlight the presence of a complex microstructure that stems from the two major composite constituents: ZIF-8 and Matrimid. It is envisaged that the multiple phases in the nanocomposites react differently to external stimuli, such as pressure and/or temperatures, creating stress risers and temperature gradients alongside competing responses within the nanocomposites, all of which underpins its mechanical performance. On this basis, information on mechanical properties, ranging from elastic moduli and yield strengths to viscoelasticity, toughness and ductility, and how they change with temperature will prove to be important to enable a wide range of challenging technological implementations [37, 39, 45].

4.3 Quasi-static mechanical properties determined from nanoindentation studies

Fig. 4.8 summarises the nanoindentation results obtained from the unannealed and annealed Matrimid/ZIF-8 nanocomposites. Using the indentation load-displacement raw data (see Appendix B.5), the Young's modulus (E) of the nanocomposites, assuming an isotropic response, were determined in accordance with the Oliver & Pharr method described in §2.3.2.2 (Eqns. 2.1 & 2.2), where the E_i and ν_i are Young's modulus and Poisson's ratio of the diamond indenter tip were taken to be 1141 GPa and 0.07, respectively. The Poisson's ratio of the sample (ν) was assumed to be ~0.2.

Intriguingly, it can be seen that the Young's modulus (E) property (Fig. 4.8(a)) is inversely proportional to the ZIF-8 nanoparticle content, although their hardness (H) response (Fig. 4.8(b)) is demonstrating an upward trend. At 30 wt.%, the stiffness of the unannealed nanocomposites decreased by ~8% with respect to the E of neat Matrimid, while that of the

annealed nanocomposites decreased by ~7%. Conversely, the H of the unannealed nanocomposites increased by ~5%, while the annealed nanocomposites increased by ~8%. In fact, this counterintuitive phenomena can be elucidated by invoking the simple Rule of Mixtures (RoM) — the Voigt and Reuss models [46], which respectively predicts the upper- and lower-bounds of E and H values on the basis of the volume-fraction-weighted contributions of the composite constituents. Herein for the RoM calculations, ZIF-8 nanoparticles correspond to: $E_{\text{ZIF-8}}$ = 3.3 GPa [33] and $H_{\text{ZIF-8}}$ ~500 MPa [32]; and for neat Matrimid unannealed: E_{Matrimid} = 4 GPa and H_{Matrimid} ~270 MPa [101]. Because $E_{\text{ZIF-8}} < E_{\text{Matrimid}}$, introducing a higher volume fraction of ZIF-8 into neat Matrimid yields, in effect, a more compliant composite (*i.e.* reduction of E). Given that the differential stiffness of the two constituents is relatively small ($\Delta E/E_{\text{Matrimid}}$ ~0.18), it follows that the deviation between the upper-and lower-bounds of E becomes equally insignificant.

In contrast, it is recognised that $H_{\text{ZIF-8}} >> H_{\text{Matrimid}}$ (specifically, hardness of ZIF-8 is about double that of neat Matrimid); the resultant composite therefore exhibits an improvement in hardness due to the higher wt.% of ZIF-8. It can subsequently be seen from Fig. 4.8(b) that the upper bound significantly overestimates the hardness; by comparison, the lower bound (Reuss model) is better at projecting the measured values. This outcome is expected as the Reuss model is derived assuming a non-continuous particulate-based composite system (assuming perfect interfaces), which better resembles the microstructural features seen in the nanocomposites (Figs. 4.1 & 4.3), though the discrepancies observed might also be associated with imperfections present at the interfaces of the nanoparticles and the matrix, thus decreasing load transfer.

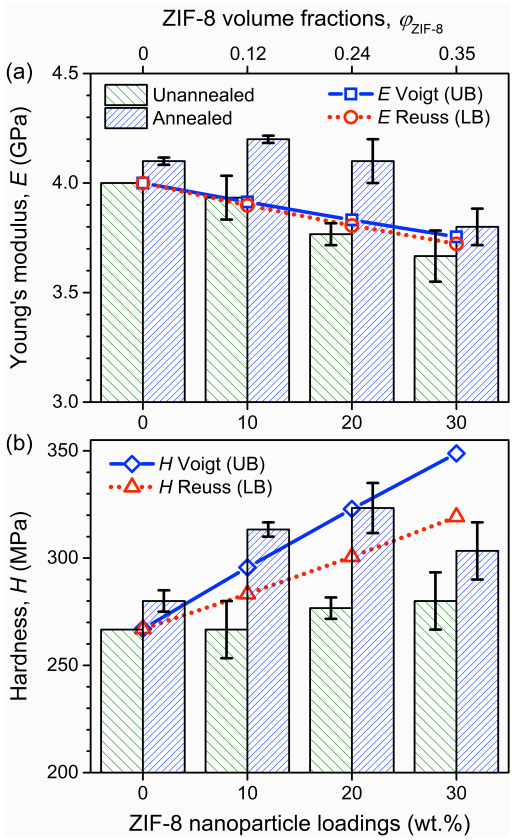

Fig. 4.8 Nanoindentation data plotted as a function of ZIF-8 nanoparticle loading (in wt.% and volume fractions φ_{ZIF-8}), where (a) Young's modulus (E), and (b) nanohardness (H). Each experimental data point corresponds to averaged measurements conducted on three different samples, each subjected to an array of 15-20 indents to a maximum surface penetration depth of 2 μm. The error bar represents standard deviations derived from 60 individual indents. The upper and lower bounds were computed based on the Rule of Mixture relationships [46], which are expressed in terms of the nanoparticle volume fractions (φ_{ZIF-8}) and elastic moduli or hardness of the composite constituents. The upper bound (UB Voigt) and lower bound (LB Reuss) for Young's modulus of nanocomposites presented in (a) are determined from $E_c = \varphi_{ZIF-8}E_{ZIF-8} + (1 - \varphi_{ZIF-8})E_{Matrimid}$ and $E_c = [(\varphi_{ZIF-8}/E_{ZIF-8}) + (1 - \varphi_{ZIF-8})/E_{Matrimid}]^{-1}$, respectively. Likewise, the two bounds for hardness in (b) were established using a corresponding set of relationships, where the moduli terms (E's) are substituted by the hardness terms (H's).

Turning to the annealed nanocomposites, it was established that the abovementioned trends persist. Following the annealing treatment, the magnitudes of E and H have both increased by up to ~9% and ~18%, respectively. Such a behaviour can be understood by scrutinising the nature of the secondary chemical bonding [157] that exists in the nanocomposites, as illustrated in Fig. 4.9. The evacuation of entrapped solvent molecules is assumed to enhance hydrogen bonding between hydroxyl groups by eliminating competition from other elements vying to form hydrogen bonds, in conjunction with π-π stacking interactions between the benzene rings that are ubiquitous in the polyimide chains (of Matrimid) and the mIm (of ZIF-8). It is anticipated that such combined molecular effects produce a stiffer and harder, yet more brittle nanocomposites. This is especially evident with annealed nanocomposites at higher wt.% loading, for example it was observed that the 30 wt.% nanocomposite cracked immediately upon removal from glove bag after curing for 24 hours at room temperature.

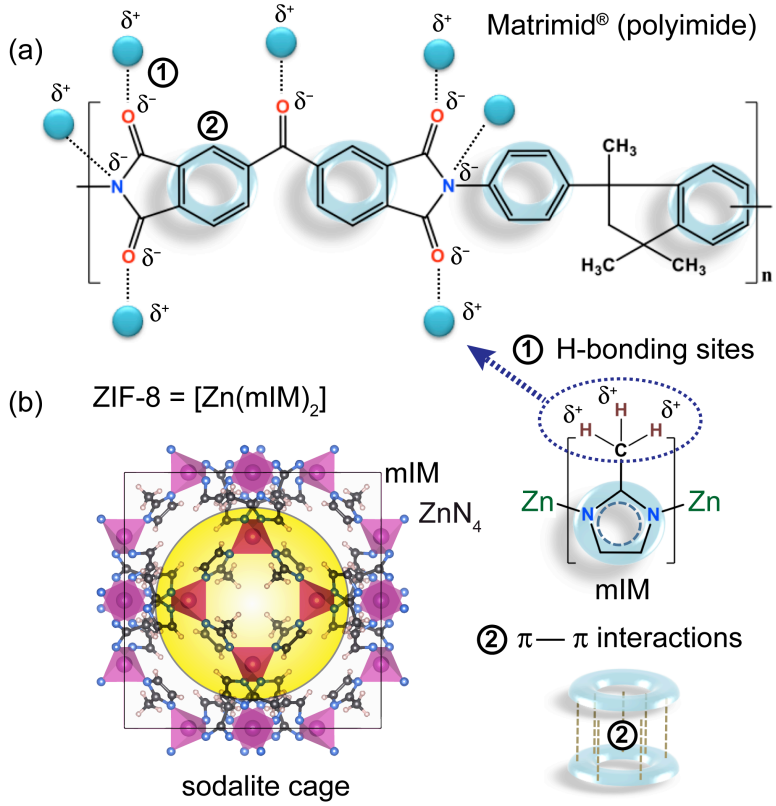

Fig. 4.9 Schematic illustrating the nature of molecular interactions in the Matrimid/ZIF-8 nanocomposites. (a) Polyimide monomer constituting the Matrimid matrix, and (b) ZIF-8, where yellow surface represents the internal porosity (*ca*. 11 Å diameter); mIm = [2-methylimidazolate] ligands. Secondary bonding sites comprise of hydrogen bonding established by the methyl groups (CH_3) of ZIF-8's organic linkers and the carbonyl and hydroxyl groups prevalent in polyimides, in addition to auxiliary π-π stacking interactions due to delocalised electrons of adjacent benzene rings. The presence of carbonyl and hydroxyl groups in polyimide enables the formation of hydrogen bonds [158] between Matrimid and ZIF-8, giving intimate adhesion between the two constituents. The strength of the H-bonds depends upon the acidity of the proton donor, suggesting that the strength of hydrogen bonds between the aldehyde and methyl group in Matrimid/ZIF-8 would be akin to weak interactions such as the *van der Waals* (vdW) forces.

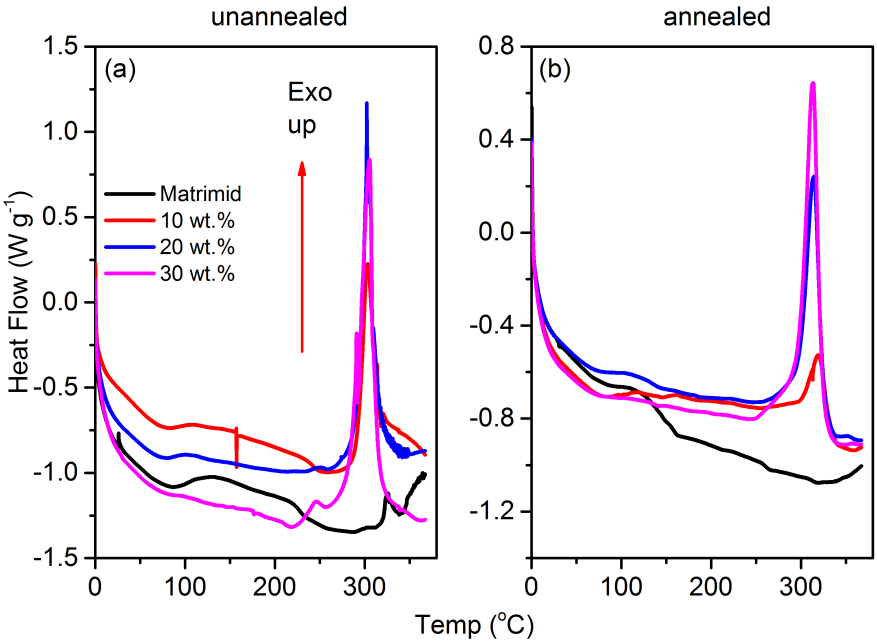

Fig. 4.10 DSC plots for the (a) unannealed and (b) annealed Matrimid/ZIF-8 nanocomposites.

Fig. 4.10 shows the DSC plots of the unannealed and annealed Matrimid/ZIF-8 nanocomposites. There are two distinctive shifts that can be observed in both plots; the glassy shifts in the region of 250-300 ºC, and the crystallization peaks in 300-350 ºC region. Uniquely, in the unannealed DSC plots, slight peaks can be observed near the crystallization peaks (secondary peaks), which can be attributed to the release of the occluded solvents ($CHCl_3$ in this case) upon heating and the occurrence of glass transitions (see Figs. 4.11 & 4.12 for similar occurrence and further explanations). These peaks are notably absent in the annealed samples due to the occluded solvents already being removed when annealing at 180 ºC for 24 h, resulting in only one distinctive peak (crystallisation) in the annealed DSC plots.

Table 4.1 The T_g and heat of fusion (ΔH) of the unannealed and annealed Matrimid/ZIF-8 nanocomposites, derived from the DSC plots in Fig. 4.10.

Samples	T_g (ºC)	Heat of fusion, ΔH (J g^{-1})
Matrimid	227	0
Matrimid/ZIF-8 10 wt.%	241	32
Matrimid/ZIF-8 20 wt.%	255	33
Matrimid/ZIF-8 30 wt.%	252	42
Matrimid annealed	246	0
Matrimid/ZIF-8 10 wt.% annealed	232	14
Matrimid/ZIF-8 20 wt.% annealed	234	46
Matrimid/ZIF-8 30 wt.% annealed	236	64

The T_g of annealed Matrimid is slightly higher than the unannealed Matrimid, but in the case of the nanocomposite samples, the unannealed samples have higher T_g compared to their annealed counterpart. This can be explained by the presence of occluded solvents in the unannealed samples, which delays the onset glass transition due to its simultaneous interactions with the ZIF-8 nanoparticles and the Matrimid polymeric chains. The glass transition can only take place after the removal of the solvents via heating and chain and bond rotations, upon which the occluded solvent is released, allowing the polymeric chain (matrix) to freely move and finally undergo phase transition. The lack of occluded solvent in the annealed samples allowed the phase transition to take place sooner, which is explained by the lower T_g in this case. The presence of only one T_g proves that the nanocomposite, unannealed and annealed, behave as one unified structure instead of two independent phases, and this could only be observed if there ZIF-8 nanoparticles and the Matrimid polymeric chains are bonded (via a collection of secondary interactions, posited in Fig. 4.9,

due to the reactive mIm ligands of the ZIF-8 nanoparticles). These collective bonds within the nanocomposite function as minor anchors that interrupt the phase transition of the samples [152, 159, 160].

The integration of the crystallisation peak in Fig. 4.10 results in the heat of fusion values tabulated in Table 4.1. The noticeable lack of a crystallization peak in the Matrimid samples (annealed and unannealed) signifies that the Matrimid itself did not undergo crystallization upon increased uptake of heat, instead the samples began decomposing beyond 400 ºC. However, the nanocomposite samples, both annealed and unannealed, exhibited significant crystallization peaks, which is proportional to the ZIF-8 nanoparticle loadings. The higher loadings of the nanoparticles resulted in increased heat of fusion in both the unannealed and annealed samples. The heat of fusion represents the amount of energy absorbed to break the intrinsic bonds between the samples and the energy released when these broken bonds are reconstituted to form new materials (recrystallization). The increased values of heat of fusion seen in Table 4.1 alongside increased ZIF-8 nanoparticles contents can be explained by the fact that the presence of collective secondary bonds (H-bonds, van der Waals, and π-π stacking) between Matrimid and ZIF-8 is reinforcing the covalent bonds between the Matrimid polymeric chains, resulting in increased energy requirement not only to break the polymeric covalent bonds between the Matrimid polymeric chains, but also the bonds between Matrimid polymeric chains and the mIm ligands of ZIF-8 nanoparticles (see Fig. 4.9) [118]. The bond strengths, lengths, and constituents, can be further probed using X-Ray photoelectron spectroscopy (XPS) [161] and Fourier Transform Infrared Spectroscopy (FTIR) [162] however, the lack of access to the former, and the (chemical) similarity between the interactions between the polymeric chains of Matrimid and the organic ligand (mIm) of the ZIF-8 nanoparticles precluded both methods from this work. The types of bonds and bond strength can also be determined using Density Functional Theory (DFT) or

its derivatives [163], however, as per the aforementioned experimental methods, this approach is beyond the scope of this thesis.

4.4 Viscoelastic properties of unannealed and annealed Matrimid/ZIF-8 nanocomposites

Details pertaining to viscoelasticity and its importance in elucidating the thermo-mechanical properties related to polymer nanocomposites (with MOF fillers) have been described in §2.3.2.3, while the experimental parameters pertaining to testing the Matrimid/ZIF-8 nanocomposites have been explained in §3.3.2.2. This section will discuss the results garnered from DMA tests and highlight the importance of its viscoelastic behaviour.

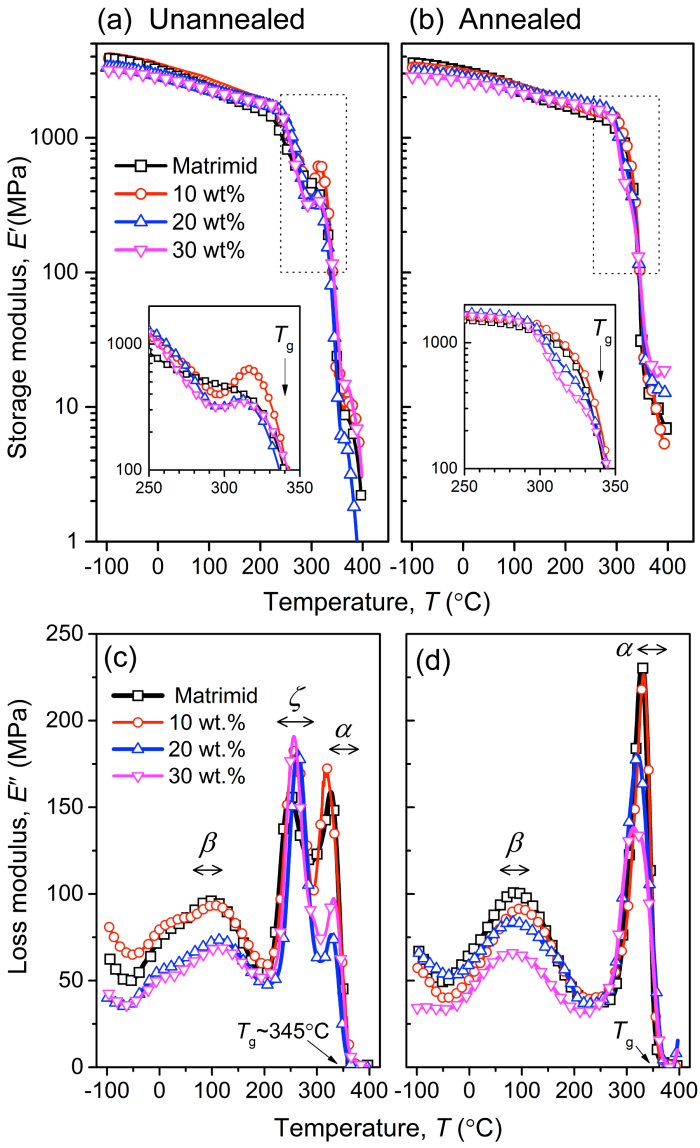

Fig. 4.11 Storage modulus (*E*' - top panels, note log scales) and loss modulus (*E*" - bottom panels) as a function of temperature and ZIF-8 nanoparticle wt.% for the (a & c) unannealed, and (b & d) annealed nanocomposites. All DMA measurements were conducted at a frequency of 10 Hz (see Appendix B.6 for additional frequency associated data). The insets in (a) and (b) highlight the variations of *E*' approaching the glass transition temperature, T_g ~345 °C. The primary relaxation is denoted as α, which corresponds to T_g. Secondary relaxations consist of β-transition due to bond rotations in polyimide chains [156], while the ζ-transition identified in this work can be linked to the dynamics associated with the extraction of residual solvent molecules.

Fig. 4.11 compiles the storage and loss moduli data for the nanocomposites as a function of temperature and nanoparticle wt.% loading. It was established that the increased addition of ZIF-8 decreased the storage and loss moduli of the nanocomposites before reaching its secondary β-relaxation temperature (80-100 ºC). Overall, the order of storage and loss moduli values for the nanocomposites are: Matrimid > 10 wt.% > 20 wt.% > 30 wt.%. However, such differential behaviour becomes negligible upon reaching the primary α-relaxation temperature (~345 ºC) [156], which is known as the glass transition temperature (T_g). It was observed that the introduction of ZIF-8 nanoparticles into Matrimid has an insignificant impact on the T_g of the resulting nanocomposites (see Appendix B.7). For instance, the variation in T_g between Matrimid and 30 wt.% nanocomposite was +0.4% and +0.6% for unannealed and annealed nanocomposites, respectively. Our data show that for temperatures at and beyond T_g, the transition region of the storage and loss moduli of the nanocomposites, whether annealed or not, essentially overlaps one another. Moreover, it was found that in the vicinity of the α-transition (~T_g), the annealed nanocomposites display relatively higher storage and loss moduli, as shown in Fig. 4.11(b, d).

The T_g of the nanocomposites can be determined using two approaches; the first, when the storage modulus drops by three orders of magnitude, and the second, when the loss modulus is at its maximum peak. The T_g is clearly visible in Fig. 4.11 (also see Appendix B.7), signifying the switch from a (stiff) glassy-to-rubbery (pliant) mechanical response. Notably, it can be pinpointed from Fig. 4.11(c) that the unannealed nanocomposites undergo an additional relaxation when approaching the T_g region, named in this thesis as ζ-relaxation. The presence of multiple transition peaks is especially striking in the unannealed samples, including neat Matrimid; however, it is absent in all the annealed samples (Fig. 4.11(d)). It should also be pointed out that the T_g reported using the DMA method is regarded as

significantly more quantitatively accurate than the T_g values reported by the DSC method, which explains the discrepancy between the T_g value reported here and in Fig. 4.10/Table 4.1.

The ζ-transition can be attributed to the residual solvent molecules ($CHCl_3$) trapped within Matrimid and ZIF-8 nanoparticles during processing, which were only partially removed in curing. During materials processing, ZIF-8 was dispersed in $CHCl_3$, while Matrimid flakes were dissolved in $CHCl_3$. The cage size (11.4 Å, see Fig. 4.9(b)) and pore volume (0.485 $cm^3\ g^{-1}$) of ZIF-8 nanoparticles allow for the $CHCl_3$ molecules to enter the porous sodalite cage [32, 164]. This is facilitated by the gate-opening dynamics of the mIm organic linkers [50]. Solution casting of the nanocomposite solution will result in trapped solvents, and although dried in a vacuum furnace for 24 hours at 60 °C (evaporation temperature of $CHCl_3$), a small amount of solvents was invariably present, which accounts for the presence of multiple peaks towards the T_g of the unannealed nanocomposites (Fig. 4.11(c)). Indeed, it was confirmed that annealing the nanocomposites at higher temperatures (180 °C for 24 hours) can eliminate the occurrence of ζ-relaxation, endorsed by the presence of only a characteristic peak (α at T_g) for the annealed nanocomposites (Fig. 4.11(d)). Annealing at a higher temperature (secondary relaxation temperature) initiates bond rotations in polyimides, which could aid in the removal of $CHCl_3$ trapped within the cages of ZIF-8 nanoparticles bonded to Matrimid by weak interactions (Fig. 4.9). Approaching T_g, there will be major intermolecular sliding amongst the polyimide chains, freeing any trapped $CHCl_3$. It is conceivable that the combined movement of Matrimid polymeric chains and the evaporation of $CHCl_3$ (from pores of Matrimid and cages of ZIF-8) cause major fluctuations in dynamic moduli, resulting in multiple peaks detected near T_g of the unannealed nanocomposites.

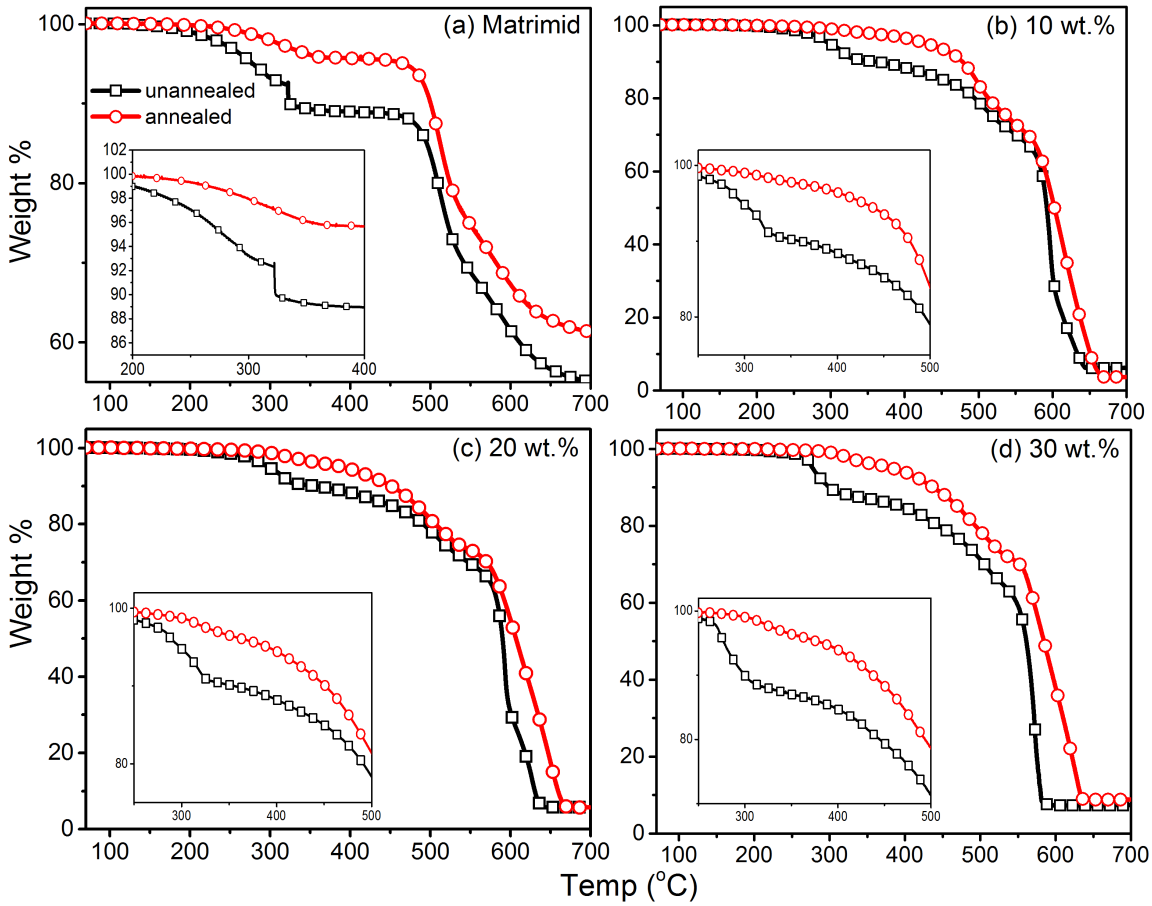

Fig. 4.12 TGA data of individual unannealed and annealed nanocomposites, with a) Matrimid, b) 10 wt.%, c) 20 wt.%, and d) 30 wt.%. As mentioned previously, the wt. % decrease in the unannealed nanocomposites is attributed to occluded solvents, corresponding to the ζ-phase seen in Fig. 4.11(c). Increased ZIF-8 nanoparticle loadings also increased the wt. % of the occluded solvents being removed from the nanocomposites, suggesting that solvents might not only be occluded in Matrimid, but in the pores of ZIF-8 as well.

The supposition that the solvents are occluded in the unannealed nanocomposites is further supported by the results reported by the TGA method (Fig. 4.12). Each of the unannealed nanocomposite show a slight wt.% drop at T ~300 °C, which corresponds to the ζ-phase shown in Fig. 4.11(c) and the slight pre-crystallisation peaks evident in Fig. 4.10.

Comparatively, the annealed nanocomposites lack this slight weight decrease prior to T ~ 400 °C. Major decomposition of the nanocomposites (both annealed and unannealed) began taking place at T ~ 500 °C, showing that once the occluded solvents were removed from the samples, the unannealed and annealed nanocomposites began acting similarly (evident by the almost overlapping peaks at T ~ 550-600 °C), in effect, making the unannealed and annealed nanocomposites almost similar. It should also be pointed out that the introduction of ZIF-8 nanoparticles resulted in an earlier initiation of degradation of the nanocomposites due to the loss of continuity in the polymer (see Appendix B.2) and the introduction of stress risers, however, the presence of ZIF-8 nanoparticles *also* helped maintain structural integrity, where it is seen that the nanocomposites are semi-intact at T ~ 600 °C (albeit rapidly decomposing), speculated to be due to the weak interactions between Matrimid (char at 345 °C) and the ZIF-8 nanoparticles. Both the unannealed and annealed nanocomposites undergo complete decomposition at T > 650 °C [165].

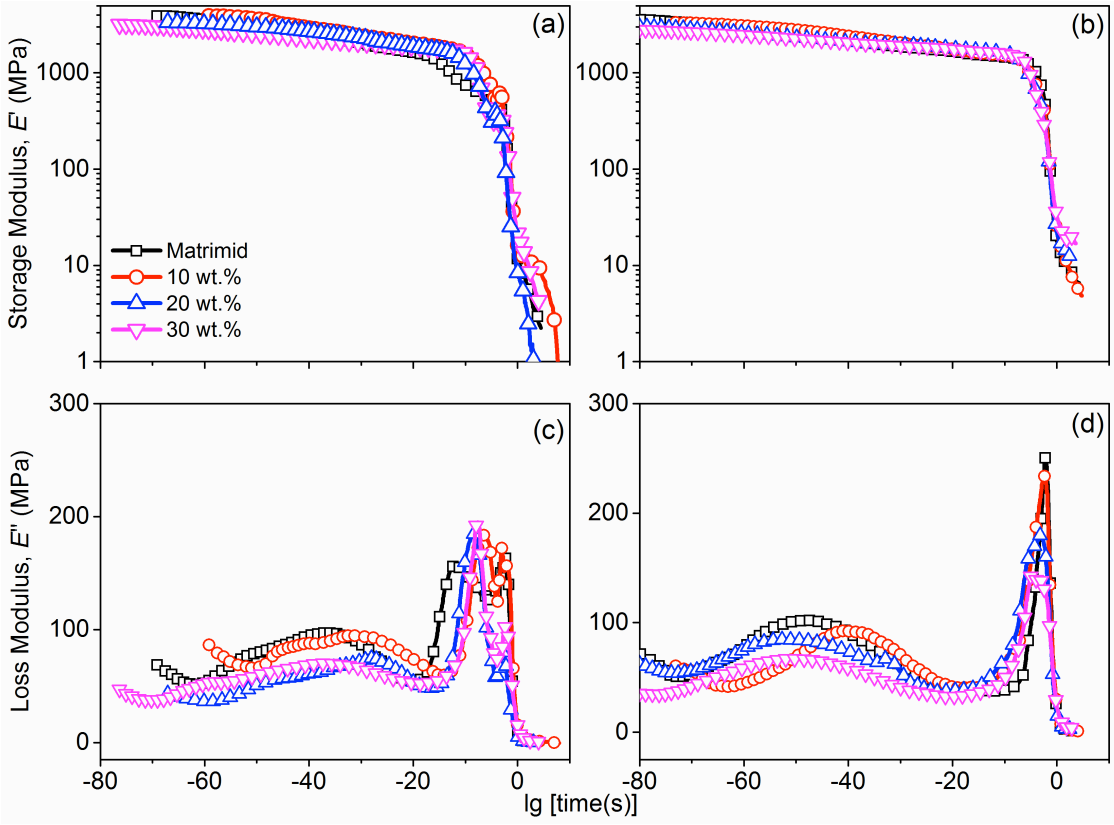

Fig. 4.13 Time-temperature superposition (TTS) master curves of the unannealed and annealed Matrimid/ZIF-8 nanocomposites, with (a) *E*' unannealed, (b) *E*' annealed, (c) *E*'' unannealed, and (d) *E*'' annealed. Note the log scale for (a) and (b). Also note the large (and small) lg (t) values, which are inaccessible by the DMA method (see Appendix B.8 for the master curve with temperature markers, lg (a_T) *vs*. T plots, and the WLF approximations plots associated with these data).

Fig. 4.13 (a-d) shows the time-temperature superposition (TTS) master curves for the storage (*E*') and loss (*E*'') moduli of the annealed and unannealed Matrimid/ZIF-8 nanocomposites. It is assumed that the samples (both Matrimid and its corresponding composites) are thermorheologically simple [166, 167], due to the fact that Matrimid makes up the structural majority of the nanocomposites. The assumption of thermorheological simplicity is particularly crucial towards TTS analyses, as it allows us to construct the

master curves shown in Fig. 4.13. At temperatures that are lower than the glass transition temperatures ($T<T_{ref\ (also\ g)}$) and shorter time spans (t<0 in the lg(t) axes), the samples are in a glassy state, where its energy storage capacity is high and energy dissipation low. Annealing the samples (Fig. 4.13 (b,d)) slightly increased its energy storage capability, although it also slightly increased the energy dissipation of the samples. It should be pointed out that the introduction of ZIF-8 nanoparticles in Matrimid, especially in the annealed samples, resulted in decreased energy dissipation overall, and it was surmised that the ZIF-8 nanoparticles within the nanocomposites and the presence of solvents molecules ($CHCl_3$) are responsible for this phenomenon (both acting as dampeners, which reduces energy dissipation). However, Matrimid did not exhibit a rubbery phase at $T>T_g$, and the sample was not recoverable post-testing (a trend that persist for both annealed and unannealed nanocomposites), leading us to conclude that the nanocomposites' structural breakdown at $T>T_g$ resulted in the loss of energy storage and dissipation capabilities. This is also reflected in the TTS master curves, where at $t>0$, the E' and E" values were almost zero. It should also be pointed out that the TTS master curves enable us to access behaviours at frequency regions that are either much too high or too low to be practically measured using the DMA test apparatus (limited between 1-100 Hz). TTS master curves are useful for materials modelling purposes, for example to derive constitutive models for finite-element simulations of engineering components.

4.5 Large-strain tensile deformation, ductility, and fracture behaviour of the Matrimid/ZIF-8 nanocomposites

The uniaxial tensile tests were performed to ascertain the macro-mechanical behaviour of the Matrimid/ZIF-8 nanocomposites when subjected to a 'large' deformation, *i.e.* exceeding the linear elastic limit. Fig. 4.14 (a, b) shows the nominal stress-strain (σ-ε) curves of the unannealed and annealed samples, respectively, while Fig. 4.15 (a-d) summarises the mechanical properties derived from the nominal σ-ε data. Most significantly, it can be seen that the introduction of ZIF-8 nanoparticles into Matrimid resulted in a ductile-to-brittle transition of the resulting nanocomposites. This trend is even more pronounced for the annealed samples, where all, including neat Matrimid, exhibiting appreciably brittle behaviour with an elongation-to-failure (ε_f) that is smaller than ~5%. While neat unannealed Matrimid undergoes substantial strain hardening after yielding (beyond σ_y ~40 MPa) due of plastic deformation, this trait has been drastically suppressed in annealed nanocomposites due to poor ductility (fast cracking).

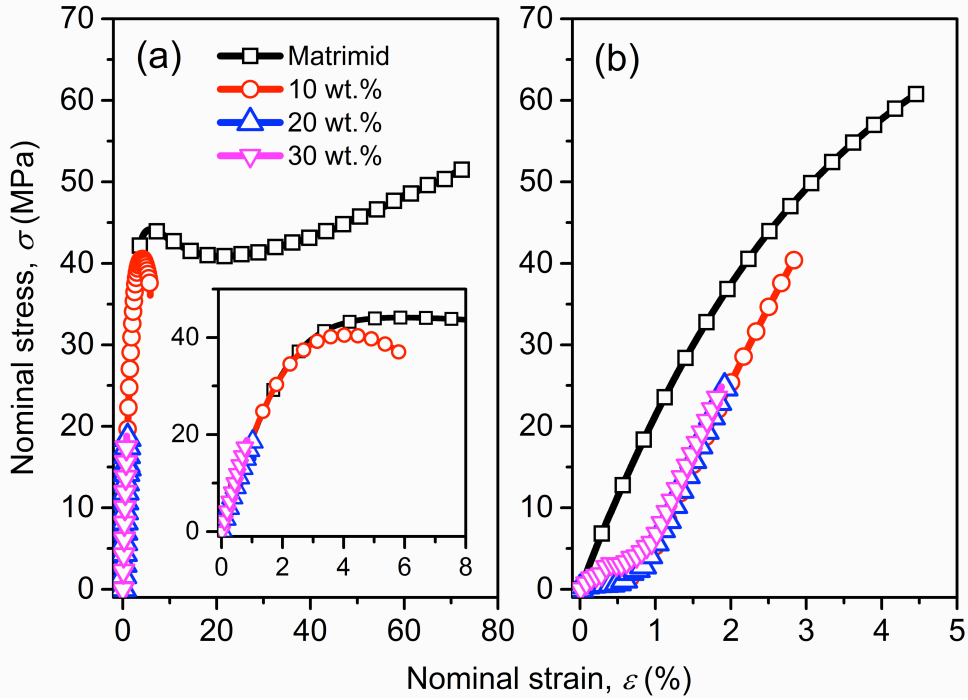

Fig. 4.14 Representative nominal stress-strain (σ-ε) curves for the Matrimid/ZIF-8 nanocomposites under uniaxial tension loadings: (a) unannealed (60 °C for 24 hours in vacuum) and (b) after annealing at 180 ºC for 24 hours in vacuum. The inset shows the small strain region, where linear elastic, yielding, and plastic deformation (strain hardening) are apparent for the unannealed samples.

It was demonstrated that at higher ZIF-8 wt.% loading, the nanocomposites are becoming increasingly brittle, and thus vulnerable to cracking and breakage under tension and bending deformation. Likewise, poor ductility is apparent for the annealed nanocomposites, see Fig. 4.14 (a), except for the fact that fracture occurs at a considerably lower strain value compared to its unannealed counterparts. To be able to compare differential nanocomposites' toughness property, the fracture energy (G_f) per unit volume of nanocomposites material can be utilised using the following relationship [168], which literally sums up the area encompassed by the σ-ε curves:

$$G_f = \int_0^{\varepsilon_f} \sigma(\varepsilon) d\varepsilon \tag{4.1}$$

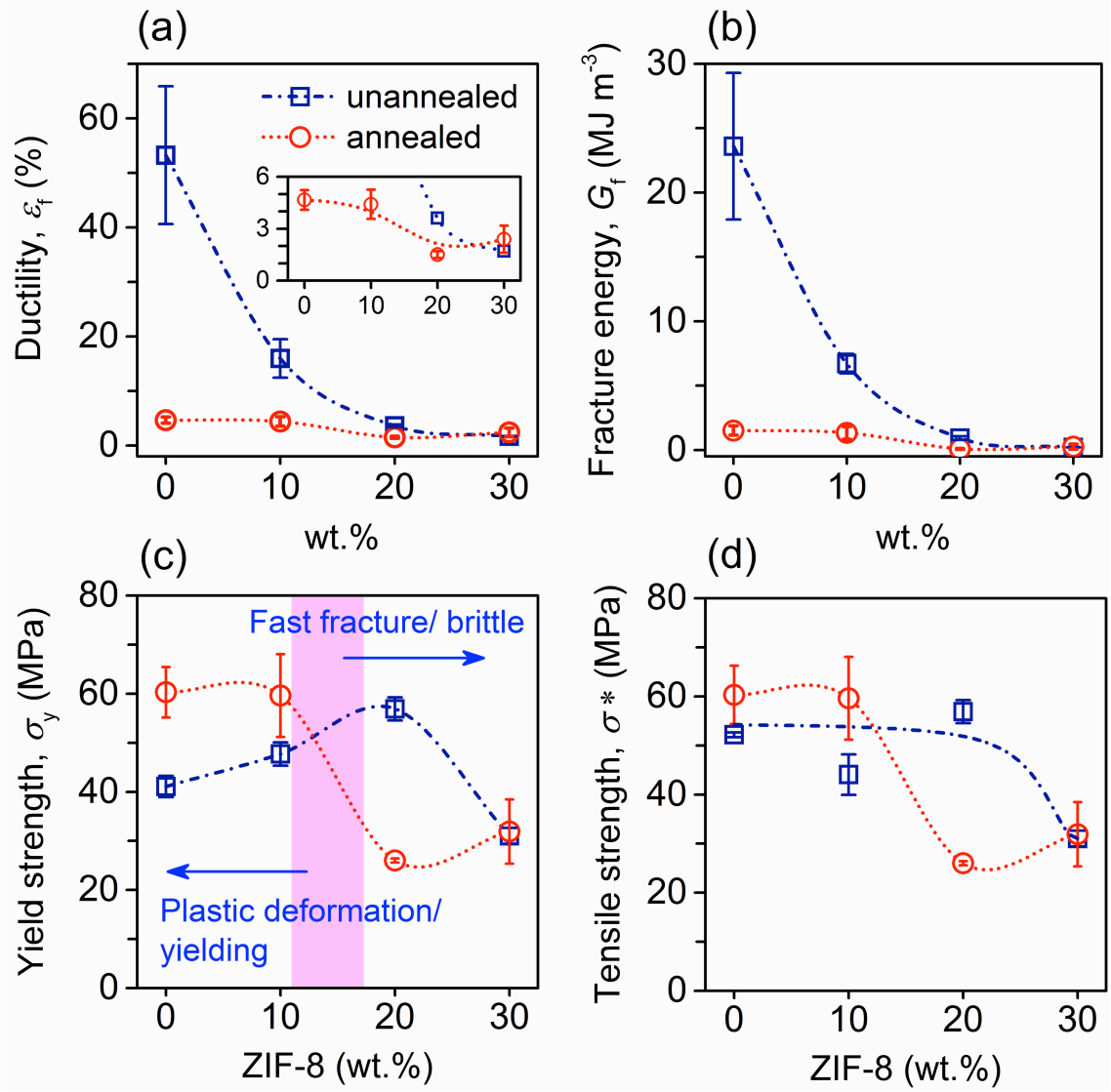

Fig. 4.15 Mechanical properties derived from the nominal stress-strain (σ-ε) plots (Fig. 4.14) against ZIF-8 wt.% loading and annealing condition. (a) Ductility, corresponding to the elongation-to-failure (%), (b) fracture energy, (c) yield strength, and (d) tensile strength. Each standard deviation was derived from three test pieces. The dotted lines serve as guides for the eye.

Fig. 4.15 (b) shows that there is a rapid fall in fracture energy of unannealed nanocomposites as a function of nanoparticle loading. Overall, G_f is inversely proportional to both the annealing condition and nanoparticle loadings. In practice, because of a sharp 80~90% decline in fracture energy (thus nanocomposites' toughness), the annealed samples with higher ZIF-8 wt.% are extremely brittle and easily fractured post-curing. Nevertheless, G_f was found to be relatively comparable for the annealed nanocomposites, suggesting that after the removal of entrapped solvents (and accompanying molecular rearrangements), the large-strain mechanical response of the Matrimid/ZIF-8 nanocomposites are controlled by the intrinsically brittle matrix phase, and in principle are becoming less sensitive towards wt.% of embedded nanoparticles. Clearly this behaviour is mirrored by ductility (Fig. 4.15 (a)), where annealing stabilised the values of elongation-to-failure (ε_f), while there is a larger variation determined for the unannealed counterparts.

The yield strength (σ_y) and tensile strength (σ^*) of the unannealed nanocomposites are also strongly affected by the ZIF-8 wt.% (Fig. 4.15 (c)-(d)). For example, the strengths dropped to ~50% level of that of the neat Matrimid when exceeding 20 wt.% loading. Below ~10 wt.%, however, it was discovered that the strengths of neat Matrimid can be improved by annealing. While the trend observed in the annealed nanocomposites are less systematic (challenging to measure accurately due to fast fracture), the embrittled nanocomposites after annealing show matching values of σ_y and σ^* since the initiation of plastic yielding do coincide with the point of fracture.

4.6 Practical implications of current findings to the future trends of glassy MOF-based nanocomposites developed for separation applications

Given that the vast majority of MOF-based nanocomposites are in fact developed with gas separations in mind [6, 45, 128], it is now timely to elucidate how the mechanical properties and viscoelastic information established in this work could offer new insights to the underpinning functional performance of nanocomposites incorporating MOF fillers. Importantly, this work intends to serve as a guidance to future rational design of next generation nanocomposite materials to yield an optimal combination of mechanical resilience and separation characteristics. Indeed, latest review articles have already recognised that there is a "gap" in literature [2, 5, 37], correlating the aforementioned factors to the real-world industrial performance of MOF-based nanocomposites. As a matter of fact, the focus of the great majority of work on MOF-based nanocomposites concerned the (positive) influence of MOF fillers towards separation performance *vis-à-vis* neat polymer membranes [6, 39, 169]. Summarised below are the key practical implications of this part of our work.

First, the presence of residual solvents affecting the overall permeability of nanocomposites can be unambiguously pinpointed by characterising its viscoelastic response. Specifically, it was shown how entrapped solvents in nanocomposites account for the relaxation anomalies highlighted in Fig. 4.11 (a, c). Despite the fact that the drying temperature was set to the boiling point of the solvent, it was demonstrated that the solvent was not fully removed from the nanocomposites, although this will only be evident when the nanocomposites are subject to cyclic-loading mechanical tests *via* dynamic mechanical analysis (DMA). By comparison, it should be noted that quasi-static techniques are insensitive to these effects, for example the application of conventional uniaxial tensile

testing on the nanocomposites [43, 105] cannot reveal such an intrinsic phenomenon associated with residual solvents. By means of DMA, however, strain energy storage and dissipation of the nanocomposites are rendered unstable (near T_g) due to occluded solvents, which can be perceived as a 'dampener' interfering with the polymer's attempt to retain or dissipate energy (quantified by E' and E") under a coupled thermo-cyclic mechanical loadings. In light of this, the viscoelastic anomalies elucidated above will be prominent for many other composite systems built from glassy polymeric matrices (T_g > room temperature (RT)), *e.g.* polybenzimidazole (PBI) [40], polyacrylonitrile (PAN) [37], polyethersulfone (PES), and a wide variety of polyimides (Ultem, 6FDA-DAM, etc) [170]. Significantly, here the universal methodology proposed using DMA is extremely powerful and it could be adopted for future studies encompassing a broad family of polymer and nanocomposites, independent of the type of solvents employed for processing.

Second, it was confirmed that the efficacy of employing nanoindentation as a viable micromechanical approach to determine the surface and sub-surface (~2 μm) Young's modulus (E) and hardness (H) behaviour of nanocomposites, featuring thicknesses to the order of 10-100s μm. It was shown that the variation of mechanical properties can be relatively small for the Matrimid/ZIF-8 nanocomposites ($\Delta E < 0.5$ GPa, $\Delta H < 50$ MPa), but remains discernible. Both properties E and H also scale reasonably well in accordance to the simple Reuss (inversed) Rule-of-Mixtures [46, 112], by assuming an idealised particulate-based filler dispersion in a continuous matrix. Furthermore, because nanoindentation measurements signify the localised fine-scale mechanical characteristics, the corresponding standard deviations provide an additional quality indicator about the homogeneity of nanoparticle dispersion at the top surface of the nanocomposites. Interestingly, combining a stiffer matrix (majority of glassy polymers) with a relatively compliant MOF as filler phase [171] will effectively reduce the E of the resultant

nanocomposite; but there might be an opposing trend in *H*, for the latter is dictated by the relative magnitude of the hardnesses [32] of the composite constituents. Informed by these outcomes, it can be projected that nanocomposites made from 'rubbery' polymer matrices (*e.g.* polyurethane (PU), polydimethylsiloxane (PDMS), polyisobutylene (PIB)), all of which with a T_g < RT and typical *E* values of the order of 10-100s MPa [171] can gain improvements in both the stiffness and hardness properties with increasing MOF wt.% (will be explored in Chapter 5).

Third, it is essential to highlight that annealing of Matrimid (Fig. 4.14 - 4.15) is detrimental to its overall ductility (reducing stretchability and bendability), thus leading to a substantial fall in damage tolerance and mechanical resilience (toughness). Likewise, unannealed nanocomposites show a rapid decline in ductility and toughness due to the inclusion of ZIF-8 nanoparticles, which can be explained from the introduction of microscopic stress risers in an otherwise undisrupted polyimide matrix. The impact on mechanical strengths, however, is far more complicated. Prior to annealing, there is evidence of improvement in yield and tensile strengths as a function of ZIF-8 inclusion of up to *ca*. 20 wt.% loading, beyond which it is likely that nanoparticle aggregation triggers premature nanocomposite cracking and brittle fractures. Nominally, annealing resulted in improved strength of the nanocomposite with up to ~10 wt.% nanoparticle loading, before the onset of brittle failure linked to reduced ductility (Fig. 4.14 (a) inset). Our findings demonstrate that additional emphasis *must* be given to the characterisation of material toughness [172], especially from the viewpoint of ductility and fracture energy. To reach practical engineering applications, it is therefore no longer sufficient to consider only elastic modulus and tensile strengths [37, 105] to adequately assess the overall mechanical performance of nanocomposites. Noteworthy, this precise need has also recently been recognised in the emergent field of

organic solar cells [173], whose structural requirements (of thin films and coatings) are reminiscent to the mechanical challenges facing nanocomposites.

Fourth, useful insights can be gained by considering the mechanical properties information presented alongside recently reported gas permeation and selectivity data of Matrimid/ZIF-8 nanocomposites [80], corresponding to the (annealed) nanocomposites engaged in this study. Fig. 4.16 summarises the selectivity *vs.* mechanical behaviour relationships, suggesting that the optimal Matrimid/ZIF-8 nanocomposites may well contain up to ~10 wt.% ZIF-8 nanoparticles, and is preferably annealed to maximise selectivity against CO_2, CH_4, and H_2. From the microstructural perspective, it can be seen in Fig. 4.3(b) that the 10 wt.% blend of Matrimid/ZIF-8 is uniform, while XRD characterisation showed distinctive peaks (Fig. 4.5) matching that of the ZIF-8 nanoparticles, corroborating its crystallinity and intrinsic porosity. Moreover, viscoelastic analysis showed that the 10 wt.% annealed nanocomposite is thermo-mechanically stable under an elastic deformation, extending to a relatively high temperature of ~300°C (Fig. 4.11(b, d)). When subjected to a large tensile deformation, it was established that the 10 wt.% annealed nanocomposite retains a respectable level of damage tolerance and mechanical robustness, without compromising its toughness relative to (annealed) neat Matrimid (Fig. 4.15), rendering us to recommend the application of up to 10 wt.% annealed sample for prospective technological applications. It is worth highlighting that recent exemplars of nanocomposites, such as the 15 wt.% ZIF-90/6FDA-DAM [170] features major enhancements of CO_2 permeability and CO_2/CH_4 selectivity performance; here the matrix termed 6FDA-DAM is a glassy polyimide akin to Matrimid, but the former is appreciably more permeable (higher flux). Yet the corresponding thermo-mechanical performance of the ZIF-90/6FDA-DAM system has not been considered to date.

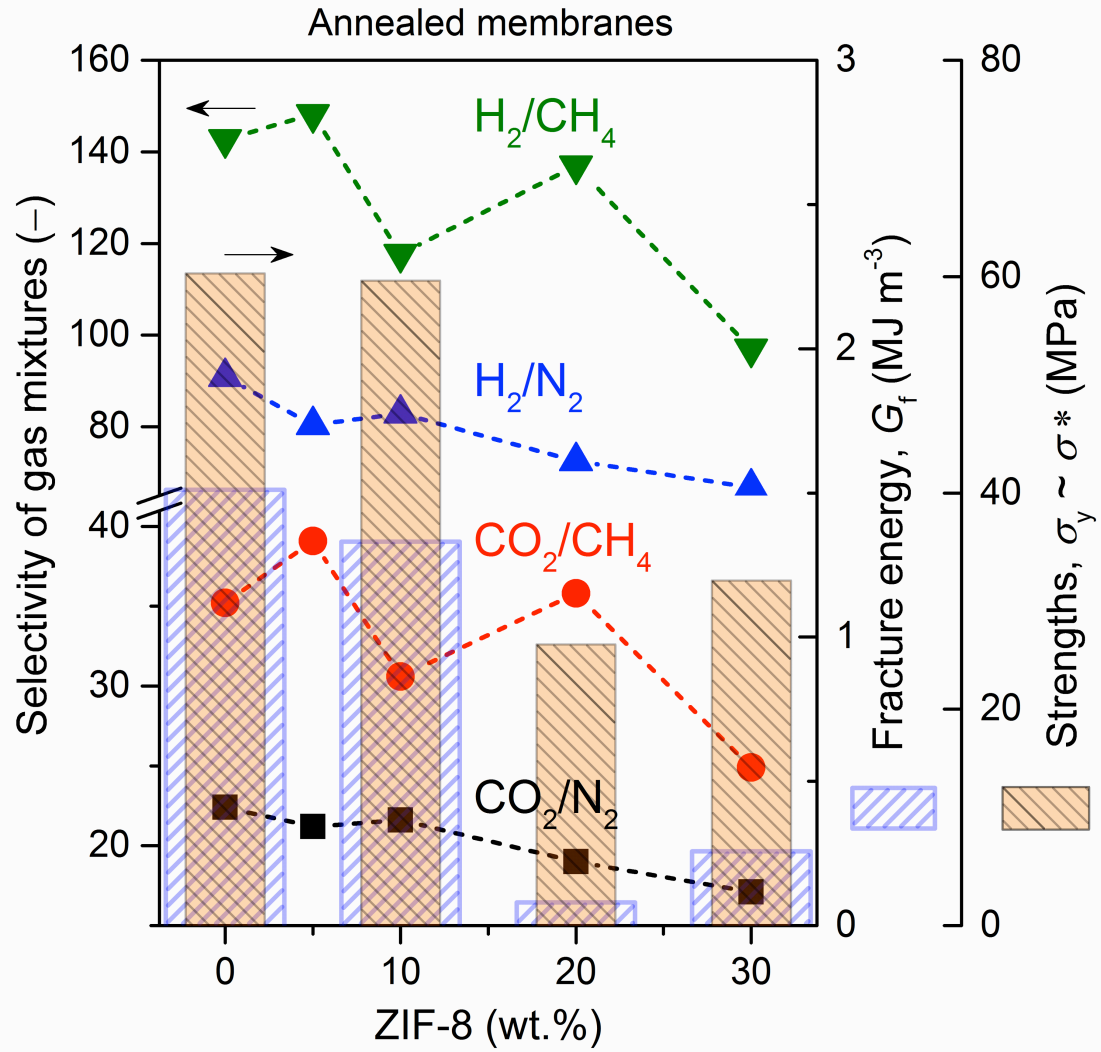

Fig. 4.16 Comparison of the gas selectivity data of Matrimid/ZIF-8 nanocomposites reported by Song *et al.* [80], derived from pure gas permeation properties of annealed nanocomposites. The mechanical properties of annealed membranes measured in this work, especially fracture energy and strengths (mean values), are plotted alongside the selectivity data to highlight the common downward trend as a function of nanoparticle wt.% loading; the dotted lines are guides for the eye. Note that during brittle fracture of annealed samples, tensile strengths are approximated by yield strengths due to the limited ductility.

While the advent of MOF-based nanocomposites represents an improvement to the performance of many polymeric membranes, there is an underlying trade-off between separation performance and mechanical robustness, which industrial practitioners will have to rationalise based on the data such as those we have reported in this study. Alas, detailed mechanical properties information such as this is still scarce, and might be system specific depending upon the polymer/MOF combination being considered. Follow-on studies in the fashion of the current proposed methodology will thus be fundamental to build up a larger picture. Ultimately, if MOF-based nanocomposites are to be successful in real-world engineering applications, the qualitative and quantitative determination methodology of the thermo-mechanical properties of the nanocomposites needs to be initiated and developed at this critical stage. In light of this, it is imperative that the findings are discussed in the wider context of current industrial practices, such as gas separation and pervaporation, due to the fact that the literature is abundant with examples of MOF-based nanocomposites developed for these applications, albeit limited at lab-scales, some showing high potential of eventual large-scale industrial utilisation.

Commercial polymer membranes are currently employed in less rigorous gas separation industrial processes, such as hydrogen separation and CO_2/CH_4 separation to afford natural gas purification [37]. Typical exposure conditions for industrial gas separation involving polymeric membranes operates at temperatures of 100-200 ºC (depending on the gas) [174] and pressures of *ca*. 10-60 bars (inlet pressure of compressed gas) [175]. Our DMA results proved that Matrimid-based nanocomposites (high T_g) containing ZIF-8 are stable up to temperatures of 300 ºC, which makes it a viable industrial candidate for gas separation. It was further demonstrated that the Matrimid/ZIF-8 nanocomposites are capable of withstanding stresses in the range of up to 60 MPa (depending on ZIF-8 nanoparticle loadings), which is important as these nanocomposites will need to be operable at high

pressures that will inevitably induce biaxial deformations (caused by pressure-differential force of the fluids/gases). For high-throughput industrial installations [176], polymeric membranes are typically stacked on top of one another within a cylindrical or ceramic module, offering additional structural support to the membranes while enhancing separation performance by subjecting the feed stock to multiple separation cycles. The nominal viability of a standalone MOF-based nanocomposite that was successfully studied in a small-scale lab setting could be translated into an up-scaled industrial setting, where a combination of multiple nanocomposites stacked in a spiral-wound module [177] may be used (instead of one single nanocomposite for the entire process). There are a few commercial gas separation polymeric systems found on the market that were designed based on this operational concept. Likewise, this configuration applies to commercial pervaporation systems utilising polymeric membranes, where operational temperature ranges are *ca*. 60-150°C, depending on the solvent mixture used, and the pressures involved are significantly smaller (~few kPa) [178]. These temperature and pressure ranges lie within the range of contemporary MOF-based nanocomposites such as Matrimid/ZIF-8. Additionally, future assessments of mechanical resilience and stability of the nanocomposites should also consider hazards associated with ageing effects, long-term thermo-mechanical degradation, and moisture tolerance, amongst others [106] (beyond the scope of this thesis).

4.7 Chapter summary

This chapter discussed the pioneering attempt at systematic mechanical characterisation study of a prototypical polymer/MOF nanocomposites, specifically, Matrimid/ZIF-8. The quasi-static nanoindentation behaviour, temperature-dependent dynamic properties, and

large-strain deformation beyond the elastic limit were investigated. The objective here was to gain new insights of the effects of ZIF-8 nanoparticle inclusions on the mechanical properties and the viscoelastic response of free-standing nanocomposites, which have been developed for emergent gas separation applications.

The next chapter will discuss the utilisation of the methods and analyses developed in this chapter to study a prototypical *rubbery* polymer/MOF nanocomposite. The combinatorial analyses of this chapter and the next will serve as an outline when intending to study the interactions of polymers and MOFs in a composite, and the subsequent effect of these interactions on its performance(s).

CHAPTER FIVE

Dynamic molecular interactions between PU and ZIF-8 in a nanocomposite: microstructure, thermo-mechanics, and viscoelastic effects

This chapter details the investigation into the intricate dynamics underpinning the molecular interactions between ZIF-8 nanoparticles and a hyperelastic polymer matrix (polyurethane, PU), representing a prototypical rubbery polymer/MOF nanocomposite. These interactions are expected to produce unique responses that differ from the ones exhibited from the glassy polymer/MOF nanocomposites detailed in Chapter 4. The results reported in this chapter will also serve as a contrast to the ones reported in the previous chapter due to the drastically different nature of the matrix (hyperelastic (rubbery) *vs.* glassy). Certain aspects pointed out in the previous chapter will serve to further refine our analyses: the nanocomposites will be annealed at a temperature that is 25 °C higher than the boiling point of its solvent, the AFM method will not be used to characterise these nanocomposites as the FEG-SEM has been shown to be effective enough for that purpose, and the ZIF-8 nanoparticle loadings will be increased to 40 wt.% due to the non-existent risk of brittle cracking of the nanocomposites. The results from this chapter, along with the previous chapter, will serve as a general outline when characterising (and projecting) the response and interaction of polymer/MOF nanocomposites in the context of industrial applications. The data presented and the works discussed in this chapter has been published in Mahdi *et al.* [179].

5.1 Rationale

Polymers, especially rubbery polymers (elastomers), are valued for their strechability [180], extended ductility (hyperelasticity) [181], and incompressibility [182]. They are made up of extremely long and loose molecular chains that are intertwined and loosely associated with one another *via* a collection of weak interactive bonds, with extended freedom of movement, mostly manifesting itself in the form of internal continuous motions of primary and secondary molecular polymeric chains [183]. This result in their distinctive and highly recognisable responses to external stimuli and malleable and highly extensible (ductile) nature [184]. They are also known for low to non-existent water absorption [185] and being electrically insulating (good dielectrics) [186]. This makes them perfect for applications such as food packaging [187] and protective clothing [188], tires for automobiles and aeroplanes [189], and heat shields [190]. This class of polymers could be synthesised *via* a variety of techniques, ranging from vulcanisation [191] to electrospinning [192].

The benefits and advantages offered by both nanosized MOFs and rubbery polymers could be brought together under one systematic purview *via* the formation of composites. Composites, by definition, constitute two or more significantly different constituents, with the resulting properties differing significantly from either [193]. Combining the malleability, ease of processability, and scalability of polymers [194], and the porosity and accessibility of hybrid inorganic-organic materials [30, 195] makes for a unique composite, exhibiting the adaptability and durability of polymeric structures [196], and the enhanced porosity [197], high surface areas [198], and multi-functionality [199] of hybrid inorganic-organic materials, all within one continuous structure [200].

The previous chapter set out to utilise and refine a few established characterisation methods to explicate the thermo-mechanical, viscoelasticity, and macro-mechanical properties of a

prototypical glassy polymer/MOF nanocomposites, in this case, Matrimid/ZIF-8. In this chapter, a detailed characterisation will be presented (adopted from the previous chapter) to elucidate the dynamic molecular interactions underpinning a polyurethane (PU)/ZIF-8 nanocomposite system, pertaining to the aforementioned factors. This approach is unique in that the structure-property relationship or the performance study of this particular combination of polymer/MOF has hitherto not been reported, and although their respective structural analogues were [201, 202], most are limited to chemical synthesis and non-mechanical performance studies. The correlation established in this work will also serve as a model for other rubbery polymer/MOF composites, allowing us to elucidate and predict their respective responses within a single system and pinpoint suitable applications *vis-à-vis* the established parameters.

5.2 Microstructural evaluation of the PU/ZIF-8 nanocomposites with the FEG-SEM method

Fig. 5.1 shows the cross-sectional images of the PU/ZIF-8 nanocomposites. The dispersion of the nanoparticles within the matrix appears to be uniform, similar to §4.2, although at lower wt.% loadings, they tend to form dispersed *clusters* within the matrix, as opposed to being dispersed as individual, isolated nanoparticles [203, 204], which drastically differed from their Matrimid/ZIF-8 counterparts. However, at higher loadings, this trend is supplanted by the more uniform and regular dispersion of the nanoparticles *everywhere* throughout the matrix. It is also evident that the majority of ZIF-8 nanoparticles retained its original configuration (rhombic dodecahedron) [205] even within the PU matrix, suggesting that the nanoparticles are nominally *attached* to the rubbery polymeric chains of the PU as opposed to being *encapsulated*/*embedded* within the matrix (see §4.2). Quantitative

assessment of the FEG-SEM images also agrees with these suppositions. The frequency of ZIF-8 nanoparticles within the nanocomposite increases with increased loadings (from an average of 12 ZIF-8 nanoparticles per μm^2 for the 10 wt.% sample, to an average of 20 ZIF-8 nanoparticles per μm^2 in the 40 wt.% sample), although there is a clear concentration of ZIF-8 nanoparticles within certain regions for lower loaded nanoparticles, as per Fig. 5.2 (a) & (b). These concentration of nanoparticles could mean agglomeration and aggregation, although the image resolution showed distinct, distinguishable nanoparticles in Fig. 5.1 (b)-(c), suggesting that even if agglomeration/aggregation did occur, it was not on a massive scale. The distribution of the ZIF-8 nanoparticles at higher loadings, as per Fig. 5.2 (c) & (d), seems to be a lot more uniform, where the frequency of the ZIF-8 nanoparticles is more consistent from grid to grid, which agrees with Fig. 5.1 (d) & (e). It should also be pointed out that the amounts of ZIF-8 nanoparticles per μm^2 is a lot higher in the case of PU/ZIF-8 as opposed to Matrimid/ZIF-8 (for example, the Matrimid/ZIF-8 10 wt.% has an average of 3 particles per μm^2 as opposed to the 17 nanoparticles on average for the PU/ZIF-8 10 wt.%) due to the ZIF-8 nanoparticles in the PU not being encapsulated by the matrix.

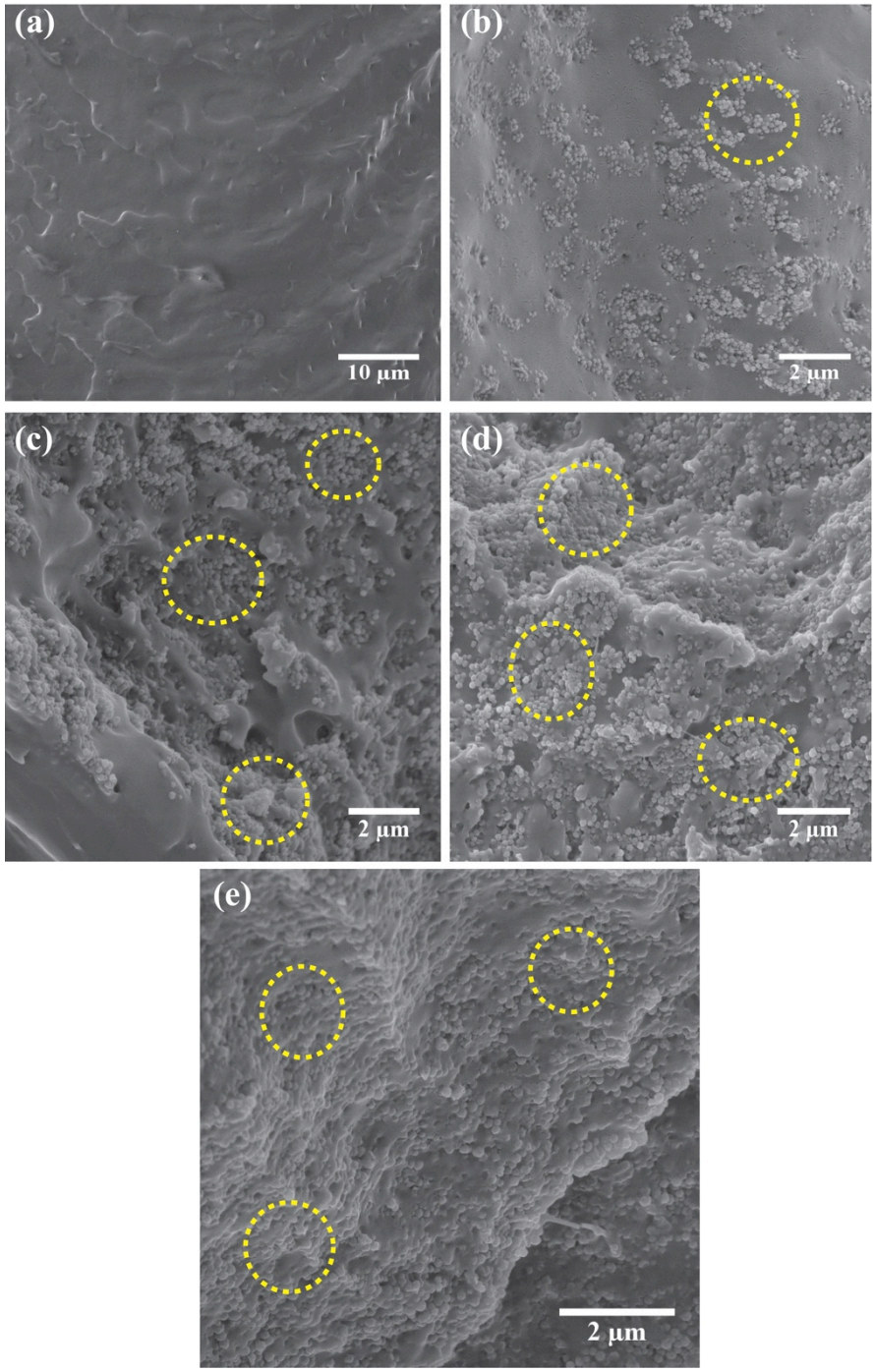

Fig. 5.1 Cross-sectional FEG-SEM images of PU/ZIF-8 nanocomposites, with (a) PU, (b) 10 wt.%, (c) 20 wt.%, (d) 30 wt.%, and (e) 40 wt.% ZIF-8 nanoparticles, at ~30,000× magnification. The yellow dashed markers are used to highlight the presence of ZIF-8 nanoparticles, and it is quite evident that they form a distinct and distinguishable phase from the PU matrix.

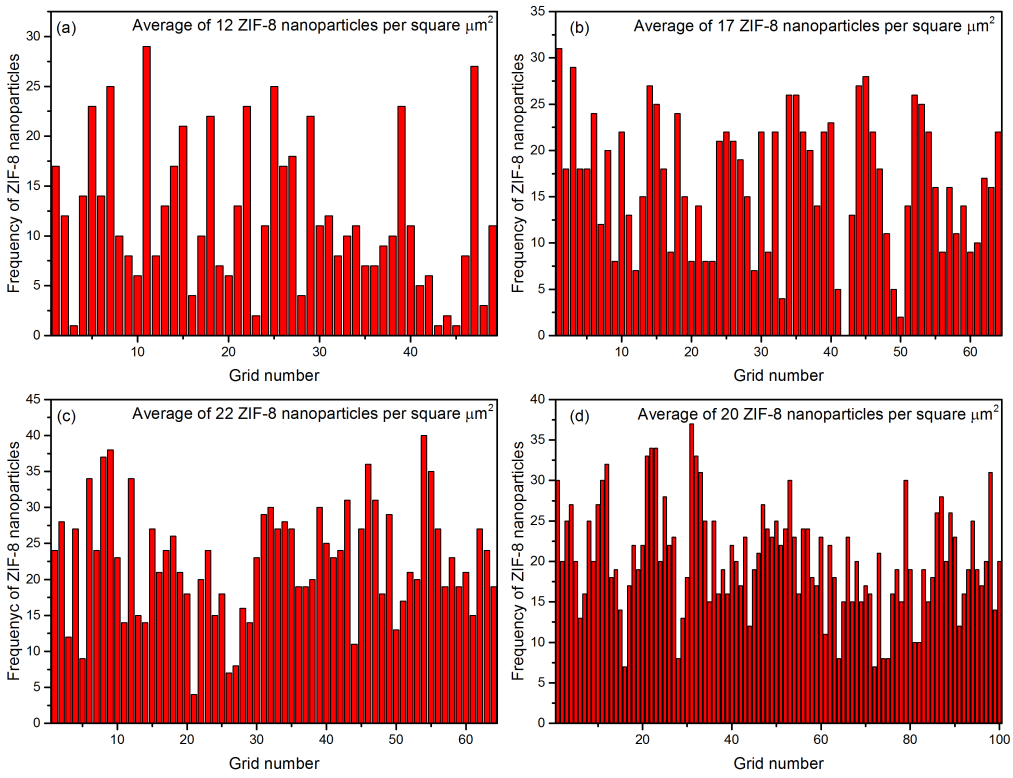

Fig. 5.2 The quantitative analyses of the distribution of ZIF-8 nanoparticles within the PU/ZIF-8 nanocomposite, where (a) PU/ZIF-8 10 wt.%, (b) PU/ZIF-8 20 wt.%, (c) PU/ZIF-8 30 wt.%, and (d) PU/ZIF-8 40 wt.%. The grid number represents an equally distributed grid that measures 1 μm^2 each [155] (see Appendix C.1).

The microstructures suggest that there is a *lack* of dedicated interfacial layers between the PU primary (hard) and secondary (soft) polymeric chain (see Fig. 3.4) and ZIF-8 nanoparticles, and that the interactions are limited to nanoparticle surface interactions, which are associated with secondary molecular interactions such as vdW forces, π-π stacking, and H-bonding [157, 158] with the 'hard' group of the PU. Due to the fact that a spherical configuration is thermodynamically favourable [206] and the well-known tendency for nanoparticles to form agglomerates/aggregates [207], it is reasoned that instead of disrupting the polymeric chain packing of PU, the ZIF-8 nanoparticles attached

themselves to the polymeric molecular chains in a manner similar to secondary groups, or in some cases, form new distinct (relatively shorter) chains (in the form of clusters) altogether within the matrix, resulting in new molecular chains of ZIF-8 or combined molecular chains of PU and ZIF-8. In fact, this interaction is evident in the PXRD scans (Fig 5.3), showing distinctive and identifiable peaks of ZIF-8 against an amorphous background of the PU matrix; at room temperature, PU is rubbery and amorphous, therefore, its molecular chains are free to slide and reconfigure themselves when subjected to external stimuli such as thermal energy (heat) or mechanical stresses/strains [208-210].

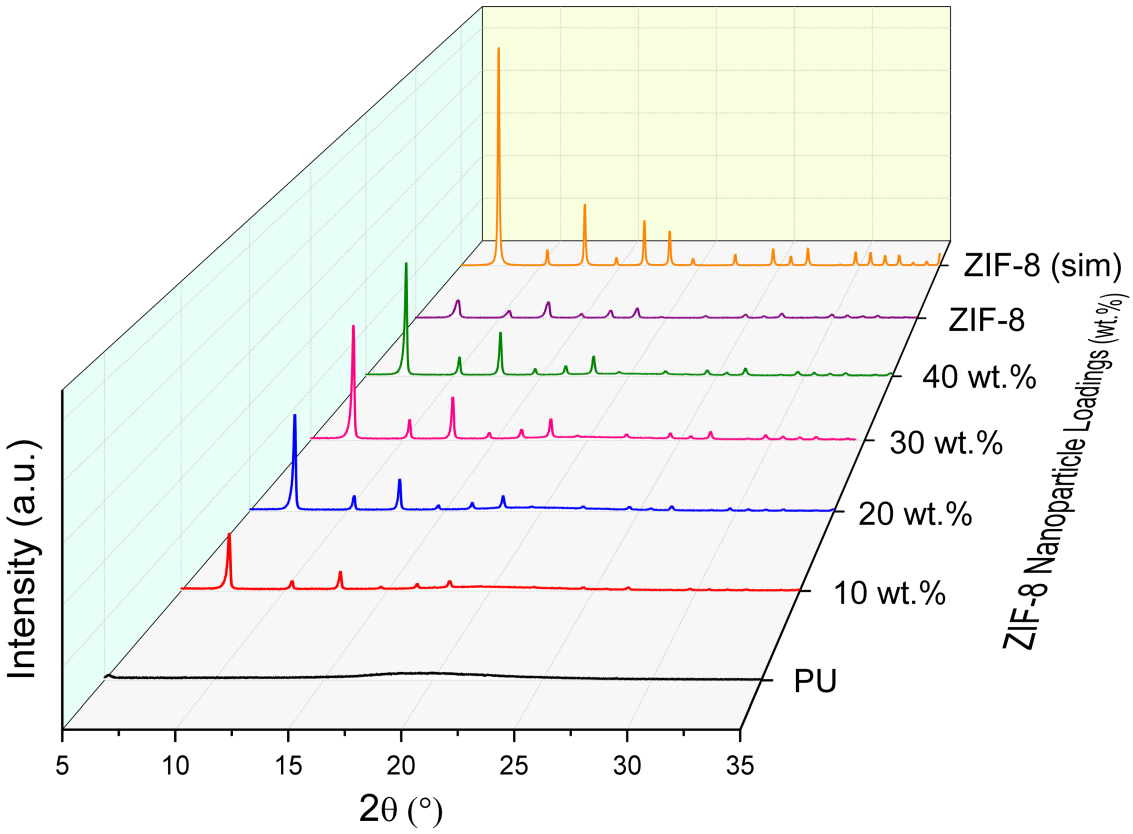

Figure 5.3 XRD diffractogram of PU, simulated (sim) ZIF-8 patterns, and PU/ZIF-8 nanocomposites. The amorphous PU matrix was converted into semi-crystalline nanocomposites, although the crystallinity increase is not significant up till 40 wt.% loading of ZIF-8 nanoparticles (see Appendix C.2).

The introduction of ZIF-8 nanoparticles will only induce (minimal) rearrangement/reformation of the polymeric molecular chain with minimal interruption of the inter-and intra-chain interactions between PU primary and secondary molecular chains, thus allowing the newly formed nanocomposites to retain its rubbery configuration despite the introduction of filler phases (herein ZIF-8 nanoparticles) within the matrix. However, at increased filler loadings, as seen in Fig. 5.1 (d)-(e), the more dominant presence of ZIF-8 nanoparticles began to underpin and curtail free slippage and movements of PU polymeric molecular chains via interactions between the mIm of ZIF-8 and PU molecular primary chains, stiffening the usually compliant PU matrix [75, 211]. This is believed to be the function of filler quantity; higher loadings of ZIF-8 nanoparticles meant increased amounts of ZIF-8 nanoparticles per volume within the nanocomposites, resulting in more and more PU (soft) molecular chains being pinned and becoming immobilised. The quantification of this molecular alteration and its qualitative effects upon the structural behaviour of nanocomposites will be discussed and detailed in §5.3-5.6 of this work *via* quasi-static and thermo-mechanical characterisation approaches.

5.3 Nanoindentation study

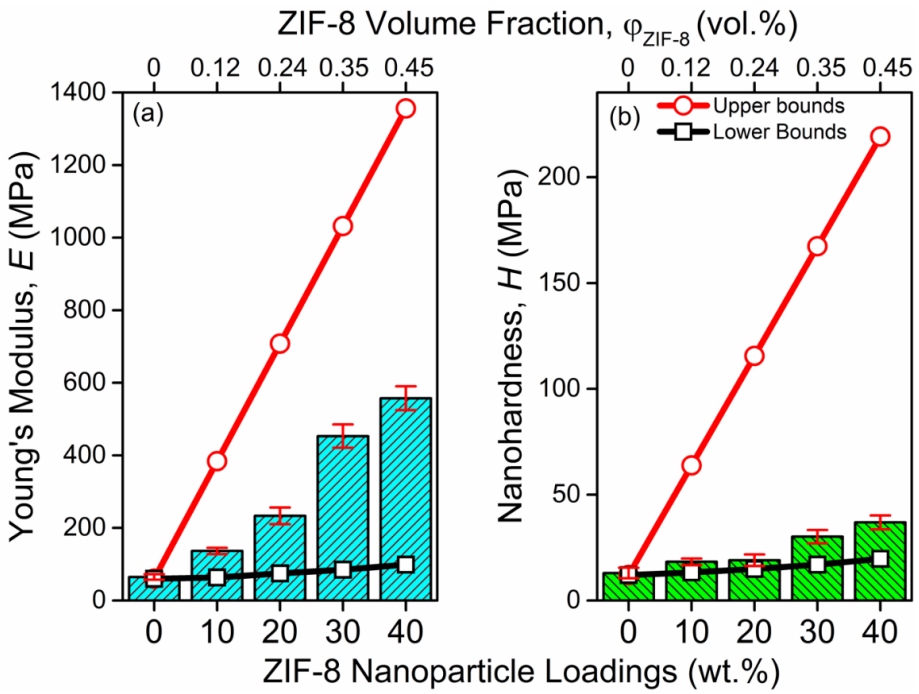

Fig. 5.4 The compilation of the nanoindentation data determined from the PU and PU/ZIF-8 nanocomposites, with (a) Young's modulus (E) and (b) nanohardness (H). The results are the average of a total of 45 indents from 3 samples upon a surface penetration depth of 2 μm. The theoretical values are determined using the simple rule of mixture, $E_{UB} = \varphi_{ZIF\text{-}8} \cdot E_{ZIF\text{-}8} + (1 - \varphi_{ZIF\text{-}8}) \cdot E_{PU}$ and $E_{LB} = [(\varphi_{ZIF\text{-}8} / E_{ZIF\text{-}8}) + (1 - \varphi_{ZIF\text{-}8}) / E_{PU}]^{-1}$, where $E_{ZIF\text{-}8} = 3.3$ GPa [33] and $H_{ZIF\text{-}8} = 500$ MPa [32], and $E_{PU} = 65$ MPa and $H_{PU} = 15$ MPa (established from measured PU samples at 0 wt.%). Notably, the major over-estimation from the upper bound (UB) model indicates that the intra-molecular interface between the ZIF-8 filler phase and the PU matrix is particularly weak, such that there has been a significant reduction in load transfer compared with the idealised (UB) equal strain model [46].

Fig. 5.4 summarises the results from the nanoindentation studies of the PU/ZIF-8 nanocomposites. The Young's modulus (*E*) and nanohardness (*H*) were calculated by assuming an isotropic response within the area being indented and using the load-displacement data derived from the indentation load-displacement curves (see Appendix C.3). This approach has been adopted in other studies on PU-based composites, where Cai *et al.* [212] reported that the incorporation of 4.4 wt.% of Graphite Oxide Nanopalletes (GONP) resulted in an increase of *E* by 900% and *H* by 327% due to the strong chemical interactions between the hard segment of the PU and the GONP, which allows for an effective load transfer.

The results indicate that the *E* and *H* are directly proportional to ZIF-8 nanoparticle loadings (wt.%). As a matter of fact, the increase of both values are quite significant *vis-à-vis* the ZIF-8 nanoparticle loadings. This is evident from looking at PU (0 wt.%) to PU/ZIF-8 (10 wt.%), where the *E* and *H* value increased from ~65 MPa to ~137 MPa (increase of ~110%) and ~13 MPa to ~18 MPa (increase of ~40%), respectively, and from PU/ZIF-8 (10 wt.%) to PU/ZIF-8 (20 wt.%), where the values increased from ~137 MPa to 233 MPa (increase of ~70%) and ~18 MPa to ~19 MPa (increase of ~4%), respectively. Overall, an increase of over 760% in *E* and 185% in *H* is observed at peak ZIF-8 loading (40 wt.%) from neat PU samples, indicating a significant increase in the relative stiffness and hardness of the nanocomposites. It could therefore be surmised that the increased ZIF-8 nanoparticle loadings are enhancing the mechanical stability of the nanocomposites while simultaneously introducing accessible porosity and active sites [78, 105].

5.4 Thermal stability analyses

Thermal stability is crucial towards the applicability of the nanocomposites, as rubbery polymers in general are known to be extremely susceptible to heat [213]. In this case, the matrix (PU), which forms a structural majority, will be greatly affected by heat, however, the ZIF-8 nanoparticles is known to be stable up till ~500 °C [32]. Establishing the thermal stability of these nanocomposite will allow us to predict, and subsequently model, their behaviour when exposed to higher temperatures, which is especially crucial if these nanocomposites are to be used for any practical applications [152, 214].

TGA analysis involves the determination of thermal stability of the samples; basically, the samples are heated at a constant rate within a set temperature range, with its subsequent relative weight decrease (%) recorded as a function of temperature (see §3.3.2.1). This results in a thermal decomposition plot, which will allow us to pinpoint the temperatures that are associated with phase changes, loss of solvents, and outright decomposition, amongst others [215].

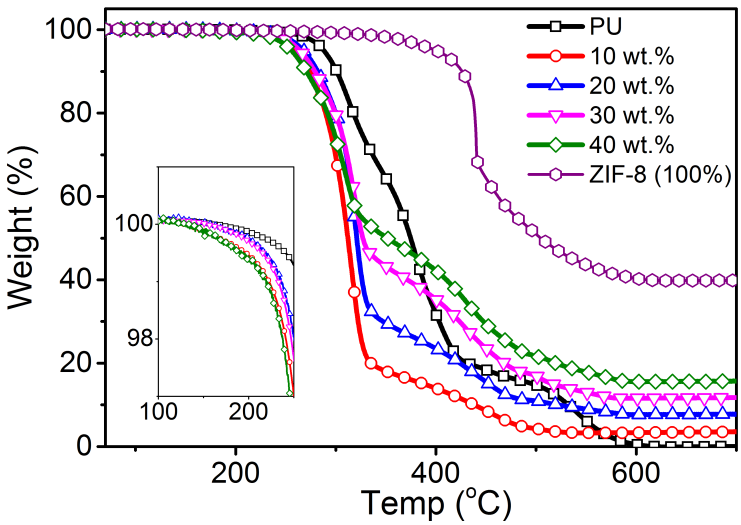

Fig. 5.5 TGA plots of the PU, PU/ZIF-8 nanocomposites, and ZIF-8 nanoparticles from room temperature (RT) to 700 °C (see Appendix C.4 for the breakdown temperature regions associated with the observed weight changes).

Fig. 5.5 shows the compilation of the TGA thermograms of the PU, PU/ZIF-8 nanocomposites (10-40 wt.%), and ZIF-8 nanoparticles (100 wt.%). It can be seen that the decomposition trend of the PU and its corresponding nanocomposites are characteristically similar, which can be attributed to the fact that PU forms the structural majority (100 wt.% to 60 wt.%) of the nanocomposite, hence dominating the internal structural makeup of the samples. The PU sample began decomposing at ~250 °C, losing 80 wt.% up till 420 °C. A slower decomposition rate was observed from 420 °C to 580 °C (20 wt.% - 0 wt.%), upon which the sample completely decomposes. The ZIF-8 nanoparticle sample began decomposing at 350 °C, which is a full 100 °C later than the PU sample, and continue to steadily decompose up to ~600 °C, which is coincidentally the temperature region where the PU sample completely decomposes. The decomposition behaviour of PU and ZIF-8 differs; the former shows two distinct decomposition phase regions (250 °C - 420 °C and 420 °C - 580 °C), while the latter shows only one (350-600 °C). The thermal decomposition temperature of PU, as per literature, is ~200 °C [216], while for ZIF-8, it is ~500 °C [116]. However, these reported decomposition temperatures can only serve as guidelines, as these values can vary based on the experimental conditions and settings and the synthesis methods employed to produce the samples itself.

Speculation can be made as to the decomposition mechanism of PU and ZIF-8 nanoparticles based on their respective physico-chemical features. As per Fig. 3.4, PU is made up of 'hard' and 'soft' segments, the former forms the core of the PU polymer, while the latter provides malleability, flexibility, and mobility that PU is known for. PU is also incompressible and has a low T_g (see Appendix C.5), making it extremely susceptible to temperature. As the temperature increases, the 'soft' segments (polymeric chains) of the PU, due to its weak inter-and intra-molecular bonds with each other (a collection of weak surface interactions

not amounting to H-bonds) and links to the 'hard' segment (covalent bonds), will began static vibrations, and eventually, large-scale rearrangements of its chains. This phenomenon will continue with greater intensity beyond the T_g, resulting in an increasingly pliant sample as the 'soft' segments are fast disassociating itself from each other and also from the 'hard' segment, but remained tenuously held together by a collection of weak secondary and covalent bonds, hence exhibiting (limited) structural integrity, although it is rapidly becoming quite weak (mechanically). This occurrence is associated with the temperature region between T_g – 250 °C. Physically, the PU becomes extremely stretchable, and its ductility may well exceed 100%. At a high enough temperature, the increased energy uptake by the PU would be adequate to overcome the tenuous bonds (weak secondary and covalent bonds) of the already weakened PU due to the disassociation of the 'soft' segments. This will result in the 'soft' segment disassociating completely from the PU structure and the structural breakdown of the sample. This occurrence is represented in the TGA thermogram in the form of the drastic weight decrease from 100 wt.% - 20 wt.% in the region of 250 - 420 °C. At the end of this process, the structure will be made up of a very small amount of remaining 'soft' segment of the PU, with the rest made up of the 'hard' segment of the PU. However, further increasing the temperature and energy uptake at this point between the region of 420-580 °C will inevitably result in the bond breakage of any remaining 'soft' segment of the PU bonded to the 'hard' segment, and the breakdown of the 'hard' segment of the PU itself, culminating in a complete decomposition seen at T>580 °C.

The thermal decomposition of ZIF-8 is less complex. ZIF-8 is made up of a Zn core coordinated by mIm linkers that forms repeated cells and 3-D cage-like structures. The Zn core remains inaccessible due to its coordinated bonds with mIm ligands, and external contact/bonds with the molecule is primarily facilitated by the mIm ligands due to its chemically active sites and ready accessibility (methyl groups, benzene rings) that allow for

the formation of H-bonds (and other weak secondary bonds) with other elements that are in close proximity (see Figs. 2.1 & 4.9). Compared to PU, ZIF-8 is significantly more thermally stable, only beginning to decompose at 350 °C. The initiation of decomposition takes place when the ZIF-8 nanoparticles, upon increased temperature, receives enough energy to overcome the bond energy between Zn (metal) and mIm linkers (organic). The bond breakage between the Zn core and the mIm ligands is a gradual process, which is represented in the TGA thermogram in the temperature region between 350 – 600 °C.

The presence of active sites in ZIF-8 and the 'hard' segment of the PU is expected to result in the formation of H-bonds between the 'hard' segment of the PU and the mIm ligands of the ZIF-8 nanoparticles due to chemical affinity between the two constituents [217, 218]. The speculated nature of the molecular interactions between the PU matrix and its ZIF-8 fillers is shown in Fig. 5.6.

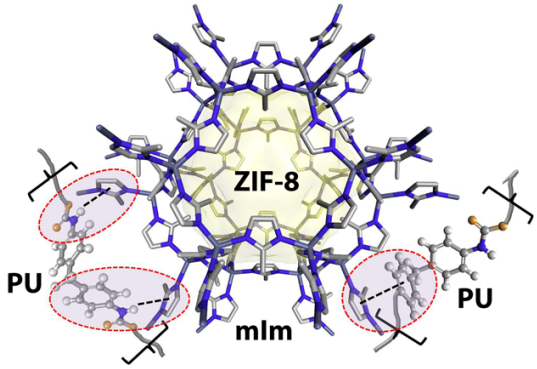

Fig. 5.6 The chemical interactions between the ZIF-8 nanoparticles (porous framework) and the active ('hard') groups of the PU (labelled as {} in the schematics). The bonds being shown in the schematic are hydrogen bonds (between the N in ZIF-8 and H in PU, designated as ----), π-π stacking (N-rings in ZIF-8 and benzene rings in PU, encompassing regions marked with ----- ellipses), and van der Waals (vdW) forces (represented by the colour grey). The strength of these bonds are relatively stronger than the bonds between primary and secondary PU polymeric chains, due to its different constituents (N as opposed to C, and the hydrogen of methyl groups), as discussed in Jensen *et al.* [158]. The yellow surface represents the solvent accessible volume (SAV) of the ZIF-8 sodalite cage. Colour scheme adopted: blue - nitrogen, light grey - carbon, dark grey - zinc, gold - oxygen, white - hydrogen.

In order to explain the TGA thermogram of the nanocomposites, it is important to elucidate the types and collection of bonds present in the structure as a whole. Based on previous explanations, the nanocomposites will intrinsically possess a collection of bonds originating from its matrix due to the dominance of the PU: covalent bonds between the 'soft' and 'hard' segments, and the collection of weak inter and intra-molecular bonds between 'soft' and 'hard' polymeric chains. The introduction of ZIF-8 nanoparticles and its active and accessible sites via its mIm linkers will result in the formation of H-bonds between the methyl group of the mIm linkers and the carbonyl/amine groups in the 'hard' segment of

the PU due to chemical affinity, and a collection of other weak secondary bonds, such as π-π stacking between the benzene rings in PU and ZIF-8, and van der Waals forces. It should be pointed out that although the discussion encompasses the formation of bonds between ZIF-8 and the 'hard' segment of the PU, it is not impossible for ZIF-8 to form links (bonds) with the 'soft' segment of the PU. However, these bonds would be very weak, and would not significantly influence the thermo-mechanical response of the nanocomposites.

Collectively, the formation of nanocomposites using PU and ZIF-8 would result in a higher collective internal bond strength between the constituents, and higher strength material as a whole (the thermo-mechanical response and quasi-static mechanical properties of the nanocomposites will be explored in the subsequent sub-sections). In the context of TGA thermogram of the nanocomposites, the effect of the introduction of ZIF-8 nanoparticles is gradual. In the 10 wt.% and 20 wt%. samples, it can be seen that the thermal decomposition is initiated at a slightly lower temperature (~230 °C), and the decomposition in the 230 - 420 °C range is slightly more severe (down to ~18 wt.%) in the case of the 10 wt.% sample. This can be attributed to the 'displacement' effect of the ZIF-8 nanoparticles within the nanocomposite. At low loadings such as 10 wt.%, the ZIF-8 nanoparticles will displace the soft segment and compete with the soft segment to form bonds with the hard segment of the PU. Therefore, the structure as a whole will lack some of the intrinsic bonds formed between the soft and hard segments of the PU, a small portion of which is replaced by the H-bonds formed between ZIF-8 and the hard segment of the PU. As per the TGA thermogram in Fig. 5.5, it can be assumed that collectively, the strength of these bonds are slightly inadequate to compensate for the loss of the 'soft-hard' segment bonds in the PU [80]. However, the small amount of ZIF-8 that are present in the nanocomposite proves to be quite thermally stable, and remained structurally semi-intact alongside its decomposing PU matrix within 420-580 °C (via its H-bonds and other weak interactions with the 'hard' segment).

The thermal stability of the nanocomposite starts increasing once the amounts of ZIF-8 nanoparticles increase. At 40 wt.%, it can be seen that despite the (slightly) lower initiation temperature of decomposition of the nanocomposite, the decomposition of the 'hard' segment is significantly delayed compared to the one exhibited by PU. At this point, the collective bonds formed between the 'hard' segment of the PU and the mIm linkers of ZIF-8 exceeded the amount needed to compensate for the loss of the bonds between the 'soft' and 'hard' segments of the PU. It can be said that the combined bond strength in the nanocomposites, due to the presence of ZIF-8, is significantly increasing. At this point, the decomposition of the 40 wt.% nanocomposite mimics that of the ZIF-8 nanoparticles, where it steadily decomposes (alongside the hard segment of the PU) from 350 -600 °C, making it a more thermally stable structure [219]. The pattern of thermal decomposition of a PU/SiC composite was discussed in Guo *et al*. [220], where it was posited that the introduction of SiC into the PU had a synergistic effect that strengthened the overall strength of the composite via the surface interactions between the SiC particles and the PU. They underlined the fact that the surface interactions (i.e. weak bonds) are responsible for the increased thermal stability and increased mechanical strength of the PU/SiC composite. This is mirrored in this work as well, as seen in Fig. 5.5 for thermal stability, and Fig. 5.11, where the macro-mechanical properties of the nanocomposite increases with increased ZIF-8 nanoparticle loadings (further discussion in §5.6). This is also evident in the DSC scan of the nanocomposites in Fig. 5.7.

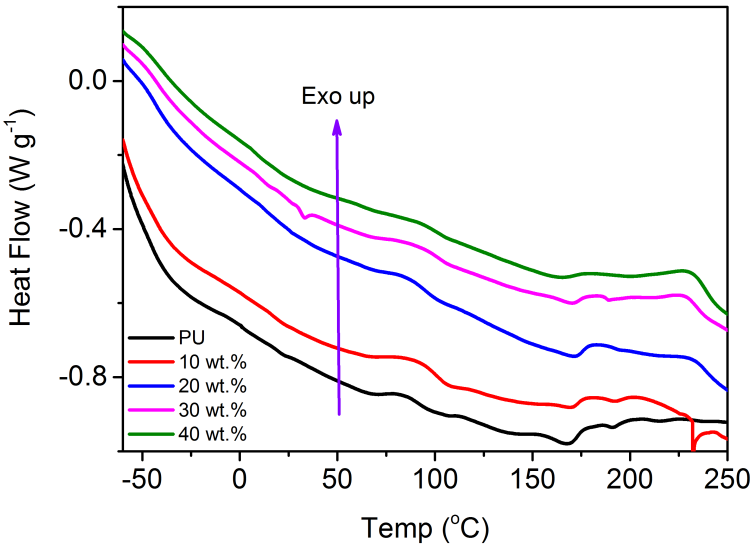

Fig. 5.7 The compilation of the DSC plots for the PU and PU/ZIF-8 nanocomposites, from -70 °C to 250 °C.

Fig. 5.7 shows the compilation of the DSC plots of the PU and its corresponding ZIF-8 nanocomposites. At higher loadings of ZIF-8 nanoparticles, the corresponding DSC thermogram is more exothermic as the temperature increases. The prevalence of H-bonds (and other collective weak interactions) between the 'hard' segment of the PU and the mIm ligands of the ZIF-8, on top of the covalent bonds and weak interactions of the PU, will result in samples that will require *and* release more energy for the breakage of the aforementioned bonds (exothermic reaction), which will entail the release of increased amounts of heat (increased heat flow). Thus, as per Fig. 5.7, the level of exothermicity of the samples are in the order of PU<10 wt.%<20 wt.%<30 wt.%<40 wt.%. Comparisons have to be made using the exothermic profile of the samples as opposed to the usual method of using the T_g from the DSC [118, 152] as the T_g peaks of the nanocomposites are almost impossible to detect in the DSC thermogram. However, the T_g of these samples have been determined using the DMA (see Appendix C.4), which is universally regarded as being more accurate at the detection of T_g than DSC. Looking at the T_g values in Appendix C.4, it can

be surmised that the slight increase in the T_g of the nanocomposite samples as opposed to neat PU is proof of bond formation (relatively weak) between ZIF-8 and PU.

The previous discussion focussed on the qualitative assessment of the bonds and bond strengths within the nanocomposites. The lack of a quantitative assessment of these bonds is attributed to the lack of access to equipment such as X-ray photoelectron spectroscopy (XPS), which enables the determination of the types of bonds in a sample and the quantification of those bonds' strength, and Fourier Transform Infrared Spectroscopy (FTIR), which allows for the determination of the types of bonds present in the sample and its corresponding vibration states at specific wavelengths (wavenumbers) [161, 162]. The lack of these equipment places the quantification of the bonds between PU and ZIF-8 firmly beyond the scope of this thesis. It should also be mentioned that there are theoretical approaches towards the quantification of the types of bonds and bond strength between the constituents in the nanocomposite, such as Density Functional Theory (DFT) and its corresponding derivatives or analogues, however its undertaking is a itself a subject of deep study with its own sets of assumptions and theoretical challenges, which places it beyond the scope of this work [163].

5.5 Viscoelastic studies

Polymeric materials in general, and rubbery polymers in particular, are known to demonstrate linear viscoelastic characteristics at small oscillatory strains. The study of viscoelasticity makes up the core fundamentals of polymeric materials; this is especially true for rubbery polymers [112]. It is vital that the viscoelastic response of the nanocomposites be determined, due to the structural dominance of PU in the

nanocomposites. This will help us analyse the molecular influence of ZIF-8 on the viscoelastic response of PU, and also model and predict the thermo-mechanical response of the subsequent PU/ZIF-8 nanocomposites. The structural and chemical changes within the internal configuration of the matrix can be quantified accurately using the dynamic modulus (E^*, Eqn. 2.3), constituting the storage modulus (E'), representing the elastic strain energy stored within the polymeric chains while undergoing oscillatory motions, and the loss modulus (E"), representing the energy dissipated by the polymer during chain or bond rotations or phase changes [112] (see §2.3.2.3).

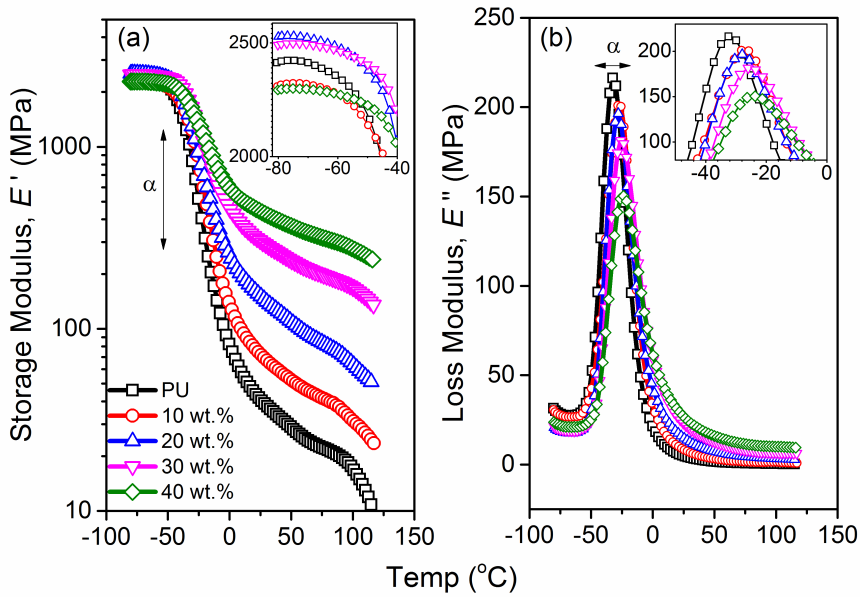

Fig. 5.8 Representative plots of (a) Storage modulus, E' (log-scale) and (b) Loss modulus, E", of the PU/ZIF-8 nanocomposites (f = 10 Hz, see Appendix C.6 for data reported by other frequencies). The insets in both (a) and (b) represent the initial loadings during the experiments, while α denotes the primary relaxation regions of the nanocomposites, which corresponds to the T_g of the nanocomposites, where the primary (hard) molecular chains of the PU and the nanocomposites are experiencing molecular shifts (deformation and modification) simultaneously throughout the nanocomposites.

The study of the viscoelastic properties of the PU/ZIF-8 nanocomposites represents an in-depth study of the molecular interactions between two distinct phases within one structure, due to the fact that polymeric materials undergo multiple phase changes at different temperature levels, the most common of which are 'glassy' and 'rubbery' regions. These phase changes are characterised by the aforementioned molecular interactions; where the glass transition temperature (T_g) marks the initiation of phase changes. The glassy region is characterised by high stiffness and interlocking bonds, with restricted molecular flows and close interactions between the molecular chains ($T < T_g$), while the rubbery region is characterised by a major shift in the polymeric primary and secondary chains and the ability of these chains to freely flow and slip past one another when exposed to external stimuli ($T > T_g$). Phase changes are termed 'relaxation' and T_g is the temperature where the polymeric chains will undergo major relaxation (also known as the primary relaxation temperature, or T_α), which explains the subsequent major shift in its physical and chemical characteristics.

Fig. 5.8 shows the (a) storage (E') and (b) loss (E") moduli of the PU/ZIF-8 nanocomposites. Although T_g remains relatively unaffected by the introduction of ZIF-8 nanoparticles, it is immediately noticeable that the relaxation modes are very much affected by the introduction of ZIF-8 nanoparticles. It is observed that the nanocomposites experience relaxations at relatively higher values of E' and lower values of E" as the wt.% of ZIF-8 nanoparticles increases, which is especially evident in the rubbery region ($T > T_g$). This is attributed to the increased presence of ZIF-8 nanoparticles within the nanocomposites and the pinning and 'locking' effect the nanoparticles have on the primary and secondary PU polymeric chains; these polymeric chains will become immobilised and have difficulty in undergoing complete relaxation (E', E" < 10 MPa) due to its association with ZIF-8 nanoparticles, which forces the occurrence of relaxation at much higher stiffness levels to accommodate the ZIF-8 nanoparticles, as seen in Fig. 5.8 (a) & (b).

Increased loadings of ZIF-8 nanoparticles translate into lesser amounts of PU polymeric chains per unit volume in the nanocomposites, which means that the polymeric chains that are loosely associated with the ZIF-8 nanoparticles undergo relaxation at a level that is common for PU. However, the hard segment of the PU is still bound to the soft PU segment and the ZIF-8 nanoparticles, and these combined bonds prevents the occurrence of relaxation at levels common to PU. The nanocomposites as a whole still undergo relaxation at higher levels, and it is speculated that at this point, the mechanical response is dictated by the ZIF-8 nanoparticles as opposed to the already relaxed PU polymeric chains.

Notably the DMA data (Fig. 5.8(a)) demonstrate that ZIF-8-loaded composite is mechanically more resilient than PU, and this is evident in the fact that the nanocomposites, at higher loadings of ZIF-8 nanoparticles, begin to exhibit more robust mechanical response as opposed to neat PU. The ability of the nanocomposites to retain, distribute, and dissipate energy (from external stimuli) also improved with the presence of ZIF-8. For instance, it was determined that the loss moduli, *E*”, peaked at 225 MPa for the PU, while it dropped to 150 MPa for the PU/ZIF-8 40 wt.% nanocomposite, corresponding to a decrease of strain energy dissipation by over 33%.

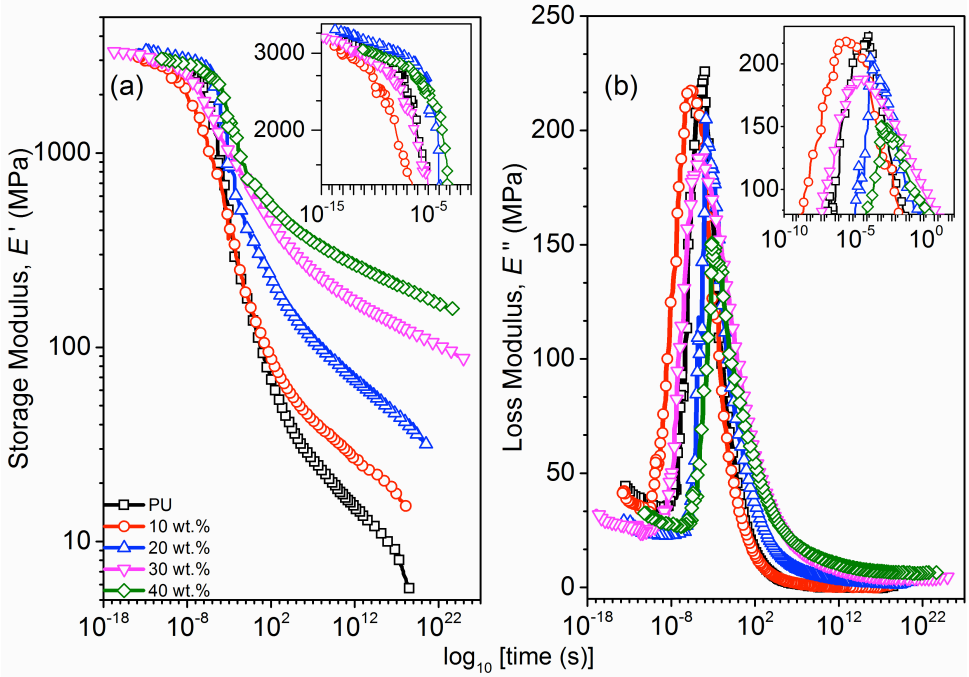

Fig. 5.9 Time-temperature superposition (TTS) master curves of the PU/ZIF-8 nanocomposites at T_{ref} = -15 °C for the (a) Storage (*E*') and (b) Loss (*E*") moduli, note the log scales for both the *E*' and time, *t*. The insets show the earlier time scales for *E*' and *E*". The TTS master curves allow us to access frequency (*f*) and time (*t*) ranges that are beyond the capabilities of the DMA experiments (see Appendix C.7).

It was assumed that in this case, as per literature, that PU is thermorheologically simple [166, 167]. Another assumption being made here is that the thermo-mechanical behaviour of the PU/ZIF-8 nanocomposites closely mirrors that of neat PU, due to the fact that PU forms the structural majority (> 60 wt.%), and henceforth, the assumption of PU being thermorheologically simple extends to the nanocomposites as well. These assumptions allowed for the construction of a corresponding master curve for both the neat PU and its ZIF-8 nanocomposites, and the plots are shown in Figs. 5.9 (a) & (b). Generally, at *lower temperatures* ($T<T_g$) and *shorter time spans*, the PU and ZIF-8 nanocomposites exhibit lower losses and dissipations while retaining higher energy storage capabilities (*E*' > 1000

MPa and *E*" = 30 MPa). The neat PU and the PU/ZIF-8 nanocomposites are physically stiff and exhibit behaviour analogous to *glassy polymers* (~3.5 GPa). However, at *longer time spans* and *higher temperatures ($T>T_g$)*, energy retention decreases; this is reflected in the values of *E*' (500-1000 MPa) and *E*" (150 – 230 MPa) of the master curve. At this stage, the neat PU and the ZIF-8 nanocomposites exhibit behaviours that are consistent with *rubbery polymers*. As previously discussed and also seen here, the presence of ZIF-8 nanoparticles decreases the dissipation and increase energy retention by ~30%. Simply put, the introduction of ZIF-8 nanoparticles increases the operational capability of the nanocomposites by dampening the initiation of the complete degradation mechanism induced by constant exposure to heat (-70 to 120 °C) and vibrations (2, 5, 10, 15, 20, 25, 30, 35, 40 Hz).

Another characteristic that can be derived from the TTS plots of the PU and its nanocomposites is its activation energy (E_a) as it changes phase from glassy-to-rubbery, via Eqn. 5.1 [221]. The values derived from the formula are shown in Fig. 5.10.

$$\ln(f) = \ln(A) - \frac{E_a}{RT_g} \tag{5.1}$$

where *f* are the frequencies garnered from the DMA test, E_a is the activation energy (in kJ/mol), *R* is the gas constant (8.3145 J mol^{-1} K^{-1}) and T_g is the reference temperature (also known as T_{ref}).

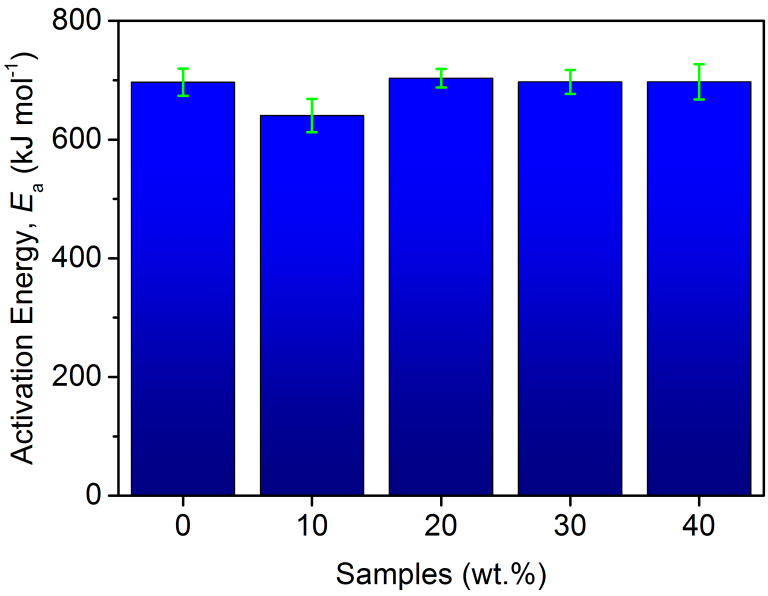

Fig. 5.10 The activation energy (E_a) of the PU/ZIF-8 nanocomposites at T_g, derived from their respective shift-factor plots using Eqn. 5.1. Herein the focus is on the general trend instead of the absolute magnitudes of E_a, as the magnitude is larger than those reported in literature (in the range of 10-100 kJ mol^{-1}) (see Appendix C.7 for the plots used to derive these values).

Similar to the T_g of the PU and its corresponding nanocomposites, the trend of the E_a remains somewhat close to one another, with small discernible differences, at PU (690 kJ mol^{-1}), 10 wt.% of ZIF-8 (640 kJ mol^{-1}), 20 wt.% of ZIF-8 (700 kJ mol^{-1}), 30 wt.% of ZIF-8 (697 kJ mol^{-1}) and 40 wt.% of ZIF-8 (697 kJ mol^{-1}). Previous sections detailed the influence of the presence of ZIF-8 nanoparticles within the nanocomposites affecting its thermo-mechanical responses, however, as seen in Fig. 5.9, E_a remains almost unaffected. This observation can be used to assume that at $T<T_g$, the thermo-mechanical response of the PU matrix and its corresponding nanocomposite are quite similar, with marked differences between the two class of materials only evident at $T>T_g$. The interactions between the primary and secondary polymeric chains in the PU matrix is rather weak and the polymeric chains are flowing and

slipping freely amongst one another, rendering the PU membrane fluid, incompressible, and pliant [222], while interactions between PU and ZIF-8 in the nanocomposite are dominated by weak secondary bonds (H-bonds), which are collectively weaker than the bonds between the 'hard' and 'soft' segments of the PU. Although these weak interactions are discernible using methods such as DMA via TTS plots and the determination of its E_a, it is nowhere near significant enough to influence the E_a required for a glassy-to-rubbery transition within the nanocomposite, which, in all of the cases, is dominated by the PU matrix (>60 wt.% PU). The influence of ZIF-8 towards the thermo-mechanical response and quasi-static mechanical properties of the nanocomposite does not seem to influence the E_a of the sample, which is also the case in the T_g of the sample, further confirming the supposition that at $T<T_g$, the behaviour of the PU matrix and its nanocomposite are rather similar.

5.6 Large strain deformation and mechanical toughness of PU/ZIF-8 nanocomposites

The previous sections dealt with the elastic deformation of the nanocomposites at small strains ($\varepsilon < 1\%$), which allowed them to retain their original configuration with the cessation of strain loading. For a complete assessments of the thermo-mechanical response of nanocomposites, it is vital that they be tested at extended deformation ranges, preferably up till the point of fracture, which will allow us to analyse the corresponding behavioural responses related to structural failure [105]. This is not without precedent in the context of PU-based composites, where Xiong et al. [223] synthesised PU/CNT composites and determined its mechanical properties via uniaxial tensile testing. They reported that the addition of 2 wt.% of CNT into the PU improved both E and σ^* of the composite, which is attributed to the strong chemical interactions between the PU and CNT (proven via FTIR)

in their work. The uniaxial tensile test was adopted for this purpose, due to the fact that it is a very well established method for determining the quasi-static mechanical response of materials towards large strain deformations. Figs. 5.11 - 5.12 show the representative nominal stress-strain (σ-ε) plots and the corresponding compilation of mechanical properties derived from the aforementioned plots.

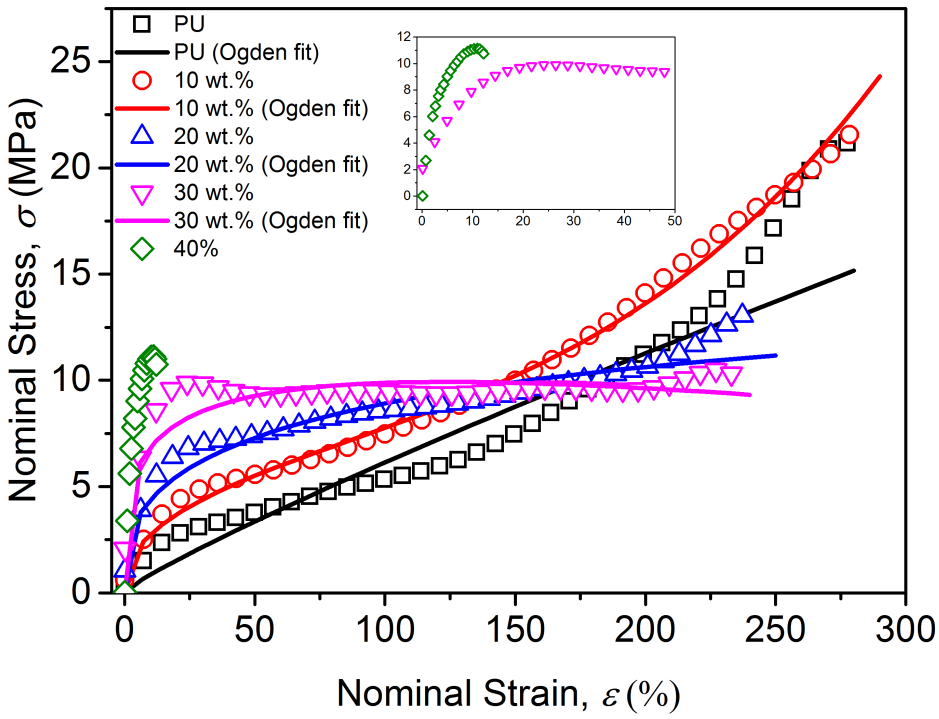

Fig. 5.11 Representative nominal stress-strain (σ-ε) plots for the PU/ZIF-8 nanocomposites derived from the uniaxial tensile tests and normalised using the Digital Image Correlation (DIC) technique *via* DaVis®. The inset shows the 30 wt.% and 40 wt.% nanocomposites, where its characteristics are more evident. The built-in hyperelastic model in Abaqus® was used to calculate the material constants associated with the Ogden model (see Table C.7 in the Appendix) and generate the corresponding σ-ε (Ogden) plots based on the experimental data. See Eqn 5.2-5.3 for the formula used to fit the experimental data to the Ogden model.

The nominal σ-ε plots clearly showed that the elongation of the samples exceeded 100% up to 30 wt.% sample, and its elongation (hence ductility) is severely reduced (<<100%) for the 40 wt.% sample. The samples seem to behave in a non-linear manner and appear to strengthen upon increased loading of ZIF-8 nanoparticles. Although this material is elastic, it behaves in a non-linear manner, which means that it cannot be assumed that this material is linear elastic as its elongation is not directly proportional to strain with a constant E. Instead, the PU and its nanocomposites can be regarded as being *hyperelastic*, where its σ-ε relation is not defined by a constant E, but is rather defined by a strain energy density function (U) and is independent of strain rates. There are many viable model for hyperelasticity that can be used to represent the stress-strain behaviour of materials, such as Neo-Hookean, Mooney-Rivlin, Arruda-Boyce, and the Ogden models. Nominally, materials that experimentally demonstrated low strain elongations can be accurately represented using the Neo-Hookean model, however, materials that experimentally demonstrated much higher values of strain elongations (>>100%) needs to be represented by more elaborate models due to their more complex mechanical response. Due to the fact that the strain elongation of the PU and its nanocomposites being ~300%, the Ogden model was selected to represent and be fitted to the samples. The strain energy density function of the Ogden model (taken directly from the Abaqus manual) is shown in Eqn. 5.2 [145]:

$$U = \sum_{i=1}^{N} \frac{2\mu_i}{\alpha_i^2}\left(\overline{\lambda}_1^{\alpha_i} + \overline{\lambda}_2^{\alpha_i} + \overline{\lambda}_3^{\alpha_i} - 3\right) + \sum_{i=1}^{N} \frac{1}{D_i}\left(J_{el} - 1\right)^{2i}$$
$$\overline{\lambda}_i = J^{-\frac{1}{3}}; \lambda_i \rightarrow \overline{\lambda}_1\overline{\lambda}_2\overline{\lambda}_3 = 1 \qquad (5.2)$$

where λ_i are the principal stretches, J is the volume ratio, and μ_i (MPa) and α_i (dimensionless) describe the shear behaviour of the materials, and D_i its compressibility (assume that it is incompressible, thus $\overline{\lambda}_1\overline{\lambda}_2\overline{\lambda}_3 = 1$).

The strain energy function can then be used to derive the σ-ε relationship as a function of principal stretches (λ_n) shown in Eqn 5.2. The steps needed to derive this function are detailed below:

In the event that the principal stretch, λ, is parallel to the uniaxial tensile stress (σ), then:

$\lambda = \lambda_1$, and

$\lambda_2 = \lambda_3$

The incompressibility implied in Eqn 5.2 results in:

$\lambda_2 = \lambda_3 = \lambda^{0.5}$

Inserting these terms into Eqn. 5.2 yields:

$$U(\lambda) = \sum_{p=1}^{n} \frac{\mu_p}{\alpha_p} (\lambda^{\alpha_p} + 2\lambda^{-0.5\alpha_p} - 3)$$

Differentiating this function with respect to stretch yields:

$$\sigma(\lambda) = \frac{\partial U(\lambda)}{\partial \lambda} = \sum_{p=1}^{n} \mu_p (\lambda^{\alpha_p - 1} - \lambda^{-0.5\alpha_p + 1}) \tag{5.3}$$

where μ_i (MPa) and α_i (dimensionless) represent the shear behaviour of the material (constants derived from Eqn. 5.2), λ is the principal stretch parallel to the uniaxial application of stress (σ).

The σ-ε relationship derived from the strain energy function (U) of the Ogden model (Eqn 5.2 & 5.3) from Abaqus® hyperelastic Ogden model are shown in Fig. 5.11, with the uniaxial experimental tests as inputs. The σ-ε plots (Ogden) closely match that of the experimental σ-ε plots, although the σ-ε plots (Ogden) for the nanocomposites closely resemble their experimental counterparts compared to the σ-ε plot (Ogden) for the PU. Again, the retention

of the physical response of the nanocomposites, experimentally and theoretically, proves that the rubbery matrix exerts considerable influence upon the macro-mechanical response of the nanocomposites despite the significant presence of the ZIF-8 nanoparticles.

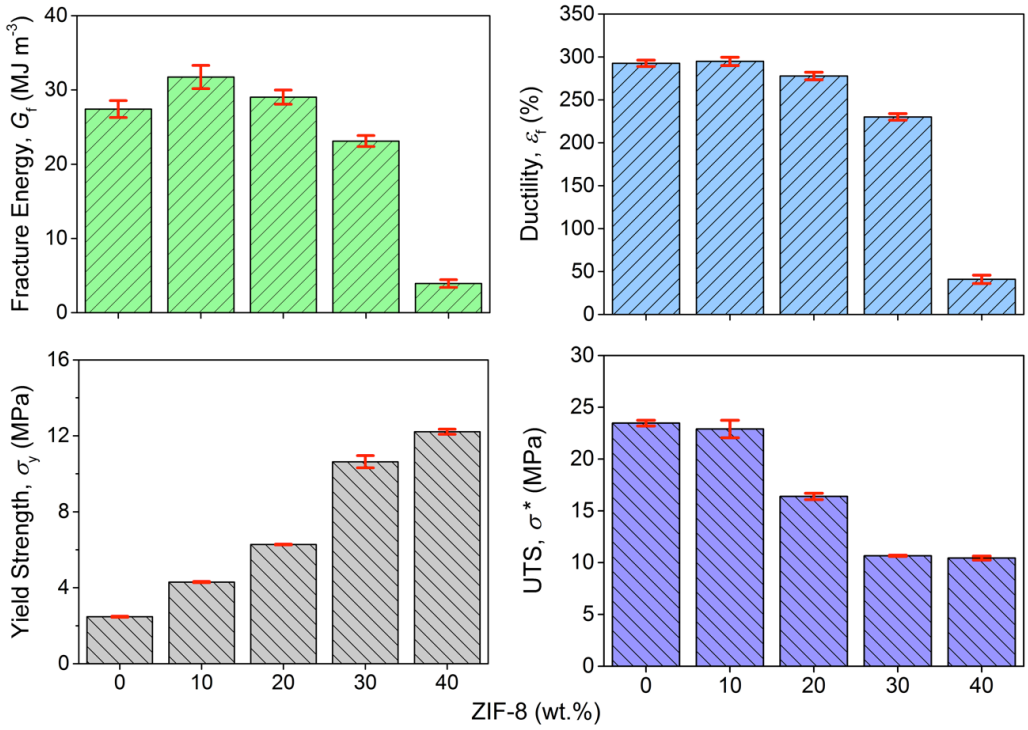

Fig. 5.12 The mechanical properties of the PU/ZIF-8 nanocomposites derived from the σ-ε plots (Fig. 5.11), with (a) ductility (ε_f), (b) fracture energy (G_f), (c) ultimate tensile strength (σ^*), and (d) yield strength (σ_y). The values were calculated and averaged from a total of three test coupons, and the corresponding standard deviations for each sample are reflected in the error bars.

It is rather obvious that the introduction of ZIF-8 nanoparticles into the PU matrix influence the mechanical properties of the resulting nanocomposites. It is immediately apparent that the elongation-to-failure (ε_f), fracture energy (G_f), and ultimate tensile strength (σ^*) are all

inversely proportional to the addition of ZIF-8 nanoparticles, while the yield strength (σ_y) is directly proportional to it (consistent with increase in hardness showed in Fig. 5.4(b)). The nanocomposites, up till 30 wt.%, retain the hyperelasticity inherent in PU (Fig. 5.12). Substantial and noticeable changes to the nanocomposites are however, more pronounced at loadings exceeding 20 wt.%.

The pinning and nominal immobilisation effect introduced by the ZIF-8 nanoparticles to the PU polymeric molecular chains are not as significant at lower loadings (< 20 wt.%), due to the scarcity of the particles within the PU matrix. This is also reflected in the FEG-SEM images of the PU/ZIF-8 nanocomposites, where the ZIF-8 nanoparticles tend to be evenly dispersed clusters throughout the matrix (Fig. 5.1 (b) – (c)). However, this changes when the ZIF-8 nanoparticle loadings are higher (> 20 wt.%), where it is noticed that ZIF-8 nanoparticles begin to dominate the structure and are more pronounced, as evident in Fig. 5.1 (d) – (e). Pinning and nominal immobilisation begin to dominate the interactions between the ZIF-8 nanoparticles and the polymeric molecular chain of the PU, resulting in loss of hyperelasticity (extended ductility), and with it, fracture energy and tensile strength. With the loss of hyperelasticity, the nanocomposites become stiffer and less stretchable (more brittle), resulting in higher yield strengths, as shown in Fig. 5.12 (d). It should also be pointed out that the Young's moduli (E) and nanohardness (H scales with yield strength σ_y), as measured by the nanoindentation technique, is directly proportional to ZIF-8 nanoparticles loading, further lending credence to this supposition. All in all, the results from nanoindentation and uniaxial tensile tests are in excellent agreement, while the chemical interaction model being proposed in Fig. 5.6 can be used to explain the pinning and immobilisation effects introduced by the ZIF-8 nanoparticles (filler phase).

5.7 Practical implications

This chapter focuses on the development and optimisation of the thermo-mechanical properties and resilience of PU/ZIF-8 nanocomposites. This particular composite has yet to be reported in literature, and this work represent the first attempt in characterising and optimising its design. Furthermore, the combination of a hyperelastic matrix (PU) and a structurally flexible MOF (ZIF-8) [33, 35] represent an interesting opposing mixture, which resulted in unique and distinctive thermo-mechanical and viscoelastic properties. Our supposition and discoveries will be summarised and detailed in the following manner.

It was confirmed that ZIF-8 and PU are linked *via* tenable collection of secondary interactions and remained semi-independent of each other at lower loadings of ZIF-8 nanoparticles (Fig. 5.1). Unlike glassy polymer matrices (e.g. Matrimid, Chapter 4) [80], ZIF-8 nanoparticles are *nominally* attached to the primary polymeric molecular chain of PU, as posited in Fig. 5.6. This basically implies that the free volume and ZIF-8 nanoparticles are not fixed, they are assumed to be a function of external stimuli; the polymeric chain of PU will deform and elongate as per stimuli such as temperature and pressure, and the location of free volume within the rubbery polymer itself will be shifted based on the motion of the polymeric chain. The ZIF-8 nanoparticles, which are nominally attached to the polymeric chains of PU, will shift alongside these motions, or will be debonded from the polymeric chain, sometimes forming independent clusters of ZIF-8 nanoparticles not-attached to the PU matrix. However, at higher loadings of ZIF-8, the nanocomposites, despite retaining a respectable elongation-to-failure (>~40%) and structural integrity, is now quickly becoming dominated by the combined secondary bonds formed between mIm (organic ligands) of ZIF-8 and the hard segments of the PU, introducing the ‘locking’ effect discussed previously, resulting in fixed free volume and ZIF-8 nanoparticles, and polymeric

chains that are not as free to deform or elongate compared with their lower loaded counterparts. This notion of filler-to-matrix pinning effects is supported by the large strain mechanical deformation data presented in Fig. 5.11.

Up till now, the formation of free volume and placement of nanofillers in polymer nanocomposites are speculated to be a random occurrence, however, the phenomenon observed with these robust PU/ZIF-8 nanocomposites open up an avenue that might lead into bespoke free volume and nanofillers within nanocomposites post-fabrication instead of pre-fabrication. This would especially be salient to the realm of certain applications (gas capture and separations, desalination), as this would also mean that the mechanical properties are tuneable and thermal properties customisable [224].

It was demonstrated that the PU/ZIF-8 nanocomposites are able to withstand significant deformation before failing; this is attributed to the hyperelastic nature of the PU matrix. Energy and heat, at moderate levels, are evenly distributed and dissipated throughout the nanocomposites *via* a combination of properties, such as viscoelasticity (elastic region; $\varepsilon <$ 1%) and hyperelasticity ($\varepsilon >>$100%) [225]. This is evident from the results garnered from DMA and quasi-static uniaxial analyses, and discussed in §5.5 & 5.6, respectively. Under oscillatory elastic strains, the nanocomposites are capable of retaining its original configuration post-load removal at an oscillatory stress of 2 GPa. Dissipated energy, in the form of *E*", falls between 180-250 MPa, implying that only ~10 % of energy is lost per oscillatory cycle, while the remainder is dampened within the nanocomposites. The introduction of ZIF-8 also increased the E_a of phase change (glassy-to-rubbery); the E_a increased by 40 % when loaded at 40 wt.% of ZIF-8 nanoparticles. This is especially useful, as the $T_g <$ RT, while operationally speaking, T_{op} would fall between RT-100 °C experienced during gas separation and pervaporation processes.

It was also determined that the addition of ZIF-8 did not significantly affect the macro-mechanical properties of the resulting nanocomposites, where it was seen in Figs. 5.11 - 5.12 that the nanocomposites exhibited macro-mechanical properties that are relatively similar to that of neat PU (hyperelastic), such as the fracture energy (a difference of 10% between PU and PU/ZIF-8 20 wt.%), elongation-to-failure (a difference of 5% between PU and PU/ZIF-8 20 wt.%), and tensile strength (a difference of 15% between PU and PU/ZIF-8 20 wt.%). The relatively small difference in these macro-mechanical properties bodes well for the nanocomposites, as literature had proven that increased content of ZIF-8 nanoparticles greatly increase the performance of nanocomposites in terms of gas separation [80], ionic/proton conductivity [161], and pervaporation [178]. By retaining hyperelasticity and the viscoelastic characteristics of the PU matrix despite the addition of ZIF-8 at unprecedented levels, it can be assumed that the performance of these nanocomposites, should it be utilised for the aforementioned applications, would result in significant improvements.

5.8 Chapter Summary

A systematic effort at understanding the thermo-mechanical and viscoelastic properties of a new system of PU/ZIF-8 nanocomposites was presented, which can be readily prepared in the form of ~100-μm thick nanocomposites. Despite the lack of this particular grade of nanocomposite in literature, i.e. rubbery polymer matrix combined with MOF nanoparticles (e.g. ZIF-8), the methods used to determine its corresponding properties are quite well established, such as quasi-static nanoindentation and uniaxial tensile tests, and dynamic mechanical analysis (DMA).

It has been established that the thermo-mechanical, viscoelastic, and static mechanical properties and the morphology of the polymer/MOF nanocomposites are crucial towards materials design and industrial applications. Having established the correlation between morphology and performance, the next two chapters will detail the use of the nanocomposites for the capture and retention of liquid (I_2) and gas (C_2H_4) elements.

CHAPTER SIX

Capture and immobilisation of iodine (I_2) utilising polymer-based ZIF-8 nanocomposites

The previous chapters carefully elucidated the thermo-mechanical responses of two classes of polymer/MOF nanocomposites, and its respective reactions towards external stimuli. Our results were also used to rationalise the results reported in literature *vis-à-vis* gas capture and separation (Chapter 4), linking intricate thermal and mechanical properties of the nanocomposites to its gas capture and separations performance. Thus far, it was discovered that the addition of ZIF-8 nanoparticles into polymer matrices (glassy and rubbery) resulted in relatively robust mechanical responses while introducing specific functionalities, which enables the nanocomposites to selectivity allow the passage of specific gas species (increased selectivity), thus increasing its permselectivity (permeability and selectivity).

This chapter will discuss the usage of previously developed polymer/MOF nanocomposites for an application that is yet to be reported in literature for these types of nanocomposites: liquid adsorption, specifically, the passive adsorption of I_2. Only two classes of the nanocomposite were used in the quest of exploring the viability of this application; the neat polymers (Matrimid and PU) and its corresponding 30 wt.% nanocomposites. This was done to establish a contrast between the neat polymers and its corresponding nanocomposites in terms of its capability of adsorbing I_2 due to the introduction of ZIF-8 nanoparticles into the polymer matrices. This chapter will detail the results gathered from the experimental methods reported in §3.4. Works discussed in this chapter has been published in Mahdi *et al.* [226].

6.1 Rationale

Nuclear technology is prominent in two sectors that are intrinsic parts of our lives: power generation [227] and medicine [228]. Nuclear power plants are regarded as a source of clean, renewable, and cost-effective energy [229], while nuclear medicine forms the core of many diagnosis techniques and treatments for chronic illnesses [230]. Nuclear-related processes produce many by-products such as isotopes of iodine (^{129}I and ^{131}I), ^{135}Cs, and ^{99}Tc, some of which emit alpha (α), beta (β), gamma (γ), and neutrons (n), all of which are hazardous to humans and the environment. Their extensive half-lives ($t_{1/2}$), some ranging to millions and billions of years, necessitates a permanent and effective disposal approach for these by-products, aptly called nuclear waste products [231, 232].

A common radionuclide that is produced as a by-product of power generation are isotopes of iodine; ^{129}I, with a $t_{1/2}$ of 1.5×10^7 years, which is detrimental to the environment, and ^{131}I, with a $t_{1/2}$ of 8.02 days, which is detrimental to human metabolic processes [233]. As such, many research works focussed on the successful capture and confinement of I_2 [234, 235]. Common industrial practice in capturing and storing I_2 is dominated by activated carbon [236, 237] and zeolite [238] filters and scrubbers, where the former reports an I_2 uptake/capture of 305 mg g^{-1}[236] and 460 mg g^{-1} [237], while the latter reports an uptake of 170 mg g^{-1} [239], all of which represent standard uptake capabilities for these materials. Recent research works on activated carbon and zeolites in the context of I_2 capture involves structural and chemical modifications to enhance I_2 capture. However, metal-organic frameworks (MOFs) [240, 241] or variants of its composites [235, 242, 243] are also being explored for I_2 uptake/capture, to varying degrees of success. Sava *et al.* [244] reported I_2 uptake of 117 wt.% of ZIF-8 *vs*. 141 wt.% of activated carbon, proving that nanoporous ZIF-8 is a viable material for I_2 uptake at levels almost rivalling that of activated carbon.

Previous attempts have been made to capture and immobilise iodine (I_2) within ZIF-8, HKUST-1, Ag, and glass powders (EG2992 and EG2998), forming a glass-composite material, which turned out to be successful, as reported by Sava *et al*. [245]. Despite the effectiveness of this reported approach, its energy intensiveness and the requirement to employ a mixture of multiple constituents within a single system might prove to be over demanding for practical engineering solutions.

Despite the effectiveness of ZIF-8 nanoparticles in I_2 uptake/capture, the problem of its deliverability remains; dispersing nanoparticles in a liquid/gaseous environment will result in a non-uniform distribution of ZIF-8 and also difficulty in retrieving the nanoparticles post-I_2 uptake/capture. Problems that are common to nanoparticles, such as agglomeration and aggregation are also prevalent in this case, and guaranteeing that the nanoparticles are free from these debilitating factors remains quite challenging. Also, the constant exposure of these nanoparticles to a volatile environment, such as the high temperature settings where volatile I_2 is released, would prove to be taxing to the ZIF-8 nanoparticles, eventually resulting in its structural degradation. The formation of a nanocomposite incorporating ZIF-8 nanoparticles, which has been proven effective in I_2 capture, and a stable, accessible, and relatively robust matrix will maximise the efficiency of I_2 capture without compromising its structure, resulting in an easily deployable and retrieved material that is just as effective in I_2 uptake/capture. The polymer/ZIF-8 nanocomposites developed in this work and thermo-mechanically characterised in the previous chapters are suitable candidates for this endeavour.

This chapter will elucidate the development, assessment, and the characterisation of the viability of polymer/ZIF-8 nanocomposites (reported in Chapters 4-5) as an I_2 capture and retention model system. Herein, one of the objectives is to also minimise the energy expenditure associated with the capture and retention process, and thus to rely upon the

molecular interactions and affinity between I_2, ZIF-8 nanoparticles, and polymer matrices (either glassy or rubbery) to expedite the uptake of I_2 into the thin composites. The introduction of this so-called *passive* polymer-based system represents an equally effective alternative that is cost effective and highly deliverable; the concept of which is potentially viable for development to enable industrial applications in the long run.

6.2 Iodine (I_2) adsorption and physical changes to the nanocomposites

The morphological features of the nanocomposites used in this experiment are elucidated in Figs. 4.3 (a, d) and 5.1 (a, d). The neat and 30 wt.% samples were selected to represent two extremes in this case to further confirm the viability of the polymer/MOF nanocomposites in the retention and release of I_2.

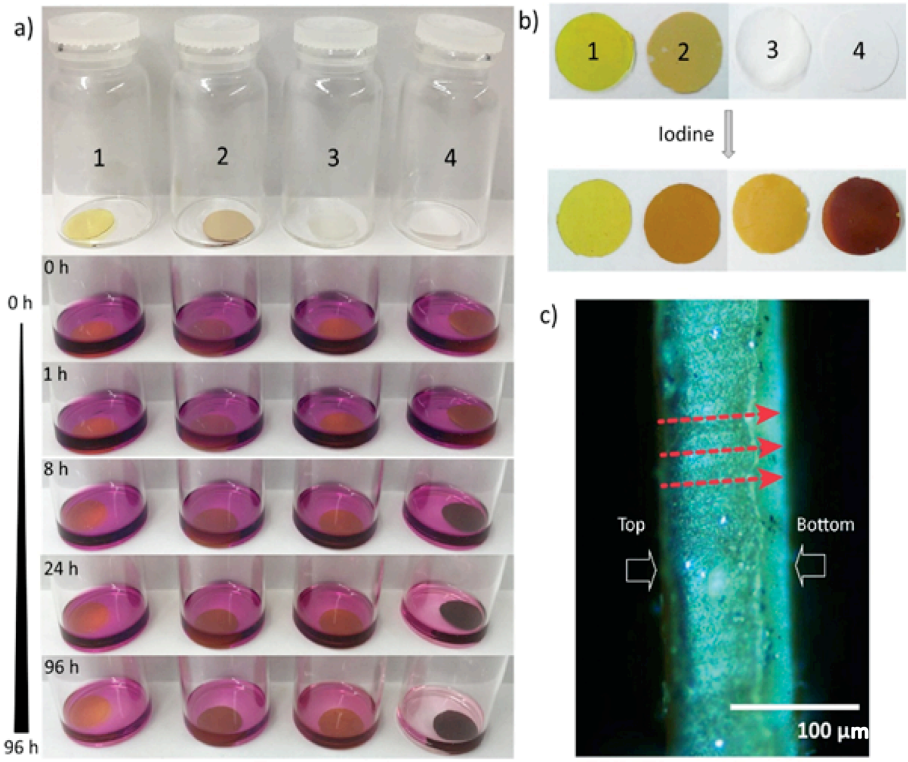

Fig. 6.1 Determination of I_2 adsorption characteristics in the polymer/MOF nanocomposites, (a) The time it took for the composites to absorb I_2 up to 96-hour exposure, where (1) Matrimid, (2) Matrimid/ZIF-8 30 wt.%, (3) PU, and (4) PU/ZIF-8 30 wt.%, (b) Nanocomposites before adsorption of I_2 (top) and after adsorption of I_2 (bottom), (c) Optical micrographs taken at the cross section of the PU/ZIF-8 30 wt.% nanocomposites, where the dotted arrows indicate the I_2 flow gradient entering the nanocomposites. The darker region corresponds to the top nanocomposite surface while the lighter region is the bottom surface (with respect to (a)). It can be seen that the mean nanocomposite thickness is ~100 µm.

Fig. 6.1 shows the vials containing the Matrimid and PU-based ZIF-8 nanocomposites, filled with I_2, at designated time intervals (0-96 hr), while Fig. 6.3 (a-c) shows the quantitative uptake capacity of the samples.

Prior to the experiments using I_2 (C_6H_{12}), the nanocomposite samples were weighed and subsequently immersed in C_6H_{12} solution for 96 hours (~1 ml). This control experiment was designed and conducted to check for the adsorbance of C_6H_{12} into the polymer and polymer/MOF nanocomposite samples. The samples were immersed in a hermetically sealed vials for 96 hours (similar to the samples immersed in the I_2 (C_6H_{12}) samples, and were later removed, had its surfaces thoroughly wiped with a paper towel, and left to dry for 20-30 minutes. After drying, the samples were weighed again, and the difference between the weight before and after the adsorbance of C_6H_{12} was compared. Table 6.1 details the results collected from the control experiment.

Table 6.1 The weight differential between pre-immersion and post-immersion of the nanocomposite samples for 96 hours in a C_6H_{12} solution (~1 ml). Two samples (S1 & S2) were tested per sample to check for repeatability of the experiments (See Appendix D.1 for experimental photographs).

Samples	$m_{\text{pre-immersion}}$ (g)	$m_{\text{post-immersion}}$ (g)	wt.% difference	mg g^{-1}
Matrimid (S1)	0.0206	0.0206	0	0
Matrimid (S2)	0.0203	0.0203	0	0
Matrimid/ZIF-8 30 wt.% (S1)	0.0268	0.0268	0	0
Matrimid/ZIF-8 30 wt.% (S2)	0.0230	0.0230	0	0
PU (S1)	0.0172	0.0172	0	0
PU (S2)	0.0173	0.0173	0	0
PU/ZIF-8 30 wt.% (S1)	0.0192	0.0192	0	0
PU/ZIF-8 30 wt.% (S2)	0.0190	0.0190	0	0

The lack of weight change of the nanocomposites, post-immersion and drying for 20-30 minutes, is taken as indicative of the fact that C_6H_{12} did not infiltrate and remained within

the nanocomposites. This could be attributed to the highly volatile nature of C_6H_{12} (boiling point of 80.74 °C and molecular weight of 84.16 g mol^{-1}) and also the big molecule size of C_6H_{12} (5.8-5.9 Å, exceeding the aperture opening of ZIF-8 molecules of 5.6 Å). The C_6H_{12} solutions are mostly concentrated on the surface of the polymers and the nanocomposites, as it is unable to infiltrate the material during immersion. Once it is removed from the C_6H_{12} solution, the remaining C_6H_{12} on the surface, after being wiped dry with a paper towel, will quickly evaporate, leaving the samples in pristine condition and at its weight pre-immersion. The large pores of the PU samples allow for the quick evaporation of the C_6H_{12}, while the densely packed Matrimid samples prevented the infiltration of C_6H_{12} in the first place, thus allowing for the quick evaporation of the volatile C_6H_{12} from its surfaces. The data presented in Table 6.1 and its accompanying explanations are indicative of the fact that the adsorbance observed in Fig. 6.1 can be conclusively attributed to I_2 molecules alone.

It can be seen in Fig. 6.1 (a) that the PU/ZIF-8 30 wt.% sample exhibited the most significant colour change associated with the adsorption of I_2 molecules after 96 h of adsorption experiments. After 96 h, the samples were removed, cleaned, and dried in open air, and photographed, as per Fig. 6.1 (b). The physical changes to the PU and PU-based nanocomposite seen in Fig. 6.1 (b) is rather pronounced, with PU exhibiting a yellowish tinge, while the PU/ZIF-8 30 wt.% membrane shows a deep purple tinge (Fig. 6.1(b)). The Matrimid-based samples, on the other hand, remained almost unchanged, while the loose ZIF-8 powders showed a similar deep purple tinge (see Appendix D.2). These physical changes are attributed to the adsorbance of the I_2 molecules by the samples. To confirm I_2 capture *within* the nanocomposite as opposed to mere surface coverage of I_2, the cross-section of the I_2-loaded nanocomposites were visually assessed (Fig. 6.1(c)). Optical images taken of the cross-section of the nanocomposite capturing the highest amount of I_2, i.e. PU/ZIF-8 30 wt.%, exhibited features suggestive of I_2-transport across the

nanocomposite's interior. The colour gradient in Fig. 6.1(c) indicates the direction of the flow of I_2, proving that I_2 was indeed absorbed by the nanocomposite as opposed to only being present on its surface. Notably, the top and bottom surfaces of the nanocomposites could be easily distinguished. It can be seen that the top surface that was exposed to I_2 exhibited a darker shade of purple, as opposed to the bottom surface of the sample. This differential colouration phenomenon elucidates that a concentration gradient is present in the nanocomposite, thus indicating that I_2 has infiltrated the nanocomposite but remained entrapped within as opposed to being filtered out.

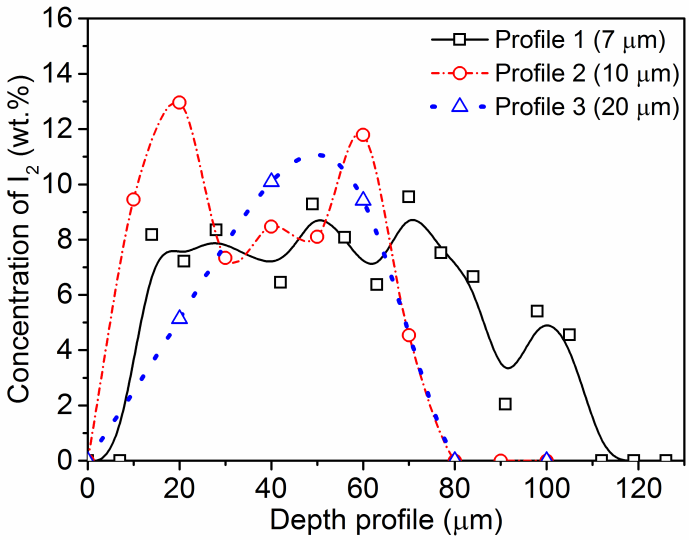

Fig. 6.2 The depth profile of the adsorption of I_2 in PU/ZIF-8 30 wt.% sample taken by the Energy Dispersive X-Ray (EDAX) apparatus. The depth profiles were taken as a wt.% of I_2 in the cross-section of the sample at intervals of 7, 10, and 20 μm (see Appendix D.3).

The Energy Dispersive X-Ray Analysis (EDAX) method was used to confirm the capture and retention of I_2 within the nanocomposites (see Fig. 6.2). Due to its perceived high uptake of I_2, the PU/ZIF-8 30 wt.% nanocomposite sample was utilised for this purpose; the sample was cleaned and freeze-fractured in LN_2, reminiscent of the cross-sectional imaging sample

preparation for FEG-SEM (see §3.3.1.1). The samples were then subjected to EDAX (Carl Zeiss Evo LS15 VP-Scanning Electron Microscope with an INCA X-Act-X-ray system) analyses at depth intervals of 7, 10, and 20 µm. The results showed high concentration of I_2 at depths of 20-80 µm (~8-13 wt.%), and lower concentrations of I_2 at 0-20 um (<~6 wt.%), and 80-120 um (<~6 wt.%), proving that indeed I_2 has infiltrated and was trapped inside the nanocomposites.

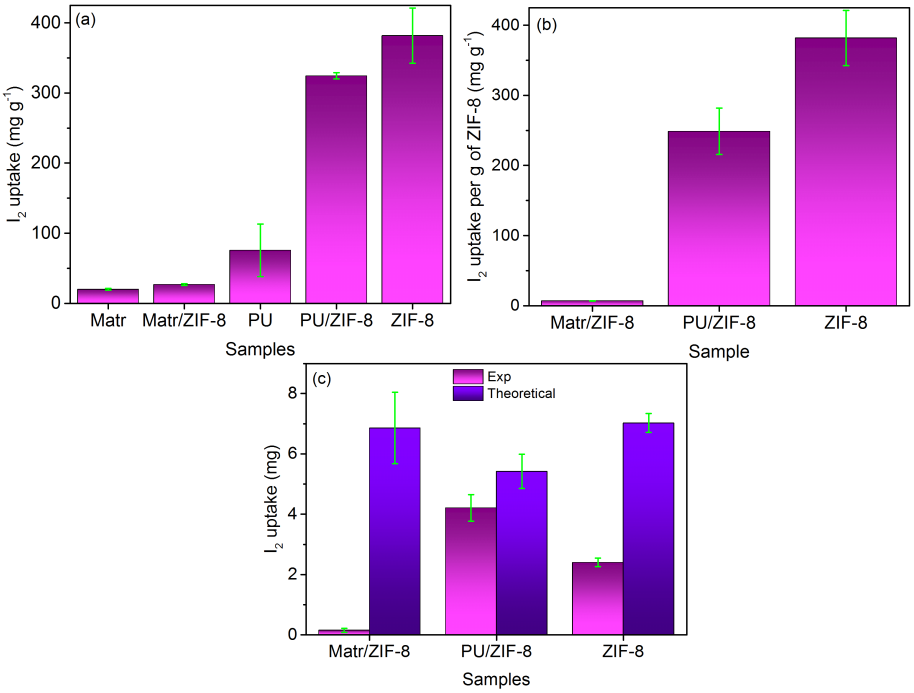

Fig. 6.3 Different modes of analyses for the uptake of I_2 by the samples, where (a) measures the I_2 uptake of the nanocomposites as a whole, (b) measures the uptake of I_2 by ZIF-8 and ZIF-8 *within* the nanocomposites (via subtraction of the uptake value of the matrix and its corresponding nanocomposites), and (c) comparison between the calculated uptake of I_2 by ZIF-8 and ZIF-8 *within* the nanocomposites (see Appendix D.4 for the calculations).

Fig. 6.3 (a) shows that the highest uptake of I_2 is by the ZIF-8 nanoparticles (~380 mg g^{-1}), followed by PU/ZIF-8 30 wt.% (~320 mg g^{-1}), PU (~75 mg g^{-1}), Matrimid/ZIF-8 30 wt.%

(~26 mg g^{-1}), and Matrimid (~20 mg g^{-1}). The I_2 uptake capacity of ZIF-8 exceeds that of zeolites, at 170 mg g^{-1}, and remains on par with activated carbon, at 300-400 mg g^{-1}.

The ZIF-8 nanoparticles are in direct contact with the I_2 solution (and molecules), which encourages the uptake of I_2 molecules by the ZIF-8 nanoparticles into its sodalite cages due to the ready accessibility of the ZIF-8 nanoparticles and the chemical affinity between the mIm ligands of the ZIF-8 nanoparticles and the I_2 molecules [244, 246]. The same explanation can also be extended to the PU/ZIF-8 30 wt.%, where the highly porous and accessible PU matrix allows for almost unhindered contact between the embedded ZIF-8 nanoparticles and the I_2 molecules. However, as pointed out previously, the I_2 uptake involves the formation of weak interactions between the mIm ligand of ZIF-8 and I_2 molecules, and the presence of secondary interactions between the polymeric chain of PU and mIm will result in a bond forming competition between I_2 molecules and the polymeric chains of PU. It is therefore reasoned that despite the close contact between the embedded ZIF-8 nanoparticles and the I_2 molecules, the I_2 uptake, in the case of PU/ZIF-8 30 wt.% sample, will not be as high as the ZIF-8 nanoparticle sample. However, this loss of I_2 uptake due to the competing bond formation between mIm and I_2 is offsetted by I_2 uptake via the PU matrix, as per Fig. 6.3 (a), which means that the formation of PU/ZIF-8 30 wt.% nanocomposite is acting in a synergistic manner when it comes to I_2 uptake. The exact opposite can be observed in the case of Matrimid, where its low accessibility and robust structure severely limits the uptake of I_2 molecules. Despite the affinity of ZIF-8 and I_2 molecules, the dense structure of Matrimid curtailed the contact between I_2 molecules and ZIF-8, which results in very poor I_2 uptake, as seen in Fig. 6.3 (a).

The previous discussion and the experimental values calculated in this work points to the fact that the I_2 uptake is significantly dependent upon the presence of ZIF-8 nanoparticles and its accessibility to the guest species that are to be captured (in this case, I_2 molecules).

Despite the importance of the ZIF-8 nanoparticles, the matrices play no less of an important role in the uptake of guest species, where it provides a robust and deliverable support structure for the ZIF-8 to function without being exposed to factors that are structurally detrimental to it (heat, moisture, etc., see §2.2.4). In order to further probe the uptake of I_2 molecules within the nanocomposite, Fig. 6.3(b) shows the I_2 molecules uptake by the ZIF-8 nanoparticles embedded within the nanocomposite only (PU/ZIF-8 30 wt.% and Matrimid/ZIF-8 30 wt.%). These values are compared to the uptake reported by the loose ZIF-8 nanoparticles. The uptake value was obtained by subtracting the I_2 uptake of the nanocomposite with the I_2 uptake of its corresponding matrix, which (presumably) results in the I_2 uptake by the ZIF-8 nanoparticles only. ZIF-8 reported the highest uptake, at ~380 mg g^{-1}, followed by the PU/ZIF-8 30 wt.% sample, at ~250 mg g^{-1}, and Matrimid/ZIF-8 30 wt.% sample, at ~7 mg g^{-1}. The uptake of loose powder ZIF-8 was explained previously. In the case of the PU/ZIF-8 30 wt.% sample, the I_2 uptake by the embedded ZIF-8 nanoparticles accounts for ~77 %, with the other ~23 % is attributed to the PU, showing that the contribution of the PU matrix towards the total adsorption of I_2 in this case is quite significant. This significance is further evident in the Matrimid/ZIF-8 30 wt.% sample, where the I_2 uptake contribution by the embedded ZIF-8 nanoparticles hovers at ~25%, and the rest (75%) of the uptake is attributed to the Matrimid matrix. The mechanisms of adsorption pertaining to the nanocomposites will be detailed in §6.5.

Fig. 6.2 (c) compares the theoretical calculated values of the I_2 uptake by the ZIF-8 within the nanocomposites (Matrimid-based and PU-based) and the ZIF-8 loose powder. The calculations pertaining to these values are detailed in Appendix D.4. There are a few assumptions being made in the course of these calculations, which are:

i) The number of ZIF-8 nanoparticles within the nanocomposites are assumed to be perfectly and homogenously distributed throughout the matrix, with the weight of the ZIF-8 nanoparticles closely matching that of its purported content.

ii) Perfect contact and surface interactions between each and every ZIF-8 nanoparticles and I_2 solution.

The difference between the calculated and the experimental values of the I_2 uptake is rather stark, with the exception of the PU/ZIF-8 30 wt.% sample. The different values in the Matrimid/ZIF-8 30 wt.% sample (0.15 mg (experimental) *vs*. 7 mg (theoretical)) can be explained by the fact that the theoretical calculations of the I_2 uptake assumes that *all* of the I_2 solution are in contact with the embedded ZIF-8 nanoparticles, which translates into the maximum uptake of I_2 molecules. However, it should be pointed out that this represents an ideal situation, where the Matrimid matrix is readily accessible, which it is not in this case. In fact, its accessibility is severely restricted due to the robust and rigid nature of the Matrimid matrix, which accounts for the much lower I_2 uptake than what was predicted by the theoretical calculations. In reality, a significant portion of the I_2 uptake in the case of Matrimid/ZIF-8 30 wt.% nanocomposite is attributed to the matrix instead of the ZIF-8 nanoparticles. The theoretical I_2 uptake values for the PU/ZIF-8 30 wt.% sample is much closer to the experimental values (5.4 mg (theoretical) *vs*. 4.2 mg (experimental)), which can be attributed to the open accessibility of the PU matrix and the close contact between the ZIF-8 nanoparticles and the I_2 solution, maximising the uptake of I_2. This represents a scenario that is as close to an ideal situation, where the polymer matrix and the MOF act in tandem to adsorb I_2 molecules, and any reduced I_2 uptake due to imperfection of the MOF nanoparticles is offsetted by the polymer matrix. The major discrepancy between the calculated values of the ZIF-8 nanoparticles uptake and the experimental I_2 uptake values (7

mg (theoretical) vs. 2.4 mg (experimental)) can be explained by the fact that as per assumption ii) in this calculation, each and every one of the nanoparticles are open and accessible, which is not exactly the case in real experimental conditions involving loose nanoparticle(s) powder. Agglomeration and aggregation would be a major problem for nanoparticles, even after extensive drying and grinding, which limits the open accessibility of the ZIF-8 nanoparticles *vis-à-vis* the I_2 solution. The (significantly) lowered accessibility of the ZIF-8 nanoparticles accounts for the significantly lowered I_2 uptake compared to the calculated I_2 uptake values. The problem of agglomeration and aggregation is less of an issue in the nanocomposites, as the formed nanocomposite solution kept the nanoparticles suspended in a polymer solution prior to casting, which minimises the chances of agglomeration. Once the nanocomposite solution was casted and dried, the ZIF-8 nanoparticles were set in place, and its bonds with the polymeric chains and the rigidity of the internal matrix structure minimises the chances of (internal) agglomeration, thus maximising its contact with the I_2 solution (if the matrix is openly accessible). This reduced contact and closed access to the porosity of parts of the ZIF-8 nanoparticles accounts for the severely lowered uptake of I_2 seen in Fig. 6.3 (c). It should be pointed out that Hughes *et al.* [246] reported that ZIF-8, as a loose powder, is capable of capturing and retaining up 125 wt.% of I_2 (25 wt.% at the surface of the ZIF-8, and 100 wt.% in the sodalite cages of ZIF-8) *via* mechanisms such as physisorption and chemisorption, assuming ideal conditions, which means that if 5 mg of ZIF-8 nanoparticles are used, the uptake of I_2 molecules would be 6.25 mg.

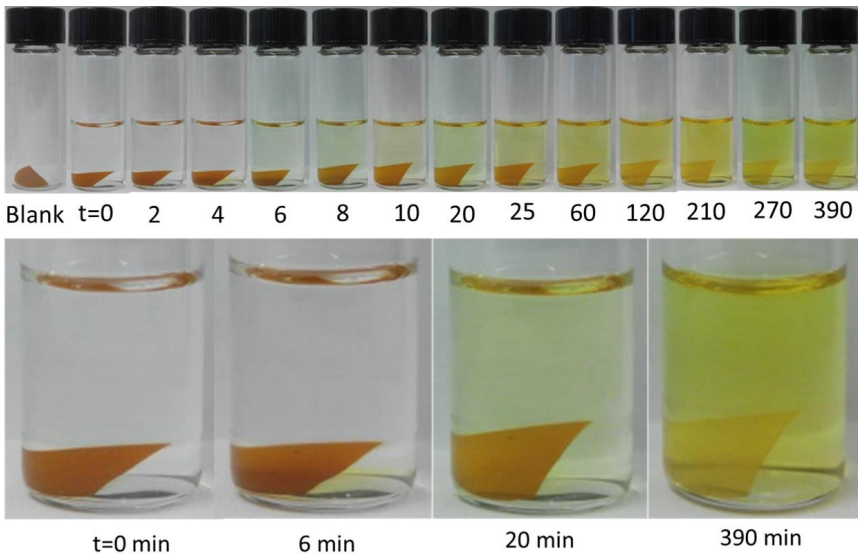

Fig. 6.4 Iodine release was investigated by monitoring the change in the colour of ethanolic solution in I_2-loaded PU/ZIF-8 30 wt.% at different time points. Since the polymer matrix in nanocomposite decreased accessibility to the high surface area of ZIF-8 pores, I_2 release in ethanol was observed to slow down and remained virtually unchanged beyond 6.5 hr (see Appendix D.5).

The I_2 release characteristics was examined by monitoring the change in colour of the solution, where I_2-loaded PU/ZIF-8 30 wt.% nanocomposite was immersed and hermetically sealed. The polymer matrices, as discussed previously, decrease accessibility to the high surface area of ZIF-8 nanoparticles, which extended the I_2 release time (beyond 6.5 hr), relative to the case of (loose) MOF powders, where a substantial release of captured I_2 was reported after only two hours [247]. Furthermore, the hydrophobicity of the polymer matrices prevented access of polar solvents to the nanoporosity of the ZIF-8 nanoparticles, allowing the nanocomposites to retain I_2 within its microstructure. This was proven by immersing the I_2-loaded PU/ZIF-8 30 wt.% into water, and after a period of 10 days (see

Appendix D.5), there were no colour changes detected in the surrounding water, signifying that I_2 remained immobilised. Importantly, this result shows that despite the affinity of I_2 towards polar solvents (e.g. water), the desorption of I_2 can be suppressed by encapsulating them within a polymer/MOF nanocomposite where the matrix is an intrinsically hydrophobic phase. It was reasoned that the complex microstructure of the nanocomposites (see Figs. 4.2 (a, d) & 5.1(a, d)) further prevented open access to the adsorption sites located inside the sodalite cages of ZIF-8 [233], such that the absorbed I_2 can remain immobilised within the nanocomposite.

6.3 Nanoindentation studies

The nanoindentation technique was used to characterise the nanomechanical properties of the polymers and their corresponding nanocomposites pre-and post-I_2 adsorption. The results are summarised in Fig. 6.5.

The application of the nanoindentation technique is a practical choice: the nanoindentation technique makes measured indents onto minute areas of the surface of the samples at controlled depths (up to ~2 μm) [109], enabling it to interrogate the delicate surface regions where the ZIF-8 nanoparticles, the polymer matrices (Matrimid and PU), and incidentally, the absorbed I_2, are actually interacting. For the polymer matrices, this translates into probing the surface where the polymeric chains and I_2 are interacting. This method will allow us to measure relatively small mechanical property differences, more precisely capturing the change in Young's modulus (elastic stiffness) and hardness (resistance against plastic deformation) of the ZIF-8 nanocomposites due to its adsorption of I_2.

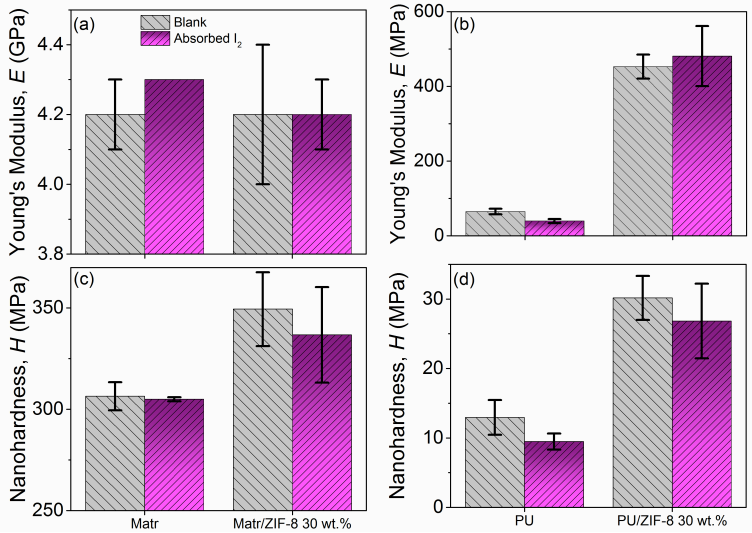

Fig. 6.5 Nanoindentation results of the Matrimid and PU-based nanocomposite nanocomposites. (a & b) Young's modulus of Matrimid-based and PU-based nanocomposites, respectively. (c & d) Nanohardness of Matrimid-based and PU-based nanocomposites, respectively. Note that glassy Matrimid matrix (whose T_g > room temperature, RT) is significantly stiffer and harder than the rubbery matrix of PU (T_g < RT). Specifically, for the blank samples, it was surmised that the fall in the Young's modulus of Matrimid/ZIF-8 30 wt.% compared with pristine Matrimid is associated with the incorporation of the ZIF-8 fillers ($E_{ZIF\text{-}8}$ ~3 GPa) [33], which are more compliant than the Matrimid phase; this effect has been explained in detail in §4.3. The nanoindentation data shown here were averaged from a surface penetration depth ranging 1 - 2 μm (see Appendix D.6).

Fig. 6.5 (a) and (c) show that the nanomechanical properties of the Matrimid-based nanocomposites are only slightly affected by the adsorption of I_2. This is reflected by the fact that the Young's modulus (E) differs by ~2% for Matrimid and no change was detected for its nanocomposite samples. While for the nanohardness (H) values, the error bars for

both samples are within range of each other, implying that the amount of I_2 absorbed by the Matrimid-based nanocomposites are relatively small (all changes falls under the ~5% range) *vis-à-vis* the nanomechanical properties. The glassy nature of the Matrimid matrix at room temperature (Matrimid glass transition temperature, T_g ~345 °C) [156] is important and may account for this outcome. It is envisaged that the molecular packing and rigidity underpinning the polymeric chains of Matrimid form an interconnected network that is sufficiently dense, thereby preventing the infiltration and uptake of I_2 guest molecules. It was found that introduction of ZIF-8 nanoparticles (fillers) into Matrimid, despite its expected disruption to the molecular packing of Matrimid (§4.2), in fact did little to boost the overall I_2 uptake capacity; thus its marginal impact on the nanomechanical properties of Matrimid-based nanocomposites.

However, a different trend was observed in the PU-based nanocomposites (Figs. 6.5 (b) & (d)). It is seen that the Young's modulus (E) and nanohardness (H) values changed by a discernible amount for neat PU (-25.5 MPa, corresponding to ~40% drop for E, and -3.5 MPa for H, corresponding to a drop of ~27%); and PU/ZIF-8 30 wt.% (28 MPa for E, corresponding to an increase of ~6%, and 3 MPa for H, corresponding to a decrease of ~11%) post-I_2 adsorption. It should be pointed out that unlike in neat Matrimid, the nanomechanical properties in the neat PU sample displayed a contradictory behaviour where E and H values declined with adsorption of I_2. This softening effect is speculated to be due to pervasiveness of I_2 into the hard and soft segments of PU (Fig. 3.4), which increased the interatomic distance between the polymeric chain, thus weakening the inter-and intra-molecular bonding interactions, and affecting its structural integrity [43]. It was also proposed that the looser molecular packing of the rubbery PU polymeric chain (T_g < RT) and nominal molecular attachment of the ZIF-8 to the PU matrix accounted for increased adsorption of I_2 into the PU/ZIF-8 30 wt.% nanocomposite, due to increased accessibility to

ZIF-8 nanoparticles. The infiltration and I_2 uptake within the ZIF-8 nanoparticles will be assisted by the size of the porous cages of ZIF-8 [164] (11.4 Å, and aperture size of 5.6 Å against the size of I_2 molecule of 5.6 Å), if the (loosely packed) rubbery polymer chains may provide an open pathway to reach the ZIF-8 pores, thereby boosting total I_2 uptake (see Fig. 6.2). Our results show that, for the PU/ZIF-8 30 wt.% nanocomposites upon I_2 adsorption, there is no major variation detected in *E* and *H*, both of which appear to be within the respective statistical errors.

6.4 Thermogravimetric analyses (TGA) of the I_2-absorbed nanocomposites

Fig. 6.6 shows the TGA profiles of the absorbed nanocomposites and their blank counterparts. It is seen from Fig. 6.6 (a)-(b) that the adsorption by the Matrimid-based nanocomposites is almost negligible, as the profile of the absorbed sample is almost identical to the blank sample, with almost minute variations throughout the thermal decomposition profile.

On the contrary, as per Fig. 6.3 (a), there is a marked increase in I_2 uptake (320 mg g^{-1}) in the PU/ZIF-8 30 wt.% sample, which is also reflected in the thermal decomposition profile of PU and PU-based nanocomposites. For PU, at ~210 °C, the I_2-loaded composite began decomposing. This is speculated to be due to the initiation of thermal degradation of organic ligands, and with PU molecular structure degradation, the I_2-bonded to the soft segment of the PU polymeric chain is being released. It should also be pointed out that the flash point of I_2 is at 184.3 °C; however, I_2 only began evaporating from PU at 210 °C, meaning that host-guest interactions from being entrapped in PU are shielding I_2 from evaporating at its characteristically lower flash temperature. It was proposed that only when the chain integrity

of PU was compromised that I_2 was exposed to surrounding thermal conditions, thus triggering its evaporation.

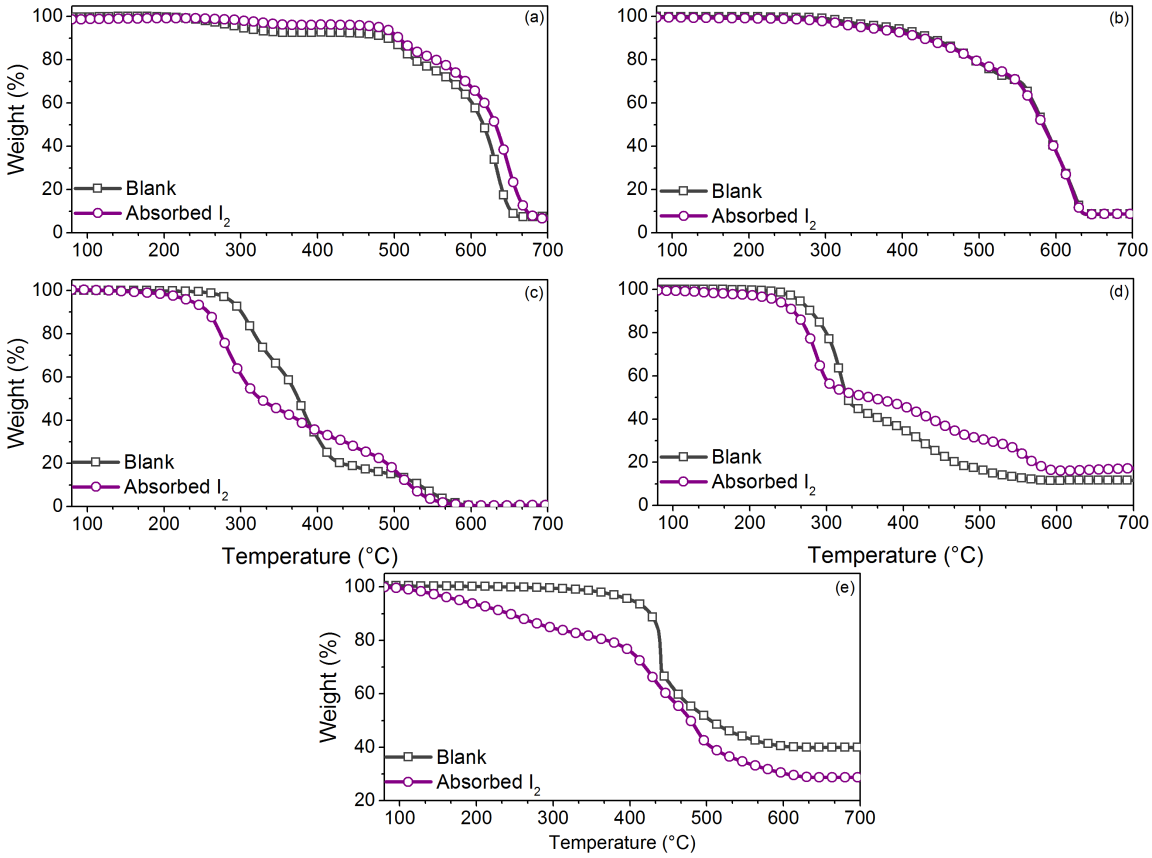

Fig. 6.6 TGA plots of the (a) Matrimid, (b) ZIF-8/Matrimid 30 wt.%, (c) PU, and (d) PU/ZIF-8 30 wt.%, (e) ZIF-8 with their respective blank counterparts. For an overall combined plots of TGA, including the ZIF-8 nanoparticles, see Appendix D.7.

The thermal decomposition of the I_2-loaded sample was more rapid compared to its blank counterpart. The decomposition of the hard segment of the PU appeared to begin at 310 °C for the I_2-loaded sample, which is earlier than the blank sample, where it began decomposing at 405 °C. The reason for this is that the I_2 loaded sample has formed an intrinsic part of the microstructure of the PU, and once I_2 began to be liberated from the hard segments (Fig. 3.4) due to structural degradation from the soft segments, the structural integrity of the hard

segment begins degrading as well, in conjunction with released I_2. A similar trend was observed in the PU/ZIF-8 30 wt.% nanocomposite, where thermal decomposition of the loaded composite began a lot sooner than the blank nanocomposite, however, it is unique in that I_2 is released from the decomposed soft segment of PU and decomposing ZIF-8 (~350 °C). Fig. 6.1 suggest that I_2 is absorbed into ZIF-8 cages as well as the soft and hard segments of PU. Upon thermal decomposition of the PU, ZIF-8 nanoparticles are exposed, and the organic ligands forming bonds with I_2 and the hard segment of PU will began decomposing, releasing I_2 and breaking the chemical and physical interactions formed with PU.

The phenomenon surrounding the release of I_2 from ZIF-8 cages is obvious in Fig. 6.6(d), where from 300-550 °C, the I_2-loaded samples were decomposing at a rate that is slower than its blank counterpart. This can be attributed to the entrapped I_2 in the ZIF-8 cages being released as the ZIF-8 cages are collapsing due to thermal decomposition [246]. At 550 °C, when I_2 was completely removed, a sharp drop was observed in the wt.% of the nanocomposites. Subsequently at 600 °C, its thermal decomposition profile matched that of its blank counterpart, showing that all the entrapped I_2 was indeed removed from both PU and ZIF-8. What is important to establish here is that, by comparing Fig. 6.6(c) to (d), there is strong evidence supporting the notion that thermal stability of the I_2-absorbed PU/ZIF-8 nanocomposite has significantly improved as a consequence of guest immobilisation.

6.5 Proposed mechanism responsible for I_2 adsorption and immobilisation in polymer/MOF nanocomposites

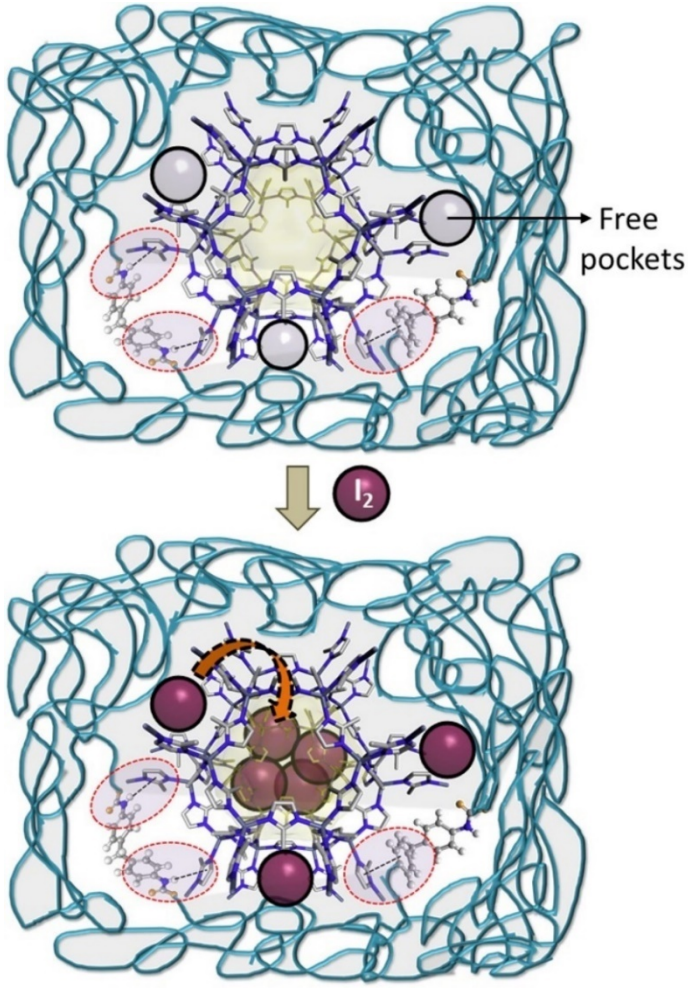

Fig. 6.7 The proposed I_2 adsorption mechanism by the polymer/MOF nanocomposite (PU/ZIF-8 30 wt.% in this case). The introduction of ZIF-8 nanoparticle within the polymer matrix offer porosity, attributed to intrinsic sodalite cages of ZIF-8 (filler phase) and free volumes arising from disruption of the molecular packing of the nanocomposite by the nanoparticle fillers. Both voids could serve as active sites, attracting I_2 molecules and forming bonds with the mIm ligands of ZIF-8, and the 'hard' and 'soft' segments of the PU (see Fig. 3.4) or the active coordination sites present in Matrimid (see Fig. 4.9).

Fig. 6.7 illustrates the proposed adsorption mechanism that explains I_2 uptake and retention by the polymer/MOF nanocomposites in this work. The high surface area of ZIF-8 nanoparticles (~1650 m^2 g^{-1}) [80] are expected to offer significant amounts of active sites to afford the adsorption of I_2 molecules [248], mostly *via* combined actions of chemisorption [246] and physisorption [233], predicated upon the accessibility of the polymer matrices. However, the *retention* of the adsorbate (I_2 molecules in this case) is significantly strengthened by the polymer matrices. Therefore, it can be surmised that the capture and immobilisation of I_2 molecules within the nanocomposite is the result of a synergistic effect between the polymer matrices and ZIF-8 nanoparticles. Both polymers (Matrimid and PU) exhibited almost negligible I_2 uptake (Fig. 6.3 (a)), and the high uptake exhibited by the nanocomposites are attributed to the I_2 molecules entering the pores of the (accessible) ZIF-8 nanoparticles instead of the free volume within the polymers formed by the presence of the nanoparticles. However, the presence of functional groups and aromatic moieties in both Matrimid and PU are potential sites for the weak molecular interactions with I_2 molecules, therefore, the possibility of I_2 storage within inter-polymer/MOF pockets (free volume) cannot be completely ruled out. This supposition is further strengthened by the uptake values demonstrated by the polymer matrices, as per Fig. 6.3 (a), where PU reported an I_2 uptake of 75 mg g^{-1}, while Matrimid reported an I_2 uptake of 20 mg g^{-1}. It is therefore more accurate to assume that the I_2 uptake mechanism of the nanocomposite, in this case, involves the synergistic affect between the ZIF-8 nanoparticles and the polymer matrices, acting in tandem to capture and guide the I_2 molecules to active sites (such as mIm ligands of ZIF-8 nanoparticles or the aromatic moieties of Matrimid and hard groups of PU), where the I_2 molecules can form a collection of weak bonds for it to be immobilised within the structure of the nanocomposites. The presence of these unoccupied pockets could also potentially serve as active molecular flexible pathways that allow for the I_2 to infiltrate the

composites and guide the I_2 molecules towards the more active and high-surface area ZIF-8 nanoparticles cages.

Fig. 6.7 details the plausible molecular level interactions between I_2, ZIF-8, and the polymers (PU in the diagram) in the PU/ZIF-8 nanocomposite system. The light yellow spheres indicate the Solvent Accessible Volume (SAV) of ZIF-8 nanoparticles, while the black circles represent the inter-polymer/ZIF-8 pockets. These free volumes could be of large and small dimensions, which is incidentally not necessary for strong interactions with I_2 when compared to the continuous array of ordered active voids of the ZIF-8 nanoparticles. Smaller volume voids with higher surface area may result in stronger nanoscale confinement with incoming foreign guest species, such as I_2 molecules. The theoretical uptake of I_2 molecules as per the number of ZIF-8 nanoparticles and the influence of free volume in the polymer matrices in this case is elucidated in Fig. 6.3 (c). This effect could be investigated in greater detail by means Positron Annihilation Lifetime Spectroscopy (PALS) [80, 249].

Furthermore, comparing the chemical structures of the polymer matrices could provide additional insights into their potential role in the capture and retention of I_2 within ZIF-8 polymer nanocomposites. PU is made up of amide linkages that are suitable for non-covalent interactions, while its flexible ether moiety could potentially provide sites for strong interaction and catalyse molecular dynamics within the matrix that improves small guest molecular mobility. However, in the case of Matrimid, its rigid aromatic backbone could potentially hinder the formation of inter-polymer/ZIF-8 pockets *via* its strong interchain aromatic interactions.

It is clear from our experimental data that the PU samples are more effective for I_2 uptake compared to the Matrimid samples. It was reasoned that the intrinsic porosity of PU and its ability to interact with guest species *via* weak interactions could explain these differences.

Molecular flexibility of the PU's primary chain allows for entropic dynamics of its rubbery structure to capture I_2 more rapidly. On the contrary, tightly packed structural configurations, which is especially prevalent in (glassy) Matrimid could result in a lower accessible surface area, rendering them less effective for I_2 immobilisation. The introduction of ZIF-8 nanoparticles into both polymer matrices will create strong "anchoring sites" and increase the free volume (due to disruption to molecular packing) that will enhance the resulting nanocomposites' capacity to immobilise I_2. On this basis, the model proposed in Fig. 6.7 represents the most probable capture and storage mechanism for the Matrimid/ZIF-8 30 wt.% and the PU/ZIF-8 30 wt.% nanocomposites studied in this work.

6.6 Chapter summary

This chapter detailed a pioneering attempt of capturing and retaining I_2 within the nanocomposites reported in Chapters 4-5. The detailed experiments and its subsequent results allowed us to demonstrate the viability of the polymer/ZIF-8 as an I_2 adsorption and retention medium. The next chapter will detail our endeavours of using the same polymer/MOF nanocomposites to study its viability for the reversible uptake of C_2H_4 (gas).

CHAPTER SEVEN

Reversible uptake of ethylene (C_2H_4) in polymer/MOF based nanocomposites

The previous chapter carefully analysed and subsequently confirmed the viability of the polymer/ZIF-8 nanocomposites for the capture/retention of I_2, and it was determined that the affinity of I_2 with ZIF-8, its narrow apertures, and the open accessibility of the PU matrix are crucial towards its ability to capture and retain I_2. This chapter intends to explore another application with the polymer/ZIF-8 nanocomposites; the reversible uptake of ethylene (C_2H_4) gas. The capability of polymer/MOF nanocomposites to capture and separate common gases or gas mixtures (CO_2, O_2, H_2, N_2) are very well documented in literature (see §2.4.1), and the consensus is that the presence of MOFs, as fillers, endows the subsequent composites with this ability due to its chemical affinity with the gases, its inherent porosity, and ready accessibility. However, studies involving the uptake of more exotic gases (hydrocarbons), such as ethylene (C_2H_4), is scarce in the context of MOF-composites, and as such, the neat matrices (Matrimid and PU) and their corresponding ZIF-8 nanocomposites (30 wt.%) will be utilised to confirm the viability and enhancements brought about by the introduction of the ZIF-8 nanoparticles *vis-à-vis* the reversible uptake of C_2H_4. This investigation is a collaborative effort with Dr J. Silvestre of the Department of Inorganic Chemistry of the University of Alicante, Spain.

7.1 Rationale

The general characteristics of MOFs, such as its inherent porosity, specific aperture sizes, and large surface areas (>1000 m^2 g^{-1}) makes it a prime candidate for the capture and separation of a wide variety of gases, ranging from atmospheric ones (O_2, N_2, H_2, CO_2) to hydrocarbons (C_2H_6, C_2H_4). This viability is further enhanced by the fact that MOFs are customisable, making it possible to produce bespoke MOFs that would respond to specific guest species *via* the tuning of its porosity, aperture, and cage sizes. As a matter of fact, there is abundant literature on the utilisation of MOFs for gas capture and separation applications, as detailed in §2.4.1.

It is well established in literature that ZIF-8 has a high chemical affinity towards CO_2, and as such, has been used for applications involving the capture and separation of CO_2 from gas mixtures [250, 251]. However, recent works explored the usage of MOFs in general, and ZIFs in particular, for the capture and separation of hydrocarbons [126, 252]. This alternative was explored due to the fact that the common separation technique for alkane/alkene (light hydrocarbon), for example, is cryogenic distillation, which is a cost and resource intensive process. Intrinsically porous materials that are readily accessible to guest species (gas molecules), such as MOFs, represents a more effective and cheaper alternative for the capture and separation of hydrocarbons in this case due to its mechanism of passive adsorption via readily accessible porosity and chemical affinity, and desorption *via* induced pressure and varied temperature.

The high surface area (1650 m^2 g^{-1}), intrinsic porosity, and the accessibility of ZIF-8 (SAV ~ 0.5) render it an ideal candidate for the capture and separation of light hydrocarbons (C1-C4 hydrocarbons). Bux *et al.* [253] reported that ZIF-8 is capable of separating ethene/ethane at selectivities of 2.8 and 2.4, respectively, owing to its aperture size (~5.6 Å)

and the accessibility that aperture size afforded the sodalite cages (11.6 Å), while Bohme *et al*. [254] reported that ZIF-8 is more selective towards ethane over ethene. The suitability of ZIF-8 in general *vis-à-vis* the separation of certain hydrocarbons species (ethylene, ethane, for example) is quite well documented in literature.

It is therefore reasoned that the excellent ability of ZIFs in general and ZIF-8 in particular to capture and separate hydrocarbons would also extend to its corresponding composites, as per the previous chapter in the case of I_2. Exploring the usage of ZIFs for gas capture and separation has been a continuous endeavour alongside the discovery and development of ZIF-based composites [153, 255]. It can also be argued that the advent of ZIF-composites further benefitted gas capture and separation; the previously delicate and fragile ZIFs can now be utilised as it comes under the purview of a more robust composite system that mitigates the effect of elevated temperatures or pressures (see Chapters 4-5). The unique ability of ZIFs and ZIF-composites to capture and retain gases is applicable to a vast array of technological applications, such as food/material packaging [256], air system filtrations [257, 258], and electrolytes in solar cells [259] (see Chapter 2). The unique features espoused by ZIFs render them immensely effective for these applications, and it is envisaged that the presence of ZIFs within a structurally stable system (i.e. MOF-composites) would result in substantial performance improvements, as detailed in §2.4. Thus far, the most comprehensive published work dealing with the viability of polymer/MOF composite in the *uptake* of hydrocarbon is Bachman *et al*. [134], who used the combination of M_2(dodbc) (M = MOF-74 and CPO-27; dodbc = 2,5-dioxido-1,4-benzenedicarboxylate) and 6FDA-DAM to form a composite for C_2H_4 capture. They reported C_2H_4 capture of 3-5 mmol g^{-1}. The prevalence of other works involving polymer/MOF composite, or any form of MOF-composite for the reversible uptake of C_2H_4 or any other hydrocarbon is *noticeably*

absent from literature, with most published works detailing the viability for the MOFs to efficiently separate mixed-hydrocarbon gases.

The capability of polymer/MOF nanocomposites to reversibly uptake hydrocarbons render it applicable for the controlled uptake and release of gas species. In this vein, the previously developed polymer/MOF nanocomposites will be tested as a packaging material for the transport of food items, especially fresh produce. Food packaging and transport takes place in a controlled environment to ensure undiminished quality. It also helps prevent the growth and propagation of harmful bacteria and microbes, which would inevitably result in economic loss, or even endanger human health should it go undetected and the product subsequently consumed. In some cases, specific gases (such as C_2H_4) are used to accelerate the ripening process [260, 261], making the product more palatable. The transportation of fresh produce takes place in a span of a few days (or more), and utilising packaging materials that can be externally controlled *via* parametric manipulation (temperature and pressure) will allow us to tune the dosage of C_2H_4 released to the products to accelerate/decelerate the ripening process, serving as a form of quality control. The utilisation of a packaging that is able to reversibly capture C_2H_4 would be most suitable for this purpose.

The robust constitution of Matrimid/ZIF-8 nanocomposites (Chapter 4) and ease of accessibility of the PU/ZIF-8 nanocomposites (Chapter 5) render both suitable for the reversible uptake of C_2H_4. A detailed investigation was made into this phenomenon using the polymer/ZIF-8 nanocomposites reported in the previous chapters and the methods outlined in §3.5. The viability of the polymer/ZIF-8 nanocomposites as packaging material for the transport and ripening of fresh produce *via* controlled exposure to C_2H_4 is expected, which would be especially beneficial to the design of a passive packaging and transportation system for fresh produce that would reduce the economic cost while preserving quality. The

work detailed in this chapter represents a pioneering attempt to quantify the *reversible uptake* of C_2H_4 by a polymer/MOF nanocomposite.

7.2 Reversible uptake of C_2H_4 (5 °C)

Fig. 7.1 shows the adsorption/desorption plots of C_2H_4, as a function of pressure, of ZIF-8 nanoparticles and the corresponding polymer/MOF nanocomposites (Matrimid/ZIF-8 30 wt.% and PU/ZIF-8 30 wt.%) at 5 °C.

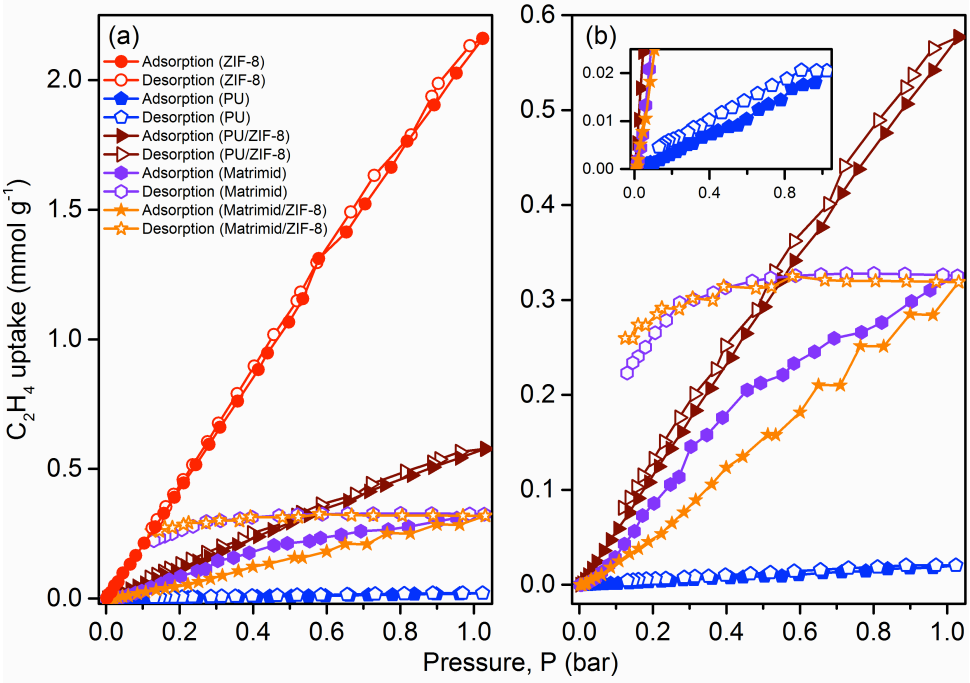

Fig. 7.1 The adsorption/desorption plots for C_2H_4 (5 °C) as a function of pressure for (a) ZIF-8 nanoparticles, Matrimid, PU, Matrimid/ZIF-8 30 wt.%, and PU/ZIF-8 30 wt.%, and (b) the polymer/MOF nanocomposites (30 wt.%).

The reversible uptake of ZIF-8 nanoparticles is relatively high, at ~2.2 mmol g^{-1}, where it can be seen that the adsorption/desorption plots are practically overlapping. The obvious

affinity for C_2H_4 towards ZIF-8 can be attributed to the readily accessible porosity of ZIF-8 (SAV~0.5) [32] and its high reactive surface area (~1650 m^2 g^{-1}) [80], both of which help maximise the exposure of ZIF-8, and its eventual uptake of C_2H_4 *via* its apertures and mIm ligands (forming a collection of weak interactions between the gas molecules and mIm ligands [233, 246]) of the ZIF-8 nanoparticles (see Fig. 4.9). The proposed reversible uptake mechanism gives way to speculation that increased amounts of ZIF-8 nanoparticles would result in increased uptake of C_2H_4 gas molecules. However, it should also be pointed out that the ZIF-8 nanoparticles tested in this study were in the form of fine powder, and its applicability and deliverability for gas sorption application remains impractical [262].

Fig. 7.1(b) shows the adsorption/desorption plots of the polymer/MOF nanocomposites as a function of absolute pressure. Matrimid exhibited a larger hysteresis (~0.31 mmol g^{-1}) compared to PU (<0.1 mmol g^{-1}). This phenomenon can be explained by the structural makeup of both polymers; Matrimid is a glassy polyimide with a rigid and robust internal structure, while PU is a rubbery polymer with soft and hard segments that grants it structural flexibility, malleability, and ease-of-processability. The glassy structure of Matrimid at 5 °C remains rigid, with its main polymeric chains exhibiting controlled vibrations (limited to bond bending and stretching along the bond length), due to the T_β of Matrimid being 80 °C ($T < T_\beta$). C_2H_4 gas molecules will have to penetrate and negotiate its way through a dense network of tightly bound polymeric chains to infiltrate Matrimid (see Fig. 4.9), which is immensely difficult, explaining the limited uptake of C_2H_4, at ~0.31 mmol g^{-1}. However, the rigid internal structure of Matrimid resulted in an unexpected benefit: The C_2H_4 gas molecules that successfully infiltrated the structure would be difficult to remove due to the severely limited possible escape routes from the heavily intertwining polymeric chains. As a result of this, the desorption plot of Matrimid in Fig. 7.1 (b) remained constant at ~0.3 mmol g^{-1} for quite some time, which implies that the majority of the adsorbed C_2H_4 gas

molecules are actually trapped within the nanocomposite, a phenomenon that can be termed a *semi-reversible* uptake (large hysteresis).

The structural makeup of the PU drastically differs from that of Matrimid. While Matrimid is glassy and rigid, the PU is soft and pliable. Also, the experiment, carried out at 5 °C, is 20 °C higher than the T_g of PU (-15 °C), where the main polymeric chain of the PU (soft and hard segments) will be mobile and constantly reorienting itself into the most favourable energy configuration (see §5.5). While it was difficult for the C_2H_4 gas molecules to penetrate and negotiate its way around Matrimid, this is not the case for the PU nanocomposites. However, this purported benefit is nullified by the constantly reorienting chains and open access pores of the PU nanocomposites: despite the ease of infiltration, the weak affinity between the main chain of the polymeric membrane and its open accessibility prevents it from *retaining* C_2H_4 within its structure (no hysteresis). This is reflected in the reversible uptake of C_2H_4 gas molecules, at < 0.1 mmol g^{-1}. It can therefore be surmised that the PU, on its own, makes for a very poor packaging material due to its greatly reduced reversible uptake capacity of C_2H_4.

The formation of ZIF-8 nanocomposites with Matrimid and PU as its matrices induced internal structural changes that were detailed in Chapters 4-5. The presence of ZIF-8 nanoparticles within the nanocomposites resulted in varying degrees of reversible uptake *vis-à-vis* C_2H_4. It is clear from Fig. 7.1(b) that the Matrimid/ZIF-8 (30 wt.%) remains less accessible compared to PU/ZIF-8 (30 wt.%). The adsorption/desorption plots of both Matrimid and Matrimid/ZIF-8 30 wt.% are almost overlapping; adsorption peaks at ~0.31 mmol g^{-1} (P = 1 bar), while desorption remained constant at ~0.3 mmol g^{-1} (P = 1- 0.4 bar) for quite some time before completely desorbing at ~0.23 mmol g^{-1} (P = 0.13 bar). This could be due to the fact that the temperature of this experiment, at 5 °C, remains under the T_β of Matrimid (~80 °C), and at $T < T_\beta$, it is quite difficult for the C_2H_4 gas molecules to

negotiate its way around the matrix *and* come into contact with the ZIF-8 nanoparticles. Also, the C_2H_4 gas molecules that do in fact come into contact and are captured by the ZIF-8 nanoparticles will also be difficult to remove due to the intricate, sturdy, and robustness of Matrimid and its affinity with C_2H_4, forming a collection of weak bonds (H-bonds, vdW interactions, and π-π stacking). It was assumed that despite the high uptake capacity of ZIF-8 nanoparticles seen in Fig. 7.1 (a), in the case of Matrimid/ZIF-8 30 wt.% nanocomposites, the matrix plays a much larger role in the reversible uptake of C_2H_4 gas molecules.

Both the PU and PU/ZIF-8 30 wt.% nanocomposite demonstrated reversible uptakes of C_2H_4 gas molecules (absence of hysteresis, see Fig. 7.1 (b)), however, the latter ultimately exhibited much greater uptake capacity of C_2H_4 gas molecules at P_{max} = 1 bar. The difference between the reversible uptake of C_2H_4 is evident between PU and PU/ZIF-8 30 wt.%; the former showed negligible C_2H_4 uptake (<0.1 mmol g^{-1}), while the latter demonstrated a reversible uptake of ~0.6 mmol g^{-1}, which is an increase of 26 times due to the presence of ZIF-8 nanoparticles, an unprecedented improvement. In the context of the nanoparticles, the uptake of C_2H_4 molecules scales with the weight percent of the nanoparticles in the nanocomposite, at 30 wt.%, an uptake of ~0.6 mmol g^{-1} is 30% of the uptake of the ZIF-8 nanoparticles (~2.1 mmol g^{-1}). At 5 °C, the PU is at its *rubbery* phase, where it is susceptible to the influence of temperature and pressure (see §5.5). Therefore, C_2H_4 gas molecules would easily infiltrate PU due to its (much) less rigid main polymeric molecular chains. Despite the ease of infiltration, the compliant PU is unable to hold onto any adsorbed C_2H_4 gas molecules due to the minimal affinity between C_2H_4 and the molecular chains of the PU, which accounts for the almost negligible uptake of the C_2H_4 gas molecules (akin to how water passes through a leaky sieve). However, the introduction of ZIF-8 nanoparticles and the formation of a PU/ZIF-8 30 wt.% nanocomposite resulted in drastic changes; instead of acting as a porous sieve, the ZIF-8 nanoparticles enabled the

reversible uptake of C_2H_4 gas molecules. This improvement can be attributed to two factors: the open accessibility of the PU matrix and the presence of ZIF-8 nanoparticles (see Chapter 5). The open accessibility allows the C_2H_4 gas molecules to infiltrate almost immediately into the nanocomposite, which will place it into direct contact with the ZIF-8 nanoparticles. The chemical affinity between C_2H_4 and the mIm ligands and the high SAV of the ZIF-8 nanoparticles serve to increase the reversible uptake of C_2H_4 gas molecules. This process is entirely reversible, as seen in Fig. 7.1(b), where the desorption plot almost overlaps the adsorption plot. Although the reversible uptake is less than 50% of that reported by the (100 wt.%) ZIF-8 nanoparticles (~2.1 mmol g^{-1}), the nanocomposites represents an excellent capture and delivery system; it is reasonably robust and thermally stable (see Chapter 5), while also remaining accessible to other elements to freely interact with the ZIF-8 fillers. The shapes and sizes of the nanocomposites are easily customisable, which makes it an ideal candidate that can be tailored to accommodate any (reasonable) conditions and settings.

7.3 Reversible uptake of C_2H_4 (35 °C)

The previous section carefully elucidated the capabilities and mechanisms associated with the reversible uptake of C_2H_4 at 5 °C using polymer matrices (PU and Matrimid) and their respective corresponding nanocomposites (at 30 wt.% ZIF-8 nanoparticle loadings). This section will detail a similar effort at a slightly elevated temperature of 35 °C. It is reasoned that the elevated temperature will alter the interactions between the C_2H_4 gas molecules and the polymer matrices and its corresponding nanocomposites, due to the fact that all three are highly susceptible to temperature; the polymers (and its corresponding nanocomposites) undergo structural changes as a function of temperature (see §2.3.2.3), while gases are more

active and volatile at higher temperatures [263]. The elevated temperature condition is intended to draw parallels between the experiments and real world operating conditions.

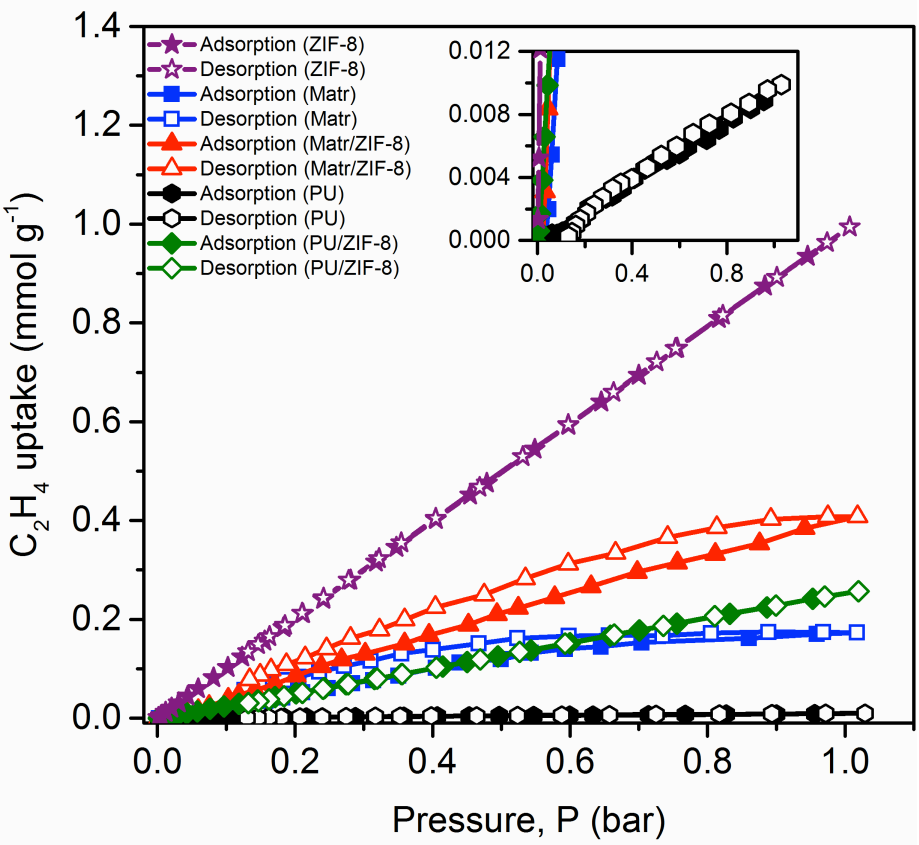

Fig. 7.2 Adsorption/desorption plots as a function of pressure for the polymers (Matrimid and PU) and polymer/MOF nanocomposites (30 wt.% of ZIF-8 nanoparticles) at 35 °C.

It can be seen in Fig. 7.2 that the reversible uptake of ZIF-8 nanoparticles is considerably reduced, at ~1 mmol g^{-1}, a decrease of ~55% from the reversible uptake reported at 5 °C. It is likely that the increased volatility of the C_2H_4 gas molecules energetically exceeded that of the collection of weak interactions (H-bonds, vdW interactions, and π-π stacking) formed between C_2H_4 gas molecules and the ZIF-8 nanoparticles, which resulted in less gas

molecules being captured. It is therefore logical to assume that increased temperatures will result in decreased reversible uptake in the case of the ZIF-8 nanoparticles.

It is also noted in Fig. 7.2 that the adsorption/desorption plots of the polymer matrices decreased by ~15% for Matrimid, while PU was lower, at << 0.1 mmol g^{-1} compared to the reversible uptake at 5 °C. The hysteresis of the Matrimid adsorption/desorption plots is also significantly smaller compared to the ones seen in Fig. 7.1 (b), implying that the removal of C_2H_4 gas molecules from Matrimid in this case actually did take place, as opposed to the previous case at 5 °C, where the C_2H_4 gas molecules remained trapped within the Matrimid. PU's lower reversible uptake capacity is a testament to its current structural condition, at 35 °C, the membrane is approaching its softening (melting) point (T_m ~85 °C), and the main polymeric molecular chain of the PU is even more loose and flow freely at rates higher than what it was at 5 °C. This, combined with the almost non-existent affinity between the PU molecules (soft and hard segments) and the C_2H_4 gas molecules accounts for the almost zero uptake of C_2H_4 gas molecules at this temperature.

The reversible uptake of C_2H_4 gas molecules by Matrimid/ZIF-8 30 wt.% nanocomposites exceeded that of the PU/ZIF-8 30 wt.% nanocomposites by ~60% (0.4 mmol g^{-1} for the former *vs*. 0.25 mmol g^{-1} for the latter). The rate of reversible uptake of C_2H_4 gas molecules of C_2H_4 at 35 °C for Matrimid/ZIF-8 30 wt.% nanocomposites exceeded even that of the PU/ZIF-8 30 wt.% nanocomposites at 5 °C by ~33% (~0.4 mmol g^{-1} for the former *vs*. ~0.31 mmol g^{-1} for the latter). This remarkable, albeit somewhat surprising reversal is attributed to the structural changes taking place in the nanocomposites at 35 °C and the volatility of the C_2H_4 gas molecules. At 35 °C, Matrimid remains at $T<T_\beta$, however, the rate of vibration and bond stretching at 35 °C exceeds that of 5 °C, and relatively, the C_2H_4 gas molecules will have an easier time penetrating and negotiating its way throughout the Matrimid/ZIF-8 30 wt.% nanocomposites due to the increased volatility of the C_2H_4 gas molecules from the

higher temperature. Both aforementioned factors increased the reversible uptake of C_2H_4 gas molecules. However, this also means that it would be easier for the C_2H_4 gas molecules to negotiate its way out of the nanocomposite, which explains the reduced hysteresis (relative to that of 5 °C) and eventual removal of ~90% of C_2H_4 gas molecules from the membrane at 35 °C.

The lower reversible uptake of PU/ZIF-8 30 wt.% nanocomposites could be attributed to the structural alterations at 35 °C, where the main polymeric chains of the PU are now sliding and slipping against each other at a much higher rate ($T >> T_g$). However, it should be pointed out that the presence of ZIF-8 nanoparticles resulted in increased structural stability well towards the T_m of the PU/ZIF-8 30 wt.% nanocomposites (see Figs. 5.5, 5.7, 5.8). The structural changes associated with the PU matrix (more porous and pliant), the volatility of the C_2H_4 gas molecules, and the affinity between ZIF-8 nanoparticles and its mIm ligands with C_2H_4 gas molecules greatly increased the potential uptake of C_2H_4 gas molecules by the nanocomposites, but this increased uptake comes at a cost: the increased volatility of the C_2H_4 gas molecules will provide enough energy for the uptaken C_2H_4 gas molecules to overcome the collection of weak interactions (H-bonds, etc) formed between mIm and C_2H_4 gas molecules, which result in the captured molecules making their way *out* of the nanocomposite, translating to poor retention capacity. The open accessibility of the PU matrix further exacerbates this situation; its intrinsic porosity is an excellent medium for the (increased) exfiltration of C_2H_4 gas molecules. Although the sample, as a whole, manage to retain a respectable amount of C_2H_4 gas molecules within its structure (~0.25 mmol g^{-1}), it remains lower than both Matrimid/ZIF-8 30 wt.% nanocomposites at 35 °C (~0.4 mmol g^{-1}) and PU/ZIF-8 30 wt.% nanocomposites at 5 °C (~0.31 mmol g^{-1}).

7.4 Nanocomposite uptake kinetics

The previous sections carefully detailed the reversible uptake capacity and capabilities of the ZIF-8 nanoparticles, the polymer matrices, and its corresponding nanocomposites at 5 °C and 35 °C. This section will focus on the adsorption/desorption kinetic mechanisms of the reversible uptake of C_2H_4 gas molecules into the aforementioned samples. The adsorption/desorption mechanism is reliant upon two factors in the context of this experiment: pressure (*P*), which induces the C_2H_4 gas molecules to infiltrate/exfiltrate from the samples, and time, which is the amount of time required for the C_2H_4 gas molecules to actually infiltrate/exfiltrate from the samples. The applied pressure and the amount of time it takes for the C_2H_4 gas molecules to adsorp/desorp will determine the viability of the nanocomposites to serve as a packaging material that can be controlled by external mechanism to uptake and release captured C_2H_4 gas molecules.

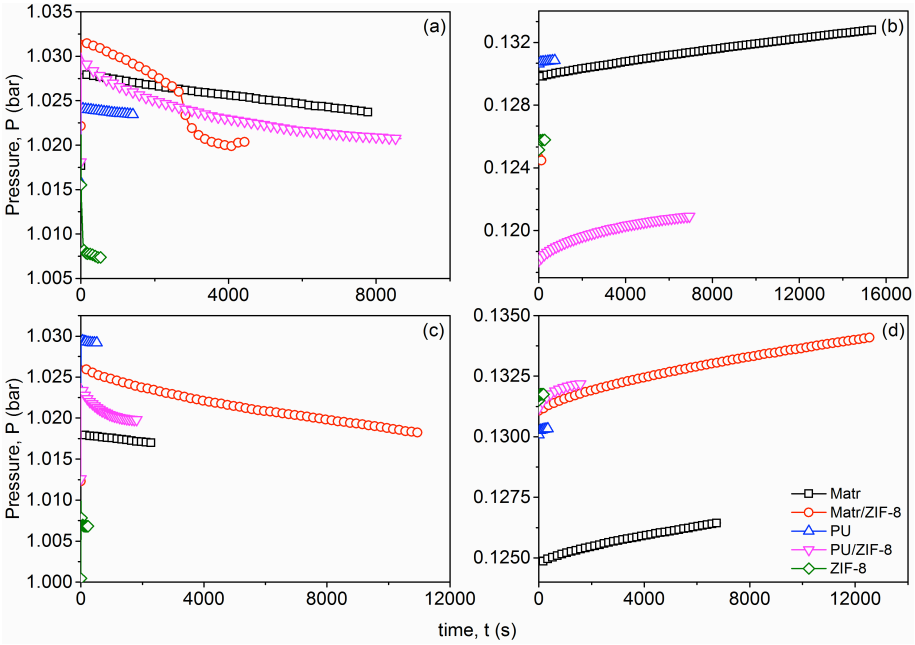

Fig. 7.3 Adsorption/desorption kinetics of C_2H_4 for ZIF-8 nanoparticles, polymer matrices (Matrimid and PU), and its corresponding nanocomposites (at 30 wt.% loading of ZIF-8 nanoparticles), with (a) adsorption kinetics at 5 °C and ~1 bar, (b) desorption kinetics at 5 °C and ~0.13 bar, (c) adsorption kinetics at 35 °C and ~1 bar, and (d) desorption kinetics at 35 °C and ~0.13 bar.

Fig. 7.3 shows the kinetics associated with the uptake of C_2H_4 gas molecules for the ZIF-8 nanoparticles, polymer matrices (Matrimid and PU), and its corresponding nanocomposites (at 30 wt.% loadings of ZIF-8 nanoparticles). In this sample data, the pressure/time data associated with the reversible uptake of C_2H_4 gas molecules was taken as close as possible to ~1 bar, as at this pressure, as established in Fig. 7.1-7.2, is where the uptake capacity of C_2H_4 gas molecules is at its highest for all of the samples. Similarly, the pressure/time data for the desorption kinetics was taken at ~0.13 bar, as at this pressure, the desorption procedure is almost complete, signifying that the C_2H_4 gas molecules are almost completely removed and unable to infiltrate the samples (at such low pressure).

In Fig. 7.3 (a), it can be seen that C_2H_4 adsorbed much quicker to ZIF-8 nanoparticles (~500 s) and PU (~1500 s) compared to Matrimid/ZIF-8 30 wt.% (~4500 s), Matrimid (~8000 s), and PU/ZIF-8 30 wt.% (~8000 s) samples. The ZIF-8 nanoparticles, in the form of fine powder, have a large surface area (~1650 m^2 g^{-1}) [80] and almost entirely open accessibility and porosity, which corresponds to quick and easy adsorption of the C_2H_4 gas molecules due to its direct exposure and interactions with ZIF-8's porosity and its chemical affinity with the mIm ligands. This open accessibility also accounts for the quick and relatively simple desorption of C_2H_4 gas molecules from ZIF-8. A similar but somewhat modified argument can be used to explain the quick adsorption time of the PU sample; despite the fact that it lacks the large surface area of ZIF-8 nanoparticles and the chemical affinity with C_2H_4 gas molecules inherent in ZIF-8 nanoparticles, its accessibility and porosity is simply too high (see Chapter 5) to competently capture C_2H_4 gas molecules, akin to how a sieve with large pores allowing water to pass through without much resistance. In effect, the C_2H_4 gas molecules merely passes through PU due to the applied pressure instead of reliably forming bonds and physiosorbing/chemisorbing with PU polymeric chain. This behaviour is reflected in its desorption plots as well (Fig. 7.3 (b)), where the desorption time for ZIF-8 nanoparticles was 300 s, while it was ~600 s for PU. The open accessibility and large surface area of the former allowed the C_2H_4 gas molecules to desorp a lot faster from the PU samples, while the (very) large pores and non-existent chemical bonds between the samples and C_2H_4 gas molecules resulted in the quick desorption of the gas molecules from the latter.

The increased adsorption time of C_2H_4 gas molecules upon Matrimid is due to its glassy nature; its main polymeric chain is configured in a manner that greatly restrict external access, and only the application of constant pressure upon the samples resulted in a small amount of C_2H_4 gas molecules penetrating (and uptaken) by the samples (also see Fig. 7.1 for the amount of uptaken C_2H_4 gas molecules for Matrimid). Despite the introduction of

ZIF-8 nanoparticles and the formation of Matrimid/ZIF-8 30 wt.% nanocomposites, the nature of Matrimid predominates: access remains highly restricted, which is reflected in the similarly high adsorption times for C_2H_4 gas molecules in the Matrimid/ZIF-8 30 wt.% sample. This is also evident in the desorption times of both samples; the desorption time of C_2H_4 gas molecules from Matrimid reaches ~15,000 s, which implies that the C_2H_4 gas molecules that do manage to infiltrate Matrimid remained trapped within the samples, as evident in Fig. 7.1 (b). However, the desorption times for Matrimid/ZIF-8 30 wt.% sample was relatively low, at ~160 s. This can be explained by the fact that the C_2H_4 gas molecules that infiltrated the nanocomposite and were adsorbed by the embedded ZIF-8 nanoparticles remained trapped within the ZIF-8 nanoparticles *and* Matrimid, making it even more difficult for it to exfiltrate from the samples. This is evident in Fig. 7.1 (b), where the hysteresis for both the Matrimid and Matrimid/ZIF-8 30 wt.% samples were relatively large.

Despite the PU sample showing almost negligible uptake of C_2H_4 gas molecules, its corresponding ZIF-8 nanocomposite showed significant increase in uptake, as per Fig. 7.1 (b). Similarly, Fig. 7.3 (a) showed increased adsorption time for the PU/ZIF-8 30 wt.% sample, which is speculated to be due to the presence of ZIF-8 nanoparticles increasing the packing density *within* the nanocomposite (which reduces accessibility and porosity) while also capturing C_2H_4 gas molecules. This significantly increased its adsorption time, and its high uptake capacity *vis-à-vis* C_2H_4 gas molecules means more and more of the gas molecules are being trapped within the nanocomposite. Similarly, its desorption time, although lower than Matrimid, is still quite significant, at 7000 s. This can be speculated to be due to the difficulty for the captured gas to break the collection of weak bonds formed with ZIF-8 nanoparticles (due to physiosorption and chemisorption) and the increased difficulty of exfiltrating from the PU/ZIF-8 30 wt.% nanocomposite samples due to the increased packing density within the nanocomposite.

At 35 °C (see Fig. 7.3 (c-d)), there are a few interesting observations in terms of the adsorption/desorption mechanisms for the C_2H_4 gas molecules. Adsorption of Matrimid/ZIF-8 30 wt.% took the longest, at 11,000 s, followed by Matrimid (~2000 s), PU/ZIF-8 30 wt.% (~1800 s), PU (~500 s), and ZIF-8 (~150 s). At 35 °C, the main polymeric chain of Matrimid gains more energy via heat, which translates into increased accessibility and increased rate of infiltration (relative) of C_2H_4 gas molecules. This implies increased contact between C_2H_4 gas molecules and ZIF-8 nanoparticles embedded within the Matrimid/ZIF-8 30 wt.% nanocomposite, which means that adsorption is taking place within both Matrimid and ZIF-8 nanoparticles, as reflected in the increased adsorption/desorption times being significantly higher than that of the other tested samples. Also, the higher temperature increased the volatility of the gas molecules, as per §7.2-7.3, which makes it more difficult for it to remain trapped within the nanocomposites. It can be reasonably speculated that despite the increased temperature increasing the volatility of the gas molecules and the accessibility of the sample, it is difficult for the sample to hold onto the captured gas molecules (low hysteresis seen in Fig. 7.2 for all of the tested samples). This is also reflected in the increased adsorption/desorption times shown in Fig. 7.3 (c-d). Despite the increased accessibility of Matrimid at 35 °C, it remains sturdy and rigid, which means that infiltration of C_2H_4 gas molecules, despite being relatively higher than that shown at 5 °C, remains quite low. Also, the rigidity and packing density of the polymeric chains of Matrimid limits the maximum amount of C_2H_4 gas molecules that could remain within the nanocomposite, which means that level of uptake of the gas molecules will be limited. This is reflected in the relatively shorter time it took for C_2H_4 gas molecules to adsorb onto/into Matrimid, and its increased desorption time (7000 s), which is due to the difficulty for the gas molecules to exfiltrate from the nanocomposites despite the increased accessibility and volatility.

It is interesting to note that the PU samples reported quite low adsorption/desorption times at 35 °C. As pointed out in §7.2-7.3, at that temperature, the PU matrix is more compliant and less robust, resulting in an almost openly accessible membrane. This translates into both the PU/ZIF-8 30 wt.% samples and its matrix (PU) requiring much shorter times to adsorb/desorb C_2H_4 gas molecules. The reason for this is quite simple: the increased volatility of the gas molecules exceeded the weak bond strength formed between ZIF-8 and the C_2H_4 gas molecules, which means that its ability to hold onto the gas molecules that were captured was significantly lowered. This decreased the total amount of captured gas molecules, which is evident in Fig. 7.3 (c), where it took ~1800 s for C_2H_4 gas molecules to adsorb onto/into PU/ZIF-8 30 wt.%. Its desorption time was low as well (~1500 s), as it was much easier for the captured gas molecules to desorb from the samples due to weak bonds and increased volatility. PU was already a poor medium to retain C_2H_4 gas molecules at 5 °C, and at 35 °C, PU is even more accessible, and its poor affinity with C_2H_4 gas molecules simply preclude it from being able to hold onto the gas molecules or retain it in any meaningful manner. This is evident in its desorption time, at ~300 s, which means that any captured gas molecules were also easily desorbed. In fact, the amount of captured C_2H_4 gas molecules in PU was almost negligible, as expounded upon in §7.2-7.3.

In the case of ZIF-8 nanoparticles, despite its high capacity for C_2H_4 gas molecules, the increased volatility of the gas molecules and the open accessibility of the fine powder sample made the adsorption/desorption times of C_2H_4 gas molecules almost negligible.

7.5 General implications

The previous subsections detailed the reversible uptake of C_2H_4 by the ZIF-8 nanocomposites at two specific temperatures (5 °C and 35 °C). The reversible uptake of C_2H_4 gas molecules is intricately linked to its viscoelastic and thermo-mechanical response and macro-mechanical properties, all of which were discussed in Chapters 4-5. This phenomenon can be translated into viable real world applications, especially for the food packaging and transport industry. The results garnered in this chapter lead to a few general implications on the reversible uptake and its viability as a packaging material.

The reversible uptake of C_2H_4 by ZIF-8 is heavily linked to its ambient temperature, where increased temperature results in decreased reversible uptakes. Therefore, pinpointing an optimal temperature for the reversible uptake of C_2H_4 that does not adversely affect the robustness of the nanocomposites and maximises uptake is especially imperative. 5 °C was utilised as a testing temperature as it is the reported temperature for the storage and transportation of bananas [264], and confirmed that indeed, at this temperature, the reversible uptake of the ZIF-8 nanoparticles and ZIF-8 nanocomposites are reasonable. It is therefore prudent to point out that the selection of matrix is important: the accessibility of the matrix needs to be at a point where it does not encourage the free passage of C_2H_4 gas molecules without offering respectable resistance, as seen in the case of PU/ZIF-8 30 wt.% nanocomposite at 35 °C. The same sample, at 5 °C, offered significant reversible uptake capability within a reasonably robust medium. It is therefore logical to assume that using a rubbery polymer matrix (or low T_g matrix) will result in a relatively high uptake of gas molecules, especially if the fillers within the nanocomposite is a MOF with a high affinity for the infiltrating gas molecules.

The kinetics of the ZIF-8 nanocomposites also serve as an interesting point. The adsorption/desorption of C_2H_4 in the samples is dictated by pressure and temperature. More robust and densely packed samples, such as Matrimid and its 30 wt.% nanocomposite, display discernible resistance towards adsorption/desorption (at 5 °C), as garnered from the adsorption/desorption times. PU, PU/ZIF-8 30 wt.% and ZIF-8 samples were more agreeable, displaying significantly shorter adsorption/desorption times at 5 °C. However, the structural variations brought about by increased temperature at 35 °C resulted in decreased uptake in PU/ZIF-8 30 wt.% to levels under that reported by the Matrimid/ZIF-8 samples, suggesting that the structural integrity of the matrix, which is temperature dependent, is crucial towards the reversible uptake of C_2H_4. It is assumed that at $T \approx T_g$, the C_2H_4 gas molecules easily infiltrated Matrimid/ZIF-8 30 wt.% due to increased accessibility afforded by the constant motion of the polymeric chains. However, the polymeric chain network remains rigid and sturdy, which translates into substantial infiltration times for the Matrimid and Matrimid/ZIF-8 30 wt.% samples. The more accessible ZIF-8 and PU samples naturally display more agreeable kinetics, as per their reduced infiltration/exfiltration times, although retention appear to be a problem.

The combination of affinity, accessibility, and kinetics means that it is indeed possible to tune the parametric control (ie. pressure and temperature) to affect controlled adsorption and desorption of C_2H_4 gas molecules. This would be especially useful in an environment where immediate uptake or release is not preferred, such as the prolonged transport of fresh produce. The intrinsic feature of these nanocomposites *vis-à-vis* the reversible uptake of C_2H_4 gas molecules will allow for the design an accurate controlled release system, which releases C_2H_4 gas molecules in controlled dosage at specific times to slowly infuse the fresh produce with the designated gas by careful manipulation of the ambient temperature and pressure. This passive release system will reduce the economic cost associated with the

transport and ripening of fresh produce while being more effective compared to near constant exposure of the product to active gases, which would preserve quality and decrease prices.

7.6 Chapter Summary

An elaborate effort on studying the reversible uptake of C_2H_4 using the polymer/ZIF-8 nanocomposites reported in Chapters 4-5 was detailed. This work represents the first attempt of using these nanocomposites in this manner, and it is envisioned that the results will be of use for the reversible uptake of similar classes of gases, such as a myriad of hydrocarbons (ethane being an example of this).

The next chapter will summarise this thesis and underline the important points made throughout this work. We will also propose possible future studies that can be pursued by other researchers in the field of MOFs and MOF-nanocomposites.

CHAPTER EIGHT

Conclusions, Recommendations, and Potential Future Pursuits

The entirety of this work is devoted to the elucidation of three aspects of polymer/MOF nanocomposites; the thermo-mechanical, viscoelastic, and macro-mechanical characterisation of the polymer/ZIF-8 nanocomposites, its application as a passive uptake/retention system for I_2, and its utilisation as a reversible uptake medium of C_2H_4 gas molecules. The utilisation of common and established experimental techniques allowed us to adapt the analyses detailed in other works for other classes of materials that are analogous to polymer nanocomposites to prudently characterise the nanocomposites developed in this work, and the preceding chapters are accurately reflective of our efforts. The reported results represent a systematic pioneering study at amalgamating structure-property relationship and the multi-faceted applications of the MOF-nanocomposites, which is unique in that it *correlates* performance to materials' design. Our collective thoughts, insights, and observations throughout this work has allowed us to arrive at a collection of intertwining conclusions detailed in the following subsections.

8.1 The physico-chemical, quasi-static, and dynamic characterisation of Matrimid/ZIF-8 nanocomposites

- It was confirmed that the dispersion and encapsulation of ZIF-8 within Matrimid, obtained *via* the colloidal solution mixing technique, was uniform and overall homogeneous. Though well dispersed, it was established that the addition of ZIF-8

nanoparticles (>10~15 wt.%) to the nanocomposite is detrimental towards mechanical properties of such thin nanocomposites, particularly its ductility, toughness, and tensile strength, making them highly susceptible to cracking by (brittle) fast fracture. This trend is even more pronounced for the annealed nanocomposites, in which further embrittlement of the polyimide matrix phase has occurred.

- While there are only subtle changes to the viscoelastic properties with the addition of ZIF-8 nanoparticles, major fluctuations associated with residual solvents in cured nanocomposites have been established near the glass transition temperature (T_g). It was demonstrated that DMA is an extremely powerful technique, whose usage should be broadened in the field of MOF-based nancomposite research to enable not only the determination of T_g, but also to address the evolution of dynamical mechanical behaviour and basic energy dissipation mechanisms, such as to pinpoint the presence of occluded solvents impacting membrane permeability and selectivity.
- As per previous work [80] reporting enhancement of gas separation behaviour of Matrimid/ZIF-8 nanocomposites, it was established in this study that while the addition of ZIF-8 nanoparticles and annealing are beneficial towards gas selectivity, it was shown that this is not always the case for certain mechanical properties. Specifically, mechanical degradation in terms of ductility and toughness can be substantial post annealing, thus weakening its structural robustness making the membrane less suitable for practical use.
- It is envisaged that the structure-property relationships between the MOF nanoparticles and glassy polymer matrices developed in this part of the work alongside the mechanical characterisation methodologies will be pertinent to many combinations of glassy polymer/MOF based systems, targeting a wide range of emergent membrane technologies. Work is certainly warranted to further establish whether the proposed

structure-property correlation is applicable to understand the performance of a broad combination of glassy-based MOF-nanocomposites.

8.2 Static and dynamic behaviours of PU/ZIF-8 nanocomposites

- The unique combination of PU (a hyperelastic rubbery polymer) and ZIF-8 (a prototypical zeolitic MOF) allowed the thermal, mechanical, and structural characteristics of both constituents to act in parallel due to the loose association of the constituents while negating the weaknesses inherent in either. This is evident from the results from TGA, DMA, and uniaxial tensile tests, where the hyperelastic and viscoelastic characteristics of PU was retained despite the introduction of ZIF-8 nanoparticles, which in turn introduced free volume and active porous sites that will be beneficial for applications such as gas capture and separation.
- The interactions between the ZIF-8 nanoparticles and PU matrix is tenuous and dominated by a collection of uniform secondary interactions, such as H-bonds, vdW forces, and π-π stacking. Due to the strengths of these bonds, at lower loadings of ZIF-8 (<~20 wt.%), it is anticipated that the free volume and pinning of the ZIF-8 nanoparticles are likely not fixed (thus mobile), and the corresponding size and shape of these free volumes within the nanocomposites are influenced by the introduction of external stimuli from coupled stress and temperature effects. However, at higher loadings of ZIF-8 nanoparticles (>~20 wt.%), the sheer increase in the amount of secondary interactions became quite significant, thereby forming a sturdier and mechanically rigid nanocomposite, which suppresses the mobility at the ZIF-8/PU interface, causing major decline in composite ductility and toughness.

- The methodologies developed in this study can be extended to other hyperelastic polymers (e.g. PDMS, PVDF, PVP, polypropylene) in combination with a vast range of existing nanostructured MOF-based materials to yield mechanically and thermally robust nanocomposites to enable practical applications.

8.3 The uptake/retention of I_2 using polymer/ZIF-8 nanocomposites

- I_2 was indeed captured and retained within the pristine polymer membranes (albeit at small, almost negligible wt.%), but the immobilisation of I_2 in nanocomposite is prominent, particularly in the case of PU/ZIF-8 30 wt.%.
- It was confirmed that the rubbery polymer matrix (e.g. PU) results in better absorptive and retention capabilities, which could be associated with the more accessible ZIF-8 pores to afford physisorption and chemisorption processes and further accompanied by physical confinement inside free volumes of the polymer matrices.
- It was projected that the mechanism that allowed I_2 to be captured and retained within the polymers and nanocomposites can be attributed to the molecular interactions and affinity between the mIm (deprotonated ligand of 2-methylimidazole) of ZIF-8, I_2 molecules, and parts of the polymeric chains of the matrices. Therefore, this passive process requires almost no injection of external energy, but relies completely on molecular and chemical affinities existing between the multiple organic-inorganic molecular constituents in the nanocomposites.
- The formation of polymer/ZIF-8 nanocomposites improved the deliverability of the samples and allowed the retention of I_2 at temperatures far beyond its flashpoint, thus boosting thermal stability as evidenced from the TGA experiments.

- Initial design proposal in the context of I_2 capture and retention would suggest that a combination between highly porous MOFs containing strong sorption sites (e.g. ZIFs [59], MILs [265, 266], CuBTC [267], and CPOs [268, 269]) and rubbery polymers, such as PU, polydimethylsiloxane (PDMS) and polyisobutylene (PIB) will be favourable for maximising I_2 capture rates in emerging class of MOF-based nanocomposites [37, 39, 128].
- There is a huge scope for future developments in the aforementioned areas, not only to better elucidate the underpinning physico-chemical mechanisms but also to design and tune suitable combinations membrane nanocomposites to yield bespoke guest immobilisation capacities.

8.4 The reversible uptake of C_2H_4 using polymer/ZIF-8 nanocomposites

- Despite the unique structural response of the polymer/ZIF-8 nanocomposites towards external factors such as temperature and pressure, the reversible uptake capability of these nanocomposites *vis-à-vis* C_2H_4 is very much reliant on the nature of the matrix, where characteristics such as sturdiness and accessibility dictates the potential amount of uptaken C_2H_4. Regardless of the affinity of the selected MOFs to the designated gas, careful selection of the matrix is paramount to ensure that the gas and the MOFs will eventually interact with one another.
- The experimental temperature plays a large role in the reversible uptake of C_2H_4, not only due to its effect on the structural changes to the nanocomposites, but also due to the increased volatility of the C_2H_4 gas molecules at high(er) temperatures. It was observed that the volatility of the gas at a higher temperature (35 °C) provided the gas molecules with enough energy to surpass the bond energy of the combined affinity and

secondary attractions with the ZIF-8 nanoparticles, resulting in almost complete desorption of the gas molecules from the nanocomposites in the case of the glassy polymer matrix.

- The accessibility of the matrix plays a large role in the kinetics of the reversible uptake of the ZIF-8 nanocomposites. Rubbery polymers are generally more accessible than its glassy counterpart, however, this accessibility may prove to be a problem, as retention of the C_2H_4 within the structure is quite poor. Glassy polymer matrix is less accessible and rigid, resulting in slow kinetics and the ability of the nanocomposites to retain C_2H_4 gas molecules within its structure. Although embedded ZIF-8 nanoparticles are responsible for the reversible uptake of C_2H_4, the matrix is responsible for preventing the C_2H_4 gas molecules from exfiltrating from the nanocomposites.
- The ability of these nanocomposites to uptake C_2H_4 gas molecules is linked to three distinct factors: the choice of matrix and MOF, and the operating temperature. Based on our results, it was assumed that the polymer/ZIF-8 nanocomposites would be suitable, for example, as a packaging material for the transport of fresh produce, especially the PU/ZIF-8 based nanocomposites, due to its ability to retain a respectable amount of C_2H_4, which allows for good retention at 1 bar and also controlled release of C_2H_4 over an extended period of time, triggered by adequately tuning pressure and temperature.

8.5 Possible future works

The methods, results, and insights detailed throughout this thesis can be extended to other combinations of polymer/MOF nanocomposites. There are thousands of reported MOFs in literature (HKUST-1, MILs, UiOs, etc), and many more glassy and rubbery polymer

matrices (PVDF, 6FDA-DAM, PS, etc) that can be used to form multiple classes of polymer/MOF nanocomposites.

- Chapter 2 detailed the many types of MOFs, defined by its metallic core and organic ligands, resulting in unique and one-of-a-kind hybrid material. The availability of many types of polymer matrices, whether glassy or rubbery, makes the possible polymer/MOF combination a boundless endeavour. The methods reported in this thesis, such as colloidal solution mixing, doctor blade casting, nanoindentation, DMA, TGA, and uniaxial tensile testing (among others) can be used to comprehensively study MOF-based nanocomposites. Accounting for this literature gap, it was surmised that there are almost endless possibilities with regards to investigating the physico-chemical properties of these nanocomposites. As a general rule of thumb based on the reported results in this thesis, a good starting point would be to work polymer/MOF composites made up of a rubbery and highly accessible matrix and a relatively (in the context of the matrix) hard MOF fillers, which has been shown in this work to result in the most significant improvements.
- The nanocomposites developed and studied in this work was utilised for the uptake/retention of I_2 and the reversible uptake of C_2H_4 gas molecules. The oft-cited characteristics of MOFs render them suitable for the many applications outlined in Chapter 2, and by extension, these applications would also be viable for the corresponding MOF-based nanocomposites outlined in §2.4. The study of the application of the polymer/MOF nanocomposites in the context of the aforementioned applications is not limited to the ZIF-8 based nanocomposites developed in this work, but can also be extended to other polymer/MOF nanocomposites.

Bibliography

[1] M. M. Pendergast and E. M. V. Hoek, "A review of water treatment membrane nanotechnologies," *Energy & Environmental Science,* vol. 4, pp. 1946-1971, 2011.

[2] D. F. Sanders, Z. P. Smith, R. Guo, L. M. Robeson, J. E. McGrath, D. R. Paul*, et al.*, "Energy-efficient polymeric gas separation membranes for a sustainable future: A review," *Polymer,* vol. 54, pp. 4729-4761, 2013.

[3] R. D. Noble, "Perspectives on mixed matrix membranes," *Journal of Membrane Science,* vol. 378, pp. 393-397, 2011.

[4] M. G. Buonomenna and J. Bae, "Membrane processes and renewable energies," *Renewable and Sustainable Energy Reviews,* vol. 43, pp. 1343-1398, 2015.

[5] Y. Zhang, J. Sunarso, S. Liu, and R. Wang, "Current status and development of membranes for CO_2/CH_4 separation: A review," *International Journal of Greenhouse Gas Control,* vol. 12, pp. 84-107, 2013.

[6] N. Du, H. B. Park, M. M. Dal-Cin, and M. D. Guiver, "Advances in high permeability polymeric membrane materials for CO_2 separations," *Energy & Environmental Science,* vol. 5, pp. 7306-7322, 2012.

[7] X. S. Feng and R. Y. M. Huang, "Liquid separation by membrane pervaporation: A review," *Industrial & Engineering Chemistry Research,* vol. 36, pp. 1048-1066, 1997.

[8] S. S. Shenvi, A. M. Isloor, and A. F. Ismail, "A review on reverse osmosis (RO) membrane technology: Developments and challenges," *Desalination,* vol. 368, pp. 10-26, 2015.

[9] Y. Baek, C. Kim, D. K. Seo, T. Kim, J. S. Lee, Y. H. Kim*, et al.*, "High performance and antifouling vertically aligned carbon nanotube membrane for water purification," *Journal of Membrane Science,* vol. 460, pp. 171-177, 2014.

[10] A. Collier, H. Wang, X. Ziyuan, J. Zhang, and D. Wilkinson, "Degradation of polymer electrolyte membranes," *International Journal of Hydrogen Energy,* vol. 31, pp. 1838-1854, 2006.

[11] M. Inaba, T. Kinumoto, M. Kiriake, R. Umebayashi, A. Tasaka, and Z. Ogumi, "Gas crossover and membrane degradation in polymer electrolyte fuel cells," *Electrochimica Acta,* vol. 51, pp. 5746-5753, 2006.

[12] B. Wu, M. Zhao, W. Shi, W. Liu, J. Liu, D. Xing*, et al.*, "The degradation study of Nafion/PTFE composite membrane in PEM fuel cell under accelerated stress tests," *International Journal of Hydrogen Energy,* vol. 39, pp. 14381-14390, 2014.

[13] C. H. Worthley, K. T. Constantopoulos, M. Ginic-Markovic, R. J. Pillar, J. G. Matisons, and S. Clarke, "Surface modification of commercial cellulose acetate membranes using surface-initiated polymerization of 2-hydroxyethyl methacrylate to improve membrane surface biofouling resistance," *Journal of Membrane Science,* vol. 385-386, pp. 30-39, 2011.

[14] Z. Q. Jiang and Z. J. Jiang, "Plasma techniques for the fabrication of polymer electrolyte membranes for fuel cells," *Journal of Membrane Science,* vol. 456, pp. 85-106, 2014.

[15] C.-H. Tsai, C.-C. Wang, C.-Y. Chang, C.-H. Lin, and Y. W. Chen-Yang, "Enhancing performance of Nafion®-based PEMFC by 1-D channel metal-organic frameworks as PEM filler," *International Journal of Hydrogen Energy,* vol. 39, pp. 15696-15705, 2014.

[16] E. Ameri, M. Sadeghi, N. Zarei, and A. Pournaghshband, "Enhancement of the gas separation properties of polyurethane membranes by alumina nanoparticles," *Journal of Membrane Science,* vol. 479, pp. 11-19, 2015.

[17] C.-W. Liew, S. Ramesh, and A. K. Arof, "Characterization of ionic liquid added poly(vinyl alcohol)-based proton conducting polymer electrolytes and electrochemical studies on the supercapacitors," *International Journal of Hydrogen Energy,* vol. 40, pp. 852-862, 2015.

[18] Y. Tang, A. Kusoglu, A. M. Karlsson, M. H. Santare, S. Cleghorn, and W. B. Johnson, "Mechanical properties of a reinforced composite polymer electrolyte membrane and its

simulated performance in PEM fuel cells," *Journal of Power Sources,* vol. 175, pp. 817-825, 2008.

[19] G. D. Vilakati, E. M. V. Hoek, and B. B. Mamba, "Probing the mechanical and thermal properties of polysulfone membranes modified with synthetic and natural polymer additives," *Polymer Testing,* vol. 34, pp. 202-210, 2014.

[20] S. Thampi, V. Muthuvijayan, and R. Parameswaran, "Mechanical characterization of high-performance graphene oxide incorporated aligned fibroporous poly(carbonate urethane) membrane for potential biomedical applications," *Journal of Applied Polymer Science,* vol. 132, p. 41809, 2015.

[21] R. Pucciariello, M. D'Auria, V. Villani, G. Giammarino, G. Gorrasi, and G. Shulga, "Lignin/Poly(epsilon-Caprolactone) blends with tuneable mechanical properties prepared by high energy ball-milling," *Journal of Polymers and the Environment,* vol. 18, pp. 326-334, 2010.

[22] R. Mahajan and W. J. Koros, "Factors controlling successful formation of mixed-matrix gas separation materials," *Industrial & Engineering Chemistry Research,* vol. 39, pp. 2692-2696, 2000.

[23] D. R. Paul and L. M. Robeson, "Polymer nanotechnology: Nanocomposites," *Polymer,* vol. 49, pp. 3187-3204, 2008.

[24] J. Zhu, W. Cao, M. Yue, Y. Hou, J. Han, and M. Yang, "Strong and stiff aramid nanofiber/carbon nanotube nanocomposites," *ACS Nano,* vol. 9, pp. 2489-2501, 2015.

[25] H. Kim, A. A. Abdala, and C. W. Macosko, "Graphene/Polymer Nanocomposites," *Macromolecules,* vol. 43, pp. 6515-6530, 2010.

[26] S. T. Meek, J. A. Greathouse, and M. D. Allendorf, "Metal-Organic Frameworks: A rapidly growing class of versatile nanoporous materials," *Advanced Materials,* vol. 23, pp. 249-267, 2011.

[27] J. C. Tan and B. Civalleri, "Metal–organic frameworks and hybrid materials: From fundamentals to applications," *CrystEngComm,* vol. 17, pp. 197-198, 2015.

[28] S. Kitagawa, R. Kitaura, and S. Noro, "Functional porous coordination polymers," *Angewandte Chemie-International Edition,* vol. 43, pp. 2334-2375, 2004.

[29] H. Furukawa, K. E. Cordova, M. O'Keeffe, and O. M. Yaghi, "The chemistry and applications of metal-organic frameworks," *Science,* vol. 341, p. 1230444, 2013.

[30] H. C. Zhou, J. R. Long, and O. M. Yaghi, "Introduction to metal-organic frameworks," *Chemical Reviews,* vol. 112, pp. 673-674, 2012.

[31] R. Banerjee, A. Phan, B. Wang, C. Knobler, H. Furukawa, M. O'Keeffe*, et al.*, "High-throughput synthesis of zeolitic imidazolate frameworks and application to CO_2 capture," *Science,* vol. 319, pp. 939-943, 2008.

[32] J. C. Tan, T. D. Bennett, and A. K. Cheetham, "Chemical structure, network topology, and porosity effects on the mechanical properties of Zeolitic Imidazolate Frameworks," *Proceedings of the National Academy of Sciences of the United States of America,* vol. 107, pp. 9938-9943, 2010.

[33] J. C. Tan, B. Civalleri, C. C. Lin, L. Valenzano, R. Galvelis, P. F. Chen*, et al.*, "Exceptionally low shear modulus in a prototypical imidazole-based metal-organic framework," *Physical Review Letters,* vol. 108, p. 095502, 2012.

[34] T. D. Bennett, D. A. Keen, J. C. Tan, E. R. Barney, A. L. Goodwin, and A. K. Cheetham, "Thermal amorphization of Zeolitic Imidazolate Frameworks," *Angewandte Chemie-International Edition,* vol. 50, pp. 3067-3071, 2011.

[35] M. R. Ryder and J. C. Tan, "Nanoporous metal-organic framework materials for smart applications," *Materials Science and Technology,* vol. 30, pp. 1598-1612, 2014.

[36] J. C. Tan, B. Civalleri, A. Erba, and E. Albanese, "Quantum mechanical predictions to elucidate the anisotropic elastic properties of zeolitic imidazolate frameworks: ZIF-4 vs. ZIF-zni," *CrystEngComm,* vol. 17, pp. 375-382, 2015.

[37] G. X. Dong, H. Y. Li, and V. K. Chen, "Challenges and opportunities for mixed-matrix membranes for gas separation," *Journal of Materials Chemistry A,* vol. 1, pp. 4610-4630, 2013.

[38] A. W. Thornton, D. Dubbeldam, M. S. Liu, B. P. Ladewig, A. J. Hill, and M. R. Hill, "Feasibility of zeolitic imidazolate framework membranes for clean energy applications," *Energy & Environmental Science,* vol. 5, pp. 7637-7646, 2012.

[39] H. B. Tanh Jeazet, C. Staudt, and C. Janiak, "Metal-organic frameworks in mixed-matrix membranes for gas separation," *Dalton Transactions,* vol. 41, pp. 14003-27, 2012.

[40] T. X. Yang, G. M. Shi, and T. S. Chung, "Symmetric and asymmetric zeolitic imidazolate frameworks (ZIFs)/Polybenzimidazole (PBI) nanocomposite membranes for hydrogen purification at high temperatures," *Advanced Energy Materials,* vol. 2, pp. 1358-1367, 2012.

[41] S. N. Liu, G. P. Liu, X. H. Zhao, and W. Q. Jin, "Hydrophobic-ZIF-71 filled PEBA mixed matrix membranes for recovery of biobutanol via pervaporation," *Journal of Membrane Science,* vol. 446, pp. 181-188, 2013.

[42] S.-L. Li and Q. Xu, "Metal-organic frameworks as platforms for clean energy," *Energy & Environmental Science,* vol. 6, pp. 1656-1683, 2013.

[43] S. N. Wijenayake, N. P. Panapitiya, S. H. Versteeg, C. N. Nguyen, S. Goel, K. J. Balkus*, et al.*, "Surface cross-linking of ZIF-8/Polyimide mixed matrix membranes (MMMs) for gas separation," *Industrial & Engineering Chemistry Research,* vol. 52, pp. 6991-7001, 2013.

[44] F. Mammeri, E. Le Bourhis, L. Rozes, and C. Sanchez, "Mechanical properties of hybrid organic-inorganic materials," *Journal of Materials Chemistry,* vol. 15, pp. 3787-3811, 2005.

[45] M. Rezakazemi, A. E. Amooghin, M. M. Montazer-Rahmati, A. F. Ismail, and T. Matsuura, "State-of-the-art membrane based CO_2 separation using mixed matrix membranes (MMMs): An overview on current status and future directions," *Progress in Polymer Science,* vol. 39, pp. 817-861, 2014.

[46] D. Hull and T. W. Clyne, An introduction to composite materials: Cambridge University Press, 1996.

[47] A. K. Cheetham, C. N. Rao, and R. K. Feller, "Structural diversity and chemical trends in hybrid inorganic-organic framework materials," *Chemical Communications,* pp. 4780-4795, 2006.

[48] M. O'Keeffe, "Nets, tiles, and metal-organic frameworks," *APL Materials,* vol. 2, p. 124106, 2014.

[49] C. N. R. Rao, A. K. Cheetham, and A. Thirumurugan, "Hybrid inorganic-organic materials: A new family in condensed matter physics," *Journal of Physics-Condensed Matter,* vol. 20, p. 083202, 2008.

[50] M. R. Ryder, B. Civalleri, T. D. Bennett, S. Henke, S. Rudic, G. Cinque*, et al.*, "Identifying the role of terahertz vibrations in metal-organic frameworks: from gate-opening phenomenon to shear-driven structural destabilisation," *Physical Review Letters,* vol. 113, p. 215502, 2014.

[51] A. M. Walker, B. Civalleri, B. Slater, C. Mellot-Draznieks, F. Cora, C. M. Zicovich-Wilson*, et al.*, "Flexibility in a metal-organic framework material controlled by weak dispersion forces: The bistability of MIL-53(Al)," *Angewandte Chemie-International Edition,* vol. 49, pp. 7501-7503, 2010.

[52] M. R. Ryder, B. Civalleri, G. Cinque, and J. C. Tan, "Discovering connections between terahertz vibrations and elasticity underpinning the collective dynamics of the HKUST-1 metal–organic framework," *CrystEngComm,* vol. 18, pp. 4303-4312, 2016.

[53] A. J. Howarth, Y. Y. Liu, P. Li, Z. Y. Li, T. C. Wang, J. Hupp*, et al.*, "Chemical, thermal and mechanical stabilities of metal-organic frameworks," *Nature Reviews Materials,* vol. 1, p. 15018, 2016.

[54] O. K. Farha, I. Eryazici, N. C. Jeong, B. G. Hauser, C. E. Wilmer, A. A. Sarjeant*, et al.*, "Metal-organic framework materials with ultrahigh surface areas: Is the sky the limit?," *Journal of American Chemical Society,* vol. 134, pp. 15016-15021, 2012.

[55] M. O'Keeffe and O. M. Yaghi, "Deconstructing the crystal structures of metal-organic frameworks and related materials into their underlying nets," *Chemical Reviews,* vol. 112, pp. 675-702, 2012.

[56] I. J. Kang, N. A. Khan, E. Haque, and S. H. Jhung, "Chemical and thermal stability of isotypic metal-organic frameworks: Effect of metal ions," *Chemistry - A European Journal,* vol. 17, pp. 6437-6442, 2011.

[57] V. Colombo, S. Galli, H. J. Choi, G. D. Han, A. Maspero, G. Palmisano*, et al.*, "High thermal and chemical stability in pyrazolate-bridged metal–organic frameworks with exposed metal sites," *Chemical Science,* vol. 2, pp. 1311-1319, 2011.

[58] S. R. Batten, N. R. Champness, X. M. Chen, J. Garcia-Martinez, S. Kitagawa, L. Ohrstrom*, et al.*, "Coordination polymers, metal-organic frameworks and the need for terminology guidelines," *CrystEngComm,* vol. 14, pp. 3001-3004, 2012.

[59] A. Phan, C. J. Doonan, F. J. Uribe-Romo, C. B. Knobler, M. O'Keeffe, and O. M. Yaghi, "Synthesis, structure and carbon dioxide capture properties of zeolitic imidazolate frameworks," *Accounts of Chemical Research,* vol. 43, pp. 58-67, 2010.

[60] S. S.-Y. Chui, S. M.-F. Lo, J. P. H. Charmant, A. G. Orpen, and I. D. Williams, "A chemically functionalisable nanoporous material $[Cu_3(TMA)_2(H_2O)_3]_n$," *Science,* vol. 283, pp. 1148-1150, 1999.

[61] J. H. Cavka, S. Jakobsen, U. Olsbye, N. Guillou, C. Lamberti, S. Bordiga*, et al.*, "A new zirconium inorganic building brick forming metal organic frameworks with exceptional stability," *Journal of American Chemical Society,* vol. 130, pp. 13850-13851, 2008.

[62] C. Janiak and J. K. Vieth, "MOFs, MILs and more: Concepts, properties and applications for porous coordination networks (PCNs)," *New Journal of Chemistry,* vol. 34, pp. 2366-2388, 2010.

[63] M. Díaz-García, Á. Mayoral, I. Díaz, and M. Sánchez-Sánchez, "Nanoscaled M-MOF-74 materials prepared at room temperature," *Crystal Growth & Design,* vol. 14, pp. 2479-2487, 2014.

[64] W. Kleist, M. Maciejewski, and A. Baiker, "MOF-5 based mixed-linker metal–organic frameworks: Synthesis, thermal stability and catalytic application," *Thermochimica Acta,* vol. 499, pp. 71-78, 2010.

[65] K. Leus, T. Bogaerts, J. De Decker, H. Depauw, K. Hendrickx, H. Vrielinck*, et al.*, "Systematic study of the chemical and hydrothermal stability of selected "stable" metal organic frameworks," *Microporous and Mesoporous Materials,* vol. 226, pp. 110-116, 2016.

[66] N. C. Burtch, H. Jasuja, and K. S. Walton, "Water stability and adsorption in metal-organic frameworks," *Chemical Reviews,* vol. 114, pp. 10575-10612, 2014.

[67] R. Adams, C. Carson, J. Ward, R. Tannenbaum, and W. Koros, "Metal organic framework mixed matrix membranes for gas separations," *Microporous and Mesoporous Materials,* vol. 131, pp. 13-20, 2010.

[68] S. Li and F. Huo, "Metal-organic framework composites: From fundamentals to applications," *Nanoscale,* vol. 7, pp. 7482-7501, 2015.

[69] A. K. Chaudhari, M. R. Ryder, and J. C. Tan, "Photonic hybrid crystals constructed from *in situ* host-guest nanoconfinement of a light-emitting complex in metal-organic framework pores," *Nanoscale,* vol. 8, pp. 6851-6859, 2016.

[70] M. Sabo, A. Henschel, H. Fröde, E. Klemm, and S. Kaskel, "Solution infiltration of palladium into MOF-5: Synthesis, physisorption and catalytic properties," *Journal of Materials Chemistry,* vol. 17, pp. 3827-3832, 2007.

[71] A. Aijaz, A. Karkamkar, Y. J. Choi, N. Tsumori, E. Ronnebro, T. Autrey*, et al.*, "Immobilising highly catalytically active Pt nanoparticles inside the pores of metal-organic framework: A double solvents approach," *Journal of American Chemical Society,* vol. 134, pp. 13926-13929, 2012.

[72] X.-W. Liu, T.-J. Sun, J.-L. Hu, and S.-D. Wang, "Composites of metal–organic frameworks and carbon-based materials: Preparations, functionalities and applications," *Journal of Materials Chemistry A,* vol. 4, pp. 3584-3616, 2016.

[73] J. Aguilera-Sigalat and D. Bradshaw, "Synthesis and applications of metal-organic framework–quantum dot (QD@MOF) composites," *Coordination Chemistry Reviews,* vol. 307, pp. 267-291, 2016.

[74] L. J. Yang, B. B. Tang, and P. Y. Wu, "Metal-organic framework-graphene oxide composites: A facile method to highly improve the proton conductivity of PEMs operated under low humidity," *Journal of Materials Chemistry A,* vol. 3, pp. 15838-15842, 2015.

[75] E. V. Perez, K. J. Balkus, J. P. Ferraris, and I. H. Musselman, "Mixed-matrix membranes containing MOF-5 for gas separations," *Journal of Membrane Science,* vol. 328, pp. 165-173, 2009.

[76] W. Li, Q. Meng, C. Zhang, and G. Zhang, "Metal-organic framework/PVDF composite membranes with high H_2 permselectivity synthesised by ammoniation," *Chemistry - A European Journal,* vol. 21, pp. 7224-7230, 2015.

[77] U. Betke, S. Proemmel, S. Rannabauer, A. Lieb, M. Scheffler, and F. Scheffler, "Silane functionalized open-celled ceramic foams as support structure in metal organic framework composite materials," *Microporous and Mesoporous Materials,* vol. 239, pp. 209-220, 2017.

[78] M. S. Denny, Jr. and S. M. Cohen, "*In situ* modification of metal-organic frameworks in mixed-matrix membranes," *Angewandte Chemie-International Edition,* vol. 54, pp. 9029-9032, 2015.

[79] L. D. O'Neill, H. Zhang, and D. Bradshaw, "Macro-/microporous MOF composite beads," *Journal of Materials Chemistry,* vol. 20, pp. 5720-5726, 2010.

[80] Q. L. Song, S. K. Nataraj, M. V. Roussenova, J. C. Tan, D. J. Hughes, W. Li*, et al.*, "Zeolitic imidazolate framework (ZIF-8) based polymer nanocomposite membranes for gas separation," *Energy & Environmental Science,* vol. 5, pp. 8359-8369, 2012.

[81] T. Rodenas, M. van Dalen, P. Serra-Crespo, F. Kapteijn, and J. Gascon, "Mixed matrix membranes based on NH_2-functionalized MIL-type MOFs: Influence of structural and operational parameters on the CO_2/CH_4 separation performance," *Microporous and Mesoporous Materials,* vol. 192, pp. 35-42, 2014.

[82] S. N. Wijenayake, N. P. Panapitiya, C. N. Nguyen, Y. Huang, K. J. Balkus, I. H. Musselman*, et al.*, "Composite membranes with a highly selective polymer skin for hydrogen separation," *Separation and Purification Technology,* vol. 135, pp. 190-198, 2014.

[83] K.-Y. Andrew Lin and H.-A. Chang, "A zeolitic imidazole framework (ZIF)–sponge composite prepared via a surfactant-assisted dip-coating method," *Journal of Materials Chemistry A,* vol. 3, pp. 20060-20064, 2015.

[84] S. Shahid, K. Nijmeijer, S. Nehache, I. Vankelecom, A. Deratani, and D. Quemener, "MOF-mixed matrix membranes: Precise dispersion of MOF particles with better compatibility via a particle fusion approach for enhanced gas separation properties," *Journal of Membrane Science,* vol. 492, pp. 21-31, 2015.

[85] R. Ostermann, J. Cravillon, C. Weidmann, M. Wiebcke, and B. M. Smarsly, "Metal-organic framework nanofibers via electrospinning," *Chemical Communications,* vol. 47, pp. 442-444, 2011.

[86] S. An, J. S. Lee, B. N. Joshi, H. S. Jo, K. Titov, J. S. Chang*, et al.*, "Freestanding fiber mats of zeolitic imidazolate framework 7 via one-step, scalable electrospinning," *Journal of Applied Polymer Science,* vol. 133, p. 43788, 2016.

[87] M. Asiabi, A. Mehdinia, and A. Jabbari, "Preparation of water stable methyl-modified metal-organic framework-5/polyacrylonitrile composite nanofibers via electrospinning and their application for solid-phase extraction of two estrogenic drugs in urine samples," *Journal of Chromatography A,* vol. 1426, pp. 24-32, 2015.

[88] M. Bechelany, M. Drobek, C. Vallicari, A. Abou Chaaya, A. Julbe, and P. Miele, "Highly crystalline MOF-based materials grown on electrospun nanofibers," *Nanoscale,* vol. 7, pp. 5794-5802, 2015.

[89] M. Gao, L. W. Zeng, J. Nie, and G. P. Ma, "Polymer-metal-organic framework core-shell framework nanofibers via electrospinning and their gas adsorption activities," *RSC Advances,* vol. 6, pp. 7078-7085, 2016.

[90] J.-J. Li, L.-T. Zhu, and Z.-H. Luo, "Electrospun fibrous membrane with enhanced swithchable oil/water wettability for oily water separation," *Chemical Engineering Journal,* vol. 287, pp. 474-481, 2016.

[91] M. Wu, Y. Ai, B. Zeng, and F. Zhao, "*In situ* solvothermal growth of metal-organic framework-ionic liquid functionalised graphene nanocomposite for highly efficient enrichment of chloramphenicol and thiamphenicol," *Journal of Chromatography A,* vol. 1427, pp. 1-7, 2016.

[92] Y. Zhu, H. Wang, J. Zhu, L. Chang, and L. Ye, "Nanoindentation and thermal study of polyvinylalcohol/graphene oxide nanocomposite film through organic/inorganic assembly," *Applied Surface Science,* vol. 349, pp. 27-34, 2015.

[93] X. Yan, X. Hu, and S. Komarneni, "Facile synthesis of mesoporous MOF/silica composites," *RSC Advances,* vol. 4, pp. 57501-57504, 2014.

[94] J. Fu, S. Das, G. Xing, T. Ben, V. Valtchev, and S. Qiu, "Fabrication of COF-MOF composite membranes and their highly selective separation of H_2/CO_2," *Journal of American Chemical Society,* vol. 138, pp. 7673-7680, 2016.

[95] Erik T. Thostenson, Zhifeng Ren, and T.-W. Chou, "Advances in the science and technology of carbon nanotubes and their composites: A review," *Composites Science and Technology,* vol. 61, pp. 1899-1912, 2001.

[96] K. T. Lau, C. Gu, and D. Hui, "A critical review on nanotube and nanotube/nanoclay related polymer composite materials," *Composites Part B-Engineering,* vol. 37, pp. 425-436, 2006.

[97] S. Wang, K. Wang, C. Dai, H. Shi, and J. Li, "Adsorption of Pb^{2+} on amino-functionalised core–shell magnetic mesoporous SBA-15 silica composite," *Chemical Engineering Journal,* vol. 262, pp. 897-903, 2015.

[98] S. Wu, T. Braschler, R. Anker, F. Wildhaber, A. Bertsch, J. Brugger*, et al.*, "Composite hydrogel-loaded alumina membranes for nanofluidic molecular filtration," *Journal of Membrane Science,* vol. 477, pp. 151-156, 2015.

[99] K. M. Liew, Z. X. Lei, and L. W. Zhang, "Mechanical analysis of functionally graded carbon nanotube reinforced composites: A review," *Composite Structures,* vol. 120, pp. 90-97, 2015.

[100] Y. Han, P. Qi, X. Feng, S. Li, X. Fu, H. Li*, et al.*, "*In situ* growth of MOFs on the surface of Si nanoparticles for highly efficient lithium storage: Si@MOF nanocomposites as anode materials for lithium-ion batteries," *ACS Applied Materials & Interfaces,* vol. 7, pp. 2178-2182, 2015.

[101] N. W. Khun, E. M. Mahdi, S. Q. Ying, T. Sui, A. M. Korsunsky, and J. C. Tan, "Fine-scale tribological performance of zeolitic imidazolate framework (ZIF-8) based polymer nanocomposite membranes," *APL Materials,* vol. 2, p. 124101, 2014.

[102] S. Neelakantan, J. C. Tan, and A. E. Markaki, "Out-of-plane auxeticity in sintered fibre network mats," *Scripta Materialia,* vol. 106, pp. 30-33, 2015.

[103] L. Diestel, N. Y. Wang, B. Schwiedland, F. Steinbach, U. Giese, and J. Caro, "MOF based MMMs with enhanced selectivity due to hindered linker distortion," *Journal of Membrane Science,* vol. 492, pp. 181-186, 2015.

[104] R. Gao, Q. Zhang, R. Lv, F. Soyekwo, A. Zhu, and Q. Liu, "Highly efficient polymer–MOF nanocomposite membrane for pervaporation separation of water/methanol/MTBE ternary mixture," *Chemical Engineering Research and Design,* vol. 117, pp. 688-697, 2017.

[105] M. J. C. Ordoñez, K. J. Balkus, J. P. Ferraris, and I. H. Musselman, "Molecular sieving realized with ZIF-8/Matrimid® mixed-matrix membranes," *Journal of Membrane Science,* vol. 361, pp. 28-37, 2010.

[106] S. J. D. Smith, C. H. Lau, J. I. Mardel, M. Kitchin, K. Konstas, B. P. Ladewig*, et al.*, "Physical aging in glassy mixed matrix membranes; tuning particle interaction for mechanically robust nanocomposite films," *Journal of Materials Chemistry A,* vol. 4, pp. 10627-10634, 2016.

[107] W. C. Oliver and G. M. Pharr, "Measurement of hardness and elastic modulus by instrumented indentation: Advances in understanding and refinements to methodology," *Journal of Materials Research,* vol. 19, pp. 3-20, 2004.

[108] W. C. Oliver and G. M. Pharr, "An improved technique for determining hardness and elastic-modulus using load and displacement sensing indentation experiments," *Journal of Materials Research,* vol. 7, pp. 1564-1583, 1992.

[109] J. C. Tan, C. A. Merrill, J. B. Orton, and A. K. Cheetham, "Anisotropic mechanical properties of polymorphic hybrid inorganic-organic framework materials with different dimensionalities," *Acta Materialia,* vol. 57, pp. 3481-3496, 2009.

[110] A. M. Díez-Pascual, M. A. Gómez-Fatou, F. Ania, and A. Flores, "Nanoindentation in polymer nanocomposites," *Progress in Materials Science,* vol. 67, pp. 1-94, 2015.

[111] S. Lee, B. G. Choi, D. Choi, and H. S. Park, "Nanoindentation of annealed Nafion/sulfonated graphene oxide nanocomposite membranes for the measurement of mechanical properties," *Journal of Membrane Science,* vol. 451, pp. 40-45, 2014.

[112] R. Lakes, Viscoelastic materials, 1st ed. New York: Cambridge University Press, 2009.

[113] N. Saba, M. Jawaid, O. Y. Alothman, and M. T. Paridah, "A review on dynamic mechanical properties of natural fibre reinforced polymer composites," *Construction and Building Materials,* vol. 106, pp. 149-159, 2016.

[114] F. Gardea, B. Glaz, J. Riddick, D. C. Lagoudas, and M. Naraghi, "Thermally activated energy dissipation in semi-crystalline polymer nanocomposites," *Composites Science and Technology,* vol. 134, pp. 275-286, 2016.

[115] M. J. M. Ridzuan, M. S. A. Majid, M. Afendi, M. N. Mazlee, and A. G. Gibson, "Thermal behaviour and dynamic mechanical analysis of Pennisetum purpureum/glass-reinforced epoxy hybrid composites," *Composite Structures,* vol. 152, pp. 850-859, 2016.

[116] K. S. Park, Z. Ni, A. P. Cote, J. Y. Choi, R. Huang, F. J. Uribe-Romo*, et al.*, "Exceptional chemical and thermal stability of zeolitic imidazolate frameworks," *Proceedings of the National Academy of Sciences of the United States of America,* vol. 103, pp. 10186-10191, 2006.

[117] Y. W. Li and R. T. Yang, "Hydrogen storage in metal-organic and covalent-organic frameworks by spillover," *AIChE Journal,* vol. 54, pp. 269-279, 2008.

[118] E. Ahmadi Feijani, A. Tavasoli, and H. Mahdavi, "Improving gas separation performance of Poly(vinylidene fluoride) based mixed matrix membranes containing metal–organic frameworks by chemical modification," *Industrial & Engineering Chemistry Research,* vol. 54, pp. 12124-12134, 2015.

[119] C. Zhang, Y. Dai, J. R. Johnson, O. Karvan, and W. J. Koros, "High performance ZIF-8/6FDA-DAM mixed matrix membrane for propylene/propane separations," *Journal of Membrane Science,* vol. 389, pp. 34-42, 2012.

[120] H. Jin, A. Wollbrink, R. Yao, Y. Li, J. Caro, and W. Yang, "A novel CAU-10-H MOF membrane for hydrogen separation under hydrothermal conditions," *Journal of Membrane Science,* vol. 513, pp. 40-46, 2016.

[121] M. Roushani, A. Valipour, and Z. Saedi, "Electroanalytical sensing of Cd^{2+} based on metal–organic framework modified carbon paste electrode," *Sensors and Actuators B: Chemical,* vol. 233, pp. 419-425, 2016.

[122] C. G. Silva, A. Corma, and H. García, "Metal–organic frameworks as semiconductors," *Journal of Materials Chemistry,* vol. 20, pp. 3141-3156, 2010.

[123] G. Wyszogrodzka, B. Marszalek, B. Gil, and P. Dorozynski, "Metal-organic frameworks: Mechanisms of antibacterial action and potential applications," *Drug Discovery Today,* vol. 21, pp. 1009-1018, 2016.

[124] S. Ding, Q. Yan, H. Jiang, Z. Zhong, R. Chen, and W. Xing, "Fabrication of Pd@ZIF-8 catalysts with different Pd spatial distributions and their catalytic properties," *Chemical Engineering Journal,* vol. 296, pp. 146-153, 2016.

[125] Y. Cui, B. Li, H. He, W. Zhou, B. Chen, and G. Qian, "Metal-organic frameworks as platforms for functional materials," *Accounts of Chemical Research,* vol. 49, pp. 483-493, 2016.

[126] Z. Bao, G. Chang, H. Xing, R. Krishna, Q. Ren, and B. Chen, "Potential of microporous metal–organic frameworks for separation of hydrocarbon mixtures," *Energy & Environmental Science,* vol. 9, pp. 3612-3641, 2016.

[127] X. Dong, Q. Liu, and A. Huang, "Highly permselective MIL-68(Al)/matrimid mixed matrix membranes for CO_2/CH_4 separation," *Journal of Applied Polymer Science,* vol. 133, pp. 43485-43493, 2016.

[128] B. Zornoza, C. Tellez, J. Coronas, J. Gascon, and F. Kapteijn, "Metal organic framework based mixed matrix membranes: An increasingly important field of research with a large application potential," *Microporous and Mesoporous Materials,* vol. 166, pp. 67-78, 2013.

[129] W. J. Koros and C. Zhang, "Materials for next-generation molecularly selective synthetic membranes," *Nature Materials,* 2017.

[130] A. Knebel, S. Friebe, N. C. Bigall, M. Benzaqui, C. Serre, and J. Caro, "Comparative study of MIL-96(Al) as continuous metal-organic frameworks layer and mixed-matrix membrane," *ACS Applied Materials & Interfaces,* vol. 8, pp. 7536-7544, 2016.

[131] J. Hou, P. D. Sutrisna, Y. Zhang, and V. Chen, "Formation of ultrathin, continuous metal-organic framework membranes on flexible polymer substrates," *Angewandte Chemie-International Edition,* vol. 55, pp. 3947-3951, 2016.

[132] J. Kim, J. Choi, Y. Soo Kang, and J. Won, "Matrix effect of mixed-matrix membrane containing CO_2-selective MOFs," *Journal of Applied Polymer Science,* vol. 133, pp. 42853-42861, 2016.

[133] I. Erucar and S. Keskin, "Computational screening of metal organic frameworks for mixed matrix membrane applications," *Journal of Membrane Science,* vol. 407, pp. 221-230, 2012.

[134] J. E. Bachman, Z. P. Smith, T. Li, T. Xu, and J. R. Long, "Enhanced ethylene separation and plasticization resistance in polymer membranes incorporating metal-organic framework nanocrystals," *Nature Materials,* vol. 15, pp. 845-849, 2016.

[135] T. L. Hu, H. Wang, B. Li, R. Krishna, H. Wu, W. Zhou*, et al.*, "Microporous metal-organic framework with dual functionalities for highly efficient removal of acetylene from ethylene/acetylene mixtures," *Nature Communications,* vol. 6, p. 7328, 2015.

[136] J. Ploegmakers, S. Japip, and K. Nijmeijer, "Mixed matrix membranes containing MOFs for ethylene/ethane separation Part A: Membrane preparation and characterization," *Journal of Membrane Science,* vol. 428, pp. 445-453, 2013.

[137] H. Ma, X. Li, T. Yan, Y. Li, Y. Zhang, D. Wu*, et al.*, "Electrochemiluminescent immunosensing of prostate-specific antigen based on silver nanoparticles-doped Pb (II) metal-organic framework," *Biosensors and Bioelectronics,* vol. 79, pp. 379-385, 2016.

[138] R. C. Huxford, J. Della Rocca, and W. Lin, "Metal-organic frameworks as potential drug carriers," *Current Opinion in Chemical Biology,* vol. 14, pp. 262-268, 2010.

[139] S. Keskin and S. Kızılel, "Biomedical applications of metal organic frameworks," *Industrial & Engineering Chemistry Research,* vol. 50, pp. 1799-1812, 2011.

[140] C. Adhikari and A. Chakraborty, "Smart approach for *In Situ* one-step encapsulation and controlled delivery of a chemotherapeutic drug using metal-organic framework-drug composites in aqueous media," *ChemPhysChem,* vol. 17, pp. 1070-1077, 2016.

[141] H. X. Zhao, Q. Zou, S. K. Sun, C. S. Yu, X. J. Zhang, R. J. Li*, et al.*, "Theranostic metal-organic framework core-shell composites for magnetic resonance imaging and drug delivery," *Chemical Science,* vol. 7, pp. 5294-5301, 2016.

[142] J. Cravillon, S. Munzer, S. J. Lohmeier, A. Feldhoff, K. Huber, and M. Wiebcke, "Rapid room-temperature synthesis and characterisation of nanocrystals of a prototypical zeolitic imidazolate framework," *Chemistry of Materials,* vol. 21, pp. 1410-1412, 2009.

[143] J. Cravillon, R. Nayuk, S. Springer, A. Feldhoff, K. Huber, and M. Wiebcke, "Controlling zeolitic imidazolate framework nano- and microcrystal formation: Insight into crystal growth by time-resolved in situ static light scattering," *Chemistry of Materials,* vol. 23, pp. 2130-2141, 2011.

[144] R. D. Widdle, A. K. Bajaj, and P. Davies, "Measurement of the poisson's ratio of flexible polyurethane foam and its influence on a uniaxial compression model," *International Journal of Engineering Science,* vol. 46, pp. 31-49, 2008.

[145] R. W. Ogden, "Large deformation isotropic elasticity - On the correlation of theory and experiment for incompressible rubberlike solids," *Proceedings of the Royal Society A,* vol. 326, pp. 565-584, 1972.

[146] E. M. Mahdi and J. C. Tan, "Mixed-matrix membranes of zeolitic imidazolate framework (ZIF-8)/Matrimid nanocomposite: Thermo-mechanical stability and viscoelasticity underpinning membrane separation performance," *Journal of Membrane Science,* vol. 498, pp. 276-290, 2016.

[147] J.-R. Li, Y. Ma, M. C. McCarthy, J. Sculley, J. Yu, H.-K. Jeong*, et al.*, "Carbon dioxide capture-related gas adsorption and separation in metal-organic frameworks," *Coordination Chemistry Reviews,* vol. 255, pp. 1791-1823, 2011.

[148] D. Banerjee, A. J. Cairns, J. Liu, R. K. Motkuri, S. K. Nune, C. A. Fernandez*, et al.*, "Potential of metal-organic frameworks for separation of xenon and krypton," *Accounts of Chemical Research,* vol. 48, pp. 211-9, 2015.

[149] B. Li, H. M. Wen, W. Zhou, and B. Chen, "Porous metal-organic frameworks for gas storage and separation: what, how, and why?," *Journal of Physical Chemistry Letters,* vol. 5, pp. 3468-79, 2014.

[150] S. R. Venna and M. A. Carreon, "Highly permeable zeolite imidazolate framework-8 membranes for CO2/CH4 separation," *Journal of American Chemical Society,* vol. 132, pp. 76-8, 2010.

[151] T. Lee, H. Kim, W. Cho, D.-Y. Han, M. Ridwan, C. W. Yoon*, et al.*, "Thermosensitive structural changes and adsorption properties of zeolitic imidazolate framework-8 (ZIF-8)," *Journal of Physical Chemistry C,* vol. 119, pp. 8226-8237, 2015.

[152] S. J. Smith, B. P. Ladewig, A. J. Hill, C. H. Lau, and M. R. Hill, "Post-synthetic Ti exchanged UiO-66 metal-organic frameworks that deliver exceptional gas permeability in mixed matrix membranes," *Scientific Reports,* vol. 5, p. 7823, 2015.

[153] T. Rodenas, I. Luz, G. Prieto, B. Seoane, H. Miro, A. Corma*, et al.*, "Metal-organic framework nanosheets in polymer composite materials for gas separation," *Nature Materials,* vol. 14, pp. 48-55, 2015.

[154] D. Ballestero, R. Juan, A. Ibarra, C. Gomez-Gimenez, C. Ruiz, B. Rubio*, et al.*, "Effect of thermal treatments on the morphology, chemical state and lattice structure of gold nanoparticles deposited onto carbon structured monoliths," *Colloids and Surfaces A-Physicochemical and Engineering Aspects,* vol. 468, pp. 140-150, 2015.

[155] H. S. Khare and D. L. Burris, "A quantitative method for measuring nanocomposite dispersion," *Polymer,* vol. 51, pp. 719-729, 2010.

[156] A. C. Comer, D. S. Kalika, B. W. Rowe, B. D. Freeman, and D. R. Paul, "Dynamic relaxation characteristics of Matrimid® polyimide," *Polymer,* vol. 50, pp. 891-897, 2009.

[157] S. Hwang, W. S. Chi, S. J. Lee, S. H. Im, J. H. Kim, and J. Kim, "Hollow ZIF-8 nanoparticles improve the permeability of mixed matrix membranes for CO_2/CH_4 gas separation," *Journal of Membrane Science,* vol. 480, pp. 11-19, 2015.

[158] S. J. K. Jensen, T. H. Tang, and I. G. Csizmadia, "Hydrogen-bonding ability of a methyl group," *Journal of Physical Chemistry A,* vol. 107, pp. 8975-8979, 2003.

[159] M. Peydayesh, S. Asarehpour, T. Mohammadi, and O. Bakhtiari, "Preparation and characterization of SAPO-34 – Matrimid® 5218 mixed matrix membranes for CO2/CH4 separation," *Chemical Engineering Research and Design,* vol. 91, pp. 1335-1342, 2013.

[160] F. Dorosti, M. Omidkhah, and R. Abedini, "Fabrication and characterization of Matrimid/MIL-53 mixed matrix membrane for CO2/CH4 separation," *Chemical Engineering Research and Design,* vol. 92, pp. 2439-2448, 2014.

[161] X. Liang, F. Zhang, W. Feng, X. Zou, C. Zhao, H. Na*, et al.*, "From metal–organic framework (MOF) to MOF–polymer composite membrane: Enhancement of low-humidity proton conductivity," *Chemical Science,* vol. 4, pp. 983-992, 2013.

[162] M. J. Neufeld, B. R. Ware, A. Lutzke, S. R. Khetani, and M. M. Reynolds, "Water-stable metal-organic framework/polymer composites compatible with human hepatocytes," *ACS Applied Materials & Interfaces,* vol. 8, pp. 19343-52, 2016.

[163] R. Semino, N. A. Ramsahye, A. Ghoufi, and G. Maurin, "Microscopic model of the metal-organic framework/polymer Interface: a first step toward understanding the compatibility in mixed matrix membranes," *ACS Applied Materials & Interfaces,* vol. 8, pp. 809-819, 2016.

[164] S. A. Moggach, T. D. Bennett, and A. K. Cheetham, "The effect of pressure on ZIF-8: Increasing pore size with pressure and the formation of a high-pressure phase at 1.47 GPa," *Angewandte Chemie-International Edition,* vol. 48, pp. 7087-7089, 2009.

[165] C. Casado-Coterillo, J. Soto, M. T. Jimaré, S. Valencia, A. Corma, C. Téllez*, et al.*, "Preparation and characterization of ITQ-29/polysulfone mixed-matrix membranes for gas separation: Effect of zeolite composition and crystal size," *Chemical Engineering Science,* vol. 73, pp. 116-122, 2012.

[166] D. G. Fesko and N. W. Tschoegl, "Time-temperature superposition in thermorheologically Complex Materials," *Journal of Polymer Science Part C-Polymer Symposium,* vol. 35, pp. 180-184, 1971.

[167] F. Schwarzl and A. J. Staverman, "Time-temperature dependence of linear viscoelastic behavior," *Journal of Applied Physics,* vol. 23, pp. 838-843, 1952.

[168] J. C. Tan and T. W. Clyne, "Ferrous fibre network materials for jet noise reduction in aeroengines part II: Thermo-mechanical stability," *Advanced Engineering Materials,* vol. 10, pp. 201-209, 2008.

[169] T. H. Bae and J. R. Long, "CO_2/N_2 separations with mixed-matrix membranes containing Mg_2(dobdc) nanocrystals," *Energy & Environmental Science,* vol. 6, pp. 3565-3569, 2013.

[170] T. H. Bae, J. S. Lee, W. L. Qiu, W. J. Koros, C. W. Jones, and S. Nair, "A high-performance gas-separation membrane containing submicrometer-sized metal-organic framework crystals," *Angewandte Chemie-International Edition,* vol. 49, pp. 9863-9866, 2010.

[171] J. C. Tan and A. K. Cheetham, "Mechanical properties of hybrid inorganic-organic framework materials: Establishing fundamental structure-property relationships," *Chemical Society Reviews,* vol. 40, pp. 1059-1080, 2011.

[172] R. O. Ritchie, "The conflicts between strength and toughness," *Nature Materials,* vol. 10, pp. 817-822, 2011.

[173] S. Savagatrup, A. D. Printz, T. F. O'Connor, A. V. Zaretski, D. Rodriquez, E. J. Sawyer*, et al.*, "Mechanical degradation and stability of organic solar cells: molecular and microstructural determinants," *Energy & Environmental Science,* vol. 8, pp. 55-80, 2015.

[174] M. G. De Angelis and G. C. Sarti, "Gas sorption and permeation in mixed matrix membranes based on glassy polymers and silica nanoparticles," *Current Opinion in Chemical Engineering,* vol. 1, pp. 148-155, 2012.

[175] J. Caro, "Are MOF membranes better in gas separation than those made of zeolites?," *Current Opinion in Chemical Engineering,* vol. 1, pp. 77-83, 2011.

[176] P. Bernardo, E. Drioli, and G. Golemme, "Membrane gas separation: A review/state-of-the-art," *Industrial & Engineering Chemistry Research,* vol. 48, pp. 4638-4663, 2009.

[177] R. W. Baker, "Future directions of membrane gas separation technology," *Industrial & Engineering Chemistry Research,* vol. 41, pp. 1393-1411, 2002.

[178] D. Hua, Y. K. Ong, Y. Wang, T. Yang, and T.-S. Chung, "ZIF-90/P84 mixed matrix membranes for pervaporation dehydration of isopropanol," *Journal of Membrane Science,* vol. 453, pp. 155-167, 2014.

[179] E. M. Mahdi and J. C. Tan, "Dynamic molecular interactions between polyurethane and ZIF-8 in a polymer-MOF nanocomposite: Microstructural, thermo-mechanical and viscoelastic effects," *Polymer,* vol. 97, pp. 31-43, 2016.

[180] P. Li, K. Sun, and J. Ouyang, "Stretchable and conductive polymer films prepared by solution blending," *ACS Applied Material Interfaces,* vol. 7, pp. 18415-18423, 2015.

[181] G. Ren, Y. Miao, L. Qiao, Y. Qin, X. Wang, and F. Wang, "Toughening of amorphous poly(propylene carbonate) by rubbery CO_2-based polyurethane: Transition from brittle to ductile," *RSC Advances,* vol. 5, pp. 49979-49986, 2015.

[182] V. Kanyanta and A. Ivankovic, "Mechanical characterisation of polyurethane elastomer for biomedical applications," *Journal of the Mechanical Behaviour of Biomedical Materials,* vol. 3, pp. 51-62, 2010.

[183] N. G. McCrum, C. P. Buckley, and C. B. Bucknall, Principles of Polymer Engineering, 2nd ed. Oxford: Oxford University Press, 1997.

[184] S. Sen, S. Patil, and D. S. Argyropoulos, "Thermal properties of lignin in copolymers, blends, and composites: A review," *Green Chemistry,* vol. 17, pp. 4862-4887, 2015.

[185] P.-Y. Le Gac, M. Arhant, P. Davies, and A. Muhr, "Fatigue behavior of natural rubber in marine environment: Comparison between air and sea water," *Materials & Design,* vol. 65, pp. 462-467, 2015.

[186] R. A. Ghunem, S. H. Jayaram, and E. A. Cherney, "The DC inclined-plane tracking and erosion test and the role of inorganic fillers in silicone rubber for DC insulation," *IEEE Electrical Insulation Magazine,* vol. 31, pp. 12-21, 2015.

[187] F. Tornuk, M. Hancer, O. Sagdic, and H. Yetim, "LLDPE based food packaging incorporated with nanoclays grafted with bioactive compounds to extend shelf life of some meat products," *LWT - Food Science and Technology,* vol. 64, pp. 540-546, 2015.

[188] M. Gorji, A. A. A. Jeddi, and A. A. Gharehaghaji, "Fabrication and characterisation of polyurethane electrospun nanofiber membranes for protective clothing applications," *Journal of Applied Polymer Science,* vol. 125, pp. 4135-4141, 2012.

[189] H. Golbakshi and M. Namjoo, "Investigating temperature effects on mechanical behavior of rubber compounds embedded in composite structure of pneumatic tires," *The International Journal of Advanced Manufacturing Technology,* vol. 7, pp. 19-25, 2014.

[190] H. Liu, X. Wang, and D. Wu, "Synthesis of a novel linear polyphosphazene-based epoxy resin and its application in halogen-free flame-resistant thermosetting systems," *Polymer Degradation and Stability,* vol. 118, pp. 45-58, 2015.

[191] M. Akiba and A. S. Hashim, "Vulcanisation and crosslinking in elastomers," *Progress in Polymer Science,* vol. 22, pp. 475-521, 1997.

[192] L. Tan, J. L. Hu, and H. F. Zhao, "Design of bilayered nanofibrous mats for wound dressing using an electrospinning technique," *Materials Letters,* vol. 156, pp. 46-49, 2015.

[193] R. M. Jones, Mechanics of Composites Materials, 2nd ed.: Taylor & Francis, 1999.

[194] L. H. Sperling, Introduction to Physical Polymer Science, 4th ed.: Wiley-Interscience, 2006.

[195] M. D. Allendorf and V. Stavila, "Crystal engineering, structure–function relationships, and the future of metal–organic frameworks," *CrystEngComm,* vol. 17, pp. 229-246, 2015.

[196] S. Shahid and K. Nijmeijer, "Performance and plasticisation behavior of polymer–MOF membranes for gas separation at elevated pressures," *Journal of Membrane Science,* vol. 470, pp. 166-177, 2014.

[197] X. L. Yang, C. Zou, Y. He, M. Zhao, B. Chen, S. Xiang*, et al.*, "A stable microporous mixed-metal metal-organic framework with highly active Cu^{2+} sites for efficient cross-dehydrogenative coupling reactions," *Chemistry - A European Journal,* vol. 20, pp. 1447-1452, 2014.

[198] R. Grunker, V. Bon, P. Muller, U. Stoeck, S. Krause, U. Mueller*, et al.*, "A new metal-organic framework with ultra-high surface area," *Chemical Communications,* vol. 50, pp. 3450-3452, 2014.

[199] B. Barth, M. Mendt, A. Pöppl, and M. Hartmann, "Adsorption of nitric oxide in metal-organic frameworks: Low temperature IR and EPR spectroscopic evaluation of the role of open metal sites," *Microporous and Mesoporous Materials,* vol. 216, pp. 97-110, 2015.

[200] M. Hegde, S. Shahid, B. Norder, T. J. Dingemans, and K. Nijmeijer, "Gas transport in metal organic framework–polyetherimide mixed matrix membranes: The role of the polyetherimide backbone structure," *Polymer,* vol. 81, pp. 87-98, 2015.

[201] M. Fang, C. Wu, Z. Yang, T. Wang, Y. Xia, and J. Li, "ZIF-8/PDMS mixed matrix membranes for propane/nitrogen mixture separation: Experimental result and permeation model validation," *Journal of Membrane Science,* vol. 474, pp. 103-113, 2015.

[202] H. Zhu, Q. Zhang, and S. Zhu, "Preparation of raspberry-like ZIF-8/PS composite spheres via dispersion polymerisation," *Dalton Transactions,* vol. 44, pp. 16752-16757, 2015.

[203] T. Yang, G. M. Shi, and T.-S. Chung, "Symmetric and asymmetric zeolitic imidazolate frameworks (ZIFs)/Polybenzimidazole (PBI) nanocomposite membranes for hydrogen purification at high temperatures," *Advanced Energy Materials,* vol. 2, pp. 1358-1367, 2012.

[204] A. F. Bushell, M. P. Attfield, C. R. Mason, P. M. Budd, Y. Yampolskii, L. Starannikova*, et al.*, "Gas permeation parameters of mixed matrix membranes based on the polymer of intrinsic microporosity PIM-1 and the zeolitic imidazolate framework ZIF-8," *Journal of Membrane Science,* vol. 427, pp. 48-62, 2013.

[205] Y. Pan, D. Heryadi, F. Zhou, L. Zhao, G. Lestari, H. Su*, et al.*, "Tuning the crystal morphology and size of zeolitic imidazolate framework-8 in aqueous solution by surfactants," *CrystEngComm,* vol. 13, pp. 6937-6940, 2011.

[206] D. Ballestero, R. Juan, A. Ibarra, C. Gómez-Giménez, C. Ruiz, B. Rubio*, et al.*, "Effect of thermal treatments on the morphology, chemical state and lattice structure of gold nanoparticles deposited onto carbon structured monoliths," *Colloids and Surfaces A: Physicochemical and Engineering Aspects,* vol. 468, pp. 140-150, 2015.

[207] R. Shankar, U. Sahoo, and V. Shahi, "Synthesis and characterisation of fluorescent polymer−metal nanocomposites comprising Poly(silylene-co-silyne)s and silver nanoparticles," *Macromolecules,* vol. 44, pp. 3240-3249, 2011.

[208] A. V. Tobolsky, D. W. Carlson, and N. Indictor, "Rubber elasticity and chain configuration," *Journal of Polymer Science,* vol. 54, pp. 175-192, 1961.

[209] G. R. Deen, E. K. Lim, C. H. Mah, and K. M. Heng, "New cationic linear copolymers and hydrogels of N-Vinyl caprolactam and N-Acryloyl-N′-ethyl piperazine: Synthesis, reactivity, influence of external stimuli on the LCST and swelling properties," *Industrial & Engineering Chemistry Research,* vol. 51, pp. 13354-13365, 2012.

[210] J. R. Collier, "Polymer deformation and orientation," *Industrial and Engineering Chemistry,* vol. 61, pp. 72-85, 1969.

[211] A. Kudasheva, S. Sorribas, B. Zornoza, C. Téllez, and J. Coronas, "Pervaporation of water/ethanol mixtures through polyimide based mixed matrix membranes containing ZIF-8, ordered mesoporous silica and ZIF-8-silica core-shell spheres," *Journal of Chemical Technology & Biotechnology,* vol. 90, pp. 669-677, 2015.

[212] D. Cai, K. Yusoh, and M. Song, "The mechanical properties and morphology of a graphite oxide nanoplatelet/polyurethane composite," *Nanotechnology,* vol. 20, p. 085712, 2009.

[213] S. Hietala, M. Koel, E. Skou, M. Elomaa, and F. Sundholm, "Thermal stability of styrene grated and sulfonated proton conducting membranes based on poly(vinylidene flouride)," *Journal of Materials Chemistry,* vol. 8, pp. 1127-1133, 1998.

[214] S. Belhaj Messaoud, A. Takagaki, T. Sugawara, R. Kikuchi, and S. T. Oyama, "Mixed matrix membranes using SAPO-34/polyetherimide for carbon dioxide/methane separation," *Separation and Purification Technology,* vol. 148, pp. 38-48, 2015.

[215] A. W. Coats and J. P. Redfern, "Thermogravimetric analysis: A review," *The Analyst,* vol. 88, pp. 906-924, 1963.

[216] G. Trovati, E. A. Sanches, S. C. Neto, Y. P. Mascarenhas, and G. O. Chierice, "Characterisation of polyurethane resins by FTIR, TGA, and XRD," *Journal of Applied Polymer Science,* vol. 115, pp. 263-268, 2010.

[217] X. Zheng, L. Wang, Q. Pei, S. He, S. Liu, and Z. Xie, "Metal–Organic Framework@Porous Organic Polymer Nanocomposite for Photodynamic Therapy," *Chemistry of Materials,* vol. 29, pp. 2374-2381, 2017.

[218] C. S. Liu, M. Chen, J. Y. Tian, L. Wang, M. Li, S. M. Fang*, et al.*, "Metal-organic framework supported on processable polymer matrix by in situ copolymerization for enhanced iron(III) detection," *Chemistry - A European Journal,* vol. 23, pp. 3885-3890, 2017.

[219] A. J. Crosby and J. Y. Lee, "Polymer nanocomposites: The “nano” effect on mechanical properties," *Polymer Reviews,* vol. 47, pp. 217-229, 2007.

[220] Z. Guo, T. Y. Kim, K. Lei, T. Pereira, J. G. Sugar, and H. T. Hahn, "Strengthening and thermal stabilization of polyurethane nanocomposites with silicon carbide nanoparticles by a surface-initiated-polymerization approach," *Composites Science and Technology,* vol. 68, pp. 164-170, 2008.

[221] C. Komalan, K. E. George, P. A. S. Kumar, K. T. Varughese, and S. Thomas, "Dynamic mechanical analysis of binary and ternary polymer blends based on nylon copolymer/EPDM rubber and EPM grafted maleic anhydride compatibiliser," *Express Polymer Letters,* vol. 1, pp. 641-653, 2007.

[222] F. G. Ornaghi, V. Pistor, and R. V. B. de Oliveira, "Thermoplastic polyurethane synthesis with modified montmorillonite prepared by torque rheometry: Investigation of morphological, thermal, chemical, and physical properties," *Journal of Applied Polymer Science,* vol. 132, pp. 42640-42650, 2015.

[223] J. W. Xiong, Z. Zheng, X. M. Qin, M. Li, H. Q. Li, and X. L. Wang, "The thermal and mechanical properties of a polyurethane/multi-walled carbon nanotube composite," *Carbon,* vol. 44, pp. 2701-2707, 2006.

[224] N. B. McKeown and P. M. Budd, "Polymers of intrinsic microporosity (PIMs): Organic materials for membrane separations, heterogeneous catalysis and hydrogen storage," *Chemical Society Reviews,* vol. 35, pp. 675-683, 2006.

[225] J. X. Ren, A. S. Silva, and R. Krishnamoorti, "Linear viscoelasticity of disordered polystyrene-polyisoprene block copolymer based layered-silicate nanocomposites," *Macromolecules,* vol. 33, pp. 3739-3746, 2000.

[226] E. M. Mahdi, A. K. Chaudhuri, and J.-C. Tan, "Capture and immobilisation of iodine (I2) utilising polymer-based ZIF-8 nanocomposite membranes," *Molecular Systems Design & Engineering,* vol. 1, pp. 122-131, 2016.

[227] A. Verbruggen, E. Laes, and S. Lemmens, "Assessment of the actual sustainability of nuclear fission power," *Renewable and Sustainable Energy Reviews,* vol. 32, pp. 16-28, 2014.

[228] V. S. Ramos, V. R. Crispim, and L. E. Brandao, "New filter for iodine applied in nuclear medicine services," *Applied Radiation and Isotopes,* vol. 82, pp. 111-118, 2013.

[229] V. H. M. Visschers, C. Keller, and M. Siegrist, "Climate change benefits and energy supply benefits as determinants of acceptance of nuclear power stations: Investigating an explanatory model," *Energy Policy,* vol. 39, pp. 3621-3629, 2011.

[230] L. G. Carneiro, E. A. de Lucena, C. d. S. Sampaio, A. L. Dantas, W. O. Sousa, M. S. Santos*, et al.*, "Internal dosimetry of nuclear medicine workers through the analysis of ^{131}I in aerosols," *Applied Radiation and Isotopes,* vol. 100, pp. 70-74, 2015.

[231] R. P. Rechard, J. H. Lee, E. L. Hardin, and C. R. Bryan, "Waste package degradation from thermal and chemical processes in performance assessments for the Yucca Mountain disposal system for spent nuclear fuel and high-level radioactive waste," *Reliability Engineering & System Safety,* vol. 122, pp. 145-164, 2014.

[232] A. Salama, M. F. El Amin, and S. Sun, "Numerical investigation of high level nuclear waste disposal in deep anisotropic geologic repositories," *Progress in Nuclear Energy,* vol. 85, pp. 747-755, 2015.

[233] D. F. Sava, M. A. Rodriguez, K. W. Chapman, P. J. Chupas, J. A. Greathouse, P. S. Crozier*, et al.*, "Capture of volatile iodine, a gaseous fission product, by zeolitic imidazolate framework-8," *Journal of American Chemical Society,* vol. 133, pp. 12398-12401, 2011.

[234] D. F. Sava, K. W. Chapman, M. A. Rodriguez, J. A. Greathouse, P. S. Crozier, H. Zhao*, et al.*, "Competitive I_2 sorption by Cu-BTC from humid gas streams," *Chemistry of Materials,* vol. 25, pp. 2591-2596, 2013.

[235] S. L. Ma, S. M. Islam, Y. Shim, Q. Y. Gu, P. L. Wang, H. Li*, et al.*, "Highly efficient iodine capture by layered double hydroxides intercalated with polysulfides," *Chemistry of Materials,* vol. 26, pp. 7114-7123, 2014.

[236] O. B. Yang, J. C. Kim, J. S. Lee, and Y. G. Kim, "Use of activated carbon-fibre for direct removal of iodine from acetic-acid solution," *Industrial & Engineering Chemistry Research,* vol. 32, pp. 1692-1697, 1993.

[237] H. Sun, P. La, Z. Zhu, W. Liang, B. Yang, and A. Li, "Capture and reversible storage of volatile iodine by porous carbon with high capacity," *Journal of Materials Science,* vol. 50, pp. 7326-7332, 2015.

[238] K. W. Chapman, P. J. Chupas, and T. M. Nenoff, "Radioactive iodine capture in silver-containing mordenites through nanoscale silver iodide formation," *Journal of American Chemical Society,* vol. 132, pp. 8897-8899, 2010.

[239] D. R. Haefner and T. J. Tranter, "Methods of gas phase capture of iodine from fuel reprocessing off-gas: a literature survey," Idaho National Laboratory, Idaho2007.

[240] B. Assfour, T. Assaad, and A. Odeh, "In silico screening of metal organic framework for iodine capture and storage," *Chemical Physics Letters,* vol. 610-611, pp. 45-49, 2014.

[241] C. Falaise, C. Volkringer, J. Facqueur, T. Bousquet, L. Gasnot, and T. Loiseau, "Capture of iodine in highly stable metal-organic frameworks: A systematic study," *Chemical Communications,* vol. 49, pp. 10320-10322, 2013.

[242] G. Massasso, J. Long, J. Haines, S. Devautour-Vinot, G. Maurin, A. Grandjean*, et al.*, "Iodine capture by Hofmann-Type clathrate $Ni^{II}(pz)[Ni^{II}(CN)_4]$," *Inorganic Chemistry,* vol. 53, pp. 4269-4271, 2014.

[243] G. Massasso, M. Rodriguez-Castillo, J. Long, A. Grandjean, B. Onida, Y. Guari*, et al.*, "Nanocomposites based on Hofmann-type structure $Ni^{II}(pz)[Ni^{II}(CN)_4]$ (pz = pyrazine)

nanoparticles for reversible iodine capture," *Journal of Materials Chemistry A,* vol. 3, pp. 179-188, 2015.

[244] D. F. Sava Gallis, I. Ermanoski, J. A. Greathouse, K. W. Chapman, and T. M. Nenoff, "Iodine Gas Adsorption in Nanoporous Materials: A Combined Experiment–Modeling Study," *Industrial & Engineering Chemistry Research,* vol. 56, pp. 2331-2338, 2017.

[245] D. F. Sava, T. J. Garino, and T. M. Nenoff, "Iodine confinement into metal–organic frameworks (MOFs): Low-temperature sintering glasses to form novel glass composite material (GCM) alternative waste forms," *Industrial & Engineering Chemistry Research,* vol. 51, pp. 614-620, 2012.

[246] J. T. Hughes, D. F. Sava, T. M. Nenoff, and A. Navrotsky, "Thermochemical evidence for strong iodine chemisorption by ZIF-8," *Journal of American Chemical Society,* vol. 135, pp. 16256-16259, 2013.

[247] S. Parshamoni, S. Sanda, H. S. Jena, and S. Konar, "Tuning CO_2 uptake and reversible iodine adsorption in two isoreticular MOFs through ligand functionalisation," *Chemistry - An Asian Journal,* vol. 10, pp. 653-660, 2015.

[248] T. D. Bennett, P. J. Saines, D. A. Keen, J. C. Tan, and A. K. Cheetham, "Ball-milling-induced amorphisation of zeolitic imidazolate frameworks (ZIFs) for the irreversible trapping of iodine," *Chemistry - A European Journal,* vol. 19, pp. 7049-7055, 2013.

[249] D. Cangialosi, H. Schut, A. van Veen, and S. J. Picken, "Positron annihilation lifetime spectroscopy for measuring free volume during physical aging of polycarbonate," *Macromolecules,* vol. 36, pp. 142-147, 2003.

[250] H. Liu, P. Guo, T. Regueira, Z. Wang, J. Du, and G. Chen, "Irreversible Change of the Pore Structure of ZIF-8 in Carbon Dioxide Capture with Water Coexistence," *Journal of Physical Chemistry C,* vol. 120, pp. 13287-13294, 2016.

[251] A. M. Marti, W. Wickramanayake, G. Dahe, A. Sekizkardes, T. L. Bank, D. P. Hopkinson*, et al.*, "Continuous flow processing of ZIF-8 membranes on polymeric porous hollow fiber supports for CO2 capture," *ACS Applied Material Interfaces,* vol. 9, pp. 5678-5682, 2017.

[252] Y. Pan and Z. Lai, "Sharp separation of C2/C3 hydrocarbon mixtures by zeolitic imidazolate framework-8 (ZIF-8) membranes synthesized in aqueous solutions," *Chemical Communications (Cambridge, England),* vol. 47, pp. 10275-10277, 2011.

[253] H. Bux, C. Chmelik, R. Krishna, and J. Caro, "Ethene/ethane separation by the MOF membrane ZIF-8: Molecular correlation of permeation, adsorption, diffusion," *Journal of Membrane Science,* vol. 369, pp. 284-289, 2011.

[254] U. Bohme, B. Barth, C. Paula, A. Kuhnt, W. Schwieger, A. Mundstock*, et al.*, "Ethene/ethane and propene/propane separation via the olefin and paraffin selective metal-organic framework adsorbents CPO-27 and ZIF-8," *Langmuir,* vol. 29, pp. 8592-8600, 2013.

[255] Y. Zhang, X. Feng, S. Yuan, J. Zhou, and B. Wang, "Challenges and recent advances in MOF–polymer composite membranes for gas separation," *Inorganic Chemistry Frontiers,* vol. 3, pp. 896-909, 2016.

[256] J.-W. Rhim, H.-M. Park, and C.-S. Ha, "Bio-nanocomposites for food packaging applications," *Progress in Polymer Science,* vol. 38, pp. 1629-1652, 2013.

[257] Y. Zhang, S. Yuan, X. Feng, H. Li, J. Zhou, and B. Wang, "Preparation of nanofibrous metal-organic framework filters for efficient air pollution control," *Journal of American Chemical Society,* vol. 138, pp. 5785-5788, 2016.

[258] E. Lopez-Maya, C. Montoro, L. M. Rodriguez-Albelo, S. D. Aznar Cervantes, A. A. Lozano-Perez, J. L. Cenis*, et al.*, "Textile/metal-organic-framework composites as self-detoxifying filters for chemical-warfare agents," *Angewandte Chemie-International Edition,* vol. 54, pp. 6790-6794, 2015.

[259] K. Fujie, R. Ikeda, K. Otsubo, T. Yamada, and H. Kitagawa, "Lithium ion diffusion in a metal–organic framework mediated by an ionic liquid," *Chemistry of Materials,* vol. 27, pp. 7355-7361, 2015.

[260] C. García-Salinas, P. A. Ramos-Parra, and R. I. Díaz de la Garza, "Ethylene treatment induces changes in folate profiles in climacteric fruit during postharvest ripening," *Postharvest Biology and Technology,* vol. 118, pp. 43-50, 2016.

[261] J. F. Kuang, L. Chen, W. Shan, S. Yang, W. J. Lu, and J. Y. Chen, "Molecular characterisation of two banana ethylene signaling component MaEBFs during fruit ripening," *Postharvest Biology and Technology,* vol. 85, pp. 94-101, 2013.

[262] J. Ren, N. M. Musyoka, H. W. Langmi, A. Swartbooi, B. C. North, and M. Mathe, "A more efficient way to shape metal-organic framework (MOF) powder materials for hydrogen storage applications," *International Journal of Hydrogen Energy,* vol. 40, pp. 4617-4622, 2015.

[263] H. Ismail, C. F. Goldsmith, P. R. Abel, P. T. Howe, A. Fahr, J. B. Halpern*, et al.*, "Pressure and temperature dependence of the reaction of vinyl radical with ethylene," *Journal of Physical Chemistry A,* vol. 111, pp. 6843-6851, 2007.

[264] Y. M. Jiang, D. C. Joyce, W. B. Jiang, and W. J. Lu, "Effects of chilling temperatures on ethylene binding by banana fruit," *Plant Growth Regulation,* vol. 43, pp. 109-115, 2004.

[265] S. H. Huo and X. P. Yan, "Metal-organic framework MIL-100(Fe) for the adsorption of malachite green from aqueous solution," *Journal of Materials Chemistry,* vol. 22, pp. 7449-7455, 2012.

[266] J. O. Hsieh, K. J. Balkus, J. P. Ferraris, and I. H. Musselman, "MIL-53 frameworks in mixed-matrix membranes," *Microporous and Mesoporous Materials,* vol. 196, pp. 165-174, 2014.

[267] A. K. Chaudhari, I. Han, and J. C. Tan, "Multifunctional supramolecular hybrid materials constructed from hierarchical self-ordering of *in situ* generated metal-organic framework (MOF) nanoparticles," *Advance Materials,* vol. 27, pp. 4438-4446, 2015.

[268] J. Kahr, R. E. Morris, and P. A. Wright, "Post-synthetic incorporation of nickel into CPO-27(Mg) to give materials with enhanced permanent porosity," *CrystEngComm,* vol. 15, pp. 9779-9786, 2013.

[269] P. D. Dietzel, P. A. Georgiev, J. Eckert, R. Blom, T. Strassle, and T. Unruh, "Interaction of hydrogen with accessible metal sites in the metal-organic frameworks M(2)(dhtp) (CPO-27-M; M = Ni, Co, Mg)," *Chemical Communications,* vol. 46, pp. 4962-4964, 2010.

APPENDIX A

A.1 The determination of particle size using a built-in function in the FEG-SEM

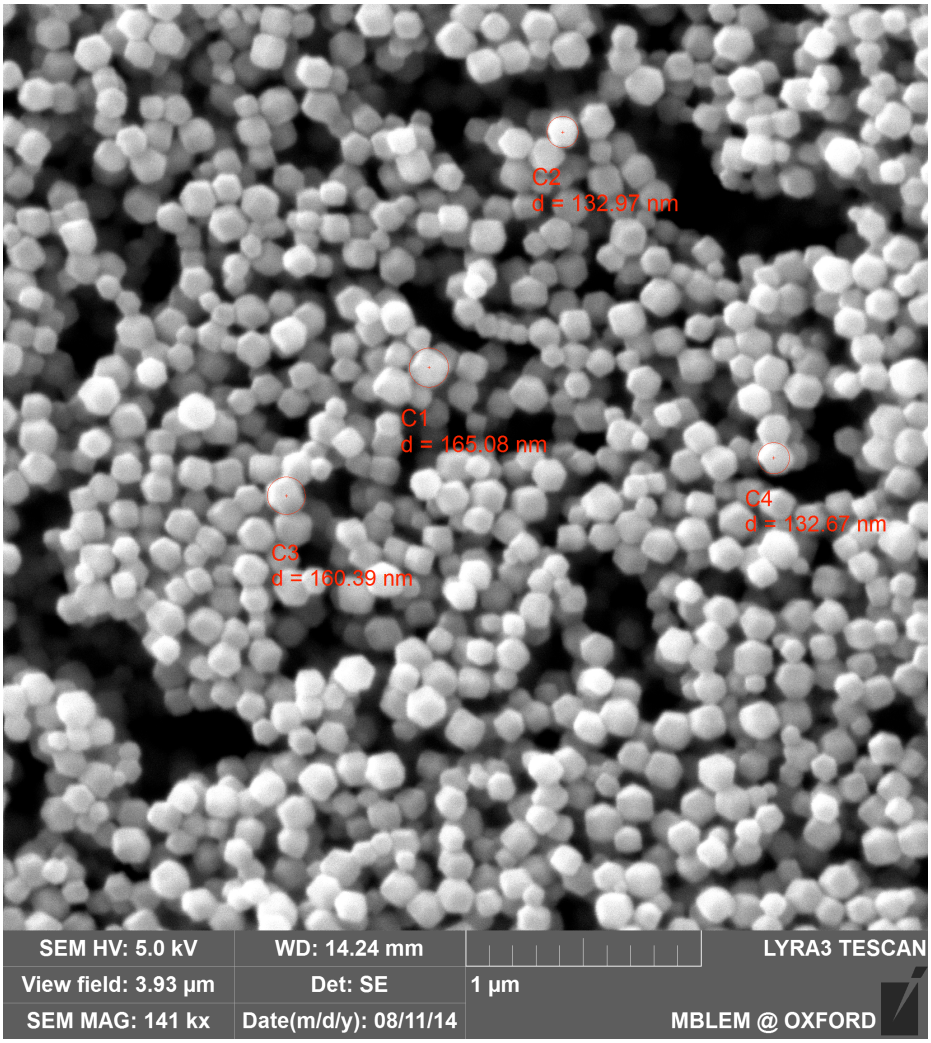

An example of measured individual particles from the FEG-SEM images for ZIF-8 nanoparticles dispersed in chloroform ($CHCl_3$), with 20 particles being measured in each image and averaged to a total of 60 particles from 3 different batches of synthesised ZIF-8. The average particle size was found to be 147.26 ± 7.05 nm.

A.2 Matlab equation used to match the DIC strain and the strain reported by the Instron machine

strain_instron = interp1(time_dic,strain_dic,time_instron)

where strain_instron is the adjusted strain data from matching DIC and instron data, interp1 is a 1-D interpolation function built into Matlab, time_dic is the time each image is captured (0.2 s), strain_dic is the strain values reported by DaVis from DIC image analysis, and time_instron is the experimental time reported by the Instron machine during the actual experiment.

APPENDIX B

B.1 Grid images for the quantitative analyses of the ZIF-8 nanoparticles distribution in the Matrimid/ZIF-8 nanocomposite.

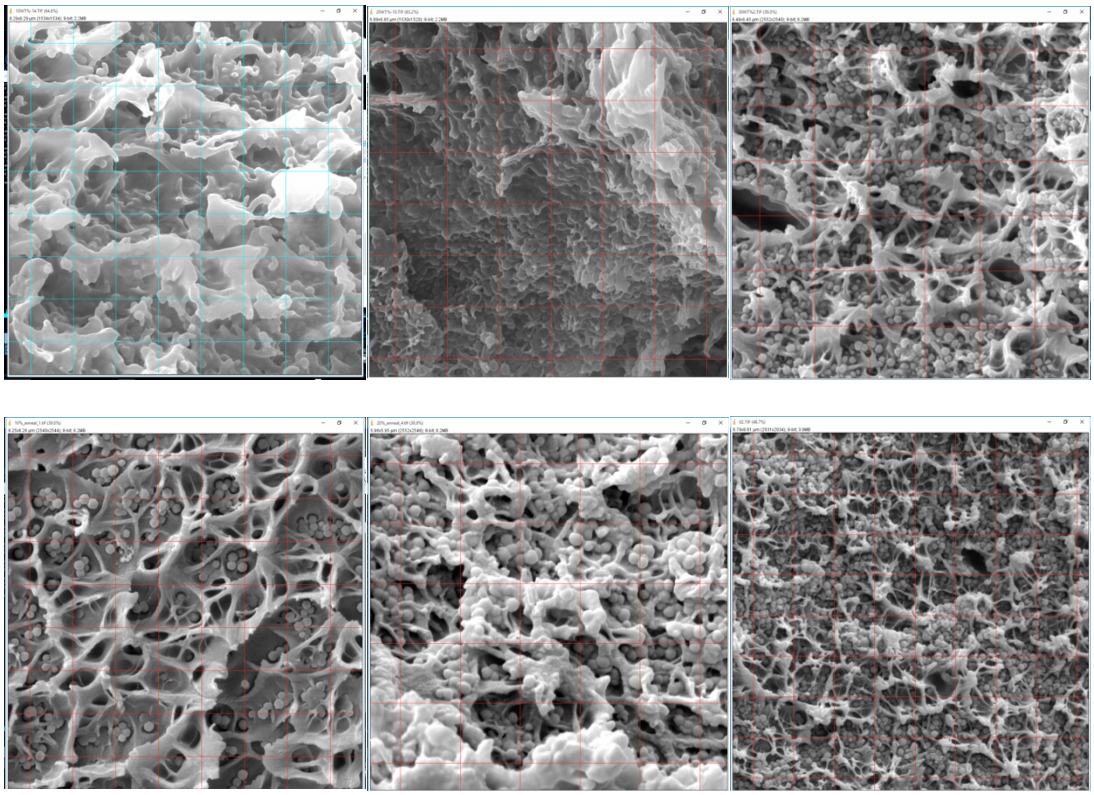

The FEG-SEM images used to quantitatively determine the distribution of ZIF-8. ImageJ software was used to divide the images into equal grids of 1 μm^2, and the number of ZIF-8 nanoparticles were manually counted and recorded per grid to obtain the frequency and distribution of the ZIF-8 nanoparticle throughout the nanocomposite, which are then plotted into bar charts representing the frequency distribution of the ZIF-8 nanoparticles. The images are of, from left to right (top), Matrimid/ZIF-8 10 wt.%, Matrimid/ZIF-8 20 wt.%, and Matrimid/ZIF-8 30 wt.%, and from left to right (bottom), Matrimid/ZIF-8 10 wt.% annealed, Matrimid/ZIF-8 20 wt.% annealed, and Matrimid/ZIF-8 30 wt.% annealed.

B.2 Possible mechanism and points of stress risers in the Matrimid/ZIF-8 nanocomposites

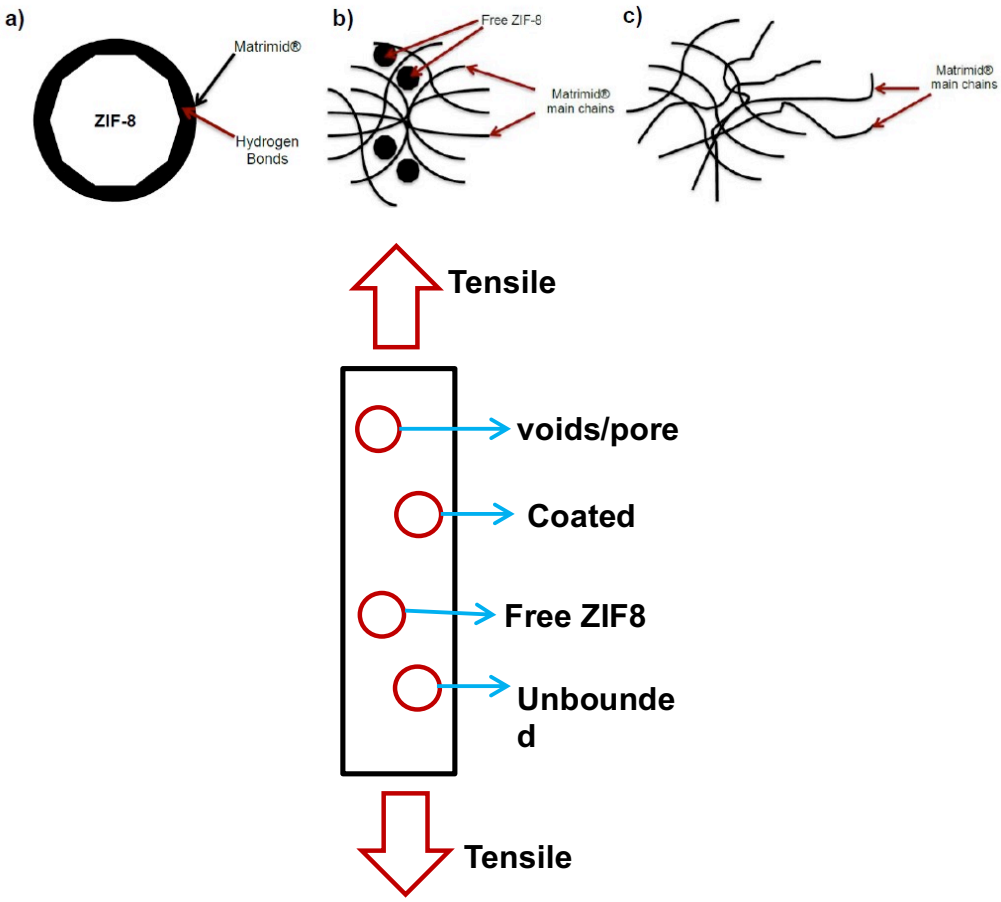

A model representing the interaction between ZIF-8 nanoparticles and Matrimid, with a) coated ZIF-8 nanoparticles, which forms the majority of the interaction in the membrane, b) unattached ZIF-8 nanoparticles that are free within the Matrimid matrix, and c) Matrimid, on its own, not coating any ZIF-8 nanoparticles or have any free ZIF-8 particles attached to its surface. Both constituents are held together by hydrogen bonding between ZIF-8 (2-methylimidazole linkers) and Matrimid (carbonyl and hydroxyl groups). Therefore, there will be free volume (microscopic gaps) between ZIF-8 and Matrimid, which contributes to the formation of pores within the structure; although due to the relatively lower loadings of the nanoparticles, these pores or free volume have negligible influence upon the macroscale

mechanical interaction of the nanocomposites. However, at a localised, microscopic level, its influence is rather significant, as seen in the results from nanoindentation.

B.3 Crystallinity of the Matrimid/ZIF-8 nanocomposites

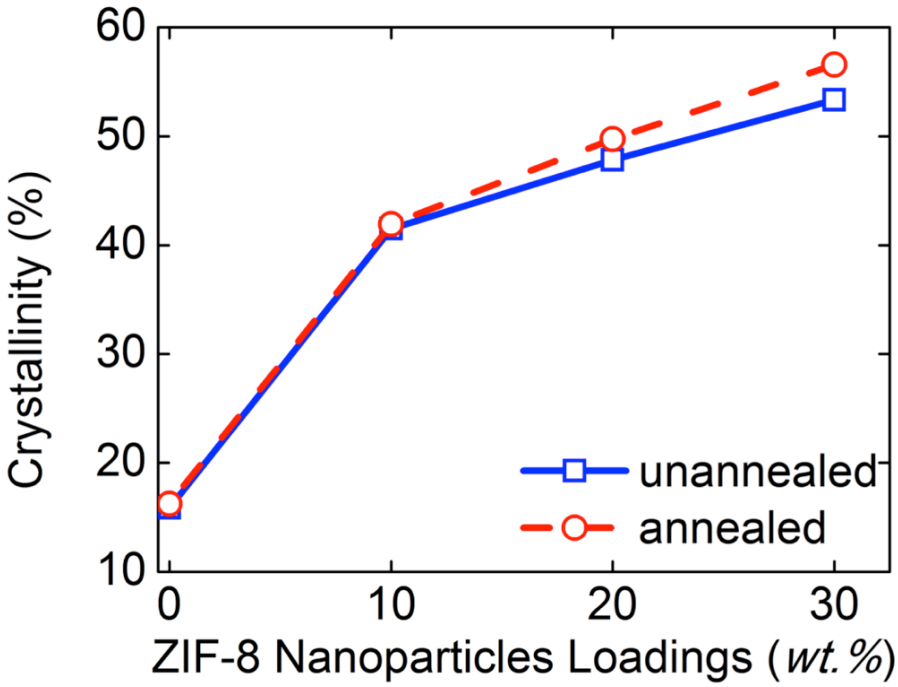

The relationship between crystallinity and ZIF-8 nanoparticle loadings derived from XRD diffractograms (Fig. 4.3). The increase in crystallinity was significant from Matrimid® (i.e. 0 wt.%) to 10 wt.% ZIF-8, which kept increasing as wt.% is increased. Annealing does increase the crystallinity of the nanocomposites, although not by a large margin.

B.4 Surface Roughness plots from the AFM scans of the unannealed and annealed Matrimid/ZIF-8 nanocomposites

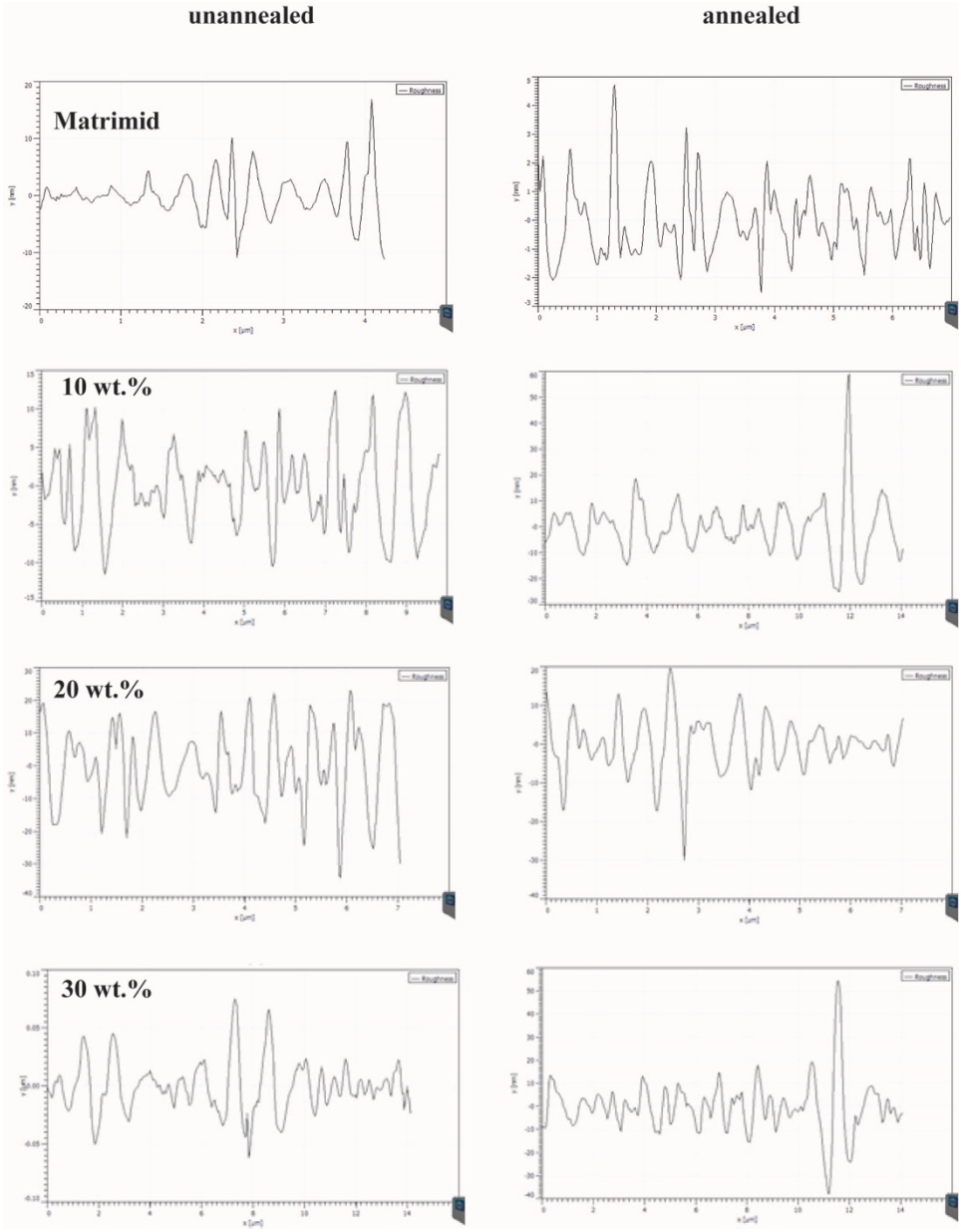

The representative surface roughness plots derived from the AFM scans of the unannealed and annealed Matrimid/ZIF-8 nanocomposites. A total of three surface roughness measurements was taken and averaged for the R_a and R_q values shown in Fig. 4.7. A diagonal line was drawn across the AFM scan images for the surface roughness values across multiple images.

B.5 Nanoindentation load-displacement data, averaged elastic moduli and hardness as a function of surface penetration depths of 2000 nm (Matrimid/ZIF-8)

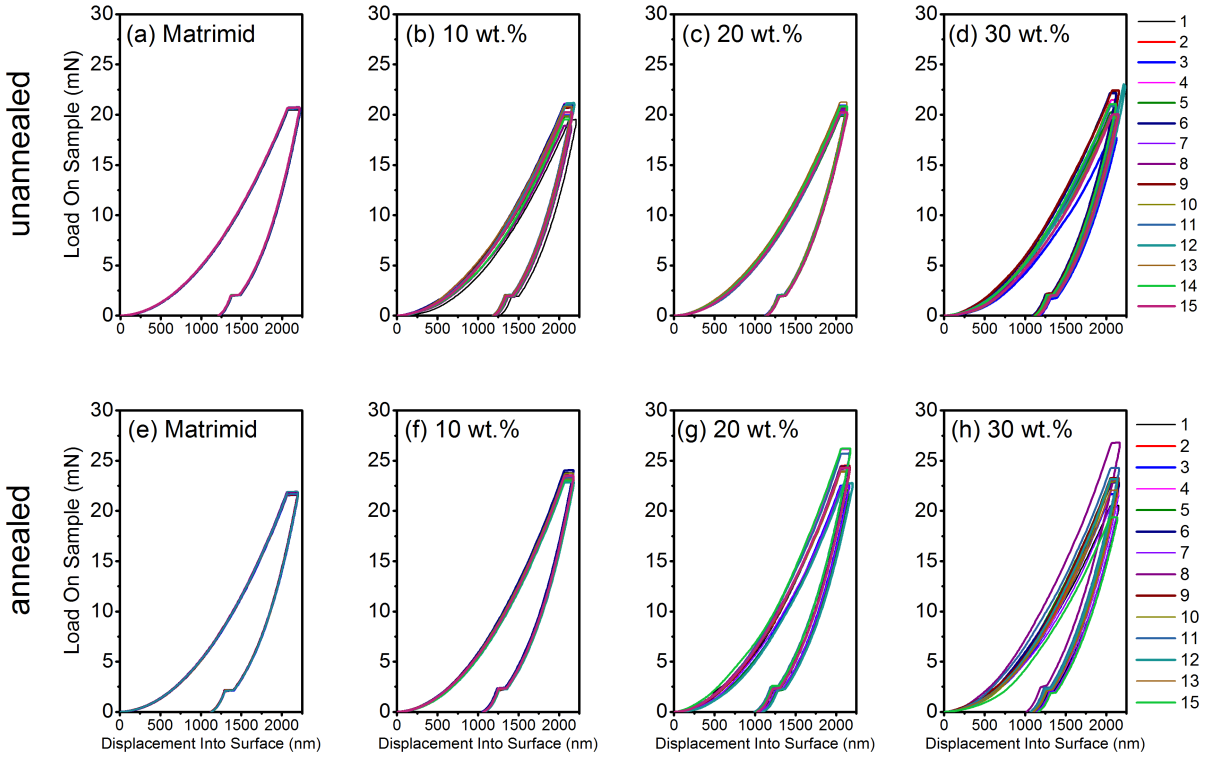

Nanoindentation load-displacement (representative) plots for Matrimid and the unannealed and annealed Matrimid/ZIF-8 nanocomposites, with a) Matrimid, b) 10 wt.% ZIF-8, c) 20 wt.% ZIF-8, d) 30 wt.% ZIF-8, while e) Matrimid (annealed), f) 10 wt.% ZIF-8 (annealed), g) 20 wt.% ZIF-8 (annealed), and h) 30 wt.% ZIF-8 (annealed). Note the relatively higher scatter as wt.% rises associated with greater local membrane inhomogeneity.

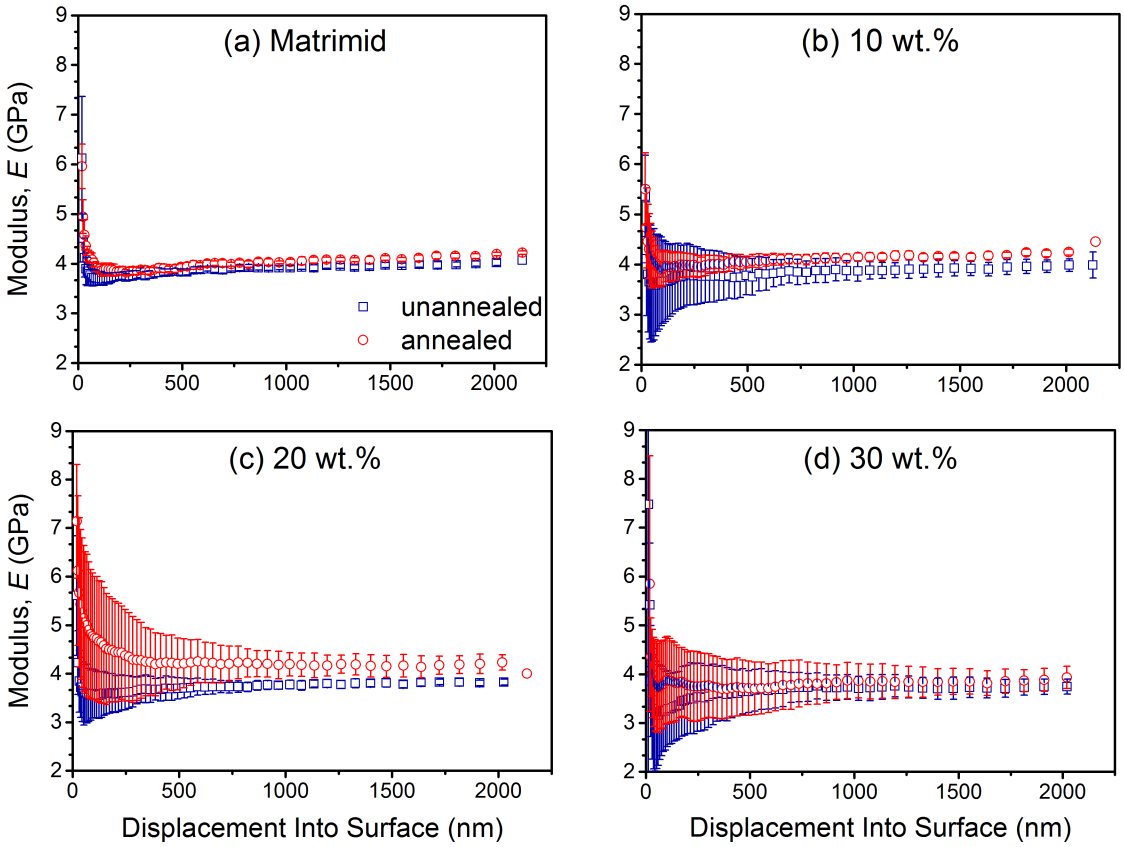

Nanoindentation averaged Young's Modulus (*E*) plots as a function of surface penetration depths (0 to 2,000 nm) for Matrimid and the unannealed and annealed ZIF-8 nanocomposites, with a) Matrimid, b) 10 wt.% ZIF-8, c) 20 wt.% ZIF-8, and d) 30 wt.% ZIF-8. Data from 1000 to 2000 nm were used to derive the average values reported in Fig. 4.5. The larger scatter at below 500 nm can be linked to imperfect tip-to-surface contacts due to roughness (asperities).

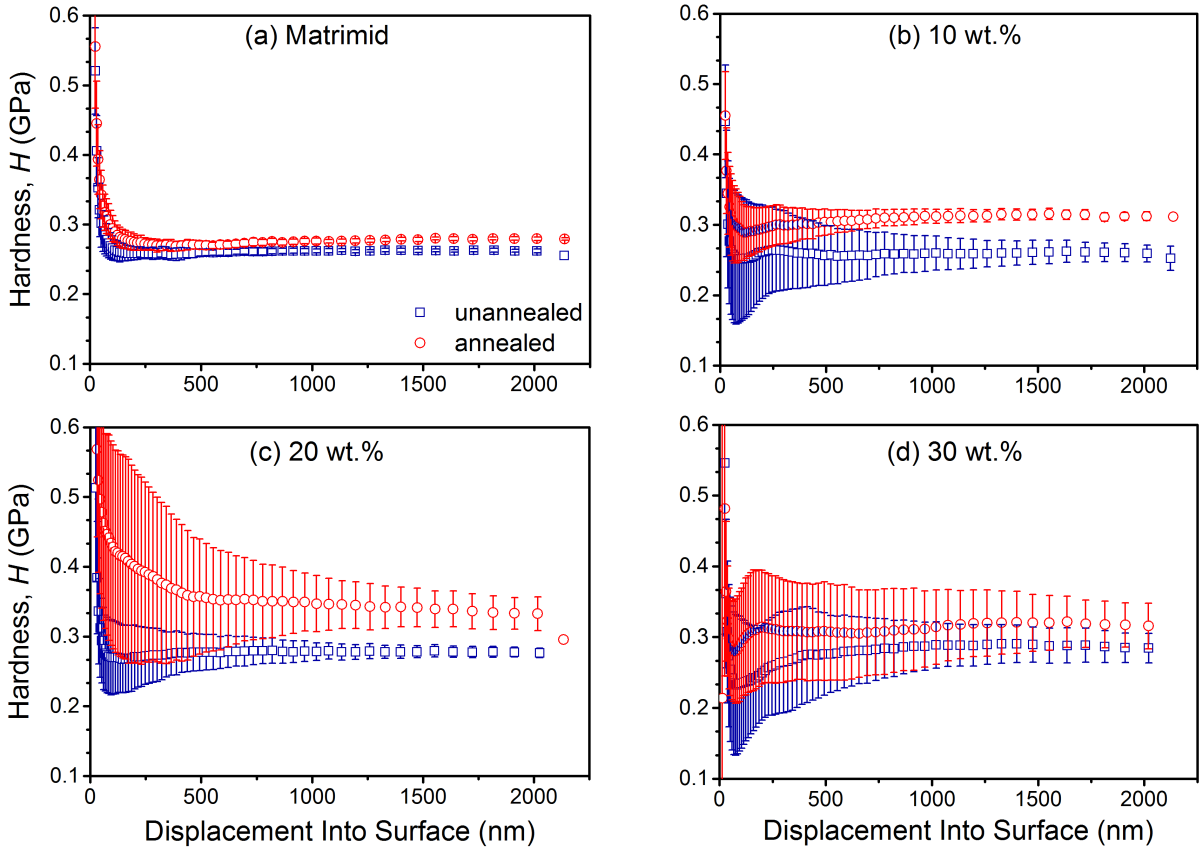

Nanoindentation averaged nanohardness (*H*) plots as a function of surface penetration depths for Matrimid and the unannealed and annealed ZIF-8 nanocomposites, with a) Matrimid, b) 10 wt.% ZIF-8, c) 20 wt.% ZIF-8, and d) 30 wt.% ZIF-8. Data from 1000 to 2000 nm were used to derive the average values reported in Fig. 4.5. The larger scatter at below 500 nm can be linked to imperfect tip-to-surface contacts due to roughness (asperities).

B.6 DMA results from the multi-strain frequency sweep tests for Matrimid/ZIF-8 nanocomposites.

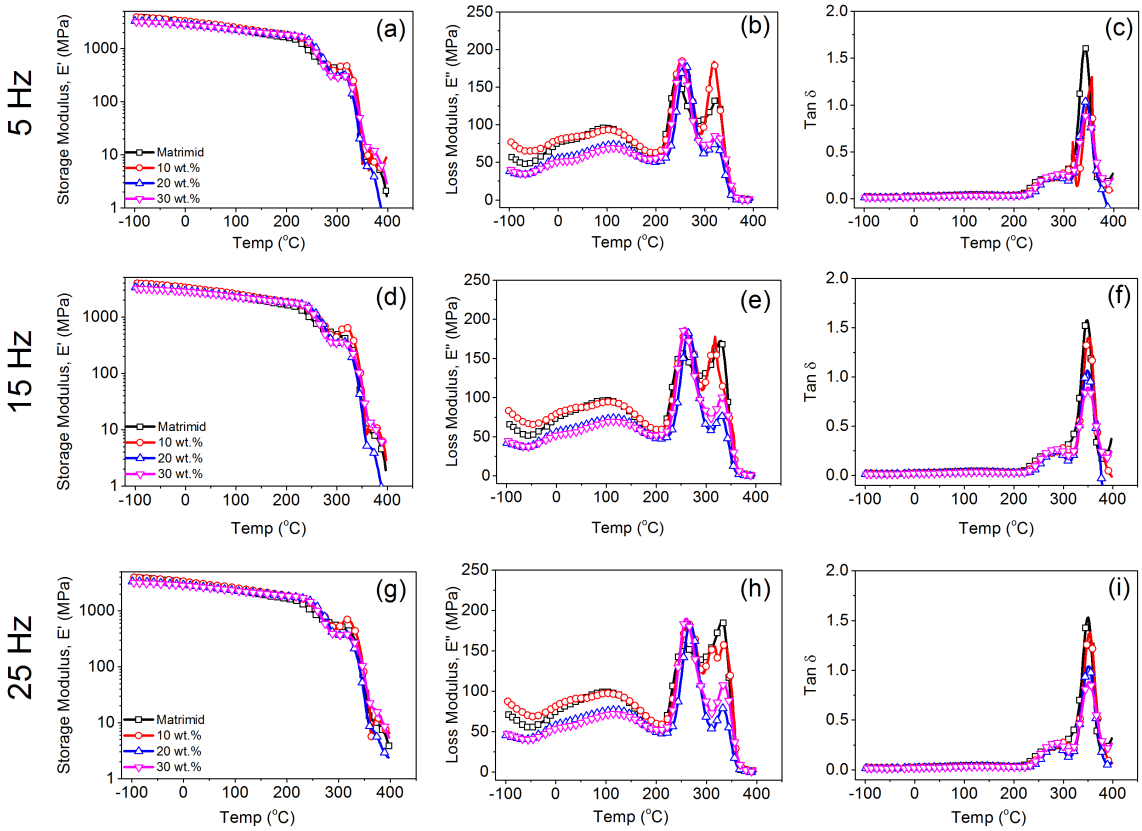

Additional data from the DMA multi-strain frequency sweep tests, classified as per its respective test frequencies for the unannealed Matrimid/ZIF-8 nanocomposites, with a) Storage modulus, *E*' (5 Hz), b) Loss modulus, *E*'' (5 Hz), c) tan δ (5 Hz), d) Storage modulus, *E*' (15 Hz), e) Loss modulus, *E*'' (15 Hz), f) tan δ (15 Hz), g) Storage modulus, *E*' (25 Hz), h) Loss modulus, *E*'' (25 Hz), and i) tan δ (25 Hz).

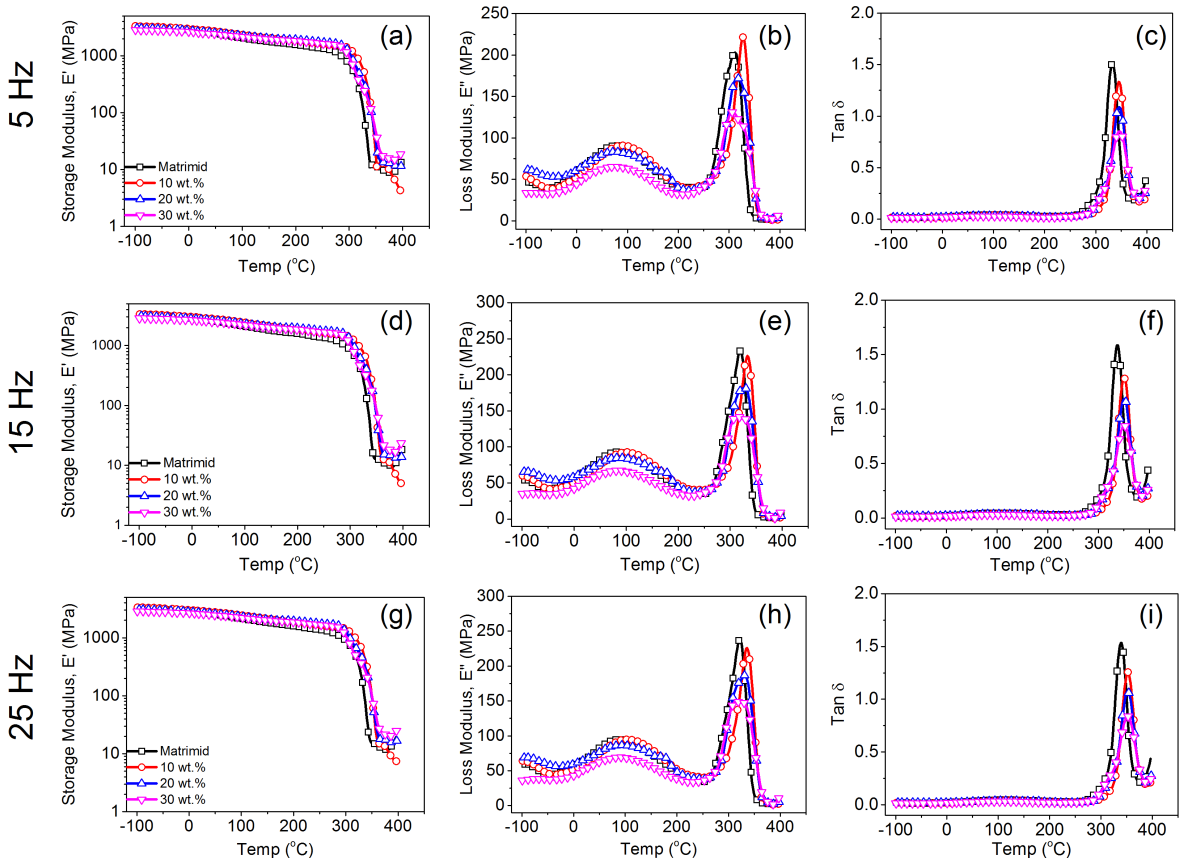

Additional data from the DMA multi-strain frequency sweep tests, classified as per its respective test frequencies for the annealed Matrimid/ZIF-8 nanocomposites, with a) Storage modulus, *E*' (5 Hz), b) Loss modulus, *E*'' (5 Hz), c) tan δ (5 Hz), d) Storage modulus, *E*' (15 Hz), e) Loss modulus, *E*'' (15 Hz), f) tan δ (15 Hz), g) Storage modulus, *E*' (25 Hz), h) Loss modulus, *E*'' (25 Hz), and i) tan δ (25 Hz).

B.7 Glass transition temperature as a function of ZIF-8 nanoparticle wt.% loading for Matrimid/ZIF-8 nanocomposites.

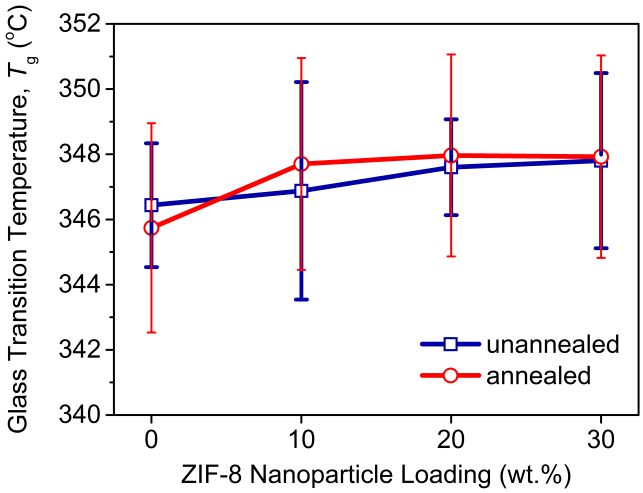

A plot correlating the glass transition temperature (T_g) and ZIF-8 nanoparticle loadings (wt.%). Overall, it can be seen that the addition of ZIF-8 nanoparticles into Matrimid does little to alter the T_g of the resulting nanocomposites, where the fluctuation of T_g is less than 5% for both the unannealed and annealed nanocomposites. This implies that near the T_g, the phase change/mechanical/thermal response is primarily dominated by the Matrimid matrix for both cases. Here the introduction of ZIF-8 fillers did not result in chain rigidification or other physical changes to the matrix, therefore the composite T_g will remain close to the T_g of the original matrix.

B.8 Raw master curve of the samples, the lg (a_T) vs. T, and the WLF approximation of the data of the Matrimid/ZIF-8 nanocomposites

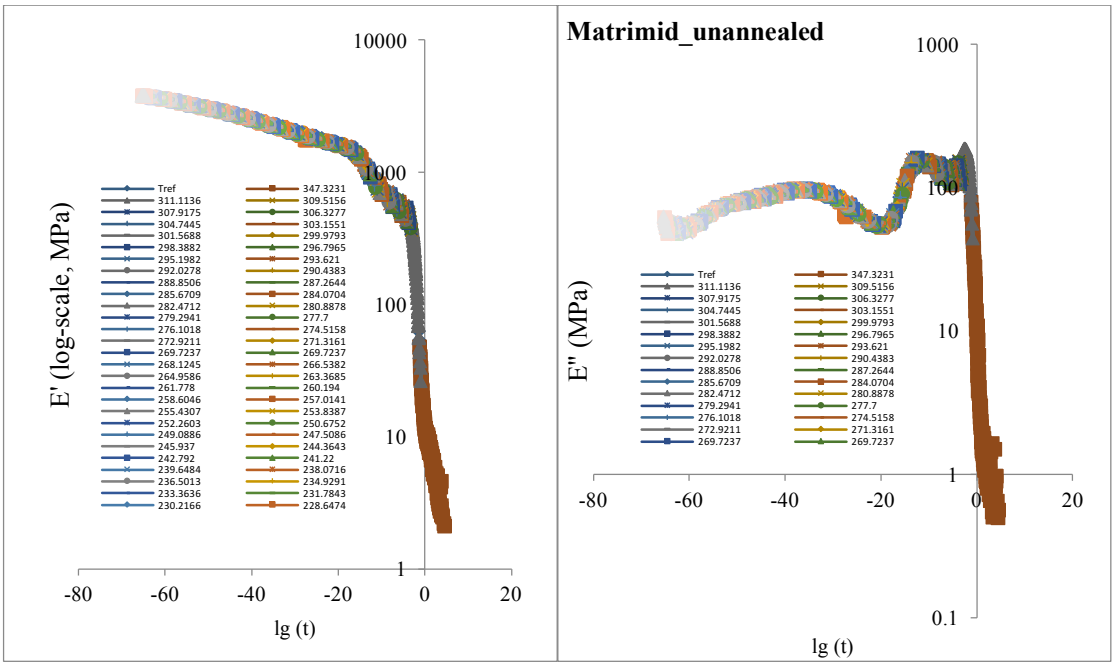

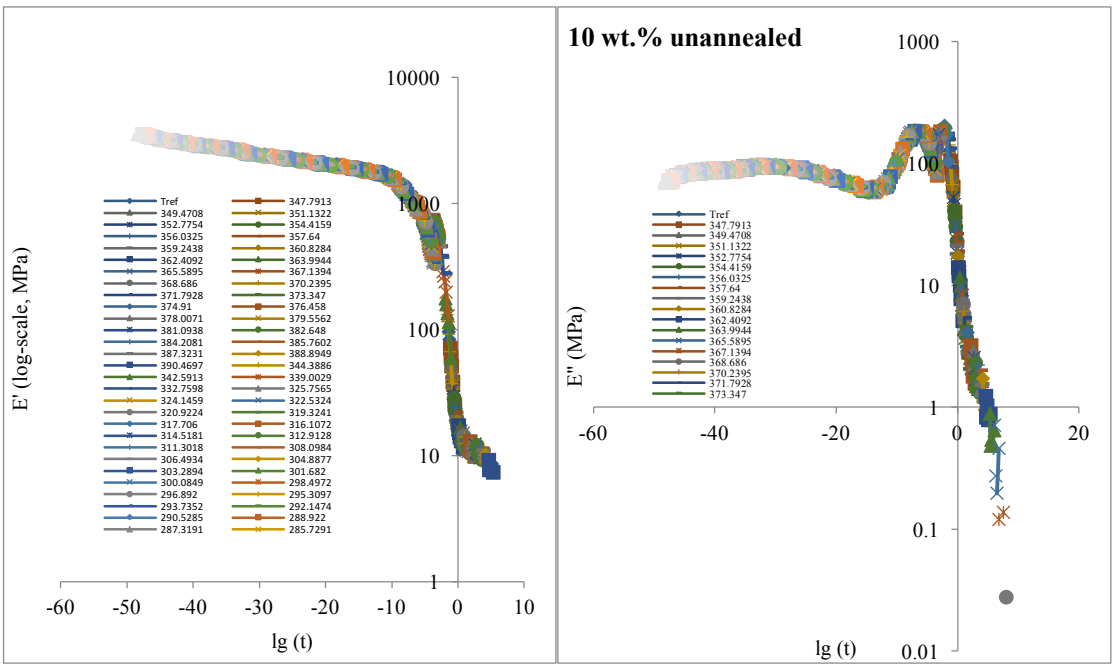

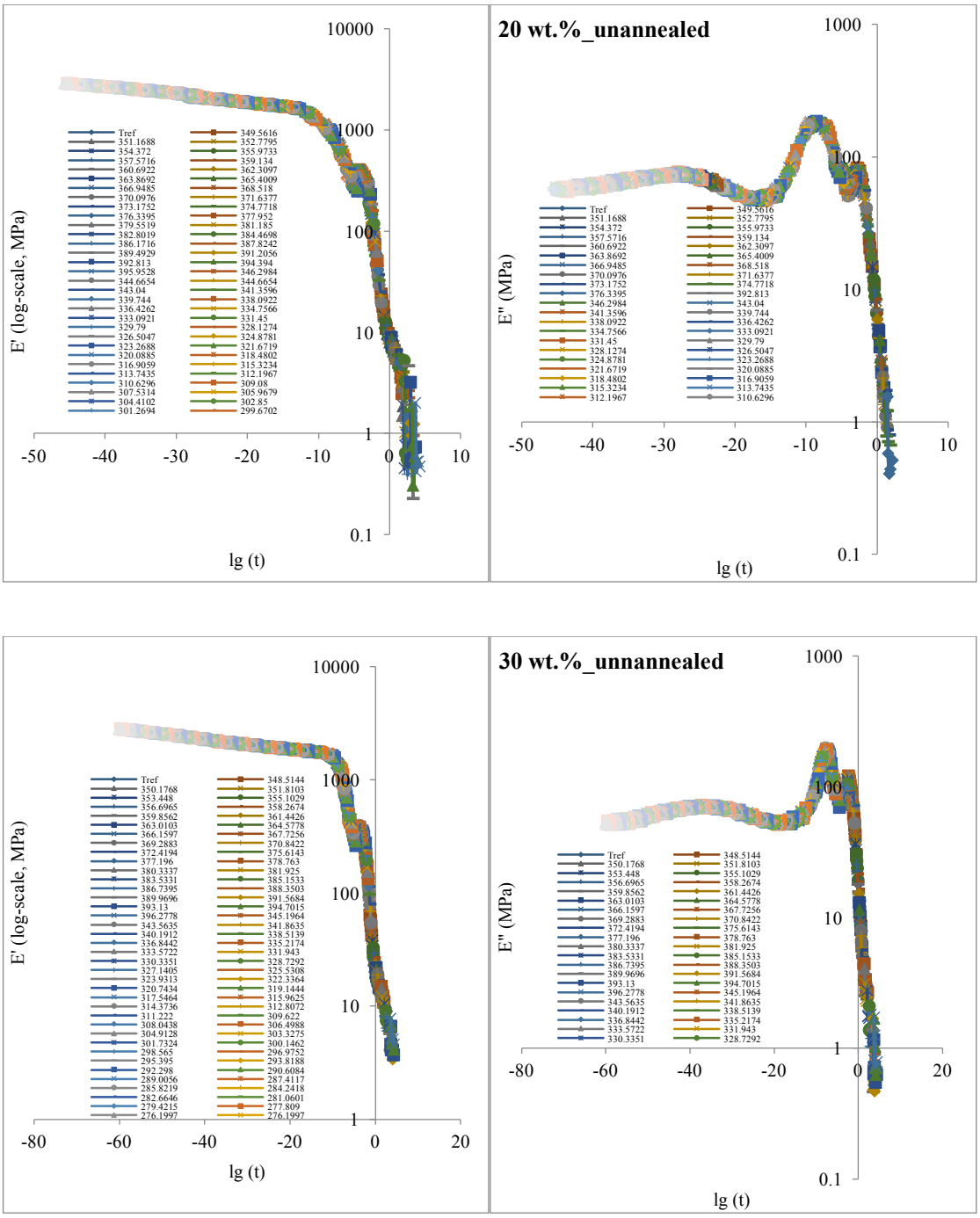

The raw data master-curve plots for the unannealed Matrimid/ZIF-8 nanocomposites, which forms the basis for the master curves shown in Fig. 4.13 (a) & (c), with the temperature markers for a cycle of frequency sweep(s) (2-25 Hz).

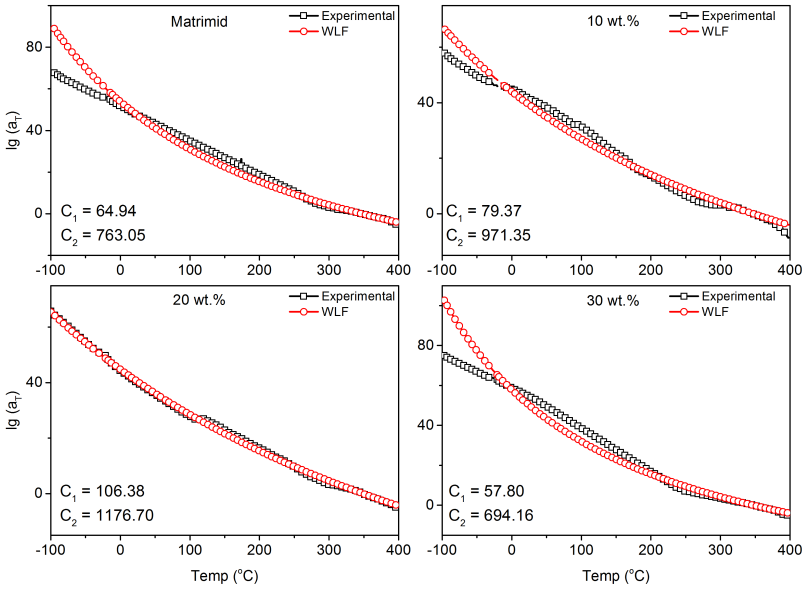

The lg (a_T) *vs*. T plots for the experimental data and the WLF approximation associated with the experimental data of the unannealed Matrimid/ZIF-8 nanocomposites. The C_1 and C_2 values associated with the WLF approximation plots are shown in the inset of each plots.

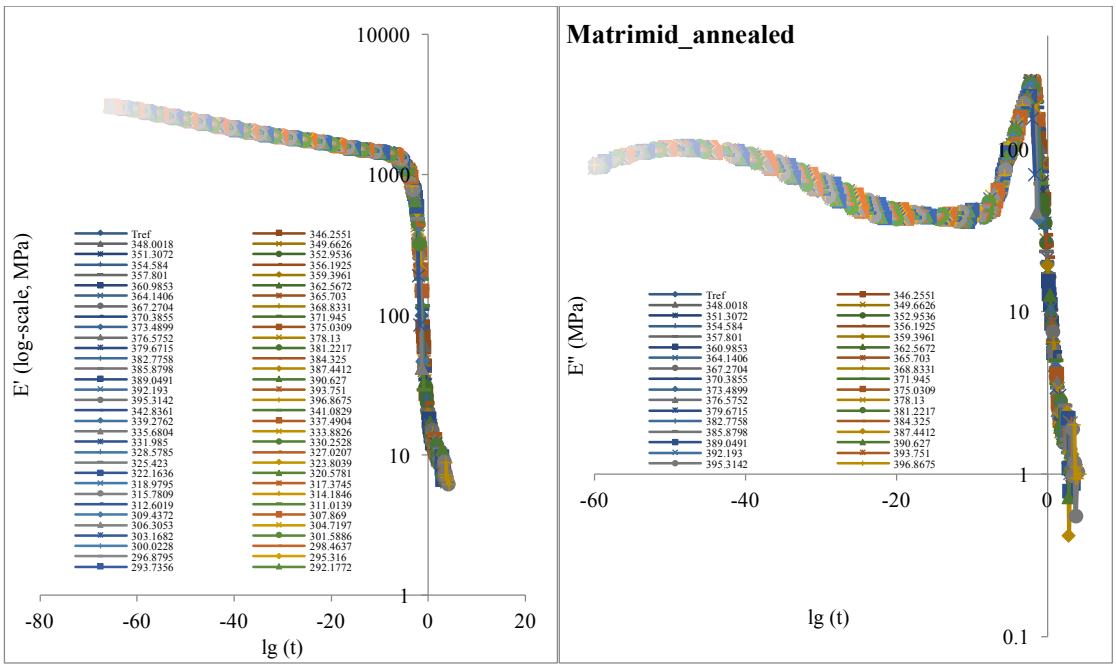

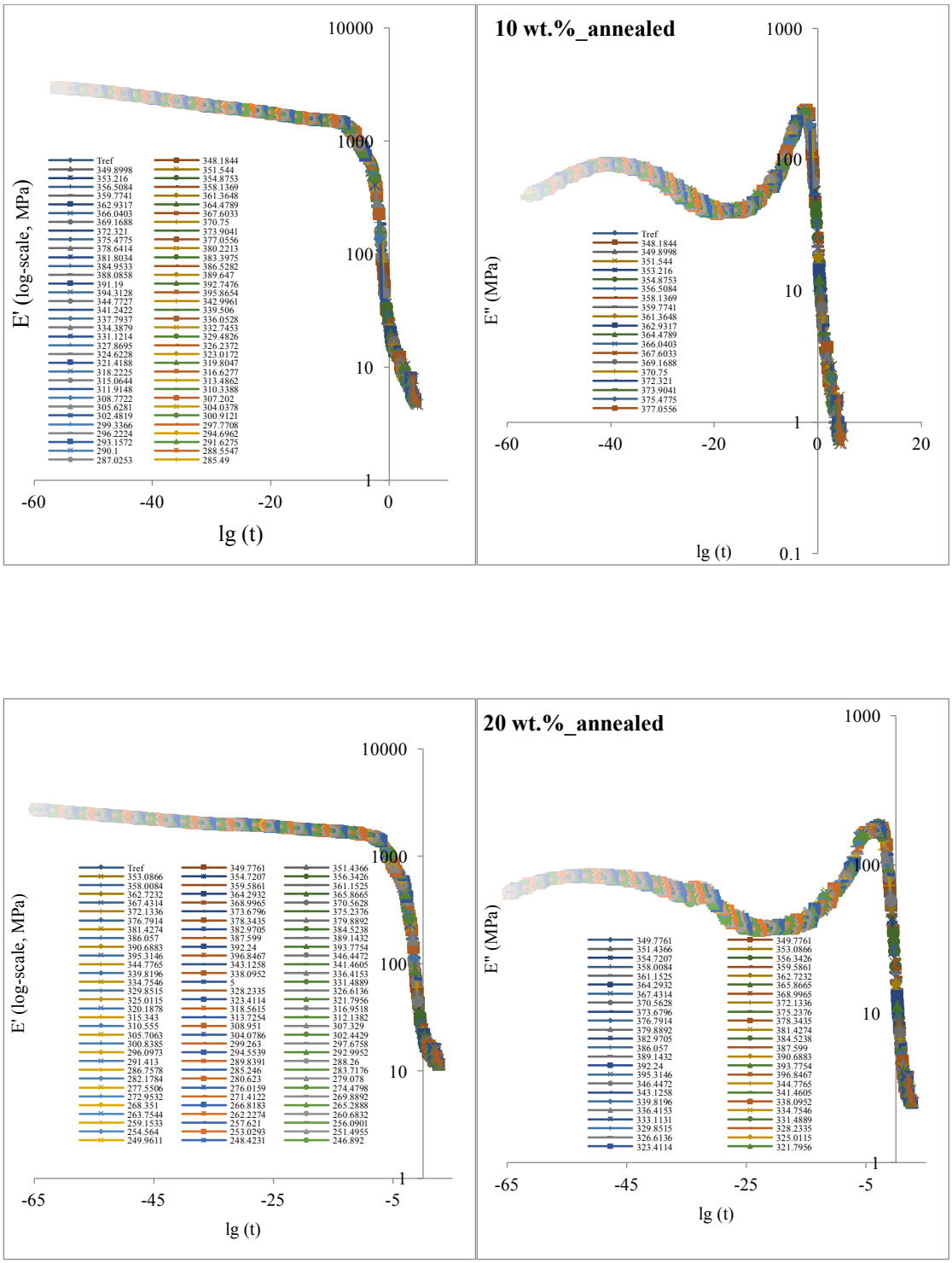
E' (log-scale, MPa)
lg (t)
10000
1000
100
10
1
-60
-40
-20
0
Tref
349.8998
353.216
356.5084
359.7741
362.9317
366.0403
369.1688
372.321
375.4775
378.6414
381.8034
384.9533
388.0858
391.19
394.3128
344.7727
341.2422
337.7937
334.3879
331.1214
327.8695
324.6228
321.4188
318.2225
315.0644
311.9148
308.7722
305.6281
302.4819
299.3366
296.2224
293.1572
290.1
287.0253
348.1844
351.544
354.8753
358.1369
361.3648
364.4789
367.6033
370.75
373.9041
377.0556
380.2213
383.3975
386.5282
389.647
392.7476
395.8654
342.9961
339.506
336.0528
332.7453
329.4826
326.2372
323.0172
319.8047
316.6277
313.4862
310.3388
307.202
304.0378
300.9121
297.7708
294.6962
291.6275
288.5547
285.49
10 wt.%_annealed
E'' (MPa)
lg (t)
1000
100
10
1
0.1
-60
-40
-20
0
20
Tref
348.1844
349.8998
351.544
353.216
354.8753
356.5084
358.1369
359.7741
361.3648
362.9317
364.4789
366.0403
367.6033
369.1688
370.75
372.321
373.9041
375.4775
377.0556
E' (log-scale, MPa)
lg (t)
10000
1000
100
10
1
-65
-45
-25
-5
Tref
353.0866
358.0084
362.7232
367.4314
372.1336
376.7914
381.4274
386.057
390.6883
395.3146
344.7765
339.8196
334.7546
329.8515
325.0115
320.1878
315.343
310.555
305.7063
300.8385
296.0973
291.413
286.7578
282.1784
277.5506
272.9532
268.351
263.7544
259.1533
254.564
249.9611
349.7761
354.7207
359.5861
364.2932
368.9965
373.6796
378.3435
382.9705
387.599
392.24
396.8467
343.1258
338.0952
5
328.2335
323.4114
318.5615
313.7254
308.951
304.0786
299.263
294.5539
289.8391
285.246
280.623
276.0159
271.4122
266.8183
262.2274
257.621
253.0293
248.4231
351.4366
356.3426
361.1525
365.8665
370.5628
375.2376
379.8892
384.5238
389.1432
393.7754
346.4472
341.4605
336.4153
331.4889
326.6136
321.7956
316.9518
312.1382
307.329
302.4429
297.6758
292.9952
288.26
283.7176
279.078
274.4798
269.8892
265.2888
260.6832
256.0901
251.4955
246.892
20 wt.%_annealed
E'' (MPa)
lg (t)
1000
100
10
1
-65
-45
-25
-5
349.7761
351.4366
354.7207
358.0084
361.1525
364.2932
367.4314
370.5628
373.6796
376.7914
379.8892
382.9705
386.057
389.1432
392.24
395.3146
346.4472
343.1258
339.8196
336.4153
333.1131
329.8515
326.6136
323.4114
349.7761
353.0866
356.3426
359.5861
362.7232
365.8665
368.9965
372.1336
375.2376
378.3435
381.4274
384.5238
387.599
390.6883
393.7754
396.8467
344.7765
341.4605
338.0952
334.7546
331.4889
328.2335
325.0115
321.7956

The raw data master-curve plots for the annealed Matrimid/ZIF-8 nanocomposites, which forms the basis for the master curves shown in Fig. 4.13 (b) & (d), with the temperature markers for a cycle of frequency sweep(s) (2-25 Hz).

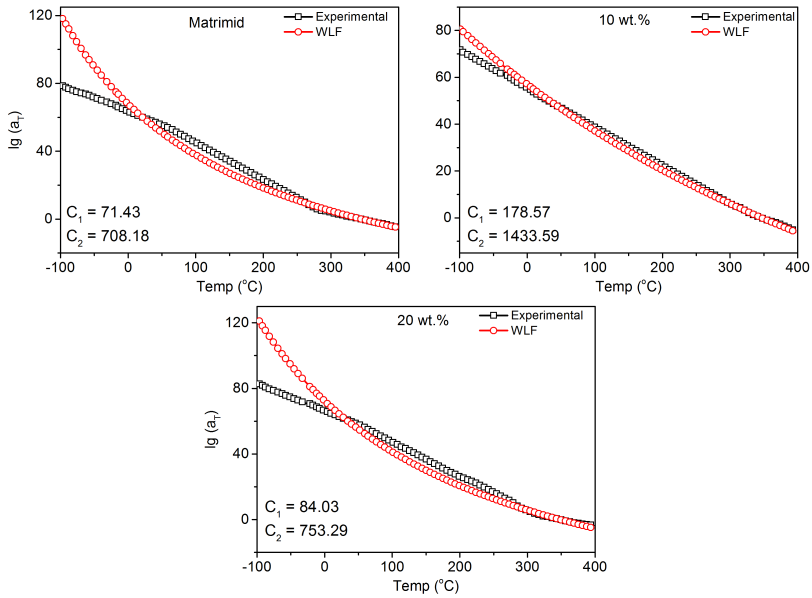

The lg (a_T) *vs*. T plots for the experimental data and the WLF approximation associated with the experimental data of the annealed Matrimid/ZIF-8 nanocomposites. The C_1 and C_2 values associated with the WLF approximation plots are shown in the inset of each plots.

APPENDIX C

C.1 Grid images for the quantitative analyses of the ZIF-8 nanoparticles distribution in the PU/ZIF-8 nanocomposite

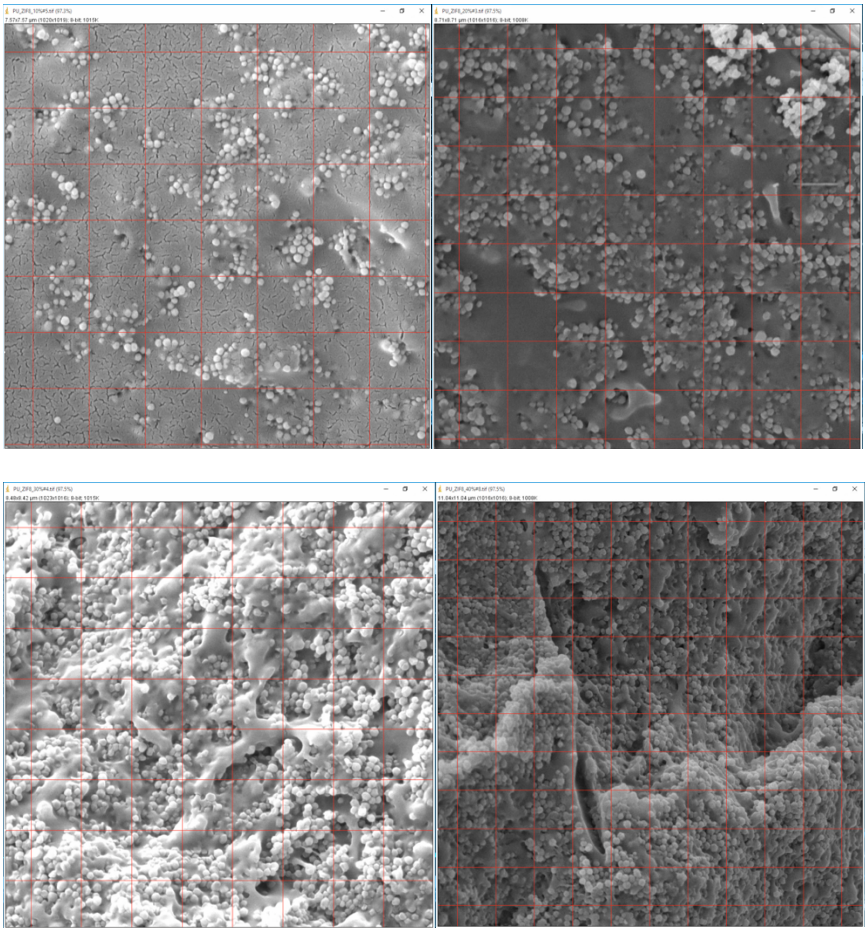

The FEG-SEM images used to quantitatively determine the distribution of ZIF-8. ImageJ software was used to divide the images into equal grids measuring 1 μm^2, and the number of ZIF-8 nanoparticles were manually counted and marked per grid to obtain the frequency and distribution of the ZIF-8 nanoparticle throughout the nanocomposite, which are then plotted into bar charts representing the frequency distribution of the ZIF-8 nanoparticles. The images are of, from left to right (top), PU/ZIF-8 10 wt.% and PU/ZIF-8 20 wt.%, and from left to right (bottom), PU/ZIF-8 30 wt.%, PU/ZIF-8 40 wt.%.

C.2 Crystallinity of the PU/ZIF-8 nanocomposites derived from the XRD data

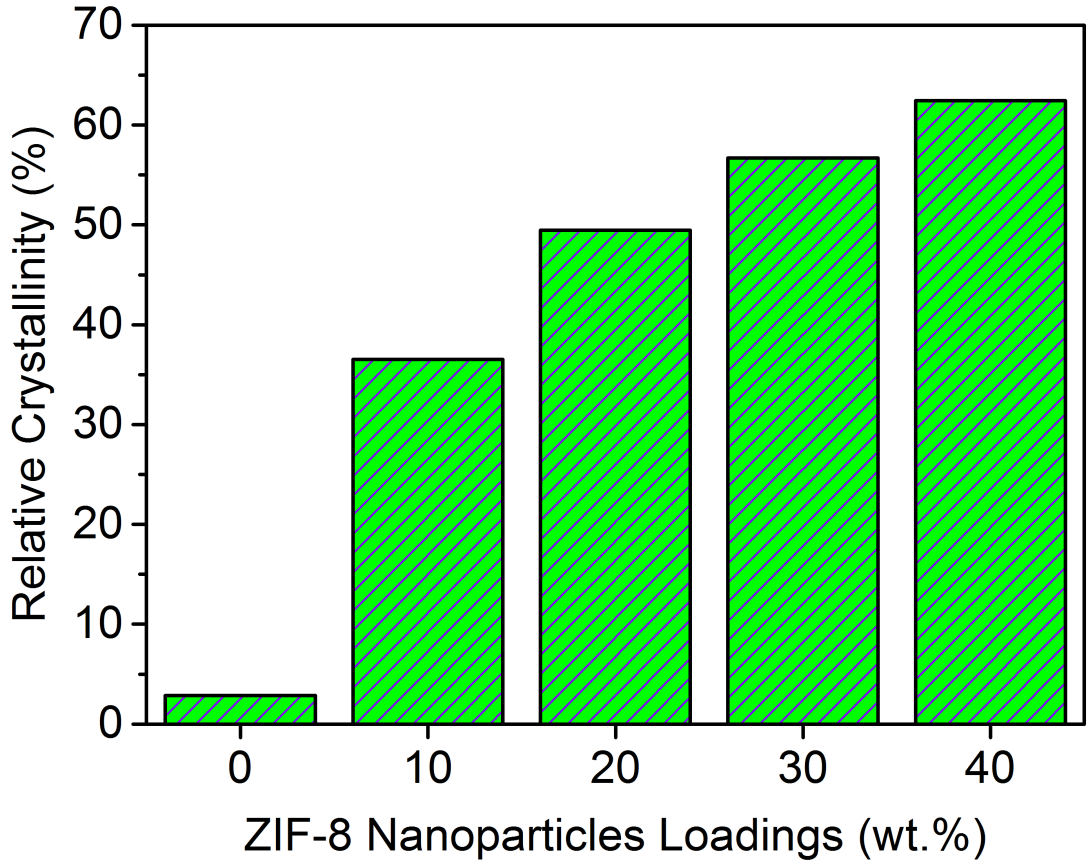

Crystallinity (wt.%) of the PU and its nanocomposites, as derived from the XRD plots and Scherrer approximation. The introduction of ZIF-8 (crystalline fillers) introduced semi-crystallinity to the nanocomposites.

C.3 Nanoindentation load-displacement data, averaged elastic moduli and hardness as a function of surface penetration depths of 2000 nm (PU/ZIF-8)

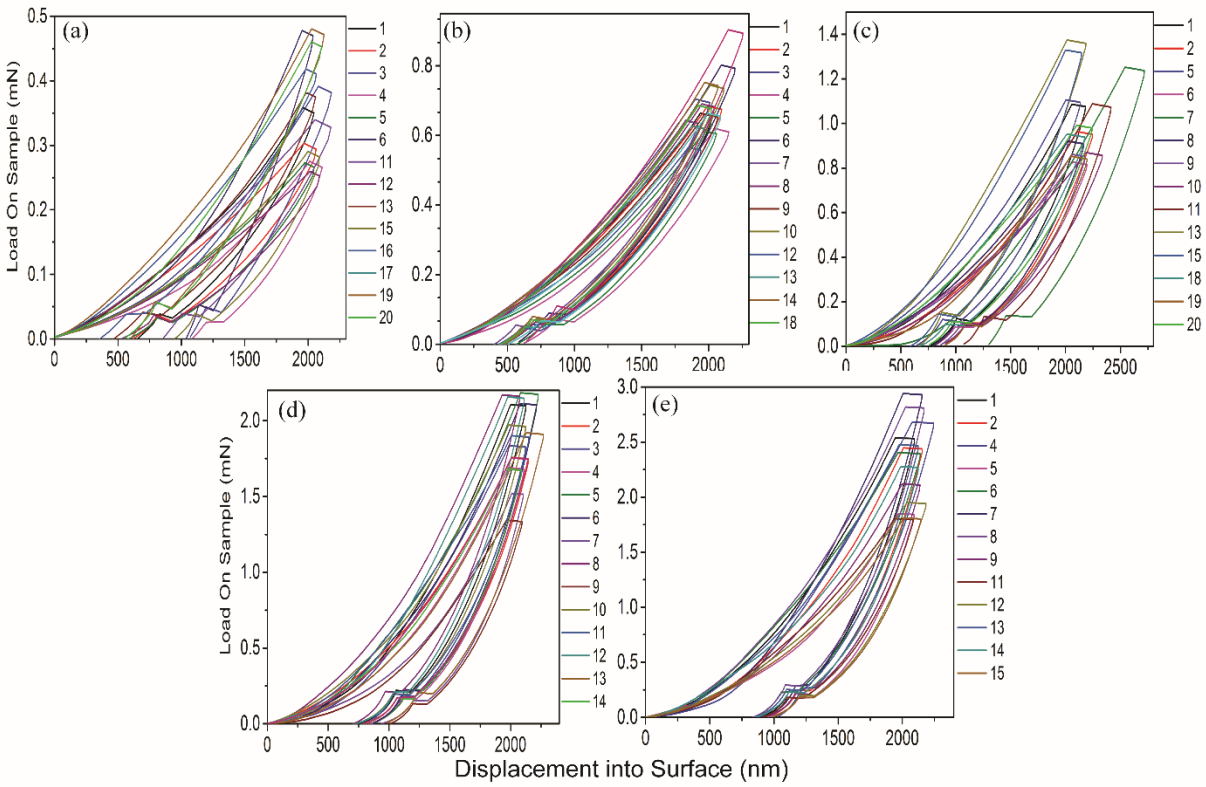

Nanoindentation load-displacement (representative) plots for PU and PU/ZIF8 nanocomposites, with a) PU, b) 10 wt.% ZIF-8, c) 20 wt.% ZIF-8, d) 30 wt.% e) 40 wt.% ZIF-8. Note the relatively higher scatter at lower wt.%, which is speculated to be associated with the difficulty of the nanoindenter in searching for an indentation surface due to the behaviour of the PU matrix.

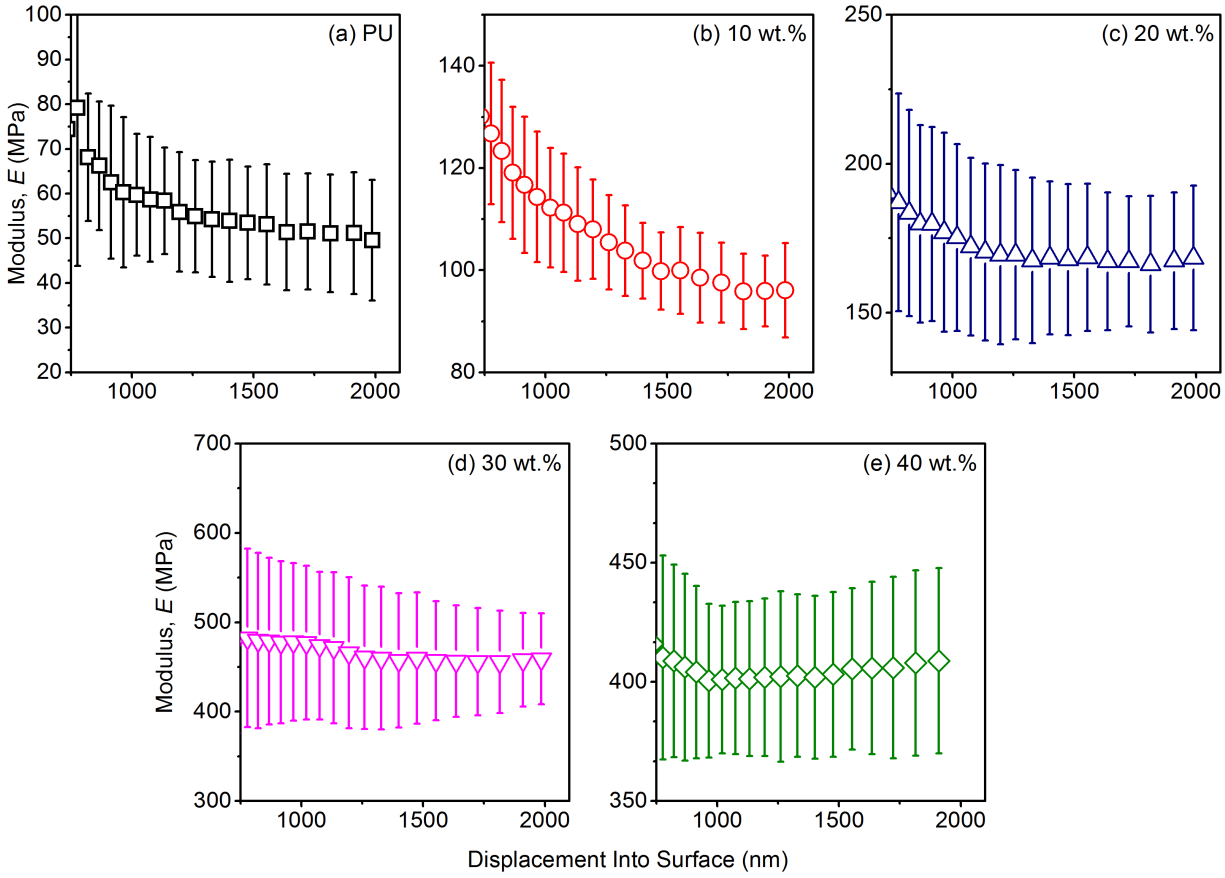

Nanoindentation averaged Young's modulus (E) plots as a function of surface penetration depths (0 - 2000 nm) for PU and the nanocomposites, with a) PU, b) 10 wt.% ZIF-8, c) 20 wt.% ZIF-8, d) 30 wt.% ZIF-8, and e) 40 wt.% ZIF-8. Data from 1000 - 2000 nm were used to derive the average values reported in Fig. 5.4. The larger scatter below 1000 nm can be linked to imperfect tip-to-surface contacts due to roughness (asperities).

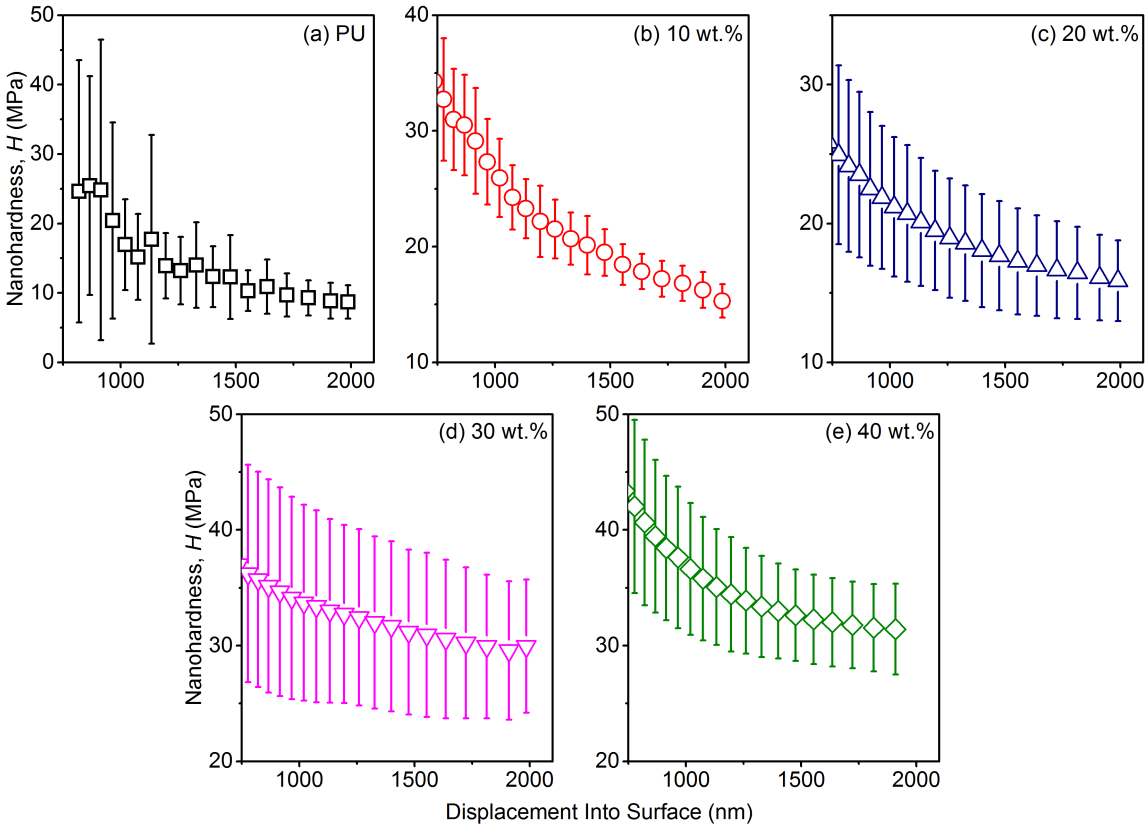

Nanoindentation averaged nanohardness (*H*) plots as a function of surface penetration depths for PU and nanocomposites, with a) PU, b) 10 wt.% ZIF-8, c) 20 wt.% ZIF-8, d) 30 wt.% ZIF-8, and e) 40 wt.% ZIF-8. Data from 1000 - 2000 nm were used to derive the averaged values reported in Fig. 5.4. The larger scatter at below 1000 nm can be linked to imperfect tip-to-surface contacts due to roughness (asperities).

C.4 TGA derived phase temperature for the PU/ZIF-8 nanocomposites

Samples (wt.%)	Stage		
	Initial Decomposition (°C)	'Hard' segment Decomposition (°C)	Complete decomposition (°C)
PU	250	420	580
10	140	320	500
20	200	320	550
30	200	320	550
40	140	320	550
ZIF-8	350		650

Compilation of the temperature at the beginning at each phase of decomposition in the PU and PU/ZIF-8 nanocomposites, derived from the TGA plots.

C.5 T_g *vs.* ZIF-8 nanoparticle loadings of the PU/ZIF-8 nanocomposites

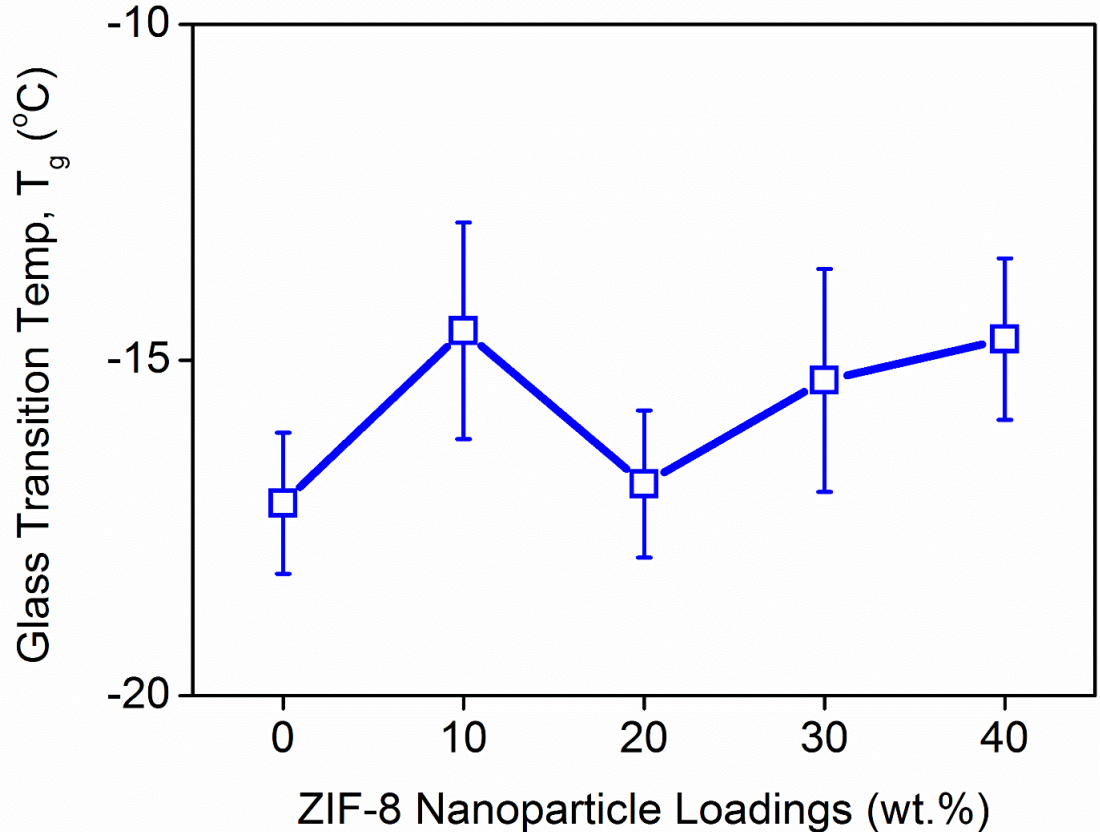

A plot correlating the glass transition temperature (T_g) and ZIF-8 nanoparticle loadings (wt.%). Overall, it can be seen that the addition of ZIF-8 nanoparticles into PU has a small effect on the T_g of the resulting nanocomposites, where the fluctuation of T_g is less than 5% for the nanocomposites. This implies that near the T_g, the phase change/thermo-mechanical response is primarily dominated by the PU matrix.

C.6 Additional DMA plots from the TTS multi-strain frequency sweep tests

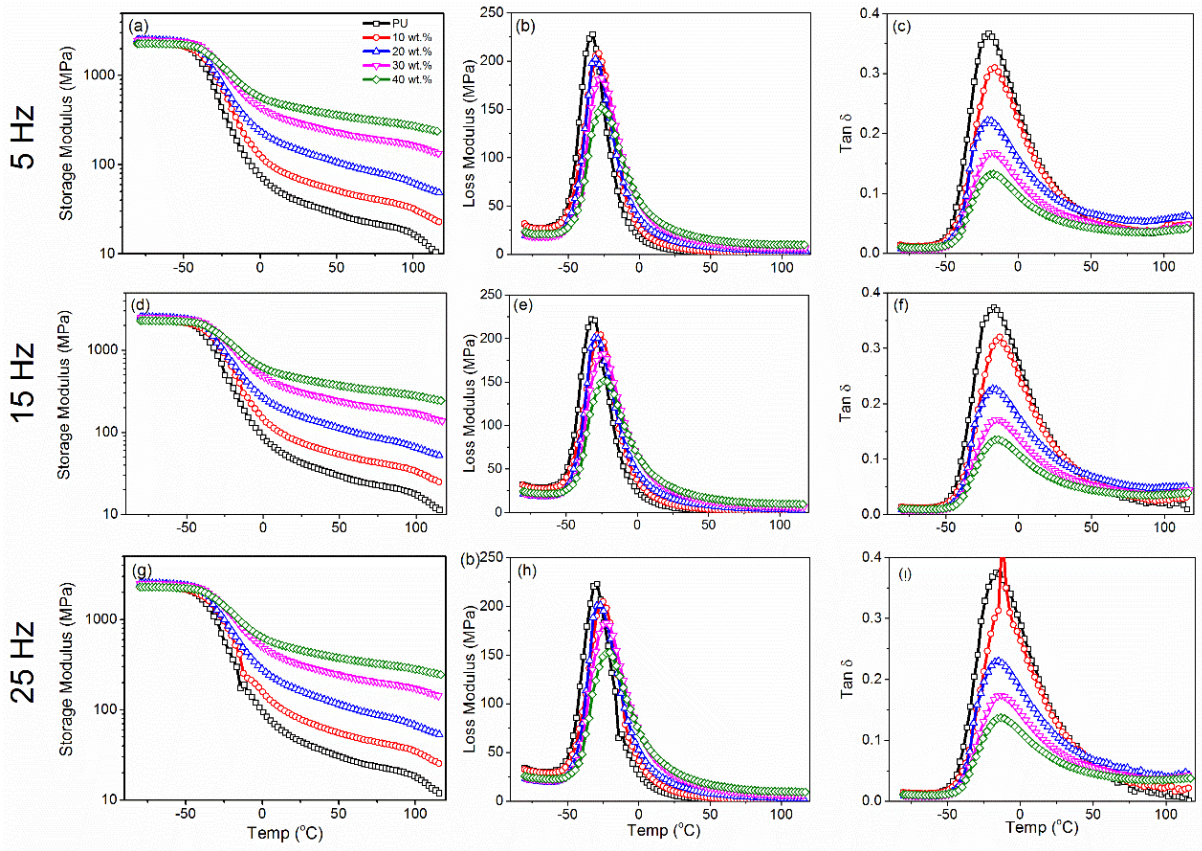

Additional data from the DMA multi-strain frequency sweep tests, classified as per its respective test frequencies for the PU/ZIF-8 nanocomposites, with a) Storage modulus, *E*' (5 Hz), b) Loss modulus, *E*" (5 Hz), c) tan δ (5 Hz), d) Storage modulus, *E*' (15 Hz), e) Loss modulus, *E*" (15 Hz), f) tan δ (15 Hz), g) Storage modulus, *E*' (25 Hz), h) Loss modulus, *E*" (25 Hz), and i) tan δ (25 Hz).

C.7 Time-shift plots and WLF approximation plots for PU/ZIF-8 nanocomposites

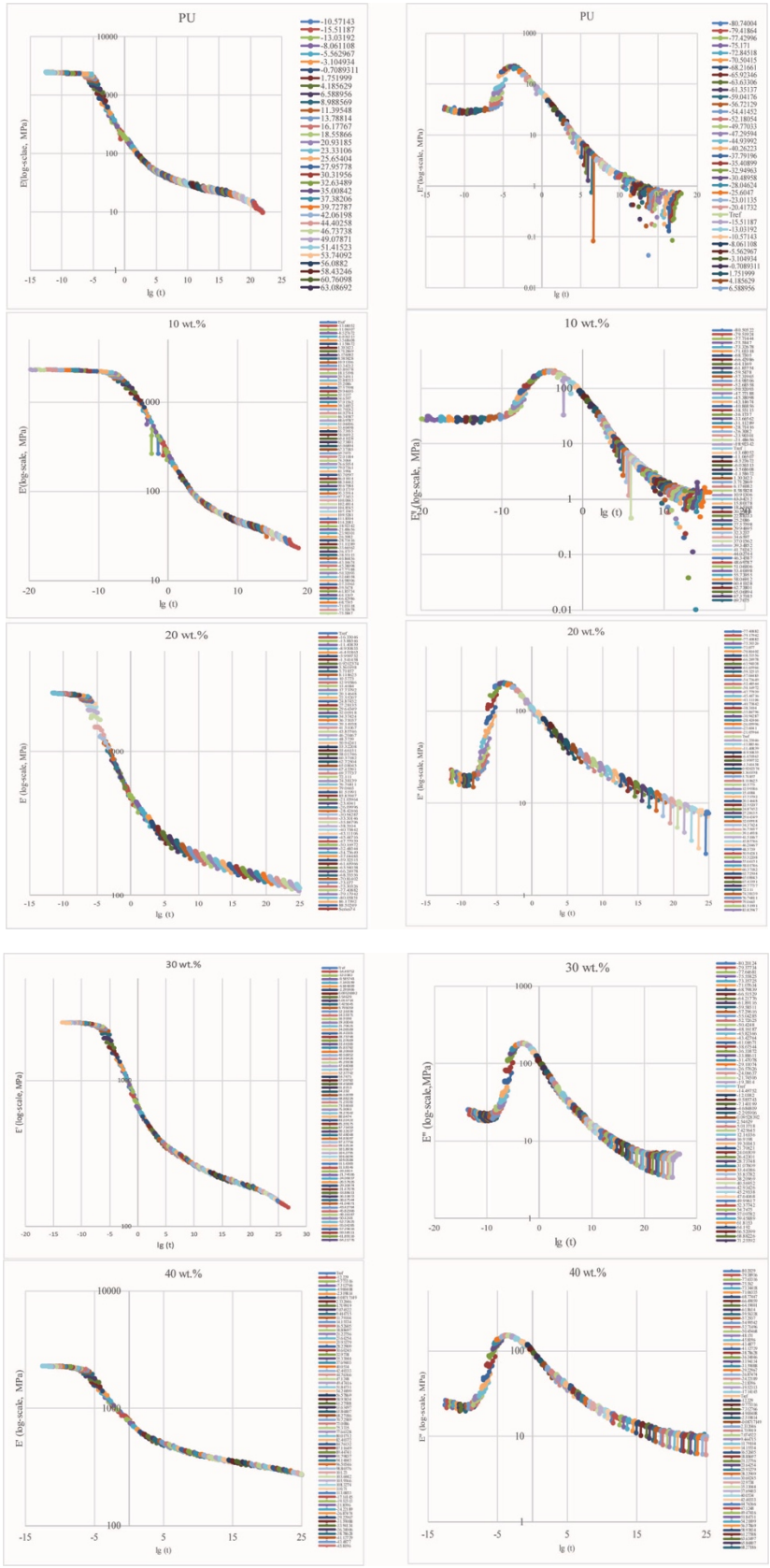

Raw data time-shift plots for the PU/ZIF-8 nanocomposites to generate a master curve

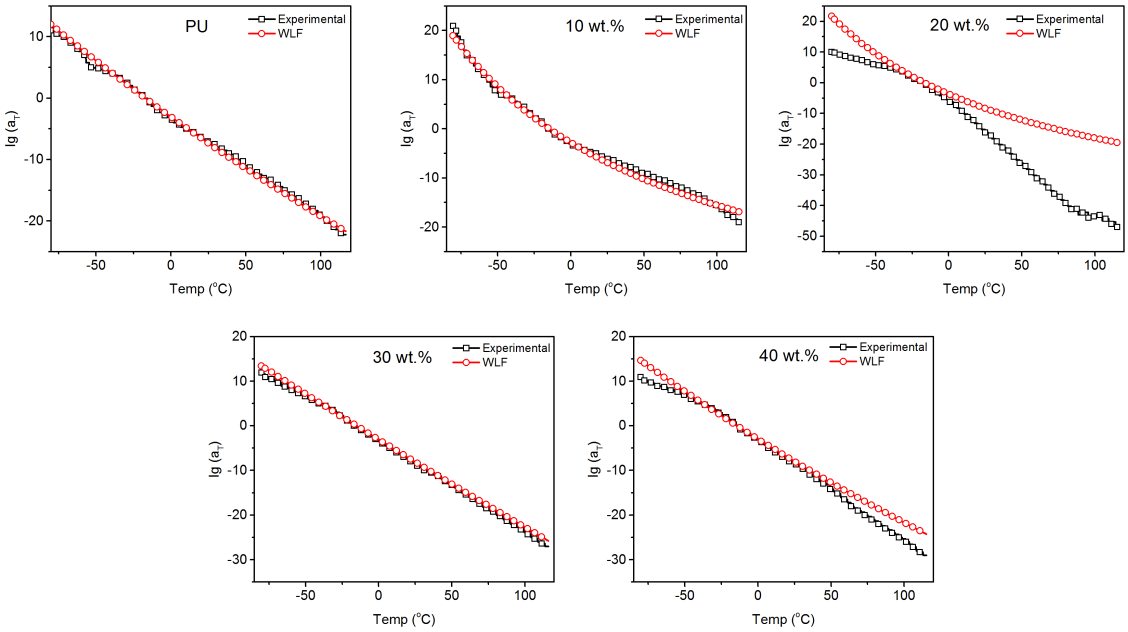

WLF approximation plots derived from the multi-frequency sweep experimental data of the PU/ZIF-8 nanocomposite. The T_{ref} in this case if the T_g of the nanocomposite, at ~-15 °C.

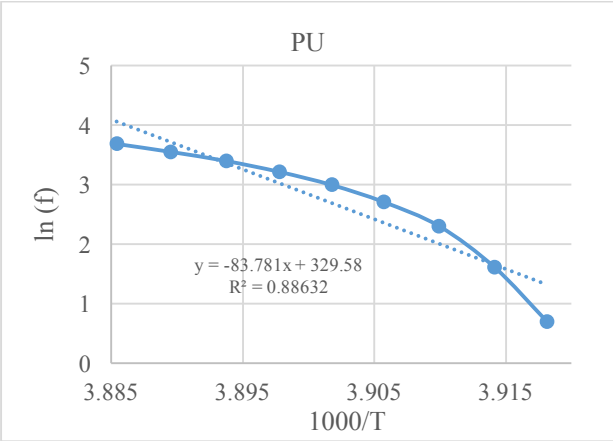

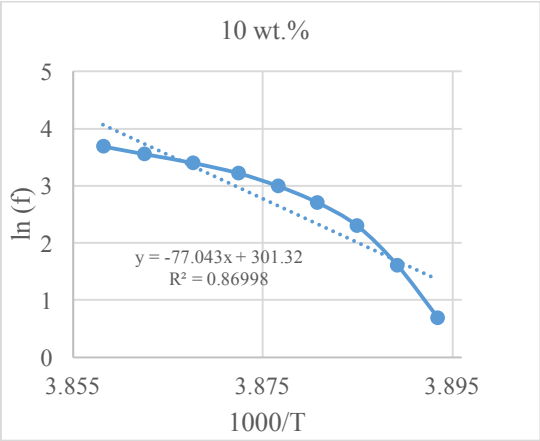

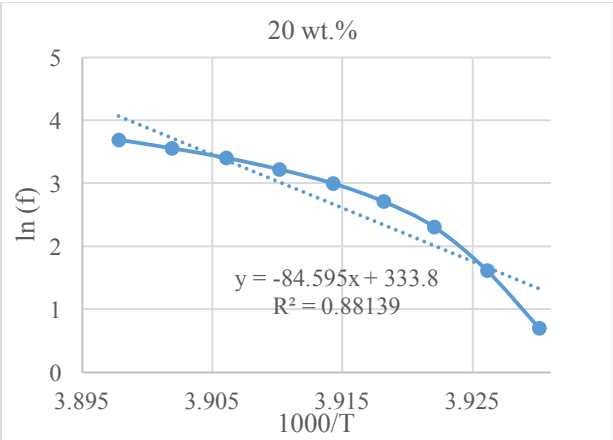

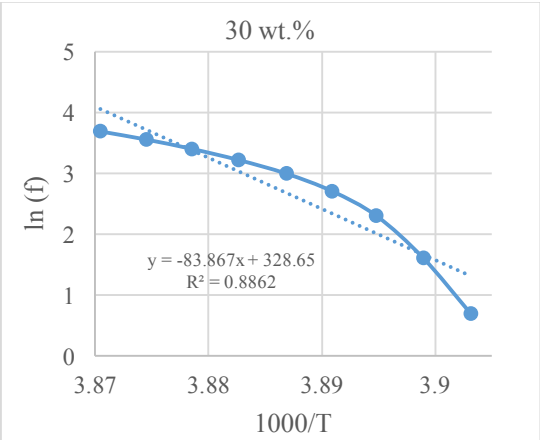

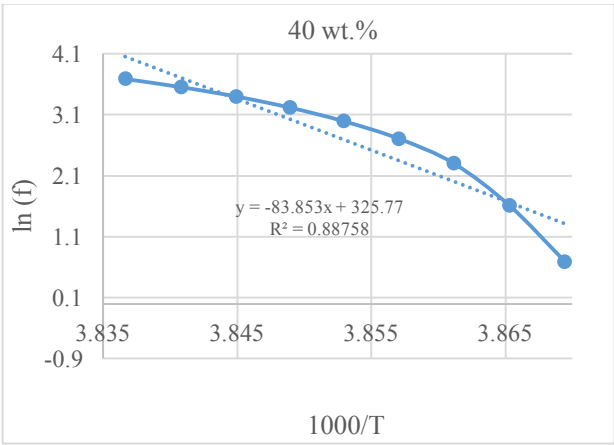

The determination of the activation energy for the PU and its nanocomposites. The straight line equation in each plots is analogous to Eqn. 5.1, where (E_a/R) = slope of the plots. The activation energies were taken from the T_g of the samples, at ~-15 °C, corresponding to the frequencies (2-40 Hz) and temperatures (within the range of -14 to -17 °C) associated with the T_g.

C.8 Modelling coefficients associated with the Ogden Model derivation

The coefficients associated with the Ogden Model of Hyperelasticity (N= 1, 2) for the nanocomposites, from PU, to PU/ZIF-8 30 wt.%, computed using Abaqus® (see Eqn. 5.2).

Samples	*N*	α_1	α_2	μ_1 (MPa)	μ_2 (MPa)
PU(S1)	1	1.89	NA	9.79E-2	NA
PU(S2)	1	1.64	NA	0.29	NA
PU(S3)	1	1.68	NA	0.26	NA
PU(S4)	1	1.70	NA	0.23	NA
PU(S5)	1	1.76	NA	0.16	NA
PU_ZIF8_10 (S1)	2	4.39	-2.89	1.19E-7	1.37
PU_ZIF8_10 (S2)	2	5.08	-2.85	2.15E-9	1.53
PU_ZIF8_10 (S3)	2	1.36	0.15	1.11	-0.76
PU_ZIF8_10 (S4)	1	1.64	NA	0.27	NA
PU_ZIF8_10 (S5)	2	1.70	-2.72	-0.36	5.32
PU_ZIF8_20 (S1)	1,2	Does not converge (*N* = 1,2)			
PU_ZIF8_20 (S2)	1,2	Does not converge (*N* = 1,2)			
PU_ZIF8_20 (S3)	2	1.81	-2.96	-0.11	2.31
PU_ZIF8_20 (S4)	2	1.72	-2.80	-0.11	2.73
PU_ZIF8_20 (S5)	1,2	Does not converge (*N* = 1,2)			
PU_ZIF8_30 (S1)	2	1.66	-2.64	-0.27	5.00
PU_ZIF8_30 (S2)	2	1.67	-2.67	-0.33	5.29
PU_ZIF8_30 (S3)	2	1.72	-2.72	-0.32	5.60
PU_ZIF8_30 (S4)	2	1.69	-2.71	-0.36	5.53
PU_ZIF8_30 (S5)	2	1.70	-2.72	-0.36	5.32

The Ogden model fitting was computed using $N = 1$, while the Ogden model fitting for the nanocomposites were computed using $N = 2$. Some samples did not converge, and the majority of the models did not converge at $N = 3$.

APPENDIX D

D.1 C_6H_{12} uptake studies (96 h)

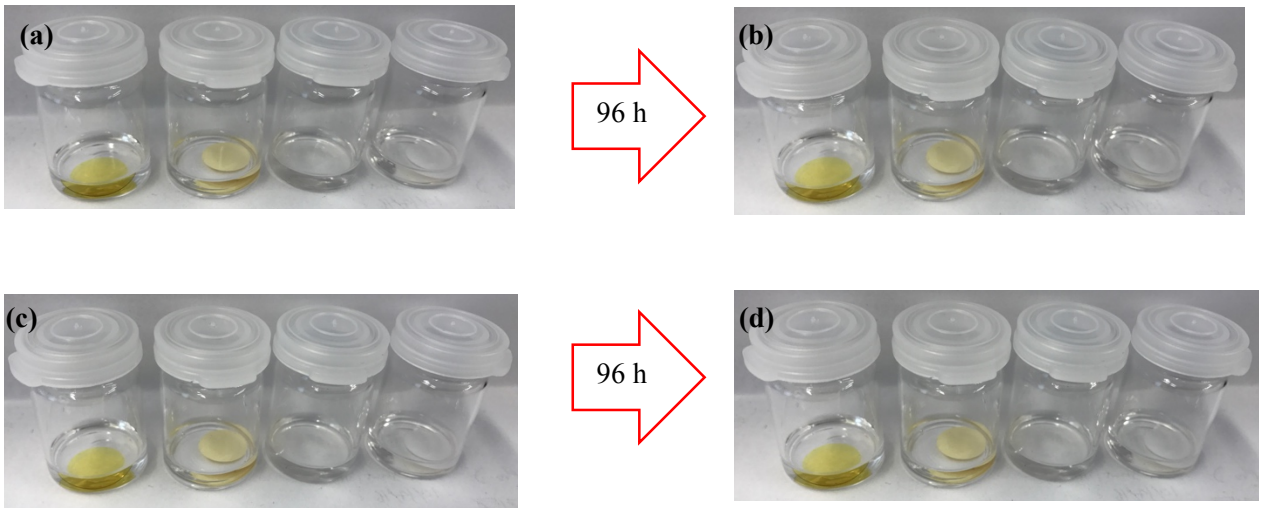

The C_6H_{12} adsorption studies, carried out for 96 h in two batches of samples to match the subsequent I_2 uptake studies of the samples and check for repeatability, where (a) sample batch 1 (from left-to-right, Matrimid, Matrimid/ZIF-8 30 wt.%, PU, PU/ZIF-8 30 wt.%) at t = 0, (b) sample batch 1 at t = 96 h, (c) sample batch 2 at t = 0, and (d) sample batch 2 at t = 96 h.

D.2 ZIF-8 capture of I_2 and C_6H_{12}

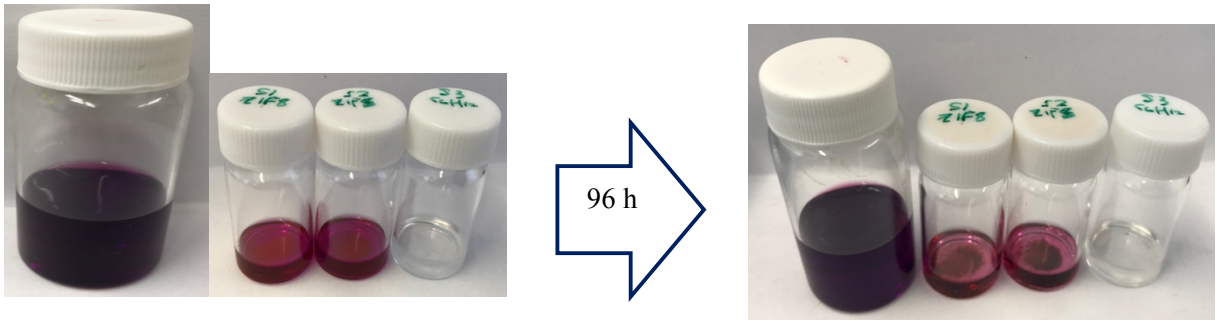

The ZIF-8 nanoparticles being immersed in I_2 (C_6H_{12}) and C_6H_{12}, with the left side representing the samples at t = 0 and the right side represents the samples at t = 96 h. The configuration in the image is, from left to right, I_2 (C_6H_{12}) acting as control sample, sample 1 of the ZIF-8 nanoparticles immersed in I_2 (C_6H_{12}), sample 2 of the ZIF-8 nanoparticles immersed in I_2 (C_6H_{12}), and ZIF-8 nanoparticles immersed in C_6H_{12}. Notice the subsequent discolouration of the I_2 solution after 96 h. It was speculated that the I_2 uptake capacity of the ZIF-8 nanoparticles (~ 6 mg) has reached its limit, hence unable to uptake anymore I_2 molecules, leaving the I_2 molecules at the same colouration after 96 h.

D.3 Sample raw data for EDAX of PU/ZIF-8 30 wt.% nanocomposite membrane with I_2

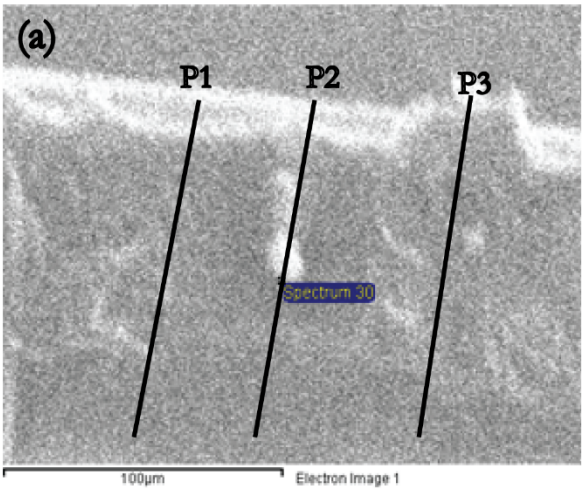

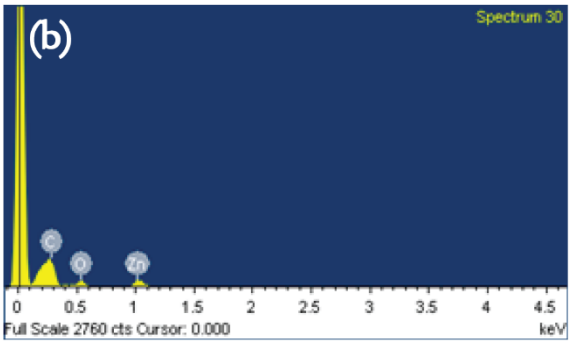

Spectrum processing: No peaks omitted

Processing option: All elements analysed (Normalised)

Number of iterations = 4

Standard:

C $CaCO_3$ 1-Jun-1999 12:00 AM

O SiO_2 1-Jun-1999 12:00 AM

Zn Zn 1-Jun-1999 12:00 AM

I Not defined 1-Jun-1999 12:00 AM

Element	Weight%	Atomic%
C K	51.49	69.09
O K	25.96	26.15
Zn L	15.84	3.91
I L	6.71	0.85
Totals	100.00	

A sample of an EDAX reading taken from a cross-sectioned PU/ZIF-8 30 wt.% sample, with (a) an SEM image of the cross section of the membrane sample, with the lines corresponding to the line scan location on the sample, where P1 = EDAX scans taken every 7 µm, P2 = EDAX scans taken every 10 µm, and P3 = EDAX scans taken every 20 µm, and (b) the elemental mapping of the samples corresponding to the scans, giving the wt. % and at. % of the elements present at that particular scan. In this case, from P2 at Spectrum 30 (see (a)). The line scans conducted at multiple locations was intended to be representative of the distribution of I_2 throughout the nanocomposite sample.

D.4 The calculation to determine the theoretical uptake of I_2 molecules in ZIF-8 sodalite cages

Size of I_2 molecules ~ 5.4 Å; size of ZIF-8 sodalite cages ~ 11.6 Å; size of ZIF-8 aperture ~ 5.6 Å; molecular weight of ZIF-8: 227.58 g mol^{-1}; molecular weight of I_2: 126 g mol^{-1}

Theoretically, 2 molecules of I_2 fits into one ZIF-8 molecule via its sodalite cage (assumption).

$$N_{\mathrm{I}_2\ uptake} = 2N_{ZIF-8}$$

$$\text{mol of } \mathrm{I}_2 = \frac{N_{\mathrm{I}_2\ uptake}}{N_A}$$

$$\text{mass of uptaken } \mathrm{I}_2 = \text{mol of } \mathrm{I}_2 * \mathrm{MW}_{\mathrm{I}_2}$$

where $N_{I2\ uptake}$ is the number of moles of I_2 uptaken by the samples, $N_{ZIF\text{-}8}$ is the number of moles of ZIF-8, N_A is the Avogadro constant, and MW_{I2} is the molecular weight of I_2.

The results of these calculations are tabulated in the table below, and used for Fig. 6.3 (b-c). Take note that the values here are assuming direct contact between I_2 and ZIF-8 nanoparticles, and also the fact that the uptake of I_2 for the nanocomposites are calculated, as the polymer matrix samples lack any ZIF-8 nanoparticles.

Samples	**mol of ZIF-8**	**# of ZIF-8 molecules**	**# of I_2 molecules**	**mol of I_2**	**mg uptaken I_2**
Matr_ZIF-8_S1	2.37E-05	1.42E+19	2.84E+19	4.74E-05	6.02
Matr_ZIF-8_S2	3.03E-05	1.82E+19	3.64E+19	6.06E-05	7.69
PU/ZIF-8_S1	1.98E-05	1.19E+19	2.37E+19	3.95E-05	5.02
PU/ZIF-8_S2	2.29E-05	1.38E+19	2.75E+19	4.59E-05	5.82
ZIF-8_S1	2.86E-05	1.71E+19	3.43E+19	5.71E-05	7.25
ZIF-8_S2	2.68E-05	1.61E+19	3.22E+19	5.36E-05	6.80

D.5 I_2 release in EtOH and H_2O

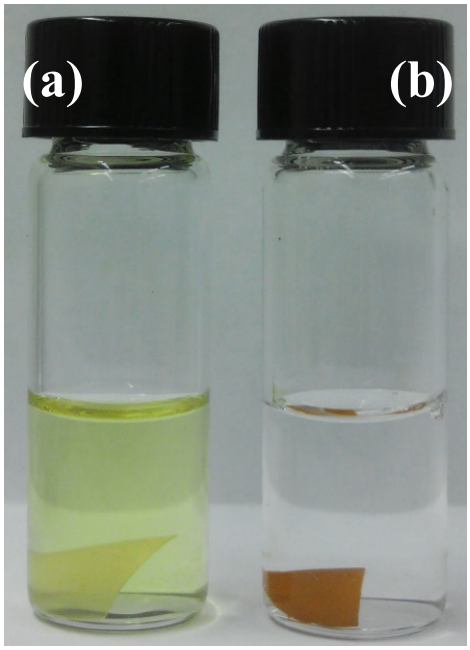

The vials above are of the PU/ZIF-8 30 wt.% I_2-absorbed samples being set up for desorption experiments, with (a) EtOH (ethanol) medium, and (b) H_2O medium. The samples were left to desorp for 10 days, and after 10 days, the I_2 desorp into EtOH, but was completely retained in H_2O, with no signs of I_2 being released into H_2O. This proves that polarity of the medium is instrumental towards the release of I_2 from the nanocomposites, however, they remain stable in H_2O.

D.6 Nanoindentation load-displacement data, averaged elastic moduli and hardness as a function of surface penetration depths of 2000 nm

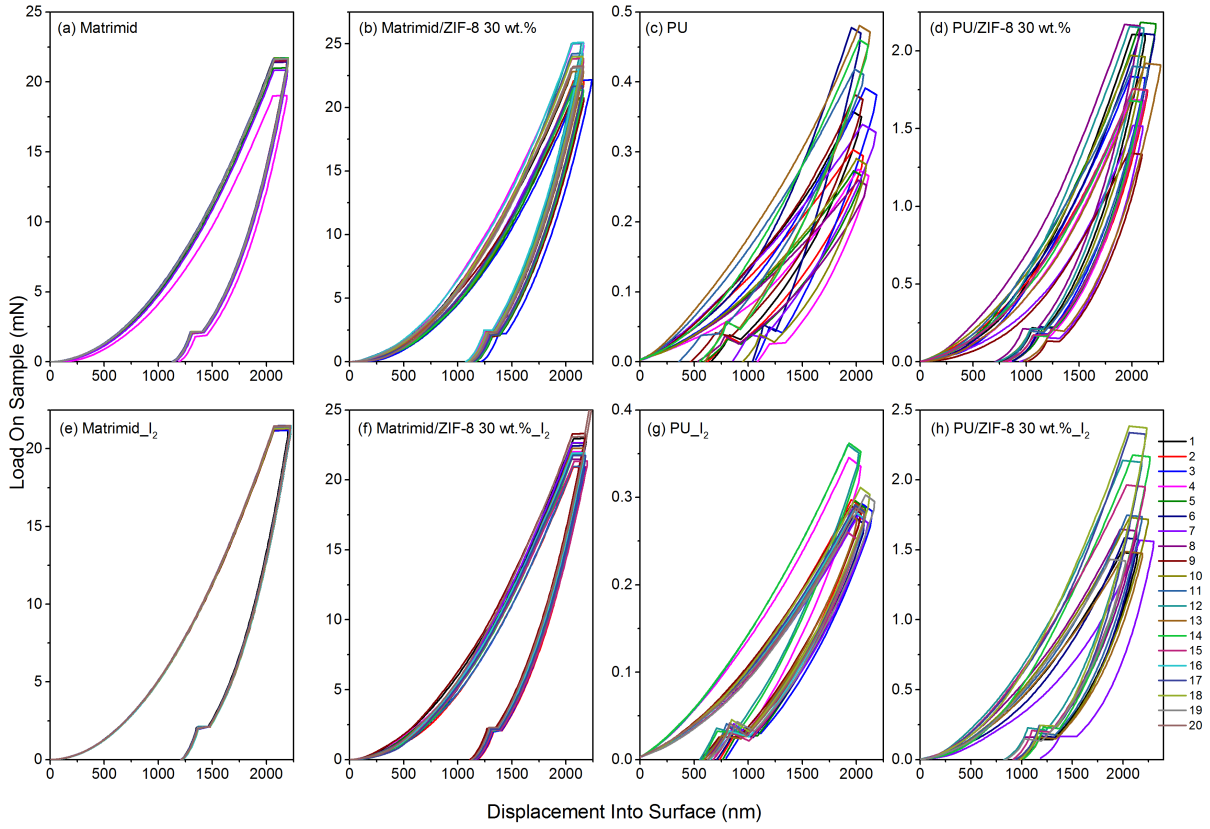

Nanoindentation load-displacement (*P*-*h* representative) plots for Matrimid, PU, and ZIF-8 nanocomposites, both blanks and loaded samples containing I_2, with (a) Matrimid (blank), (b) Matrimid/ZIF-8 30 wt.% (blank), (c) PU (blank), (d) PU/ZIF-8 30 wt.% (blank), (e) Matrimid (I_2 absorbed), (f) Matrimid/ZIF-8 30 wt.% (I_2 absorbed), (g) PU (I_2 absorbed), (h) PU/ZIF-8 30 wt.% (I_2 absorbed). Note that the relatively higher scatter for the PU and PU nanocomposite could be attributed to the hyperelastic response of PU matrix.

D.7 Complete compilation of the TGA plots

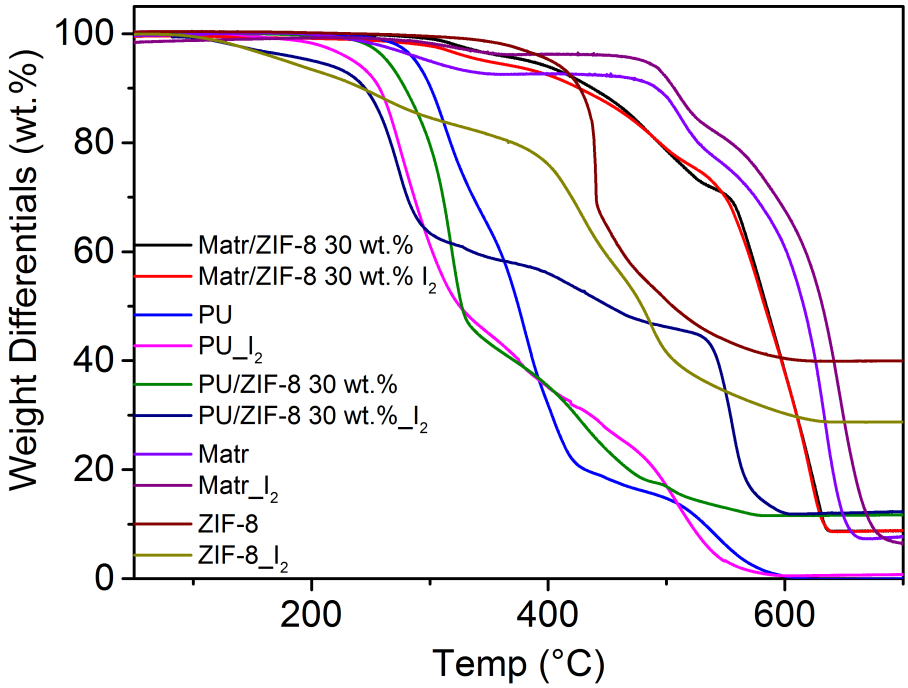

Compilation of the raw data pertaining to the TGA analyses of the polymers (PU, Matrimid), its nanocomposites (PU/ZIF-8 30 wt.% and Matrimid/ZIF-8 30 wt.%) and ZIF-8 nanoparticles pre-and post- I_2 adsorption.